UCLA
UCLA Electronic Theses and Dissertations

Title
Analytical Techniques to Investigate the Neurochemical Basis of Behavior

Permalink
https://escholarship.org/uc/item/425887vz

Author
Perrotta, Katie

Publication Date
2022

Peer reviewed|Thesis/dissertation

eScholarship.org
Powered by the California Digital Library
University of California

UNIVERSITY OF CALIFORNIA

Los Angeles

Analytical Techniques to Investigate the Neurochemical Basis of Behavior

A dissertation submitted in partial satisfaction of the
requirements for the degree Doctor of Philosophy
in Chemistry

by

Katie Perrotta

2022

© Copyright by

Katie Perrotta

2022

ABSTRACT OF THE DISSERTATION

Analytical techniques to investigate the neurochemical basis of behavior

by

Katie Perrotta

Doctor of Philosophy in Chemistry

University of California, Los Angeles, 2022

Professor Anne M. Andrews, Chair

My research combines electrochemistry, chromatography, and chemometrics to enable brain neurotransmitter monitoring *in vivo*. Microdialysis coupled with high performance liquid chromatography with electrochemical detection (HPLC-ECD) and voltammetry capitalize on the electrochemical properties of monoamine neurotransmitters, such as serotonin and dopamine. Electrochemical detection is a sensitive and selective detection method, which is beneficial in neurochemical analyses where brain neurotransmitters are present at nanomolar to micromolar concentrations

Fast-scan cyclic voltammetry (FSCV) has spatial and temporal advantages, but has poor analyte selectivity due to overlapping oxidation (and reduction) profiles of structurally similar neurochemicals and cannot be used to determine information on basal (tonic) neurotransmitter levels due to background subtraction. Dopamine is found at higher concentrations than other electroactive neurotransmitters in most brain areas, which makes it difficult to resolve other lower concentration neurotransmitters and to monitor multiple neurotransmitters simultaneously. No voltammetric techniques are currently available to monitor serotonin and dopamine simultaneously across timescales (phasic and tonic), despite the fact that these neurotransmitters play integrated roles in modulating behavior.

In my thesis research, I worked on developing a novel method for neurotransmitter co-detection— rapid pulse voltammetry coupled with partial least squares regression (RPV-PLSR). This approach is adapted from multielectrode systems (*i.e.*, electronic tongues). We constructed an initial RPV waveform using key oxidation and reduction potentials. In addition to faradaic currents, RPV utilizes capacitive currents, which are important for analyte identification. Including capacitive current also enables simultaneous tonic and stimulated neurotransmitter measurements. I carried out RPV-PLSR *in vivo*, to differentiate and quantify tonic and stimulated serotonin and dopamine associated with striatal recording electrode position, optogenetic stimulation frequency, and antidepressant administration. I investigated the contributions of cations and metabolites interferents to RPV and developed strategies to mitigate their effects. My research advanced our understanding of the interplay between the serotonin and dopamine

In addition to voltammetry, I used microdialysis for serotonin and dopamine co-detection throughout my thesis work. Microdialysis is used to monitor neurotransmitters in the extracellular fluid when combined with HPLC. Microdialysis experiments have commonly been performed using 20-minute sampling times to collect sufficient analyte for HPLC detection. However, long sampling times cause researchers to miss biologically relevant information happening at shorter timescales. Our group developed fast microdialysis that enables serotonin and dopamine co-detection with 2-5-min real-time sampling in awake-behaving mice. Using microdialysis, we discovered that selective optogenetic stimulation of dopamine neurons produces dopamine and serotonin release in the striatum highlighting the importance of multiplexed measurements and the interconnectedness of these transmitter systems.

Recently I discovered that selective optogenetic stimulation of dopamine neurons produces dopamine and serotonin release in the striatum highlighting the importance of being able to make multiplexed measurements and the interconnectedness of these transmitter systems in modulating behavior. I also used microdialysis to probe the effects of maternal stress and/or citalopram administration during pregnancy on adult offspring neurochemistry. Male offspring in the chronic unpredictable stress group had elevated serotonin levels during citalopram infusion and kappa opioid agonist injection compared to other treatment groups. These effects were paralleled with increased depressive- and anxiety-like behavior during the forced swim test and novelty suppressed feeding test in male offspring in the chronic unpredictable stress group.

Throughout the duration of my graduate studies I was a teaching assistant (TA) for the CHEM 184 Instrumental Analysis course at UCLA. As a TA I developed and implemented a new analytical chemistry lab for the course. Students detected mercury levels in various fish samples using Inductively Coupled Plasma Mass Spectrometry (ICP-MS) to learn about standard reference materials, matrix effects, and how to best optimize instrument parameters (kinetic energy discrimination). This work was recently published in the Journal of Chemical Education as a guide to carry out this experiment at other universities.

The dissertation of Katie Perrotta is approved.

Chong Liu

Kate Wassum

Joseph Ambrose Loo

Anne M. Andrews, Committee Chair

University of California, Los Angeles

2022

For Erin Beebe

1996- 2022

Table of Contents

Acknowledgements

First, I must acknowledge all the people I hold dear to me across the country. To my family- for their constant support and love. To my friends, especially Suzi, Chris, Nebiyat, and Joe- who manage to hold me up even from many miles away. You are all irreplaceable and a huge reason I was able to hit this milestone. To my friend Erin, who passed away unexpectedly this year- my biggest cheerleader from undergrad to all the way to graduate school and a person who had the purest love of science I have ever seen. To Keegan for all the nights spent working on our theses together.

Next, to my support system in Los Angeles. To Jonah- thank you, your parents, and brother for being the family I needed in LA. To Gabby- for being a comforting soul when I felt overwhelmed about graduate school and always going above and beyond for me. To Anthony- for being by my side from the very beginning of our Ph. D. program. To KC- for helping me through difficult moments and always believing in me. To Eli- for all your support during this transformative period of my life.

Finally, I must acknowledge everyone from UCLA who has made obtaining my degree a reality. To my mentor, Dr. Anne Andrews- thank you for all of your support and guidance throughout the duration of my graduate studies. To my committee members Dr. Kate Wassum and Dr. Chong Lui- for all their assistance on various research projects I worked on. To Dr. Joseph Loo- who I spent many years TAing for and has supported my endeavors. To my labmates, Olena, Merel, Sara, Cameron, and Noelle- you are all the most wonderful co-workers and even greater friends. I will always cherish the time we've spent together and the life-long relationships we've developed. Thank you, I literally could not have done it without all of you.

Vita

I received my Bachelor of Science in Chemistry and Neuroscience at Muhlenberg College in Allentown, PA. At Muhlenberg, I was actively involved in the chemistry department as an undergraduate researcher, student representative, and as president of the American Chemical Society Chemistry Club. I was a member of the Omicron Delta Kappa-National Leadership Honor Society, which recognized my strong leadership skills and academic standing. My research at Muhlenberg initially focused on using GC-MS to study olfactive synergy. However, my long-term research project investigated flavonoids in passion flower extract using HPLC/DAD-MS under the supervision of Dr. Christine Ingersoll. Passion flower extract was simultaneously evaluated for its ability to modulate the $GABA_A$ receptor by members of Dr. Jeremy Teissere's laboratory. I presented this research at the American Chemical Society Meeting in spring 2017.

During the summer of 2017, I participated in an NSF funded Research Experience for Undergraduates at the University of Michigan. There I worked for Dr. Julie Biteen and studied the thermal dependence of gold nanoparticle optical properties for nanothermometry. Through working on this project, I learned super-resolution fluorescence microscopy, spectroscopy, and dark-field microscopy.

I began my graduate studies in 2018 at the University of California, Los Angeles (UCLA) in the Chemistry and Biochemistry Department. I joined the lab of Dr. Anne Andrews in July of 2018. In Dr. Andrews' group, my research has focused on developing microdialysis methods and rapid pulse voltammetry for improved neurochemical detection. I presented data from the maternal stress project at Pittcon in 2019.

CHAPTER I

The Role of Serotonin in Depression and Anxiety

Introduction: The Serotonin Theory of Depression

The serotonin system has long been linked to the pathology of depression and anxiety. The serotonin hypothesis of depression stemmed from the monoamine hypothesis and a series of correlational studies, which suggested that low levels of serotonin are related to increased depressive symptoms.[1-4] In the 1950s, physicians noted that tuberculosis medications, namely isoniazid and iproniazid, improved the mood of hospitalized tuberculosis patients. Isoniazid and iproniazid were discovered to be monoamine oxidase inhibitors (MAOIs).[5] Monoamine oxidase is responsible for the metabolism of monoamine neurotransmitters, *i.e.*, dopamine, norepinephrine, and serotonin.[6] The MAOIs prevent degradation of the monoamine neurotransmitters, thus increasing their concentrations in brain tissue.[7] The tricyclic antidepressants (TCAs) were also serendipitously discovered to inhibit the reuptake of monoamine neurotransmitters. The MAOIs and TCAs are referred to as first-generation antidepressants.

The fact that MAOIs and TCAs improved mood and reduced anxiety led to the catecholamine hypothesis of depression proposed by Schildkraut, Bunney, and Davis in 1965.[8, 9] A role for serotonin came later when the TCA imipramine was discovered to inhibit serotonin reuptake, in addition to norepinephrine reuptake. Because TCAs were shown to inhibit serotonin reuptake and MAOIs were shown to affect serotonin synthesis, Coppen proposed that serotonin was important in the mood-improving properties of MAOIs and TCAs.[4] The serotonin theory has grown through studies that investigated the effects of tryptophan depletion on behavior, plasma or cerebrospinal fluid levels of serotonin and its metabolite 5-hydroxyindoleacetic acid (5-HIAA) in depressed patients or those with suicidal ideation, and brain serotonin levels in post mortem suicide victims.[1, 10-12]

Based on the evolving serotonin hypothesis and the fact that MAOIs and TCAs had many adverse side effects, *e.g.*, seizures, cardiac dysfunction, pharmaceutical companies set out to discover drugs that selectively impacted the serotonin system. In 1972, the pharmaceutical company Eli Lilly reported on the properties of fluoxetine, which was designated the most powerful and selective serotonin reuptake inhibitor at the time. Selective serotonin reuptake inhibitors (SSRIs) are currently the first line of treatment for depression and anxiety. The SSRIs block the reuptake of serotonin into presynaptic neurons. As per the serotonin theory of depression, many believe that treatment with SSRIs is associated with increased extracellular serotonin in the brain.[13] However, human brain serotonin levels after long-term SSRI use have never been measured directly.

Positron emission tomography (PET) imaging has been used to estimate brain extracellular serotonin levels in humans, rodents, pigs, and primates.[14] Although, PET does not directly measure serotonin levels, PET experiments have been performed simultaneously with microdialysis to measure extracellular serotonin levels directly in the medial prefrontal cortex of pigs. These experiments showed strong correlations between changes in extracellular serotonin determined by microdialysis and using PET to determine 5HT1B[15] and 5HT2A[16] occupancy, which indirectly approximates endogenous serotonin. A number of PET studies have been done in humans that investigated the effects of acute SSRI treatment.[17-20] Interestingly, some found no differences in endogenous serotonin levels between the SSRI group *vs.* the control group. [18, 20]

The distribution and binding of serotonin transporters (SERT) was studied with PET in patients with major depression and/or anxiety who received long-term SSRI treatment.[21] Several studies have shown decreased SERT binding in patients with major depressive disorder.[22-24] However, other studies observed increased SERT binding in specific brain regions in depressed subjects[25, 26] and, Meyer and coworkers did not observe changes in SERT binding potential between subjects with major depressive episodes and non-depressed subjects.[27, 28] Due to an association between serotonin levels and SERT expression, it is hypothesized that low SERT binding is related to lower serotonin levels in those regions.[21]

Treatment response to escitalopram or citalopram was related to the ratio of SERT binding in the amygdala or habenula to SERT binding in the median raphe nucleus prior to treatment.[29] The larger this ratio was, the larger the improvement in depression symptoms. Similarly, when comparing responders to SSRIs *vs.* non-responders, responders had larger ratios of SERT binding in the striatum to SERT binding in the raphe nucleus than non-responders.[30] These studies highlight that differences in SERT binding in serotonin neuron projection areas *vs.* the raphe nucleus can serve as predictors for antidepressant treatment success.

Because brain imaging is costly and because brain extracellular serotonin levels cannot be directly measured in humans, plasma serotonin levels have been investigated as a biomarker in patients diagnosed with depression.[31-33] Plasma serotonin levels are regulated by SERT on blood platelets.[32] Serotonin from the plasma is taken up into platelets, where it is either stored in granules or degraded. In an 8-week study, patients with major depressive disorder were treated with an SSRI and blood was taken at baseline, 4 weeks, and 8 weeks into the study.[33] Plasma serotonin levels were measured using an HPLC electrochemical coulometric array metabolomics platform[33] or UPLC MS/MS[31]. Patients who had higher baseline plasma serotonin levels and/or had the largest decrease in plasma serotonin concentrations over the course of treatment were determined to be the most responsive to treatment.[33] In a similar study, all depressed patients had an overall decrease in plasma serotonin concentration with SSRI treatment, but the distinguishing factor between those who responded to treatment *vs.* those who did not respond to SSRI treatment was the magnitude of the decrease in plasma serotonin concentration.[31] These studies point to using blood plasma levels, a more accessible assay than PET imagining, as a predictor of antidepressant treatment response. A limitation of these studies are that while SERT is encoded by the same gene in the periphery as the brain, plasma serotonin levels cannot be directly related to brain serotonin levels. An extensive review on measuring plasma serotonin levels in platelet-poor exposes large variability across .[34] A larger survey of literature that explores plasma biomarkers in depression and SSRI treatment can be found in these featured reviews, overall it is unclear whether plasma serotonin is suitable as a biomarker for depression.[35-38]

There are studies in rodents that directly investigate changes in extracellular serotonin following chronic SSRI administration. One microdialysis study using BALB/cJ mice, a mouse strain considered to have elevated anxiety-related behavior, investigated the long-term effects of fluoxetine administration.[39] While extracellular serotonin levels in the dorsal raphe nucleus (DRN) and hippocampus were higher overall in the fluoxetine group compared to the control group, serotonin levels decreased each week within the fluoxetine group. By day 28, extracellular serotonin in the hippocampus was no longer statistically different between the fluoxetine and control groups, which contradicts that idea that sustained elevations in serotonin levels is what causes SSRIs to have antidepressant effects. Another microdialysis study investigated the effects of infusing the SSRI, fluvoxamine, subcutaneously for two weeks *via* minipumps.[40] These authors observed increases in extracellular serotonin in the frontal cortex, but no changes in serotonin in the raphe nucleus after two weeks. These findings point to inhibitory auto receptors on serotonin neurons in the raphe nucleus regulating serotonin levels. However, it also supports the argument that elevated serotonin levels are not the cause of antidepressant response.

A current perspective on the serotonin hypothesis is that serotonin plays a complex role in encoding stress, anxiety, and depression that is not as simple as reduced brain/extracellular serotonin being causative of major depressive disorder or anxiety disorders.[41] However, the studies above highlight that disruption of the serotonin system has a large effect on SSRI treatment outcome, and depression and anxiety-like behavior even if the relationship between serotonin levels and behavior is not straightforward. Experiments that monitor changes in extracellular serotonin levels in the brain during behavior would help to unravel the complexities of the involvement of serotonin in the etiology of depression and anxiety disorders. In the next section, I discuss *in vivo* neurochemical sensing techniques for serotonin detection.

Neurochemical Sensors

Overview

Sensing neurochemicals *in vivo* presents an analytical challenge. Neurotransmitters can be present over wide ranges of concentrations, from micromolar to picomolar levels. The brain matrix contains proteins, amino acids, mono- and divalent cations, anions, and structurally similar metabolites of commonly studied neurotransmitters. Neurotransmitter detection *in vivo* requires methods that have high sensitivity and selectivity, ample temporal resolution to monitor fast neurochemical changes, yet are stable over time in the dynamic brain matrix to detect homeostatic changes, and are small enough to not induce major tissue damage. Sensing serotonin is especially difficult because serotonin is found at lower concentrations than structurally similar neurotransmitters and metabolites (*e.g.* dopamine, 5-HIAA, etc.) in most brain regions. Below are examples of neurochemical monitoring methods that have been adapted to sense serotonin in the brain.

Microdialysis

Microdialysis is a sampling technique that is coupled with chromatography to measure neurotransmitters with high selectivity. Microdialysis has been used extensively to correlate changes in neurochemistry with changes in behavior; some key studies will be discussed in later sections. In its early stages, the sampling time of microdialysis was 10-20 minutes. Long sampling times were required to accumulate enough dialysate for detecting low levels of neurotransmitters. Even with long accumulation times, serotonin concentrations are often close to the limit of detection. In older studies, SSRIs were used to elevate the basal serotonin levels to mitigate problems with detecting low serotonin levels. However, SSRIs modulate depressive and anxiety-like behaviors, potentially confounding behavioral data.[42]

Improvements in chromatographic columns, e.g., smaller stationary phase particle sizes, detectors, and instrumentation enabled us to reduce sampling times for serotonin from 20 min to 3 min[43] with standard high-performance liquid chromatography (HPLC) and ~1 min[44-46] with ultra-high pressure liquid chromatography (UPLC) for serotonin detection. Improved microdialysis sampling times enable us to observe that an injection of saline (an mild acute stressor) induced brief serotonin release in the ventral hippocampus (vHPC), a brain region that processes emotionally salient information.[43] Increases in basal serotonin levels post saline injection were captured when sampling at 6-min intervals, but not when using 30-min sample intervals. Improving sampling rates in microdialysis has been vital for capturing biologically relevant changes in neurochemicals that would have been previously missed. However, microdialysis still does not have the resolution to measure transient neurochemical release occurring on the order of hundreds of milliseconds.

Voltammetry

Voltammetry is another widely used neurochemical monitoring method that capitalizes on the electrochemical properties of monoamine neurotransmitters. Unlike microdialysis, fast-scan cyclic voltammetry (FSCV) has been used to detect endogenous dopamine transients.[47] Here, scan rates are 400-1000 V/s, which causes large capacitive currents. These capacitive currents (100s of mA) are much larger than the faradaic current (10s of nA) produced by electrochemical species in the brain. To monitor the faradaic current resulting directly from electron transfer when monoamine neurotransmitters (serotonin, dopamine, norepinephrine, histamine) are oxidized, the capacitive current must be removed through background subtraction in FSCV. Consequently, FSCV is only used to measure stimulated and not basal neurotransmitter levels in neurotransmitters. The latter is subtracted with the background. Additionally, fast scan rates shift the oxidation and reduction potentials of analytes such as neurotransmitters; oxidation and reduction peaks that are separated using slow-wave cyclic voltammetry now overlap using FSCV. Typically, the oxidation potential for dopamine, serotonin, and norepinephrine is ~0.6 V during FSCV, making these species difficult to distinguish from one another, particularly in a complex matrix such as the brain having other oxidizable species.

Serotonin is also difficult to monitor with FSCV because it produces oxidative byproducts that can foul electrode surfaces. The ‘Jackson’ waveform, a waveform developed for serotonin detection, used increased scan rates (400 V/s for dopamine *vs.* 1000 V/s for serotonin to "outrun" the adsorption of such byproducts.[48, 49] The waveform also resembles an ‘N’-shape (**Fig. I.1b.**), rather than the traditional triangle shaped voltage ramp used for dopamine detection (**Fig. I.1a.**), because the starting and hold potentials (0.2 V) are higher than the potential required to reduce serotonin (-0.1 V).

Altering aspects of the FSCV waveform has proven helpful in improving the detection of serotonin. The Venton group modified the Jackson waveform by extending the peak potential from 1.0 V to 1.3 V, resulting in the extended serotonin waveform (ESW).[50] They also made further modifications by using a slower scan rate and holding the peak potential at 1.3 V for 1 s, which they called the extended hold serotonin waveform (EHSW). Overall, the EHSW was more sensitive and the ESW was more selective, and both waveforms reduced electrode fouling by 50% compared to the Jackson waveform. Using a different approach, Shin and coworkers combined aspects of the Jackson waveform with square-wave voltammetry by superimposing square wave steps onto the N-shaped sweep.[51] This method, which they called N-shaped fast cyclic square-wave voltammetry, also allowed serotonin to be monitored with greater sensitivity than by the original Jackson waveform.

Like traditional FSCV, the aforementioned techniques cannot be used to measure basal serotonin levels. However, a voltammetry method called fast-scan controlled-adsorption voltammetry (FSCAV) was used to measure basal but not stimulated levels of neurotransmitters.[52] The FSCAV method employs long delay times (0.2-20 s) to accumulate serotonin on the electrode surface and the fast scan rates to oxidize the accumulated serotonin. The accumulated serotonin concentration estimates basal levels when delay times are long enough that serotonin accumulation plateaus. Another technique, called N-shaped multiple cyclic square wave voltammetry (N-MCSWV)[53] has also been developed for basal serotonin monitoring and has a higher temporal resolution (10 s) than FSCAV (20 s).

Because none of the above techniques can measure both stimulated and basal levels of neurotransmitters, our group developed a new technique called rapid pulse voltammetry (RPV) and coupled it with partial least squares regression (PLSR) for multiplexed detection of dopamine and serotonin across timescales.[54] Unlike the voltammetry methods discussed above, RPV-PLSR uses fast voltage pulses rather than sweeps to oxidize and reduce analytes

(**Fig. I.1c.**). Additionally, instead of subtracting capacitive current, RPV-PLSR identifies information in both the capacitive and faradaic currents as predictors for neurotransmitter concentrations, rather than relying solely on faradaic current. The voltammograms from pulse waveforms have unique decay characteristics, in which the capacitive and faradaic currents decay at different exponential rates, with capacitive current decaying faster. The difference in decay yields unique information about specific analytes at specific sampling points (we typically measure 8000 points per voltammogram). This information is used by a regression model, such as PLSR, to distinguish one analyte from another. Since the sampling rates for RPV-PLSR are very high (1 MHz) the decay profile contains a lot of unique information. We have used RPV-PLSR to identify and quantitate serotonin and dopamine at the same time so changes in these neurotransmitters can be related to one another.

Uniquely, a NeuroString sensor was reported for neurotransmitter monitoring in the brain and gut.[55] The NeuroString sensor was fabricated from a tissue-mimicking material consisting of a metal-complexed polyimide layer patterned onto an interconnected graphene/nanoparticle network that was then embedded into an elastomer. When coupled with FSCV, the NeuroString could multiplex dopamine and serotonin measurements in the gut and the brain. Dopamine and serotonin were distinguished during Pavlovian fear learning and when SSRIs were administered. The NeuroString also conformed to the gut to measure serotonin release by enterochromaffin cells.

Despite voltammetry being an effective way to observe and quantify fast neurochemical events, most voltammetry experiments are performed on head-fixed or anesthetized animals rather than freely moving (lightly tethered) animals, such as is done in microdialysis. A technique with high temporal resolution that can be used in truly freely moving animals will require wireless set-ups that are light weight so as not to interfere with movement or evoke stress responses. Wireless head-stage amplifiers have been reported for voltammetry in mice.[56-58] Once these are even lighter and more widely available, voltammetry techniques like RPV-PLSR can be used to answer more clearly how changes in extracellular serotonin encodes certain stress-associated behaviors and behaviors in large, more native environments.

Fluorescent Sensors

Fluorescent sensors have gained popularity mainly because they are more straightforward for neuroscientists to implement, have fast response times, and can be incorporated with behavior paradigms or optogenetics. Many labs that use optogenetics and calcium imaging can learn to transduce genetically modified fluorescent neurotransmitter sensors and to detect them with fiber photometry or two-photon imaging. Additionally, when genetically modified fluorescent sensors are used with two-photon imaging, changes in neurochemicals can be monitored at the single cell level.

Genetically modified fluorescent sensors have been developed for glutamate,[59, 60] GABA,[61] oxytocin,[62] endocannabinoids,[63] histamine,[64] norepinephrine,[65] acetylcholine,[66, 67] dopamine,[68-71] and serotonin.[72-74] To construct genetically modified fluorescent sensors, the Li group at Peking University used various G-protein coupled receptors as scafolds that were modified to include a fluorophore, which is quenched in the ligand-unbound state. When neurotransmitter (ligand) binds to the sensor, fluorescence emission increases. For example, to generate the $\text{GRAB}_{5\text{HT}}$ sensor, a circularly permutated green fluorescent protein (GFP) was inserted into the third intracellular loop of different serotonin receptors.[73] Due to better performance, the 5HT_{2C} receptor chimera was selected for further optimization and the improved sensor was called 5-HT 1.0. The 5-HT 1.0 sensor could be used to sense changes in serotonin *in vivo* during the sleep-wake cycle. In the basal forebrain there were increases in extracellular serotonin during wakefulness compared to sleep and lower levels during REM sleep compared to non-REM sleep, which were consistent with previous findings in the literature made using electromyogram and delta electroencephalogram recordings.[75]

The iSeroSnFR was developed by the Tian group at UC Davis using machine learning to optimize the binding of serotonin to an iAChSnFR scaffold.[72] Unlike the G-protein coupled receptor (GPCR) based sensors described above, iSeroSnFR is a microbial periplasmic binding protein- (PBP) based sensor, which means iSeroSnFR can be targeted to intracellular regions and had reduced responsiveness to exogenous drugs. The iSeroSnFR sensor also was also used to measure changes in serotonin levels in the sleep-wake cycle, as well as during social interaction paradigms. Interesting, iSeroSnFR was used to characterize human SERT activity in cell culture due to the ability of the sensor to be expressed both intracellularly and on the plasma membrane. Another approach to genetically encoded serotonin sensors was to use a serotonin-binding lipocalin tick protein as a scaffold for a fluorescent sensor.[76] The green fluorescent genetically encoded serotonin sensor (G-GESS) was similar to iSeroSnFR in that it could be expressed on both intracellular membranes and plasma membranes.

Another GPCR-based serotonin sensor, called PsychLight, was made using the $5HT_{2A}$ receptor.[74] The $5HT_{2A}$ receptor sensor was not only used to measured changes in serotonin levels, but it was incorporated into a cell-based pharmacological assay to predict the hallucinogenic potential of drugs that target $5HT_{2A}$ receptors. Drugs used to treat neuropsychiatric disorders target the $5HT_{2A}$ receptor. Atypical antipsychotics are most often used to treat schizophrenia and bipolar disorder. However, some atypical antipsychotics, like Abilify[77] and Rexulti,[78] have been approved for adjunctive treatment with SSRIs for major depressive disorder. By definition, psychedelics are considered to be psychoplasogens, *i.e.* small molecules that can induce neuroplasticity in a short period of time.[79] New data suggests that the antidepressant effect of psychedelics, which are also being investigated for the treatment of psychiatric disorders, stems from their ability to increase neuroplasticity.[80]

The Olsen group at UC Davis has been developing psychoplastogens that exhibit antidepressant effects but no longer have hallucinogenic properties.[81] Psychoplastogens were screened for hallucinogenic potential and differentiated from drugs that did not bind to $5HT_{2A}$ receptors using a assay based on PsychLight.[74] Drugs were considered to have hallucinogenic potential if the response of the sensor was above one standard deviation from vehicle when the assay was ran in agonist mode. Drugs that could bind to $5HT_{2A}$ receptor but did not have hallucinogenic potential did not cause the sensor to respond in agonist mode but would instead decrease signal in antagonist mode. Dong *et. al.* screened a designer drug, AAZ-A-154, for its hallucinogenic potential using the PsychLight assay. They determined that AAZ-A-154 lacked hallucinogenic properties by the assay and confirmed behaviorally *in vivo* the lack of hallucinogenic effects by the absence of head twitches. Overall, AAZ-A-154 was determined to be a non-hallucinogenic psychoplastogen that demonstrated promising antidepressant effects *in vivo.*

Aptamer-based Sensors

Methods for continuous recordings of brain neurochemical activity are constrained by the chemical properties of the analyte. For example, many neurotransmitters are not electrochemically active and thus, are not candidates for direct monitoring by voltammetry. Other neurotransmitters have no known selective catabolic enzymes that produce a product that can be monitored electrochemically.[82-84] The use of aptamers, single-stranded DNA or RNA, as biorecognition elements in sensing architectures is enabling an expansion of types of neuroactive molecules that can be selectively detected.

Our group has been developing In_2O_3 aptamer-field effect transistor sensors (aptamer FETs) for the selective and sensitive monitoring of various neurotransmitters.[85, 86] Sensing mechanisms using FETs involve detecting changes in charge distributions, *e.g.*, electric fields, at the surfaces of FET semiconductor channels. Like the fluorescent sensors, aptamers exist in either bound or unbound conformations. In one conformation, a majority of the aptamer is closer to the sensor surface while in the other conformation, the majority of the aptamer (and associated solvent ions) is closer to the sensor surface. Changes in bound *vs.* unbound conformations impact semiconductor conductance and hence, source-drain electrode current in a nonlinear manner with respect to target concentrations.

Recently, we developed and deployed aptamer FET probes *in vivo* to measure changes in serotonin.[87] The serotonin-aptamer-functionalized FETs on these Si probes detected changes in striatal serotonin levels prior to and following electrical stimulation of the dorsal raphe nucleus (DRN). Additionally, Gao and coworkers developed a graphene-based aptamer-FET sensor based on our serotonin and dopamine aptamers that was used for multiplexed dopamine and serotonin monitoring with limited crosstalk.[88] These graphene-based aptamer FET sensors were flexible and had reduced inflammatory responses,[89] as detected by histology for activated astrocyte (glial fibrillary acidic protein) and microglial (Iba1) markers. These multiplexed probes have not yet been used *in vivo*. Nonetheless, the Zhang group also developed dopamine-aptamer graphene-FET probes that detected changes in dopamine levels *in vivo* related to local administration of high potassium and bicuculline, a competitive antagonist of $GABA_A$ receptors. Another aptamer-FET sensor was developed by Lim *et. al.* that immobilized aptamers on carboxyl-functionalized polyacrylonitrile/poly(3,4-ethylenedioxythiophene) (PAN/PEDOT) nanohybrids.[90] This aptamer-FET sensor detected changes in serotonin in 0.6 s, which was faster than previously reported using aptamer FET sensors. Despite promising data *in vitro*, the PAN/PEDOT aptamer FET sensors have not yet been implemented *in vivo*.

Near-infrared Fluorescent Single-walled Carbon Nanotubes

To enable chemical imaging of neurotransmission in the extracellular space, the Landry group at UC Berkeley has developed a near infrared serotonin nanosensor (nIRHT).[91] The nIRHTs employ single-walled carbon nanotubes (SWCNTs) functionalized with a single-stranded DNA sequence (not an aptamer). These nanosensors had a large increase in relative fluorescence in the NIR II range (1000 to 1300 nm). When tested in brain slices, serotonin was detectable in the presence of 100 µM fluoxetine, MDMA, 25I-NMOMe, and quetiapine (drug molecules that are structurally similar to serotonin). These findings indicated that exogenous substrates did not interfere with serotonin detection. The library of DNA-based SWCNT sensors was expanded using machine learning.[92] Sequence features of DNA were used to train a convolutional neural network model that designated DNA ligands as being either high or low affinity for serotonin. Support vector machine models then predicted DNA sequence optical responses. Data from both models were used to predict large responses of DNA-SWCNTs. Overall, the machine learning approach produced five new candidate DNA-SWCNTs for serotonin that had higher relative fluorescence responses than the original nIRHT.

The NIR II spectral window had utility in transcranial imaging in mice, reaching a depth of greater than 2 mm with less than 10-µm resolution.[93] By administering nIRHT sensors intravenously into the tail vein, the need for craniotomy is circumvented, which eliminates tissue damage, immunological responses, and trauma associated with intracranial probe implantation that can affect neurochemical measurements.[93] A similar DNA-based single-walled carbon nanotube sensor was used *in vivo* to noninvasively measure endolysosomal lipid accumulation in Niemann-Pick disease, atherosclerosis, and nonalcoholic fatty liver disease models in mice.[94] The use of DNA-SWCNTs *in vivo* for lipid accumulation sensing makes their use in the brain a plausible future application.

Conclusions—Sensing Serotonin

Many advances have been made in the field of neurochemical monitoring since its inception in the 1980s. While it was previously difficult to sense serotonin in behaving animals, new techniques have been developed that expand the toolbox of serotonin sensing. The field of neuroscience has also grown with the development of optogenetics and chemogenetics for real-time circuit manipulation. Now, neurochemical monitoring can be coupled with circuit manipulation to record spatially and temporally resolved measurements in serotonin that relate to specific pathways and behaviors. In the next section, I will review studies that have already incorporated neurochemical monitoring with behavior.

Serotonin Sensing During Behavior

Behavior Tests

Laboratory tests such as the elevated plus maze (EPM), open field test (OFT), and novelty suppressed feeding test (NSF) are used to quantify anxiety-related behavior.[95] The EPM, OFT, and NSF place animals in an approach-avoidance conflict, *i.e.*, a brightly lit test area, In the NSF, animals are food-deprived for 12-24h prior to testing.[96] The forced swim test (FST), tail suspension test (TST), and sucrose preference test (SPT) are used to assess depressive-like behaviors, though these tests are generally less robust in their translational value.[97, 98]

The FST and TST place animals in stressful situations for short periods of time, *i.e.*, mice or rats are briefly forced to swim in a cylinder of water and or are suspended by their tails--in both cases, they cannot escape.[99] While the FST, TST, and SPT tests have been used extensively to predict antidepressant efficacy, the interpretation of their behavioral outputs is contested.[98, 100] Regardless, when taken together, these tests provide information about behavioral changes between animal control and treatment groups even if the interpretation of the behavioral changes is open to interpretation.

Learned Helplessness

The learned helplessness paradigm is used to model a particular aspect of human depression.[101] In the learned helplessness paradigm, rats or mice are subjected to shock stressors in which one group, the escapable stress group, has the ability to terminate the stimulus for both groups. The other group, the inescapable stress group, has no control over termination of the stressor and develops learned helplessness.

Inhibition of the medial prefrontal cortex (mPFC) by muscimol, a $GABA_A$ agonist, causes the behavioral and neurochemical phenotypes between controllable and uncontrollable stress during a learned helplessness paradigm to become indistinguishable.[102] Microdialysis was used to monitor changes in extracellular serotonin levels in the dorsal raphe nucleus (DRN) during the learned helplessness paradigm in rats in the inescapable and escapable stress groups. Untreated rats in the inescapable group had elevated levels of extracellular serotonin in the DRN in response to the shock stressor, which were sustained even after the shock was terminated. Untreated rats in the escapable stress group did not have changes in extracellular serotonin. When muscimol was injected into the mPFC, rats in the inescapable stress group had elevated basal extracellular serotonin levels, the same as untreated rats in the inescapable stress group. However, when muscimol was injected into the mPFC of rats in the escapable stress group, they began to have sustained increases in extracellular serotonin levels in the DRN during the stressor, similar to what was observed in the inescapable stress group.

Both groups were conditioned to context and taught how to escape a shuttlebox, where freezing and escape efficiency were assessed. When muscimol was injected in the mPFC, the escapable stress group displayed increased freezing behavior and poor escape from the shuttlebox compared to mice in the escapable stress group that did not receive muscimol. This study implicates the mPFC and serotonin release in the DRN as important in distinguishing controllable stress *vs.* uncontrollable stress in learned helplessness.

A voltammetry study demonstrated that extracellular serotonin levels decrease in the DRN when the mPFC was electrically stimulated, which reinforces the connection between the modulation of the mPFC and changes in extracellular serotonin levels in the DRN.[103] The escapable stress group displayed no change in extracellular serotonin levels in the DRN when presented with the stresser, which suggests that when you have the choice to escape, the mPFC becomes engaged.[104] By this logic, when you do not have the choice to escape the mPFC would then become inhibited. If inescapable stress results in inhibition of the mPFC, it would support that muscimol injection into the mPFC did not change behavior or neurochemistry in the inescapable stress group, since this region would already be under inhibitory control. A means of inhibiting glutamate neurons in the mPFC is to activate GABA interneurons in the mPFC.

In a similar study by Amat *et.al.*, extracellular serotonin levels were elevated in the vHPC during the stressor in the inescapable stress group.[105, 106] Activation of the pathway from the vHPC to the mPFC plays a role in anxiogenic behaviors.[107] Fibers from the vHPC make a direct synapse onto GABAergic neurons in the mPFC[108] and these GABAergic interneurons project onto glutamatergic pyramidal neurons, which are the main output neurons of the mPFC.[109] Glutamatergic outputs from the mPFC to the DRN project predominantly onto GABAergic neurons in the DRN, which then inhibit DRN serotonin neurons. Taken together, increased serotonin levels in the hippocampus during inescapable stress could lead to increased levels of serotonin in the DRN through inhibition of glutamatergic neurons in the mPFC and disinhibition of serotonin neurons in the DRN.

Alternatively, the amygdala is an important brain region in processing and detecting threatening and fearful stimuli that also sends projections to the mPFC.[110] Similar to inputs from the hippocampus, the projections from a subregion of the amygdala, the basolateral amygdala (BLA), to the mPFC are primarily glutamatergic and synapse onto either GABA or glutamate neurons.[111] There is a robust amount of information about involvement of the BLA in fear learning, especially the communication of the BLA with the central amygdala (CeA) to drive fearful behaviors when a conditioned stimulus (CS) was presented.[112]

The BLA also had increased extracellular serotonin levels when the rat was presented with an inescapable stressor.[113] Similar to how glutamatergic projections from the vHPC could activate GABA interneurons in the mPFC, glutamatergic projections from the BLA could also inhibit the mPFC through activation of GABA interneurons. However, isolated changes in extracellular serotonin levels in the BLA, vHPC, and DRN does not provide a complete picture of what could be a very complex circuit that is being relayed through the mPFC. A table summarizing relative changes in serotonin during the learned helplessness paradigm can be found in **Table I.1**.

Fear Conditioning

Fear conditioning is an associative learning paradigm. Fear conditioning is based on classical conditioning first reported by Pavlov in the early 20th century. The same terms used to describe classical conditioning have been adapted for use in fear conditioning.[114] Typically, fear conditioning involves learning an association between a neutral stimulus and an unconditioned stimulus.[115] A neutral stimulus, e.g., tone or light, evokes no inherent behavioral response. By contrast, an unconditioned stimulus, e.g., foot shock, evokes a naturally occurring (unlearned, automatic) behavioral response. In the case of fear conditioning, the unconditioned stimulus specifically evokes a fear-related response, e.g., freezing or darting in rodents. Once an association is learned, the neutral stimulus is "conditioned" and will produce the same behavior as the unconditioned stimulus.

In a microdialysis study, rats were contextually conditioned to their test arena (shock chamber).[116] Extracellular serotonin levels in the mPFC were recorded while the rats were in their home cage and when they were returned to the shock chamber for 30 minutes. When rats were placed back into the shock chamber, extracellular serotonin levels in the mPFC increased. Interestingly, freezing behavior did not positively correlate with extracellular serotonin. Extracellular serotonin levels also increased as freezing behavior decreased with time spent in the chamber, which further implicated that changes in serotonin did not directly correlate with fearful behavior resulting from fear conditioning.

In another microdialysis study, rats were exposed to two foot shocks that were one hour apart.[117] During the first foot shock, there were large increases in extracellular serotonin in the vHPC. The authors claim there was no change in extracellular serotonin levels during the second shock, however, in this experimental paradigm 10-minute sampling was used, which may be too long to detect smaller acute changes in extracellular serotonin. Although there was no significant increase in extracellular serotonin, there appears to be a slight increase in the time course that could be distinguished with a more temporally resolved method.

In fact, when psychLight was used to measure changes in serotonin levels in the bed nucleus of the stria terminalis (BNST), DRN, BLA, and the orbitofrontal cortex (OFC) complex changes were observed during behavior.[74] In the BNST, serotonin decreased during the shock before returning to baseline. In the DRN, serotonin initially increased when the shock was initiated, but ultimately decreased during the shock. Oppositely, in the BLA and OFC serotonin decreased during the shock but then increased after the shock was terminated. Decreased serotonin levels in the BLA during the administration of a foot shock that then increased was also observed using the 5HT 1.0 sensor.[73] The 5HT 1.0 sensor authors also monitored serotonin in the BLA and mPFC when the cue was presented prior to the shock during their fear learning paradigm. During presentation of the cue BLA serotonin levels gradually increased across the 10 s period. Serotonin levels in the mPFC quickly increased and plateaued when the 10 s cue was presented, but then decreased when the shock was presented before increasing once more.

In many of the fear conditioning studies serotonin levels changed in opposite directions compared to what was observed during the presentation of the shock in the learned helplessness paradigm above. There are two possible reasons for this: 1) inescapable stress in the learned helplessness paradigm does not involve Pavlovian learning and/or 2) many of the learned helplessness studies used microdialysis whereas the fear conditioning studies used genetically modified fluorescent sensors. Differences in temporal resolution may provide different outcomes in the data.

For example, a foot shock induced a decrease in serotonin levels in the BLA that then increased following the shock. Using microdialysis with 20 min sampling, the brief decrease in serotonin would be missed and it may appear that the observed increase was due to the shock itself. Further experimentation would be required to fully understand the region-specific differences in serotonin responses between learned helplessness and fear conditioning paradigms. A table summarizing relative changes in serotonin during the fear conditioning paradigm can be found in **Table I.2**.

Forced Swim Test

The forced swim test is also used to assess depressive-like behavior.[100] The mouse or rat is placed in a cylinder of water, where researchers observe the mobility of the subject. It is thought that mice float because they have given up and are therefore more depressed.

However, there has been recent skepticism of whether immobility is actually a sign of a depressive-like phenotype or if they become immobile for other reasons.

When a deep brain stimulation treatment was administered prior to the forced swim test, rats exhibited increased antidepressant-like behavior compared to those not receiving deep brain stimulation.[118] Deep brain stimulation of the subcallosal cingulate gyrus has been a promising treatment option for human patients that have treatment-resistant depression. To study further the effects of deep brain stimulation treatment in rats, experiments were conducted in a homologous region, the medial prefrontal cortex (mPFC).[119] By performing microdialysis during deep brain stimulation of the mPFC, Hamani *et al.* observed increased in extracellular serotonin levels in the dorsal hippocampus during stimulation that were sustained after the treatment was terminated.

The hippocampus is a brain region of interest in the study of depression and anxiety, however the current experimental design did not provide a way of directly connecting increased dorsal hippocampal extracellular serotonin levels during deep brain stimulation of the mPFC to reductions in immobility during the FST following treatment. Despite the pathway not being studied directly, hippocampal serotonin release in the extracellular space during deep brain stimulation cannot be entirely ruled out as a possible mechanism for reductions in immobility during FST following deep brain stimulation.

Other microdialysis studies demonstrated that extracellular serotonin levels decrease in the vHPC and the mPFC, did not change in the DRN, and increase in the amygdala and medial raphe nucleus (MRN) during 5 minutes of forced swim stress.[120, 121] However, longer periods of forced swim stress 8-30 min resulted in extracellular serotonin increasing in the mPFC and striatum, and decreasing in the amygdala.[120, 122] It is possible that longer periods of forced swim stress were processed differently in the brain than acute swim stress, resulting in increased extracellular serotonin in the mPFC and decreased extracellular serotonin in amygdala. However, changes in extracellular serotonin levels in the vHPC during forced swim stress were inconclusive because 5-minute and 30-minute swim stress resulted in decreased extracellular serotonin levels, whereas 8-minute swim stress caused increased hippocampal serotonin.[122] In the 8-minute study, serotonin was sampled at 3 minutes, and the other studies used 10-20 minute sampling. The 3-minute sampling could have caught information that longer sampling times were missing since extracellular serotonin levels dipped below baseline immediately following forced swim stress before increasing. A table summarizing relative changes in serotonin during the forced swim test can be found in **Table I.3**.

Social Interaction

Rodents are social creatures, so studying aspects of their social interactions is helpful in trying to investigate disorders where social behaviors are altered like in autism spectrum disorder and social anxiety.[123] One of the oldest social behavior tests, the social interaction test, was developed to measure anxiety in a very simple and straightforward way. Another test to measure anxiety is the social approach/avoidance test. In the approach/avoidance test, the apparatus contains three chambers, one which contains the unfamiliar animal and is separated by a transparent wall. The other two chambers are unequal.[124] The larger chamber is connected to the transparent wall and considered the social compartment. The smaller chamber is further from the transparent wall and considered the non-social compartment. Beyond these tests, other social behavior tests to analyze social avoidance are the social preference-avoidance test, the three-chambered social approach test, the partition test, and the modified Y-maze test.

Genetically modified fluorescent sensors are advantageous because they provide the opportunity to record from multiple brain regions at once using multi-site fiber photometry.[72]

Changes in serotonin levels were monitored simultaneously in the OFC, BNST, and BLA during social interaction. In the presence of an intruder, serotonin increased in the OFC and BLA but didn't change in the BNST.

Lv *et al.* implicates the DRN → mPFC pathway to be involved in social exploration behaviors when mice had been socially isolated for 5 weeks.[125] Following social isolation, mice displayed increased social interaction behaviors in the three-chamber social preference test compared to control mice. However, when the DRN → mPFC was activated using chemogenetics, the mice that were socially isolated became more antisocial. Additionally, serotonin levels were measured in the mPFC by 5HT 1.0. Following the onset of sniffing behavior when mice were initially introduced to one another, mice that were group housed had a large increase in serotonin levels, but mice that underwent chronic social isolation did not. A table summarizing relative changes in serotonin during social interaction tests can be found in **Table I.4**.

Elevated Plus Maze

The elevated plus maze (EPM) is an approach-avoidance behavior test.[95] It is the most frequently used behavior test to study anxiety-related behavior. Findings from our lab have shown a positive correlation between elevated anxiety-related behavior in the EPM and increased extracellular basal serotonin in the vHPC.[126] The raphe nucleus contains serotonin cell bodies which send serotonin projections across the brain. The dorsal raphe nucleus (DRN) projects primarily to the dHPC, while the median raphe nucleus (MRN) projects primarily to the vHPC. Changes in EPM behavior and serotonin release in the vHPC have been studied when the DRN[127] and MRN[128] were lesioned.

When subjects were placed in an aversive environment, like the EPM, extracellular serotonin levels in the vHPC increased. Both rats that had DRN lesions and sham lesions, had increased serotonin levels in the vHPC when in the EPM.[127] However, when rats had MRN lesions, serotonin levels in the vHPC no longer change when the rats were in the EPM.[128] Interestingly, rats with either DRN and MRN lesions had no differences in % entries into open arms or % time spent in open arms compared to control and sham lesioned rats.[127, 128] Therefore, according to this study, anxiogenic behavior in the EPM is not be related to acute serotonin increases in the vHPC. A table summarizing relative changes in serotonin during social interaction tests can be found in **Table I.5**.

Conclusion

The above studies highlight the utility of monitoring serotonin during behavior. However, the experimental design of these studies made it difficult to implicate the involvement of certain pathways during a behavior. Many of the above studies suggest that increased serotonin in the vHPC was related to increased anxiety-like behaviors. However, microdialysis in lesioned rats during the elevated plus maze, one of the most robust behavior tests to assess anxiety-like behavior, suggests that changes in serotonin levels in the vHPC did not impact anxiety-like behavior. Lesion studies did not represent endogenous conditions and inhibition of serotonin neurons in DRN → vHPC or MRN → vHPC by optogenetics or chemogenetics may be a better indicator of how changes in these pathways modulate anxiety-like behavior. In the next section I will highlight literature that used optogenetics and chemogenetics to modulate serotonin circuits during specific behaviors.

Optogenetics and Chemogenetics During Behavior

Optogenetics and Chemogenetics

Optogenetics is a genetically engineered method of controlling subpopulations of neurons with light.[129, 130] An opsin, a naturally occurring light responsive protein, becomes selectively expressed in specific neuronal types through transduction of an adeno-associated virus (AAV) containing the opsin. Once expressed, LEDs or lasers can then be used to activate or inhibit these neurons. The concept of optogenetics was first published in 2005 by Boyden *et. al.* using channelrhodopsin 2.[131] However, since then there have been a number of new excitatory and inhibitory opsins developed with varying excitation wavelengths and temporal dynamics.[132-135]

Alternatively, chemogenetics modulates neuronal populations using designer receptors exclusively activated by designer drugs (DREADDs).[136-138] Similar to opsins, DREADDs are expressed in specific neurons through the transduction of AAVs. The DREADDs are made by modifying G-protein coupled receptors so that they are activated by synthetic compounds that are not endogenous to the brain.[139] One of these drugs is clozapine N-oxide (CNO), though other synthetic ligands have since been developed for chemogenetics because CNO is metabolized into clozapine, an antipsychotic.[140]

DRN

DRN → BNST

Serotonin neurons projecting from the DRN to the BNST play a role in fear behavior.[141] During a footshock *c-fos* was significantly elevated in DRN neurons that specifically project to the BNST. When serotonin neurons projecting from the DRN to the BNST were optically stimulated during a fear conditioning paradigm, NSF, and the EPM, mice demonstrated increased freezing behavior during both cued and contextual fear recall, increased latency to feed, and spent less time in the open arms during the EPM compared to control mice. More specifically, activation of serotonin neurons in the BNST that express $5HT_{2C}R$ were important in increased latency to feed.

Conversely, Garcia-Garcia showed that BNST activation decreased latency to feed and resulted in anxiolytic behavior in the EPM.[142] When an antagonist of $5HT_{1A}$ receptors, WAY 100 635, was locally infusing into the BNST, stimulation of the BNST then induced increased latency to feed and decreased open arm time compared to control mice. These data suggested that $5HT_{1A}R$ activation in the BNST was what caused anxiolytic behavior. Additionally, when BNST neurons were inhibited, mice would then explore the open arms less than control mice. However, Marcinkiewcz *et. al.* suggests that $5HT_{1A}$ receptors on BNST neurons did not modulate anxiety behavior under basal conditions but become involved during threatening conditions.[143] While Garcia-Garcia suggest that activation of the DRN → BNST is anxiolytic, nonspecific optical stimulation of the BNST supports the findings by Marcinkiewcz that excitation of DRN → BNST anxiogenic and inhibition was anxiolytic.[144, 145]

DRN → LHb

Zhang and coworkers demonstrated that stimulation of serotonin neurons in the DRN → lateral habenula (LHb) pathway reversed depressive-like behavior induced by chronic unpredictable mild stress (CUMS).[146] Mice that underwent CUMS had increased immobility in the FST. However, when the DRN → LHb pathway was optically activated, CUMS mice then had immobility time that was no different from control mice.

DRN → VTA/SN

Activation of serotonin neurons in the DRN but not the MRN induced decreased immobility in the FST.[147] Similar effects were observed when serotonin terminals in the ventral tegmental area/substantia nigra (VTA/SN) were stimulated. Together, these data suggested that serotonin projections from the DRN to the VTA/SN were likely involved in antidepressant behavior. A table summarizing relative changes in serotonin when projections from the DRN are activated or inhibited can be found in **Table I.6**.

mPFC → DRN

Hamani and coworkers used electrical stimulation of the mPFC to evoke antidepressant behavior in the FST.[118] When the mPFC was non-specifically optically activated, mice did not display changes in immobility in the FST.[148] However, when the specific glutamatergic pathway between the mPFC and the DRN was stimulated, the mice had increased kicking frequency compared to when the laser was not turned on.

Faye *et. al.* showed that when the mPFC → DRN pathway was optically activated mice had decreased latency to feed and increased number of open arm entries. that appears to be mediated by $5HT_4$ receptors in the mPFC.[149] Activation of $5HT_4R$ receptors in the mPFC were important in reducing anxiety-like behavior. Local infusion of a $5HT_4R$ agonist, RS67333, into the mPFC induced anxiolytic behavior in the EMP and NSF without impacting overall locomotor behavior or food consumption. Similarly, when mice were systemically given a $5HT_4R$ agonist, mice demonstrated anxiolytic behavior that was terminated when the mPFC → DRN pathway was optically inhibited.

When the glutamatergic pathway between the mPFC and the DRN was optically stimulated, mice that underwent social defeat stress had increased latency to their first entry into the interaction zone when a novel target was present.[150] Conversely, when the pathway was inhibited, socially defeated mice had decreased first latency into the interaction zone and spend more time in the interaction zone compared to when the laser was off. Grizzell and coworkers showed that acute social defeat stress activated the mPFC → DRN pathway.[151] The more the mPFC → DRN pathway was engaged the higher the likelihood of the hamster to fight back and/or the longer it took for the hamster to be overtaken by the aggressor, which overall pointed to higher stress resilience.

In a study by Prakash and coworkers, mice that underwent social defeat stress were characterized as being either resilient or susceptible to stress.[152] In both resilient and susceptible mice, there were a reduced number of GLUT3+ neurons in the DRN. However, the number of VGLUT3+ and TPH2+ co-expressing neurons were only decreased in stressed mice that were in the resilient group. A table summarizing relative changes in serotonin when projections from the mPFC are activated or inhibited can be found in **Table I.7**.

MRN

When serotonin neurons in Ai32 X ePet-Cre+ transgenic mice were stimulated in the MRN mice displayed increased approach and feeding latency (min) during NSF compared to control mice that received a sham surgery.[153] Optical activation of serotonin neurons in the MRN also caused mice to spend less time in the open arms compared to the control mice.[153, 154] However, control mice that had sham surgery in the MRN spent significantly more time in the open arms (~70%) compared to control mice that received sham surgery in the MRN (~40%), which suggests that surgery placement may have had an effect on behavior in the EPM. The underlying mechanism of anxiogenic behavior related to MRN activation may involve $5HT_{2C}$ receptors. Bi-trangenic mice that expressed tetO-ChR2 in Tph2 neurons were further crossed with $5HT_{2C}$R-KO mice to make triple-transgenic mice.[147] When the MRN was stimulated in the tri-transgenic mice, mice no longer exhibited anxiogenic behavior in the EPM. While activation of the MRN impacted anxiety-like behaviors, stimulation of serotonin neurons in the MRN had no impact on immobility in the FST.[147] A table summarizing relative changes in serotonin when projections from the MRN are activated or inhibited can be found in **Table I.8**.

Hippocampus

dHPC

When Ai32 X ePet-Cre+ transgenic mice were stimulated in the dHPC, mice displayed increased approach and feeding latency (min) compared to control mice.[153] However, control mice with sham surgery in the dHPC had increased feeding latency compared to control mice that received sham MRN surgery, which suggests that surgery placement may have had an effect on behavior during NSF . When mice received optical stimulation in the dHPC during the EPM, they spend the same amount of time in the open arms as the control mice the received a sham surgery.[153]

vHPC

Optical activation of serotonin neurons in the vHPC did not impact immobility in the FST.[147] However, when the vHPC was optically stimulated during the EPM, mice spent less time in the open arms and travel a shorter overall distance.[147] Optical stimulation of the vHPC was correlated with increased serotonin in the vHPC, which supports earlier microdialysis studies. Additionally, when mice entered the anxiogenic open arms of the EPM, Ca^{2+} transients in the vCA1 region of the hippocampus increase compared to when mice were in the closed arm.[155] When the specific neurons in the vCA1 region that project to the lateral hypothalamus (LH) and the basal amygdala (BA), respectively, were monitored during the EPM; there was more $Ca+$ transient activity in the vCA1 → LH neurons when mice were in the open arm than in the vCA1 → BA neurons. Overall, chemogenetic inhibition of glutamatergic neurons from the vHPC caused an increase in open arm entries. When glutamatergic neurons from the vHPC to the mPFC were specifically activated and inhibited, respectively, anxiogenic and anxiolytic behavior in the EPM was induced.[156] A table summarizing relative changes in serotonin when projections from the hippocampus are activated or inhibited can be found in **Table I.9**.

Conclusions

Optogenetic activation of serotonin neurons in the MRN and vHPC clarify that changes in serotonin levels in the vHPC were involved in anxiogenic behaviors. Beyond the previous lesion study mentioned above, there is a body of literature that suggests increased serotonin in the vHPC and activation of the MRN → vHPC pathway induces anxiety. However, activation of the MRN and vHPC did not appear to impact depressive-like behavior in the FST, suggesting that the MRN → vHPC specifically mediates anxiety-like behaviors.

In addition to serotonergic inputs to the vHPC inducing anxiety behaviors, glutamatergic outputs from the vHPC to several different brain regions (BA, LH, mPFC, etc) also induced anxiety-like behavior. The vHPC → BA circuit was important for encoding and retrieval of contextual fear memories; however, optical activation of the vHPC → LH circuit induced avoidance in a place preference test.[155] The vHPC → mPFC circuit induced anxiety as measured by the EPM, open field test (OFT), and NSF.[156, 157]

The mPFC → DRN has involved in a number of behavior tests within this review. Activation of this pathway induced antidepressant and anxiolytic phenotypes across the learned helplessness paradigm, FST, NSF, and EPM. Glutamatergic neurons from the mPFC project primarily onto GABAergic interneurons in the DRN, which in turn modulate serotonergic neurons in the DRN.[150, 158] Within the mPFC, glutamatergic pyramidal neurons express both inhibitory $5HT_{1A}$ and excitatory $5HT_{2A}$ receptors, suggesting a serotonin mediated stop-go system that oversees the projection from the mPFC to the DRN.[159]

While data on activating serotonergic circuits from the DRN to the BNST and anxiety behavior were unclear, it's possible that neither study is wrong. One suggested an excitatory $5HT_{2C}$ mediated mechanism, while the other suggested an inhibitory $5HT_{1A}$ mediated mechanism. A compelling follow up experiment would ask which serotonin receptors on DRN → BNST neurons were endogenously activated during certain anxiety-related behaviors.

Overall, involvement of the BNST is necessary in prolonged anxiety responses.[160] Activation of glutamatergic neurons from the vHPC → BNST induces anxiolytic behavioral phenotypes.[161] Glutematergic oversight by inputs from the hippocampus and BLA to the BNST may be more important in modulating anxiety-like and fear behavior than serotonergic inputs from the DRN.[160] In the next section of this review, I will synthesize neurochemical findings with optogenetic and behavior data to point to where the field could combine these tools to better understand the etiology of depression and anxiety.

Conclusions and Challenges

The Interplay Between Serotonin and Glutamate

The serotonin hypothesis is simple, it suggests that a depletion of serotonin results in depressive-like and anxiety-like behaviors. The serotonin hypothesis has encouraged that SSRIs treat depression and anxiety solely by elevating serotonin levels in the brain to combat reduced serotonin levels. However, in many of the highlighted studies that measured extracellular serotonin levels, elevated levels of serotonin resulted in depressive- and anxiety-like behaviors. In other studies that involved circuit modulation, the activation of the pathway of the mPFC → the DRN, which showed promising antidepressant and anxiolytic effects, resulted in serotonin neurons in the DRN becoming inhibited.

While the focus of this review is the role of serotonin transmission in depression and anxiety, an overwhelming amount of studies pointed to the involvement of the glutamatergic projections from the mPFC → DRN as a moderator of depression and anxiety. [162] There were early works that demonstrated that administration of NMDA-R antagonists reduced depression.[162-164] A theory for depression that focused on the glutamate system, also highlighted the impact of neuroplasticity on mood disorders.[165] Neuroplasticity is the an adaptive process of the brain in which connections are strengthened and reorganized. Neuronal connections can be strengthened *via* the arborization of axons and dendrites and changes in post synaptic receptor expression. Dysregulated neuroplasticity in the prefrontal cortex and hippocampus has been implicated in the etiology of depression.[166-169]

Stress was a known risk factor for depression and anxiety, which impacted plasticity of glutamatergic neurons. Increases in stress lead to decreases in dendritic density in glutamate neurons in the mPFC, which were reversible or preventable by the administration of tricyclics or SSRIs.[162, 170-172] Additionally, acute stressors had been associated with increased glutamate levels in the prefrontal cortex, amygdala, and hippocampus, as measured by microdialysis.[173-175] As per this review, we know that changes in serotonin levels in the prefrontal cortex, amygdala, and hippocampus have also been associated with stress, anxiety-like, and depressive-like behaviors.

It is well known that serotonin and glutamate interact with one another. Some serotonin neurons in the DRN co-express the glutamate transporter, VGLUT3.[176-178] Amilhon and coworkers highlighted a subset of VGLUT3 containing serotonin neurons projecting to limbic regions that played a role in anxiety-related behaviors.[179] Additionally, SERT was co-expressed in thalamic glutamate neurons.[180] Overall, the serotonin system is thought to modulate the glutamatergic system through the expression and distribution of serotonin receptors on glutamate neurons.[181]

There are a number of serotonin receptors that are expressed on glutamatergic neurons that have been implicated in the pathology of depression and anxiety, including $5HT_{1A}$, $5HT_{1B}$, $5HT_{2A}$, $5HT_{2C}$, $5HT_4$, $5HT_6$, and $5HT_7$.[182] Serotonin receptors were distributed differently throughout the brain, which could be utilized when developing drugs to target specific brain regions of interest.[183, 184] As the most widely expressed serotonin receptors, $5HT_{1A}$ and $5HT_{2A}$ have been suggested to oversee ‘adaptive responses to adversity’.[185] The inhibitory $5HT_{1A}$ receptor was involved in passive coping through the activation of heteroreceptors in limbic regions.[186] Drugs like SSRIs desensitized $5HT_{1A}$ autoreceptors but not heteroreceptors, which disinhibited serotonin neurons and resulted in more serotonin release in these limbic regions. Alternatively, the excitatory $5HT_{2A}$ receptor was involved in active coping and promoted plasticity in the cortex. Drugs like psychedelics strengthened pathways that express $5HT_{2A}$.

Recently, there has been an influx of research on the use of psilocybin and ketamine for the treatment of depression and anxiety. have been of particular interest. A meta-analysis on psilocybin treatment showed that subjects had reduced anxiety and depression post treatment across studies.[187] While psilocybin is a serotonergic psychedelic that is an agonist for the $5HT_{2A}$ receptor, the drug induces neuroplasticity in glutamatergic neurons in the frontal cortex.[188] Increased neuroplasticity is one of the leading hypotheses of how psychedelics treat anxiety and depression.[80, 189, 190] Ketamine is an NMDA receptor antagonist and dissociative that was previously used as an anesthetic. The mechanism underlying ketamine's antidepressant effects was unclear and is actively being studied for the development of novel drug targets. Leading theories on the antidepressant mechanism of ketamine included direct inhibition of NMDA receptors and/or induction of synaptic plasticity.[191, 192]

A new drug was released that modulates the serotoninergic and glutamatergic systems, as well as the dopaminergic and norepinephrine systems. Auvelity, a combination of dextromethorphan and bupropion, is an NMDA receptor antagonist, σ1 receptor agonist, serotonin–norepinephrine reuptake inhibitor, norepinephrine–dopamine reuptake inhibitor and nicotinic acetylcholine receptor antagonist.[193] Auvelity was FDA approved in the United States in 2022, and claims to reduce symptoms of depression in 1 week. Overall, there is mounting evidence of a shift towards synthesizing glutamatergic antidepressants.[194]

Neurochemical Sensing, Circuit Modulation, and Behavior

Neurochemical sensing during behavior can serve as a tool to guide optogenetic and chemogenetic experiments. Neurochemical sensors can be deployed to multiplex serotonin and glutamate levels in key brain regions such as the hippocampus, mPFC, and DRN during anxiety and depressive-like behaviors. Once the direction of change in these neurochemicals during specific behaviors is clear, neuromodulation experiments of specific pathways can be designed to then induce those neurochemical changes. For example, if there are increases in serotonin in the hippocampus during high anxiety behaviors in the EPM, specific serotonergic inputs to the hippocampus can then be targeted to see if optical activation of this pathway induces the same anxiogenic behavior. In theory activating serotonin neurons that project from the raphe nucleus to the hippocampus should also induce increased in serotonin levels in the hippocampus, which has been confirmed to be true through microdialysis.

Although it is intuitive to think that selective stimulation of a population of neurons should result in selective release of that neuron's respective neurotransmitter, a recent study by our group indicated that may not always be the case. We transduced the excitatory opsin, Crimson, into dopamine neurons expressing the dopamine transporter.[195] When dopamine cell bodies were optically activated, we observed increases in dopamine, serotonin, and 3-methoxytyramine in the striatum. Neurochemical monitoring can be used simultaneously with optogenetic and chemogenetic modulation of circuits to investigate if modulation of certain circuits induces changes in multiple neurotransmitters. The use of SERT-Cre mice would necessitate simultaneous monitoring of serotonin and glutamate, since populations of serotonin neurons that co-release serotonin and glutamate would be targeted.

Neurochemical sensing during pharmacological or genetic modulation of certain serotonin receptor subtypes can gleam information into how normal serotonin release is disrupted by inhibition or the knockout of key receptors on serotonin or glutamate neurons.

For example, the role of serotonin during inescapable stress can be further probed using $5HT_{1A}$ or $5HT_{2A}$ knockout mice, to see if sustained elevations in DRN serotonin levels due to inescapable stress are mediated by one of these receptors. Also, the $5HT_{1A}$ and $5HT_{2A}$ receptors are expressed on glutamatergic neurons that project from the mPFC to the DRN and can either inhibit or excite this pathway respectively. Understanding how changes in serotonin and glutamate levels in the mPFC results in differential activation of either of these receptors during specific behaviors would aid in understanding how antidepressant and anxiolytic behaviors are modulated by the mPFC → DRN circuit.

Challenges

Simultaneous detection of serotonin and glutamate is a technical challenge. Serotonin is an electrochemically active monoamine neurotransmitter, while glutamate is an amino acid that requires special derivatization to become electrochemically active.[196] Glutamate can be electrochemically detected through the use of immobilized enzymes[197] or a genetically engineered periplasmic glutamate binding protein,[198] but cannot be directly detected. Therefore, most voltammetry techniques and microdialysis with electrochemical detection are not suitable to co-detect serotonin and glutamate. However, it may be possible to use RPV-PLSR to detect glutamate if changes in glutamate levels were to affect double-layer rearrangement in some way, thereby changing the capacitive current.

Tissue serotonin and glutamate can be simultaneously detected using LC-MS.[199] However, designing a microdialysis method with a mass spectrometry detector that can simultaneously detect both glutamate and serotonin, while having adequate sensitivity for serotonin *in vivo*, may be challenging. Nonetheless, microdialysis is unable to detect millisecond changes in neurochemicals, which would be favorable when monitoring neurochemical levels during behaviors that may only last several minutes.

Genetically modified fluorescent sensors have been developed for both serotonin and glutamate, however, a red shifted version of one of these sensors would need to be developed in order to successfully multiplex. Aptamer-FET sensors can bind any substrate that an aptamer exists for. However, *in vivo* aptamer-FET probes have currently focused on multiplexing serotonin and dopamine, and haven't been used to make *in vivo* recordings of glutamate.

In this review the focus was on serotonin's interaction with glutamate, however, there are a number of plausible theories that suggest that the interaction of the serotonin system with the dopamine,[200-202] norepinephrine,[203,204] and GABA[205-207] systems also impact depression and anxiety. In order to elucidate the role of serotonin in depression and anxiety, scientists must study the interactions between serotonin and other neurotransmitter systems because serotonin does not act in isolation. A number of neurochemical sensing techniques have been expanded to multiplex dopamine and other neurotransmitters.[70,71,88,89,208] Patriarchi and coworkers have demonstrated the feasibility of multiplexing dopamine and glutamate using genetically engineered fluorescent sensors.[70] The development of a red-shifted genetically engineered fluorescent sensor for serotonin would allow for serotonin to be multiplexed with glutamate,[59, 60] GABA,[61] oxytocin,[62] endocannabinoids,[63] histamine,[64] norepinephrine,[65] acetylcholine,[66, 67] or dopamine[68-71], which would open a new avenue in how serotonin is studied.

Figures

Figure I.1

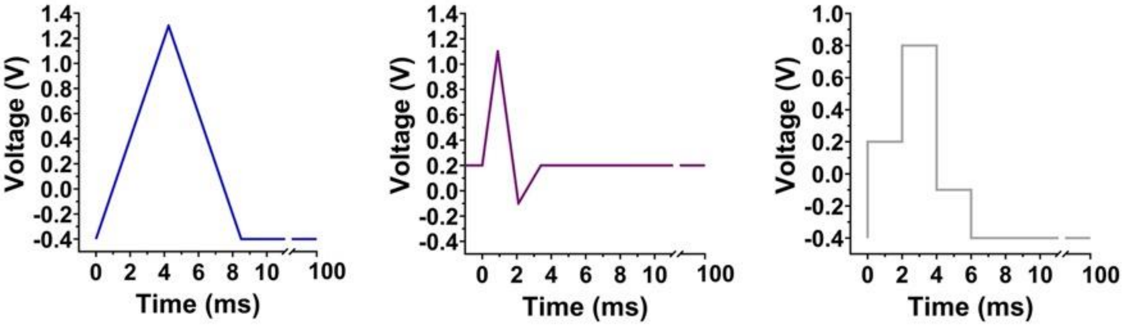

Figure I.1 Voltammetry waveforms. Blue is triangle waveform for FSCV. Purple is the N-shape waveform for serotonin. Grey is the RPV-PLSR waveform.

Table I.1

Condition	**Brain region**	**Change in serotonin**
Escapable stress	DRN	No change
Escapable stress + muscimol in mPFC	DRN	Increased
Inescapable stress	DRN	Increased
Escapable stress	vHPC	No change
Inescapable stress	vHPC	Increased
Escapable stress	BLA	No change
Inescapable stress	BLA	Increased

Table I.1. Changes in serotonin levels during the learned helplessness paradigm.

Table I.2

Condition	**Brain region**	**Change in serotonin**
During shock	vHPC	Increase
Decrease in freezing	vHPC	Increase
During cue	mPFC	Increase
During shock	mPFC	Decrease
During cue	BLA	Increase
During shock	BLA	Decrease
During shock	DRN	Decrease
During shock	OFC	Decrease
During shock	BNST	Decrease

Table I.2. Changes in serotonin levels during fear conditioning.

Table I.3

Condition	Brain region	Change in serotonin
DBS of mPFC	dHPC	Increase
Forced swim stress	vHPC	Decrease and increase
Forced swim stress	mPFC	Decrease and increase
Forced swim stress	DRN	No change
Forced swim stress	amygdala	Increase and decrease
Forced swim stress	MRN	Increase
Forced swim stress	striatum	Increase

Table I.3. Changes in serotonin levels during the forced swim test.

Table I.4

Condition	Brain region	Change in serotonin
Intruder present	BLA	Increase
Intruder present	OFC	Increase
Intruder present	BNST	No change
Sniffing- group housed	mPFC	Increase
Sniffing- chronic social isolation	mPFC	No change

Table I.4. Changes in serotonin levels during social interaction.

Table I.5

Condition	**Brain region**	**Change in serotonin**
DRN lesion during EPM	vHPC	Increase
MRN lesion during EMP	vHPC	No change

Table I.5. Changes in serotonin levels during the elevated plus maze.

Table I.6

Pathway/brain region	Modulation	Associated receptors	Behavior Test	Change in behavior
DRN → BNST (5HT)	stimulate	$5HT_{2C}R$	Fear Conditioning, NSF, EPM	↑ anxiety
DRN → BNST (5HT)	stimulate	$5HT_{1A}R$	NSF, EPM	↓ anxiety
DRN → BNST (5HT)	inhibit	$5HT_{1A}R$	EPM	↑ anxiety
DRN → BNST (non-specific)	stimulate	N/A	EPM	↑ anxiety
DRN → BNST (non-specific)	inhibit	N/A	EPM	↓ anxiety
DRN → LHb (5HT)	stimulate	N/A	FST	↓ depression
DRN (5HT)	stimulate	N/A	FST	↓ depression
VTA/SN (5HT)	stimulate	N/A	FST	↓ depression

Table I.6. Changes in serotonin levels when projections from the DRN are stimulated or inhibited.

Table I.7

Pathway/brain region	Modulation	Associated receptors	Behavior Test	Change in behavior
mPFC → DRN (non-specific)	stimulate	N/A	FST	No change
mPFC → DRN (Glu)	stimulate	N/A	FST	↓ depression
mPFC → DRN (Glu)	stimulate	$5HT_4R$	NSF	↓ anxiety
mPFC → DRN (Glu)	stimulate	$5HT_4R$	EPM	↓ anxiety
mPFC → DRN (Glu)	stimulate	N/A	Social Interaction	↓ sociability
mPFC → DRN (Glu)	inhibit	N/A	Social Interaction	↑ sociability
mPFC → DRN (Glu)	Endogenous activation	N/A	Social Interaction	↑ stress resilience

Table I.7. Changes in serotonin levels when projections from the mPFC are stimulated or inhibited.

Table I.8

Pathway/brain region	Modulation	Associated receptors	Behavior Test	Change in behavior
MRN (5HT)	stimulate	$5HT_{2C}R$	EPM	↑ anxiety
MRN (5HT)	stimulate	N/A	NSF	↑ anxiety
MRN (5HT)	stimulate	N/A	FST	No change

Table I.8. Changes in serotonin levels when projections from the MRN are stimulated or inhibited.

Table I.9

Pathway/brain region	Modulation	Associated receptors	Behavior Test	Change in behavior
dHPC (5HT)	stimulate	N/A	NSF	↑ anxiety
dHPC (5HT)	stimulate	N/A	EPM	No change
vHPC (5HT)	stimulate	N/A	EPM	↑ anxiety
vHPC	Endogenous activation	N/A	EPM	↑ anxiety
vHPC (Glu)	inhibit	N/A	EPM	↓ anxiety
vHPC → mPFC (Glu)	stimulate	N/A	EPM	↑ anxiety
vHPC → mPFC (Glu)	inhibit	N/A	EPM	↓ anxiety

Table I.9. Changes in serotonin levels when projections from the hippocampus are stimulated or inhibited.

References

1. Booij, L.; Van der Does, W.; Benkelfat, C.; Bremner, J. D.; Cowen, P. J.; Fava, M.; Gillin, C.; Leyton, M.; Moore, P.; Smith, K. A.; Van der Kloot, W. A., Predictors of mood response to acute tryptophan depletion: A reanalysis. *Neuropsychopharmacology* **2002,** *27* (5), 852-861.

2. Fakhoury, M., Revisiting the serotonin hypothesis: Implications for major depressive disorders. *Molecular Neurobiology* **2016,** *53* (5), 2778-2786.

3. Baumeister, A. A.; Hawkins, M. F.; Uzelac, S. M., The myth of reserpine-induced depression: Role in the historical development of the monoamine hypothesis. *Journal of the History of the Neurosciences* **2003,** *12* (2), 207-220.

4. Coppen, A., The biochemistry of affective disorders. *Br J Psychiatry* **1967,** *113* (504), 1237-64.

5. Tretter, F., Mental illness, synapses and the brain–behavioral disorders by a system of molecules within a system of neurons? *Pharmacopsychiatry* **2010,** *43* (S 01), S9-S20.

6. Ramachandraih, C. T.; Subramanyam, N.; Bar, K. J.; Baker, G.; Yeragani, V. K., Antidepressants: From maois to ssris and more. *Indian journal of psychiatry* **2011,** *53* (2), 180.

7. Andrews, A. M.; Murphy, D. L., 2'-nh2-mptp in swiss webster mice: Evidence for long-term (6-month) depletions in cortical and hippocampal serotonin and norepinephrine, differential protection by selective uptake inhibitors or clorgyline and functional changes in central serotonin neurotransmission. . *J Pharmacol Exp Ther* **1993,** *267 (3), 1432-9.*

8. Schildkraut, J. J., The catecholamine hypothesis of affective disorders: A review of supporting evidence. *American journal of Psychiatry* **1965,** *122* (5), 509-522.

9. Pereira, V. S.; Hiroaki-Sato, V. A., A brief history of antidepressant drug development: From tricyclics to beyond ketamine. *Acta neuropsychiatrica* **2018,** *30* (6), 307-322.

10. Kerr, C. W., The serotonin theory of depression. *Jefferson Journal of Psychiatry* **1994,** *12* (1), 4.

11. Mann, J. J.; Arango, V.; Marzuk, P. M.; Theccanat, S.; Reis, D. J., Evidence for the 5-ht hypothesis of suicide. A review of post-mortem studies. *Br J Psychiatry Suppl* **1989,** (8), 7-14.

12. Mann, J. J.; Malone, K. M.; Sweeney, J. A.; Brown, R. P.; Linnoila, M.; Stanley, B.; Stanley, M., Attempted suicide characteristics and cerebrospinal fluid amine metabolites in depressed inpatients. *Neuropsychopharmacology* **1996,** *15* (6), 576-586.

13. Chu, A.; Wadhwa, R., Selective serotonin reuptake inhibitors. 2022.

14. Townsend, D. W., Physical principles and technology of clinical pet imaging. *Ann Acad Med Singap* **2004,** *33* (2), 133-45.

15. Jørgensen, L. M.; Weikop, P.; Svarer, C.; Feng, L.; Keller, S. H.; Knudsen, G. M., Cerebral serotonin release correlates with [(11)c]az10419369 pet measures of 5-ht(1b) receptor binding in the pig brain. *J Cereb Blood Flow Metab* **2018,** *38* (7), 1243-1252.

16. Jørgensen, L. M.; Weikop, P.; Villadsen, J.; Visnapuu, T.; Ettrup, A.; Hansen, H. D.; Baandrup, A. O.; Andersen, F. L.; Bjarkam, C. R.; Thomsen, C.; Jespersen, B.; Knudsen, G. M., Cerebral 5-ht release correlates with [(11)c]cimbi36 pet measures of 5-ht2a receptor occupancy in the pig brain. *J Cereb Blood Flow Metab* **2017,** *37* (2), 425-434.

17. Selvaraj, S.; Turkheimer, F.; Rosso, L.; Faulkner, P.; Mouchlianitis, E.; Roiser, J. P.; McGuire, P.; Cowen, P. J.; Howes, O., Measuring endogenous changes in serotonergic neurotransmission in humans: A [11c]cumi-101 pet challenge study. *Mol Psychiatry* **2012,** *17* (12), 1254-1260.

18. Selvaraj, S.; Turkheimer, F.; Rosso, L.; Faulkner, P.; Mouchlianitis, E.; Roiser, J. P.; McGuire, P.; Cowen, P. J.; Howes, O., Measuring endogenous changes in serotonergic neurotransmission in humans: A [11c]cumi-101 pet challenge study. *Mol Psychiatry* **2012,** *17* (12), 1254-60.

19. Nord, M.; Finnema, S. J.; Halldin, C.; Farde, L., Effect of a single dose of escitalopram on serotonin concentration in the non-human and human primate brain. *Int J Neuropsychopharmacol* **2013,** *16* (7), 1577-86.

20. Gryglewski, G.; Klöbl, M.; Berroterán-Infante, N.; Rischka, L.; Balber, T.; Vanicek, T.; Pichler, V.; Kautzky, A.; Klebermass, E.-M.; Reed, M. B.; Vraka, C.; Hienert, M.; James, G. M.; Silberbauer, L.; Godbersen, G. M.; Unterholzner, J.; Michenthaler, P.; Hartenbach, M.; Winkler-Pjrek, E.; Wadsak, W.; Mitterhauser, M.; Hahn, A.; Hacker, M.; Kasper, S.; Lanzenberger, R., Modeling the acute pharmacological response to selective serotonin reuptake inhibitors in human brain using simultaneous pet/mr imaging. *European Neuropsychopharmacology* **2019,** *29* (6), 711-719.

21. Spies, M.; Knudsen, G. M.; Lanzenberger, R.; Kasper, S., The serotonin transporter in psychiatric disorders: Insights from pet imaging. *The Lancet Psychiatry* **2015,** *2* (8), 743-755.

22. Parsey, R. V.; Hastings, R. S.; Oquendo, M. A.; Huang, Y. Y.; Simpson, N.; Arcement, J.; Huang, Y.; Ogden, R. T.; Van Heertum, R. L.; Arango, V.; Mann, J. J., Lower serotonin transporter binding potential in the human brain during major depressive episodes. *Am J Psychiatry* **2006,** *163* (1), 52-8.

23. Gryglewski, G.; Lanzenberger, R.; Kranz, G. S.; Cumming, P., Meta-analysis of molecular imaging of serotonin transporters in major depression. *J Cereb Blood Flow Metab* **2014,** *34* (7), 1096-103.

24. Ichimiya, T.; Suhara, T.; Sudo, Y.; Okubo, Y.; Nakayama, K.; Nankai, M.; Inoue, M.; Yasuno, F.; Takano, A.; Maeda, J.; Shibuya, H., Serotonin transporter binding in

patients with mood disorders: A pet study with [11c](+)mcn5652. *Biol Psychiatry* **2002,** *51* (9), 715-22.

25. Cannon, D. M.; Ichise, M.; Rollis, D.; Klaver, J. M.; Gandhi, S. K.; Charney, D. S.; Manji, H. K.; Drevets, W. C., Elevated serotonin transporter binding in major depressive disorder assessed using positron emission tomography and [11c]dasb; comparison with bipolar disorder. *Biol Psychiatry* **2007,** *62* (8), 870-7.

26. Reivich, M.; Amsterdam, J. D.; Brunswick, D. J.; Shiue, C. Y., Pet brain imaging with [11c](+)mcn5652 shows increased serotonin transporter availability in major depression. *J Affect Disord* **2004,** *82* (2), 321-7.

27. Jeffrey H. Meyer, M.D., Ph.D. ,; Alan A. Wilson, Ph.D. ,; Sandra Sagrati, M.Ed. ,; Doug Hussey, B.Sc. ,; Anna Carella, B.Sc. ,; William Z. Potter, M.D. ,; Nathalie Ginovart, Ph.D. ,; Edgar P. Spencer, Ph.D. ,; Andy Cheok, M.D. , and; Sylvain Houle, M.D., Ph.D., Serotonin transporter occupancy of five selective serotonin reuptake inhibitors at different doses: An [11c]dasb positron emission tomography study. *American Journal of Psychiatry* **2004,** *161* (5), 826-835.

28. Meyer, J. H.; Houle, S.; Sagrati, S.; Carella, A.; Hussey, D. F.; Ginovart, N.; Goulding, V.; Kennedy, J.; Wilson, A. A., Brain serotonin transporter binding potential measured with carbon 11-labeled dasb positron emission tomography: Effects of major depressive episodes and severity of dysfunctional attitudes. *Arch Gen Psychiatry* **2004,** *61* (12), 1271-9.

29. Lanzenberger, R.; Kranz, G. S.; Haeusler, D.; Akimova, E.; Savli, M.; Hahn, A.; Mitterhauser, M.; Spindelegger, C.; Philippe, C.; Fink, M.; Wadsak, W.; Karanikas, G.; Kasper, S., Prediction of ssri treatment response in major depression based on serotonin transporter interplay between median raphe nucleus and projection areas. *Neuroimage* **2012,** *63* (2), 874-81.

30. Yeh, Y. W.; Ho, P. S.; Kuo, S. C.; Chen, C. Y.; Liang, C. S.; Yen, C. H.; Huang, C. C.; Ma, K. H.; Shiue, C. Y.; Huang, W. S.; Shyu, J. F.; Wan, F. J.; Lu, R. B.; Huang, S. Y., Disproportionate reduction of serotonin transporter may predict the response and adherence to antidepressants in patients with major depressive disorder: A positron emission tomography study with 4-[18f]-adam. *Int J Neuropsychopharmacol* **2015,** *18* (7), pyu120.

31. Holck, A.; Wolkowitz, O. M.; Mellon, S. H.; Reus, V. I.; Nelson, J. C.; Westrin, Å.; Lindqvist, D., Plasma serotonin levels are associated with antidepressant response to ssris. *Journal of Affective Disorders* **2019,** *250*, 65-70.

32. Mercado, C. P.; Kilic, F., Molecular mechanisms of sert in platelets: Regulation of plasma serotonin levels. *Mol Interv* **2010,** *10* (4), 231-41.

33. Gupta, M.; Neavin, D.; Liu, D.; Biernacka, J.; Hall-Flavin, D.; Bobo, W. V.; Frye, M. A.; Skime, M.; Jenkins, G. D.; Batzler, A.; Kalari, K.; Matson, W.; Bhasin, S. S.; Zhu, H.; Mushiroda, T.; Nakamura, Y.; Kubo, M.; Wang, L.; Kaddurah-Daouk, R.; Weinshilboum, R. M., Tspan5, erich3 and selective serotonin reuptake inhibitors in major

depressive disorder: Pharmacometabolomics-informed pharmacogenomics. *Molecular Psychiatry* **2016,** *21* (12), 1717-1725.

34. Brand, T.; Anderson, G. M., The measurement of platelet-poor plasma serotonin: A systematic review of prior reports and recommendations for improved analysis. *Clin Chem* **2011,** *57* (10), 1376-1386.

35. Altieri, S. C.; Singh, Y. S.; Sibille, E.; Andrews, A. M., Serotonergic pathways in depression. *Neurobiology of Depression* **2012,** *20115633*, 143-70.

36. Pan, J.-X.; Xia, J.-J.; Deng, F.-L.; Liang, W.-W.; Wu, J.; Yin, B.-M.; Dong, M.-X.; Chen, J.-J.; Ye, F.; Wang, H.-Y.; Zheng, P.; Xie, P., Diagnosis of major depressive disorder based on changes in multiple plasma neurotransmitters: A targeted metabolomics study. *Translational Psychiatry* **2018,** *8* (1), 130.

37. Huang, X.; Yin, H.; Wan, X.-x.; Fu, B.; Tang, B.; Lei, J., Maternal plasma serotonin level not suitable as postpartum depression diagnostic biomarker: Results from a prospective cohort study. *Journal of Affective Disorders* **2022,** *298*, 284-291.

38. Yubero-Lahoz, S.; Robledo, P.; Farre, M.; de la Torre, R., Platelet sert as a peripheral biomarker of serotonergic neurotransmission in the central nervous system. In *Current medicinal chemistry*, Bentham Science Publishers: 2013; Vol. 20.

39. Popa, D.; Cerdan, J.; Repérant, C.; Guiard, B. P.; Guilloux, J.-P.; David, D. J.; Gardier, A. M., A longitudinal study of 5-ht outflow during chronic fluoxetine treatment using a new technique of chronic microdialysis in a highly emotional mouse strain. *European Journal of Pharmacology* **2010,** *628* (1), 83-90.

40. Bel, N.; Artigas, F., Chronic treatment with fluvoxamine increases extracellular serotonin in frontal cortex but not in raphe nuclei. *Synapse* **1993,** *15* (3), 243-5.

41. Moncrieff, J.; Cooper, R. E.; Stockmann, T.; Amendola, S.; Hengartner, M. P.; Horowitz, M. A., The serotonin theory of depression: A systematic umbrella review of the evidence. *Molecular Psychiatry* **2022**.

42. Sharp, T.; Bramwell, S. R.; Clark, D.; Grahame-Smith, D. G., In vivo measurement of extracellular 5-hydroxytryptamine in hippocampus of the anaesthetized rat using microdialysis: Changes in relation to 5-hydroxytryptaminergic neuronal activity. *Journal of Neurochemistry* **1989,** *53* (1), 234-240.

43. Yang, H.; Thompson, A. B.; McIntosh, B. J.; Altieri, S. C.; Andrews, A. M., Physiologically relevant changes in serotonin resolved by fast microdialysis. *ACS Chemical Neuroscience* **2013,** *4* (5), 790-798.

44. Zhang, J.; Jaquins-Gerstl, A.; Nesbitt, K. M.; Rutan, S. C.; Michael, A. C.; Weber, S. G., In vivo monitoring of serotonin in the striatum of freely moving rats with one minute temporal resolution by online microdialysis–capillary high-performance liquid chromatography at elevated temperature and pressure. *Analytical Chemistry* **2013,** *85* (20), 9889-9897.

45. Liu, Y.; Zhang, J.; Xu, X.; Zhao, M. K.; Andrews, A. M.; Weber, S. G., Capillary ultrahigh performance liquid chromatography with elevated temperature for sub-one minute separations of basal serotonin in submicroliter brain microdialysate samples. *Anal Chem* **2010,** *82* (23), 9611-6.

46. Zhang, J.; Liu, Y.; Jaquins-Gerstl, A.; Shu, Z.; Michael, A. C.; Weber, S. G., Optimization for speed and sensitivity in capillary high performance liquid chromatography. The importance of column diameter in online monitoring of serotonin by microdialysis. *J Chromatogr A* **2012,** *1251*, 54-62.

47. Robinson, D. L.; Zitzman, D. L.; Williams, S. K., Mesolimbic dopamine transients in motivated behaviors: Focus on maternal behavior. *Front Psychiatry* **2011,** *2*, 23.

48. Jackson, B. P.; Dietz, S. M.; Wightman, R. M., Fast-scan cyclic voltammetry of 5-hydroxytryptamine. *Analytical Chemistry* **1995,** *67* (6), 1115-1120.

49. Dankoski, E. C.; Wightman, R. M., Monitoring serotonin signaling on a subsecond time scale. *Front Integr Neurosci* **2013,** *7*, 44.

50. Dunham, K. E.; Venton, B. J., Improving serotonin fast-scan cyclic voltammetry detection: New waveforms to reduce electrode fouling. *Analyst* **2020,** *145* (22), 7437-7446.

51. Shin, H.; Oh, Y.; Park, C.; Kang, Y.; Cho, H. U.; Blaha, C. D.; Bennet, K. E.; Heien, M. L.; Kim, I. Y.; Lee, K. H.; Jang, D. P., Sensitive and selective measurement of serotonin in vivo using fast cyclic square-wave voltammetry. *Analytical Chemistry* **2020,** *92* (1), 774-781.

52. Abdalla, A.; Atcherley, C. W.; Pathirathna, P.; Samaranayake, S.; Qiang, B.; Peña, E.; Morgan, S. L.; Heien, M. L.; Hashemi, P., In vivo ambient serotonin measurements at carbon-fiber microelectrodes. *Analytical Chemistry* **2017,** *89* (18), 9703-9711.

53. Shin, H.; Goyal, A.; Barnett, J. H.; Rusheen, A. E.; Yuen, J.; Jha, R.; Hwang, S. M.; Kang, Y.; Park, C.; Cho, H.-U.; Blaha, C. D.; Bennet, K. E.; Oh, Y.; Heien, M. L.; Jang, D. P.; Lee, K. H., Tonic serotonin measurements in vivo using n-shaped multiple cyclic square wave voltammetry. *Analytical Chemistry* **2021,** *93* (51), 16987-16994.

54. Movassaghi, C. S.; Perrotta, K. A.; Yang, H.; Iyer, R.; Cheng, X.; Dagher, M.; Fillol, M. A.; Andrews, A. M., Simultaneous serotonin and dopamine monitoring across timescales by rapid pulse voltammetry with partial least squares regression. *Analytical and Bioanalytical Chemistry* **2021,** *413* (27), 6747-6767.

55. Li, J.; Liu, Y.; Yuan, L.; Zhang, B.; Bishop, E. S.; Wang, K.; Tang, J.; Zheng, Y.-Q.; Xu, W.; Niu, S., A tissue-like neurotransmitter sensor for the brain and gut. *Nature* **2022,** *606* (7912), 94-101.

56. Corva, D. M.; Adams, S. D.; Bennet, K. E.; Berk, M.; Kouzani, A. Z., Miniature fscv devices: A review. *IEEE Sensors Journal* **2021,** *21* (12), 13006-13018.

57. Bledsoe, J. M.; Kimble, C. J.; Covey, D. P.; Blaha, C. D.; Agnesi, F.; Mohseni, P.; Whitlock, S.; Johnson, D. M.; Horne, A.; Bennet, K. E.; Lee, K. H.; Garris, P. A., Development of the wireless instantaneous neurotransmitter concentration system for intraoperative neurochemical monitoring using fast-scan cyclic voltammetry: Technical note. *Journal of Neurosurgery JNS* **2009,** *111* (4), 712-723.

58. Johnson, D.; Harmon, H.; Gabbert, S.; Johnson, M.; Wilson, G., Wireless fast scan cyclic voltammetry for rats.

59. Marvin, J. S.; Borghuis, B. G.; Tian, L.; Cichon, J.; Harnett, M. T.; Akerboom, J.; Gordus, A.; Renninger, S. L.; Chen, T.-W.; Bargmann, C. I.; Orger, M. B.; Schreiter, E. R.; Demb, J. B.; Gan, W.-B.; Hires, S. A.; Looger, L. L., An optimized fluorescent probe for visualizing glutamate neurotransmission. *Nature Methods* **2013,** *10* (2), 162-170.

60. Marvin, J. S.; Scholl, B.; Wilson, D. E.; Podgorski, K.; Kazemipour, A.; Müller, J. A.; Schoch, S.; Quiroz, F. J. U.; Rebola, N.; Bao, H.; Little, J. P.; Tkachuk, A. N.; Cai, E.; Hantman, A. W.; Wang, S. S. H.; DePiero, V. J.; Borghuis, B. G.; Chapman, E. R.; Dietrich, D.; DiGregorio, D. A.; Fitzpatrick, D.; Looger, L. L., Stability, affinity, and chromatic variants of the glutamate sensor iglusnfr. *Nature Methods* **2018,** *15* (11), 936-939.

61. Marvin, J. S.; Shimoda, Y.; Magloire, V.; Leite, M.; Kawashima, T.; Jensen, T. P.; Kolb, I.; Knott, E. L.; Novak, O.; Podgorski, K.; Leidenheimer, N. J.; Rusakov, D. A.; Ahrens, M. B.; Kullmann, D. M.; Looger, L. L., A genetically encoded fluorescent sensor for in vivo imaging of gaba. *Nature Methods* **2019,** *16* (8), 763-770.

62. Qian, T.; Wang, H.; Wang, P.; Geng, L.; Mei, L.; Osakada, T.; Tang, Y.; Kania, A.; Grinevich, V.; Stoop, R.; Lin, D.; Luo, M.; Li, Y., Compartmental neuropeptide release measured using a new oxytocin sensor. *bioRxiv* **2022**, 2022.02.10.480016.

63. Dong, A.; He, K.; Dudok, B.; Farrell, J. S.; Guan, W.; Liput, D. J.; Puhl, H. L.; Cai, R.; Wang, H.; Duan, J.; Albarran, E.; Ding, J.; Lovinger, D. M.; Li, B.; Soltesz, I.; Li, Y., A fluorescent sensor for spatiotemporally resolved imaging of endocannabinoid dynamics in vivo. *Nature Biotechnology* **2022,** *40* (5), 787-798.

64. Dong, H.; Li, M.; Yan, Y.; Qian, T.; Lin, Y.; Ma, X.; Vischer, H. F.; Liu, C.; Li, G.; Wang, H.; Leurs, R.; Li, Y., Genetically encoded sensors for measuring histamine release both in vitro and in vivo. *bioRxiv* **2022**, 2022.08.19.504485.

65. Feng, J.; Zhang, C.; Lischinsky, J. E.; Jing, M.; Zhou, J.; Wang, H.; Zhang, Y.; Dong, A.; Wu, Z.; Wu, H.; Chen, W.; Zhang, P.; Zou, J.; Hires, S. A.; Zhu, J. J.; Cui, G.; Lin, D.; Du, J.; Li, Y., A genetically encoded fluorescent sensor for rapid and specific in vivo detection of norepinephrine. *Neuron* **2019,** *102* (4), 745-761.e8.

66. Jing, M.; Zhang, P.; Wang, G.; Feng, J.; Mesik, L.; Zeng, J.; Jiang, H.; Wang, S.; Looby, J. C.; Guagliardo, N. A.; Langma, L. W.; Lu, J.; Zuo, Y.; Talmage, D. A.; Role, L. W.; Barrett, P. Q.; Zhang, L. I.; Luo, M.; Song, Y.; Zhu, J. J.; Li, Y., A genetically encoded fluorescent acetylcholine indicator for in vitro and in vivo studies. *Nature Biotechnology* **2018,** *36* (8), 726-737.

67. Jing, M.; Li, Y.; Zeng, J.; Huang, P.; Skirzewski, M.; Kljakic, O.; Peng, W.; Qian, T.; Tan, K.; Zou, J.; Trinh, S.; Wu, R.; Zhang, S.; Pan, S.; Hires, S. A.; Xu, M.; Li, H.; Saksida, L. M.; Prado, V. F.; Bussey, T. J.; Prado, M. A. M.; Chen, L.; Cheng, H.; Li, Y., An optimized acetylcholine sensor for monitoring in vivo cholinergic activity. *Nature Methods* **2020,** *17* (11), 1139-1146.

68. Sun, F.; Zeng, J.; Jing, M.; Zhou, J.; Feng, J.; Owen, S. F.; Luo, Y.; Li, F.; Wang, H.; Yamaguchi, T.; Yong, Z.; Gao, Y.; Peng, W.; Wang, L.; Zhang, S.; Du, J.; Lin, D.; Xu, M.; Kreitzer, A. C.; Cui, G.; Li, Y., A genetically encoded fluorescent sensor enables rapid and specific detection of dopamine in flies, fish, and mice. *Cell* **2018,** *174* (2), 481-496.e19.

69. Patriarchi, T.; Cho, J. R.; Merten, K.; Howe, M. W.; Marley, A.; Xiong, W.-H.; Folk, R. W.; Broussard, G. J.; Liang, R.; Jang, M. J.; Zhong, H.; Dombeck, D.; von Zastrow, M.; Nimmerjahn, A.; Gradinaru, V.; Williams, J. T.; Tian, L., Ultrafast neuronal imaging of dopamine dynamics with designed genetically encoded sensors. *Science* **2018,** *360* (6396), eaat4422.

70. Patriarchi, T.; Mohebi, A.; Sun, J.; Marley, A.; Liang, R.; Dong, C.; Puhger, K.; Mizuno, G. O.; Davis, C. M.; Wiltgen, B.; von Zastrow, M.; Berke, J. D.; Tian, L., An expanded palette of dopamine sensors for multiplex imaging in vivo. *Nature Methods* **2020,** *17* (11), 1147-1155.

71. Sun, F.; Zhou, J.; Dai, B.; Qian, T.; Zeng, J.; Li, X.; Zhuo, Y.; Zhang, Y.; Wang, Y.; Qian, C.; Tan, K.; Feng, J.; Dong, H.; Lin, D.; Cui, G.; Li, Y., Next-generation grab sensors for monitoring dopaminergic activity in vivo. *Nature Methods* **2020,** *17* (11), 1156-1166.

72. Unger, E. K.; Keller, J. P.; Altermatt, M.; Liang, R.; Matsui, A.; Dong, C.; Hon, O. J.; Yao, Z.; Sun, J.; Banala, S.; Flanigan, M. E.; Jaffe, D. A.; Hartanto, S.; Carlen, J.; Mizuno, G. O.; Borden, P. M.; Shivange, A. V.; Cameron, L. P.; Sinning, S.; Underhill, S. M.; Olson, D. E.; Amara, S. G.; Temple Lang, D.; Rudnick, G.; Marvin, J. S.; Lavis, L. D.; Lester, H. A.; Alvarez, V. A.; Fisher, A. J.; Prescher, J. A.; Kash, T. L.; Yarov-Yarovoy, V.; Gradinaru, V.; Looger, L. L.; Tian, L., Directed evolution of a selective and sensitive serotonin sensor via machine learning. *Cell* **2020,** *183* (7), 1986-2002.e26.

73. Wan, J.; Peng, W.; Li, X.; Qian, T.; Song, K.; Zeng, J.; Deng, F.; Hao, S.; Feng, J.; Zhang, P.; Zhang, Y.; Zou, J.; Pan, S.; Shin, M.; Venton, B. J.; Zhu, J. J.; Jing, M.; Xu, M.; Li, Y., A genetically encoded sensor for measuring serotonin dynamics. *Nature Neuroscience* **2021,** *24* (5), 746-752.

74. Dong, C.; Ly, C.; Dunlap, L. E.; Vargas, M. V.; Sun, J.; Hwang, I.-W.; Azinfar, A.; Oh, W. C.; Wetsel, W. C.; Olson, D. E.; Tian, L., Psychedelic-inspired drug discovery using an engineered biosensor. *Cell* **2021,** *184* (10), 2779-2792.e18.

75. Xu, M.; Chung, S.; Zhang, S.; Zhong, P.; Ma, C.; Chang, W.-C.; Weissbourd, B.; Sakai, N.; Luo, L.; Nishino, S.; Dan, Y., Basal forebrain circuit for sleep-wake control. *Nature Neuroscience* **2015,** *18* (11), 1641-1647.

76. Morgan, C. W.; Ren, J., Making a tick protein talk as a serotonin sensor. *Nature Methods* **2021,** *18* (3), 240-241.

77. Pae, C.-U.; Serretti, A.; Patkar, A. A.; Masand, P. S., Aripiprazole in the treatment of depressive and anxiety disorders. *CNS Drugs* **2008,** *22* (5), 367-388.

78. Diefenderfer, L. A.; Iuppa, C., Brexpiprazole: A review of a new treatment option for schizophrenia and major depressive disorder. *Mental Health Clinician* **2017,** *7* (5), 207-212.

79. Olson, D. E., Psychoplastogens: A promising class of plasticity-promoting neurotherapeutics. *J Exp Neurosci* **2018,** *12*, 1179069518800508.

80. Artin, H.; Zisook, S.; Ramanathan, D., How do serotonergic psychedelics treat depression: The potential role of neuroplasticity. *World J Psychiatry* **2021,** *11* (6), 201-214.

81. Vargas, M. V.; Meyer, R.; Avanes, A. A.; Rus, M.; Olson, D. E., Psychedelics and other psychoplastogens for treating mental illness. *Front Psychiatry* **2021,** *12*, 727117.

82. Okon, S. L.; Ronkainen, N. J., Enzyme-based electrochemical glutamate biosensors. *Electrochem. Sens. Technol* **2017,** *13*.

83. Weltin, A.; Kieninger, J.; Urban, G. A., Microfabricated, amperometric, enzyme-based biosensors for in vivo applications. *Analytical and Bioanalytical Chemistry* **2016,** *408* (17), 4503-4521.

84. Tavakolian-Ardakani, Z.; Hosu, O.; Cristea, C.; Mazloum-Ardakani, M.; Marrazza, G., Latest trends in electrochemical sensors for neurotransmitters: A review. *Sensors* **2019,** *19* (9), 2037.

85. Nakatsuka, N.; Yang, K.-A.; Abendroth, J. M.; Cheung, K. M.; Xu, X.; Yang, H.; Zhao, C.; Zhu, B.; Rim, Y. S.; Yang, Y.; Weiss, P. S.; Stojanović, M. N.; Andrews, A. M., Aptamer field-effect transistors overcome debye length limitations for small-molecule sensing. *Science* **2018,** *362* (6412), 319-324.

86. Liu, Q.; Zhao, C.; Chen, M.; Liu, Y.; Zhao, Z.; Wu, F.; Li, Z.; Weiss, P. S.; Andrews, A. M.; Zhou, C., Flexible multiplexed in2o3 nanoribbon aptamer-field-effect transistors for biosensing. *iScience* **2020,** *23* (9), 101469.

87. Zhao, C.; Cheung, K. M.; Huang, I.-W.; Yang, H.; Nakatsuka, N.; Liu, W.; Cao, Y.; Man, T.; Weiss, P. S.; Monbouquette, H. G.; Andrews, A. M., Implantable aptamer field-effect transistor neuroprobes for in vivo neurotransmitter monitoring. *Science Advances* **2021,** *7* (48), eabj7422.

88. Gao, Z.; Wu, G.; Song, Y.; Li, H.; Zhang, Y.; Schneider, M. J.; Qiang, Y.; Kaszas, J.; Weng, Z.; Sun, H.; Huey, B. D.; Lai, R. Y.; Zhang, Y., Multiplexed monitoring of neurochemicals via electrografting-enabled site-selective functionalization of aptamers on field-effect transistors. *Analytical Chemistry* **2022,** *94* (24), 8605-8617.

89. Wu, G.; Zhang, N.; Matarasso, A.; Heck, I.; Li, H.; Lu, W.; Phaup, J. G.; Schneider, M. J.; Wu, Y.; Weng, Z.; Sun, H.; Gao, Z.; Zhang, X.; Sandberg, S. G.; Parvin, D.; Seaholm, E.; Islam, S. K.; Wang, X.; Phillips, P. E. M.; Castro, D. C.; Ding, S.; Li, D.-P.; Bruchas,

M. R.; Zhang, Y., Implantable aptamer-graphene microtransistors for real-time monitoring of neurochemical release in vivo. *Nano Letters* **2022,** *22* (9), 3668-3677.

90. Lim, S. G.; Seo, S. E.; Park, S. J.; Kim, J.; Kim, Y.; Kim, K. H.; An, J. E.; Kwon, O. S., Real-time monitoring of serotonin with highly selective aptamer-functionalized conducting polymer nanohybrids. *Nano Converg* **2022,** *9* (1), 31.

91. Jeong, S.; Yang, D.; Beyene, A. G.; Del Bonis-O'Donnell, J. T.; Gest, A. M. M.; Navarro, N.; Sun, X.; Landry, M. P., High-throughput evolution of near-infrared serotonin nanosensors. *Science Advances* **2019,** *5* (12), eaay3771.

92. Kelich, P.; Jeong, S.; Navarro, N.; Adams, J.; Sun, X.; Zhao, H.; Landry, M. P.; Vuković, L., Discovery of DNA-carbon nanotube sensors for serotonin with machine learning and near-infrared fluorescence spectroscopy. *ACS Nano* **2021**.

93. Hong, G.; Diao, S.; Chang, J.; Antaris, A. L.; Chen, C.; Zhang, B.; Zhao, S.; Atochin, D. N.; Huang, P. L.; Andreasson, K. I.; Kuo, C. J.; Dai, H., Through-skull fluorescence imaging of the brain in a new near-infrared window. *Nature Photonics* **2014,** *8* (9), 723-730.

94. Galassi, T. V.; Jena, P. V.; Shah, J.; Ao, G.; Molitor, E.; Bram, Y.; Frankel, A.; Park, J.; Jessurun, J.; Ory, D. S.; Haimovitz-Friedman, A.; Roxbury, D.; Mittal, J.; Zheng, M.; Schwartz, R. E.; Heller, D. A., An optical nanoreporter of endolysosomal lipid accumulation reveals enduring effects of diet on hepatic macrophages in vivo. *Science Translational Medicine* **2018,** *10* (461), eaar2680.

95. Griebel, G.; Holmes, A., 50 years of hurdles and hope in anxiolytic drug discovery. *Nature reviews Drug discovery* **2013,** *12* (9), 667-687.

96. Bach, D. R., Cross-species anxiety tests in psychiatry: Pitfalls and promises. *Molecular Psychiatry* **2022,** *27* (1), 154-163.

97. van der Staay, F. J.; Arndt, S. S.; Nordquist, R. E., Evaluation of animal models of neurobehavioral disorders. *Behavioral and Brain Functions* **2009,** *5* (1), 1-23.

98. Ledford, H., If depression were cancer. *Nature* **2014,** *515* (7526), 182.

99. Belovicova, K.; Bogi, E.; Csatlosova, K.; Dubovicky, M., Animal tests for anxiety-like and depression-like behavior in rats. *Interdisciplinary toxicology* **2017,** *10* (1), 40.

100. Anyan, J.; Amir, S., Too depressed to swim or too afraid to stop? A reinterpretation of the forced swim test as a measure of anxiety-like behavior. *Neuropsychopharmacology* **2018,** *43* (5), 931-933.

101. Anisman, H.; Merali, Z., Rodent models of depression: Learned helplessness induced in mice. *Current Protocols in Neuroscience* **2001,** *14* (1), 8.10C.1-8.10C.15.

102. Maswood, S.; Barter, J. E.; Watkins, L. R.; Maier, S. F., Exposure to inescapable but not escapable shock increases extracellular levels of 5-ht in the dorsal raphe nucleus of the rat. *Brain research* **1998,** *783* (1), 115-120.

103. Srejic, L. R.; Wood, K. M.; Zeqja, A.; Hashemi, P.; Hutchison, W. D., Modulation of serotonin dynamics in the dorsal raphe nucleus via high frequency medial prefrontal cortex stimulation. *Neurobiol Dis* **2016,** *94*, 129-38.

104. Amat, J.; Baratta, M. V.; Paul, E.; Bland, S. T.; Watkins, L. R.; Maier, S. F., Medial prefrontal cortex determines how stressor controllability affects behavior and dorsal raphe nucleus. *Nature neuroscience* **2005,** *8* (3), 365-371.

105. Amat, J.; Matus-Amat, P.; Watkins, L. R.; Maier, S. F., Escapable and inescapable stress differentially and selectively alter extracellular levels of 5-ht in the ventral hippocampus and dorsal periaqueductal gray of the rat. *Brain Research* **1998,** *797* (1), 12-22.

106. Linthorst, A. C.; Reul, J. M., Stress and the brain: Solving the puzzle using microdialysis. *Pharmacology Biochemistry and Behavior* **2008,** *90* (2), 163-173.

107. Padilla-Coreano, N.; Bolkan, S. S.; Pierce, G. M.; Blackman, D. R.; Hardin, W. D.; Garcia-Garcia, A. L.; Spellman, T. J.; Gordon, J. A., Direct ventral hippocampal-prefrontal input is required for anxiety-related neural activity and behavior. *Neuron* **2016,** *89* (4), 857-866.

108. Sun, Q.; Li, X.; Li, A.; Zhang, J.; Ding, Z.; Gong, H.; Luo, Q., Ventral hippocampal-prefrontal interaction affects social behavior via parvalbumin positive neurons in the medial prefrontal cortex. *iScience* **2020,** *23* (3), 100894.

109. Steketee, J. D., Neurotransmitter systems of the medial prefrontal cortex: Potential role in sensitization to psychostimulants. *Brain Research Reviews* **2003,** *41* (2), 203-228.

110. Baxter, M. G.; Croxson, P. L., Facing the role of the amygdala in emotional information processing. *Proceedings of the National Academy of Sciences* **2012,** *109* (52), 21180-21181.

111. Sun, T.; Song, Z.; Tian, Y.; Tian, W.; Zhu, C.; Ji, G.; Luo, Y.; Chen, S.; Wang, L.; Mao, Y.; Xie, W.; Zhong, H.; Zhao, F.; Luo, M.-H.; Tao, W.; Wang, H.; Li, J.; Li, J.; Zhou, J.; Wang, K.; Zhang, Z., Basolateral amygdala input to the medial prefrontal cortex controls obsessive-compulsive disorder-like checking behavior. *Proceedings of the National Academy of Sciences* **2019,** *116* (9), 3799-3804.

112. Sun, Y.; Gooch, H.; Sah, P., Fear conditioning and the basolateral amygdala. *F1000Res* **2020,** *9*.

113. Maier, S. F.; Watkins, L. R., Stressor controllability, anxiety, and serotonin. *Cognitive Therapy and Research* **1998,** *22* (6), 595-613.

114. Anagnostaras, S.; Sage, J.; Carmack, S., Pavlovian fear conditioning. *Encyclopedia of Psychopharmacology* **2015**, 1237-1240.

115. Homberg, J. R., Serotonergic modulation of conditioned fear. *Scientifica* **2012,** *2012*.

116. Hashimoto, S.; Inoue, T.; Koyama, T., Effects of conditioned fear stress on serotonin neurotransmission and freezing behavior in rats. *European Journal of Pharmacology* **1999,** *378* (1), 23-30.

117. Hajós-Korcsok, É.; Robinson, D. D.; Yu, J. H.; Fitch, C. S.; Walker, E.; Merchant, K. M., Rapid habituation of hippocampal serotonin and norepinephrine release and anxiety-related behaviors, but not plasma corticosterone levels, to repeated footshock stress in rats. *Pharmacology Biochemistry and Behavior* **2003,** *74* (3), 609-616.

118. Hamani, C.; Diwan, M.; Macedo, C. E.; Brandão, M. L.; Shumake, J.; Gonzalez-Lima, F.; Raymond, R.; Lozano, A. M.; Fletcher, P. J.; Nobrega, J. N., Antidepressant-like effects of medial prefrontal cortex deep brain stimulation in rats. *Biological psychiatry* **2010,** *67* (2), 117-124.

119. Hamani, C.; Diwan, M.; Isabella, S.; Lozano, A. M.; Nobrega, J. N., Effects of different stimulation parameters on the antidepressant-like response of medial prefrontal cortex deep brain stimulation in rats. *Journal of Psychiatric Research* **2010,** *44* (11), 683-687.

120. Kirby, L. G.; Allen, A. R.; Lucki, I., Regional differences in the effects of forced swimming on extracellular levels of 5-hydroxytryptamine and 5-hydroxyindoleacetic acid. *Brain Research* **1995,** *682* (1), 189-196.

121. Adell, A.; Casanovas, J. M.; Artigas, F., Comparative study in the rat of the actions of different types of stress on the release of 5-ht in raphe nuclei and forebrain areas. *Neuropharmacology* **1997,** *36* (4-5), 735-41.

122. Fujino, K.; Yoshitake, T.; Inoue, O.; Ibii, N.; Kehr, J.; Ishida, J.; Nohta, H.; Yamaguchi, M., Increased serotonin release in mice frontal cortex and hippocampus induced by acute physiological stressors. *Neuroscience Letters* **2002,** *320* (1), 91-95.

123. Acikgoz, B.; Dalkiran, B.; Dayi, A., An overview of the currency and usefulness of behavioral tests used from past to present to assess anxiety, social behavior and depression in rats and mice. *Behavioural Processes* **2022,** *200*, 104670.

124. Toth, I.; Neumann, I. D., Animal models of social avoidance and social fear. *Cell and tissue research* **2013,** *354* (1), 107-118.

125. Lv, Z.; Zhang, Y.; Zhang, L.; Hou, W.; Lin, M.; Xun, Y.; Ma, H.; Li, Y.; Li, Y.; Tai, F.; He, Z., Involvement of dr→mpfc 5-htergic neural projections in changes of social exploration behaviors caused by adult chronic social isolation in mice. *Brain Research Bulletin* **2022,** *186*, 16-26.

126. Altieri, S. C.; Yang, H.; O'Brien, H. J.; Redwine, H. M.; Senturk, D.; Hensler, J. G.; Andrews, A. M., Perinatal vs genetic programming of serotonin states associated with anxiety. *Neuropsychopharmacology* **2015,** *40* (6), 1456-70.

127. Rex, A.; Thomas, H.; Hörtnagl, H.; Voits, M.; Fink, H., Behavioural and microdialysis study after neurotoxic lesion of the dorsal raphe nucleus in rats. *Pharmacology Biochemistry and Behavior* **2003,** *74* (3), 587-593.

128. Thomas, H.; Fink, H.; Sohr, R.; Voits, M., Lesion of the median raphe nucleus: A combined behavioral and microdialysis study in rats. *Pharmacology Biochemistry and Behavior* **2000,** *65* (1), 15-21.

129. Fenno, L.; Yizhar, O.; Deisseroth, K., The development and application of optogenetics. *Annu Rev Neurosci* **2011,** *34*, 389-412.

130. Lee, C.; Lavoie, A.; Liu, J.; Chen, S. X.; Liu, B. H., Light up the brain: The application of optogenetics in cell-type specific dissection of mouse brain circuits. *Front Neural Circuits* **2020,** *14*, 18.

131. Boyden, E. S.; Zhang, F.; Bamberg, E.; Nagel, G.; Deisseroth, K., Millisecond-timescale, genetically targeted optical control of neural activity. *Nature Neuroscience* **2005,** *8* (9), 1263-1268.

132. Klapoetke, N. C.; Murata, Y.; Kim, S. S.; Pulver, S. R.; Birdsey-Benson, A.; Cho, Y. K.; Morimoto, T. K.; Chuong, A. S.; Carpenter, E. J.; Tian, Z.; Wang, J.; Xie, Y.; Yan, Z.; Zhang, Y.; Chow, B. Y.; Surek, B.; Melkonian, M.; Jayaraman, V.; Constantine-Paton, M.; Wong, G. K.; Boyden, E. S., Independent optical excitation of distinct neural populations. *Nat Methods* **2014,** *11* (3), 338-46.

133. Vierock, J.; Rodriguez-Rozada, S.; Dieter, A.; Pieper, F.; Sims, R.; Tenedini, F.; Bergs, A. C. F.; Bendifallah, I.; Zhou, F.; Zeitzschel, N.; Ahlbeck, J.; Augustin, S.; Sauter, K.; Papagiakoumou, E.; Gottschalk, A.; Soba, P.; Emiliani, V.; Engel, A. K.; Hegemann, P.; Wiegert, J. S., Bipoles is an optogenetic tool developed for bidirectional dual-color control of neurons. *Nature Communications* **2021,** *12* (1), 4527.

134. Adesnik, H.; Abdeladim, L., Probing neural codes with two-photon holographic optogenetics. *Nature Neuroscience* **2021,** *24* (10), 1356-1366.

135. Kim, C. K.; Adhikari, A.; Deisseroth, K., Integration of optogenetics with complementary methodologies in systems neuroscience. *Nature Reviews Neuroscience* **2017,** *18* (4), 222-235.

136. Whissell, P. D.; Tohyama, S.; Martin, L. J., The use of dreadds to deconstruct behavior. *Front Genet* **2016,** *7*, 70.

137. Roth, B. L., Dreadds for neuroscientists. *Neuron* **2016,** *89* (4), 683-94.

138. Sternson, S. M.; Roth, B. L., Chemogenetic tools to interrogate brain functions. *Annual Review of Neuroscience* **2014,** *37* (1), 387-407.

139. Armbruster, B. N.; Li, X.; Pausch, M. H.; Herlitze, S.; Roth, B. L., Evolving the lock to fit the key to create a family of g protein-coupled receptors potently activated by an inert ligand. *Proceedings of the National Academy of Sciences* **2007,** *104* (12), 5163-5168.

140. Nagai, Y., [a novel ligand for chemogenetic receptors, deschloroclozapine, enables rapid and selective modulation of neuronal activity and behavior in living animals]. *Nihon Yakurigaku Zasshi* **2022,** *157* (4), 233-237.

141. Marcinkiewcz, C. A.; Mazzone, C. M.; D'Agostino, G.; Halladay, L. R.; Hardaway, J. A.; DiBerto, J. F.; Navarro, M.; Burnham, N.; Cristiano, C.; Dorrier, C. E.; Tipton, G. J.; Ramakrishnan, C.; Kozicz, T.; Deisseroth, K.; Thiele, T. E.; McElligott, Z. A.; Holmes, A.; Heisler, L. K.; Kash, T. L., Serotonin engages an anxiety and fear-promoting circuit in the extended amygdala. *Nature* **2016,** *537* (7618), 97-101.

142. Garcia-Garcia, A. L.; Canetta, S.; Stujenske, J. M.; Burghardt, N. S.; Ansorge, M. S.; Dranovsky, A.; Leonardo, E. D., Serotonin inputs to the dorsal bnst modulate anxiety in a 5-ht1a receptor-dependent manner. *Molecular Psychiatry* **2018,** *23* (10), 1990-1997.

143. Marcinkiewcz, C. A.; Bierlein-De La Rosa, G.; Dorrier, C. E.; McKnight, M.; DiBerto, J. F.; Pati, D.; Gianessi, C. A.; Hon, O. J.; Tipton, G.; McElligott, Z. A.; Delpire, E.; Kash, T. L., Sex-dependent modulation of anxiety and fear by 5-ht1a receptors in the bed nucleus of the stria terminalis. *ACS Chemical Neuroscience* **2019,** *10* (7), 3154-3166.

144. Sparta, D. R.; Jennings, J. H.; Ung, R. L.; Stuber, G. D., Optogenetic strategies to investigate neural circuitry engaged by stress. *Behavioural Brain Research* **2013,** *255*, 19-25.

145. Kim, S.-Y.; Adhikari, A.; Lee, S. Y.; Marshel, J. H.; Kim, C. K.; Mallory, C. S.; Lo, M.; Pak, S.; Mattis, J.; Lim, B. K., Diverging neural pathways assemble a behavioural state from separable features in anxiety. *Nature* **2013,** *496* (7444), 219-223.

146. Zhang, H.; Li, K.; Chen, H.-S.; Gao, S.-Q.; Xia, Z.-X.; Zhang, J.-T.; Wang, F.; Chen, J.-G., Dorsal raphe projection inhibits the excitatory inputs on lateral habenula and alleviates depressive behaviors in rats. *Brain Structure and Function* **2018,** *223* (5), 2243-2258.

147. Ohmura, Y.; Tsutsui-Kimura, I.; Sasamori, H.; Nebuka, M.; Nishitani, N.; Tanaka, K. F.; Yamanaka, A.; Yoshioka, M., Different roles of distinct serotonergic pathways in anxiety-like behavior, antidepressant-like, and anti-impulsive effects. *Neuropharmacology* **2020,** *167*, 107703.

148. Warden, M. R.; Selimbeyoglu, A.; Mirzabekov, J. J.; Lo, M.; Thompson, K. R.; Kim, S.-Y.; Adhikari, A.; Tye, K. M.; Frank, L. M.; Deisseroth, K., A prefrontal cortex–brainstem neuronal projection that controls response to behavioural challenge. *Nature* **2012,** *492* (7429), 428-432.

149. Faye, C.; Hen, R.; Guiard, B. P.; Denny, C. A.; Gardier, A. M.; Mendez-David, I.; David, D. J., Rapid anxiolytic effects of rs67333, a serotonin type 4 receptor agonist, and diazepam, a benzodiazepine, are mediated by projections from the prefrontal cortex to the dorsal raphe nucleus. *Biological psychiatry* **2020,** *87* (6), 514-525.

150. Challis, C.; Beck, S. G.; Berton, O., Optogenetic modulation of descending prefrontocortical inputs to the dorsal raphe bidirectionally bias socioaffective choices after social defeat. *Front Behav Neurosci* **2014,** *8*, 43.

151. Grizzell, J. A.; Clarity, T. T.; Graham, N. B.; Dulka, B. N.; Cooper, M. A., Activity of a vmpfc-drn pathway corresponds with resistance to acute social defeat stress. *Front Neural Circuits* **2020,** *14*, 50.

152. Prakash, N.; Stark, C. J.; Keisler, M. N.; Luo, L.; Der-Avakian, A.; Dulcis, D., Serotonergic plasticity in the dorsal raphe nucleus characterizes susceptibility and resilience to anhedonia. *The Journal of Neuroscience* **2020,** *40* (3), 569-584.

153. Abela, A. R.; Browne, C. J.; Sargin, D.; Prevot, T. D.; Ji, X. D.; Li, Z.; Lambe, E. K.; Fletcher, P. J., Median raphe serotonin neurons promote anxiety-like behavior via inputs to the dorsal hippocampus. *Neuropharmacology* **2020,** *168*, 107985.

154. Ohmura, Y.; Tanaka, K. F.; Tsunematsu, T.; Yamanaka, A.; Yoshioka, M., Optogenetic activation of serotonergic neurons enhances anxiety-like behaviour in mice. *International Journal of Neuropsychopharmacology* **2014,** *17* (11), 1777-1783.

155. Jimenez, J. C.; Su, K.; Goldberg, A. R.; Luna, V. M.; Biane, J. S.; Ordek, G.; Zhou, P.; Ong, S. K.; Wright, M. A.; Zweifel, L.; Paninski, L.; Hen, R.; Kheirbek, M. A., Anxiety cells in a hippocampal-hypothalamic circuit. *Neuron* **2018,** *97* (3), 670-683.e6.

156. Parfitt, G. M.; Nguyen, R.; Bang, J. Y.; Aqrabawi, A. J.; Tran, M. M.; Seo, D. K.; Richards, B. A.; Kim, J. C., Bidirectional control of anxiety-related behaviors in mice: Role of inputs arising from the ventral hippocampus to the lateral septum and medial prefrontal cortex. *Neuropsychopharmacology* **2017,** *42* (8), 1715-1728.

157. Hare, B. D.; Duman, R. S., Prefrontal cortex circuits in depression and anxiety: Contribution of discrete neuronal populations and target regions. *Mol Psychiatry* **2020,** *25* (11), 2742-2758.

158. Varga, V.; Székely, A. D.; Csillag, A.; Sharp, T.; Hajós, M., Evidence for a role of gaba interneurones in the cortical modulation of midbrain 5-hydroxytryptamine neurones. *Neuroscience* **2001,** *106* (4), 783-792.

159. Celada, P.; Puig, M.; Martín-Ruiz, R.; Casanovas, J. M.; Artigas, F., Control of the serotonergic system by the medial prefrontal cortex: Potential role in the etiology of ptsd and depressive disorders. *Neurotoxicity research* **2002,** *4* (5), 409-419.

160. Calhoon, G. G.; Tye, K. M., Resolving the neural circuits of anxiety. *Nature Neuroscience* **2015,** *18* (10), 1394-1404.

161. Xia, F.; Kheirbek, M. A., Circuit-based biomarkers for mood and anxiety disorders. *Trends in Neurosciences* **2020,** *43* (11), 902-915.

162. Sanacora, G.; Treccani, G.; Popoli, M., Towards a glutamate hypothesis of depression: An emerging frontier of neuropsychopharmacology for mood disorders. *Neuropharmacology* **2012,** *62* (1), 63-77.

163. Trullas, R.; Skolnick, P., Functional antagonists at the nmda receptor complex exhibit antidepressant actions. *European journal of pharmacology* **1990,** *185* (1), 1-10.

164. Sanacora, G.; Zarate, C. A.; Krystal, J. H.; Manji, H. K., Targeting the glutamatergic system to develop novel, improved therapeutics for mood disorders. *Nature reviews Drug discovery* **2008,** *7* (5), 426-437.

165. Pittenger, C.; Duman, R. S., Stress, depression, and neuroplasticity: A convergence of mechanisms. *Neuropsychopharmacology* **2008,** *33* (1), 88-109.

166. Price, R. B.; Duman, R., Neuroplasticity in cognitive and psychological mechanisms of depression: An integrative model. *Molecular psychiatry* **2020,** *25* (3), 530-543.

167. Aleksandrova, L. R.; Wang, Y. T.; Phillips, A. G., Evaluation of the wistar-kyoto rat model of depression and the role of synaptic plasticity in depression and antidepressant response. *Neuroscience & Biobehavioral Reviews* **2019,** *105*, 1-23.

168. Marsden, W., Synaptic plasticity in depression: Molecular, cellular and functional correlates. *Progress in Neuro-Psychopharmacology and Biological Psychiatry* **2013,** *43*, 168-184.

169. Duman, R. S.; Aghajanian, G. K.; Sanacora, G.; Krystal, J. H., Synaptic plasticity and depression: New insights from stress and rapid-acting antidepressants. *Nature medicine* **2016,** *22* (3), 238-249.

170. Norrholm, S. D.; Ouimet, C. C., Altered dendritic spine density in animal models of depression and in response to antidepressant treatment. *Synapse* **2001,** *42* (3), 151-163.

171. Hajszan, T.; Dow, A.; Warner-Schmidt, J. L.; Szigeti-Buck, K.; Sallam, N. L.; Parducz, A.; Leranth, C.; Duman, R. S., Remodeling of hippocampal spine synapses in the rat learned helplessness model of depression. *Biological psychiatry* **2009,** *65* (5), 392-400.

172. Radley, J. J.; Rocher, A. B.; Rodriguez, A.; Ehlenberger, D. B.; Dammann, M.; McEwen, B. S.; Morrison, J. H.; Wearne, S. L.; Hof, P. R., Repeated stress alters dendritic spine morphology in the rat medial prefrontal cortex. *Journal of Comparative Neurology* **2008,** *507* (1), 1141-1150.

173. Bagley, J.; Moghaddam, B., Temporal dynamics of glutamate efflux in the prefrontal cortex and in the hippocampus following repeated stress: Effects of pretreatment with saline or diazepam. *Neuroscience* **1997,** *77* (1), 65-73.

174. Lowy, M. T.; Gault, L.; Yamamoto, B. K., Rapid communication: Adrenalectomy attenuates stress-induced elevations in extracellular glutamate concentrations in the hippocampus. *Journal of neurochemistry* **1993,** *61* (5), 1957-1960.

175. Moghaddam, B., Stress preferentially increases extraneuronal levels of excitatory amino acids in the prefrontal cortex: Comparison to hippocampus and basal ganglia. *Journal of neurochemistry* **1993,** *60* (5), 1650-1657.

176. Gras, C.; Herzog, E.; Bellenchi, G. C.; Bernard, V.; Ravassard, P.; Pohl, M.; Gasnier, B.; Giros, B.; El Mestikawy, S., A third vesicular glutamate transporter expressed by cholinergic and serotoninergic neurons. *The Journal of Neuroscience* **2002,** *22* (13), 5442-5451.

177. Voisin, A. N.; Mnie-Filali, O.; Giguère, N.; Fortin, G. M.; Vigneault, E.; El Mestikawy, S.; Descarries, L.; Trudeau, L., Axonal segregation and role of the vesicular glutamate transporter vglut3 in serotonin neurons. *Front Neuroanat* **2016,** *10*, 39.

178. Belmer, A.; Beecher, K.; Jacques, A.; Patkar, O. L.; Sicherre, F.; Bartlett, S. E., Axonal non-segregation of the vesicular glutamate transporter vglut3 within serotonergic projections in the mouse forebrain. *Front Cell Neurosci* **2019,** *13*, 193.

179. Amilhon, B.; Lepicard, È.; Renoir, T.; Mongeau, R.; Popa, D.; Poirel, O.; Miot, S.; Gras, C.; Gardier, A. M.; Gallego, J.; Hamon, M.; Lanfumey, L.; Gasnier, B.; Giros, B.; El Mestikawy, S., Vglut3 (vesicular glutamate transporter type 3) contribution to the regulation of serotonergic transmission and anxiety. *The Journal of Neuroscience* **2010,** *30* (6), 2198-2210.

180. Lebrand, C.; Cases, O.; Adelbrecht, C.; Doye, A.; Alvarez, C.; El Mestikawy, S.; Seif, I.; Gaspar, P., Transient uptake and storage of serotonin in developing thalamic neurons. *Neuron* **1996,** *17* (5), 823-835.

181. Ciranna, L., Serotonin as a modulator of glutamate- and gaba-mediated neurotransmission: Implications in physiological functions and in pathology. *Curr Neuropharmacol* **2006,** *4* (2), 101-14.

182. Żmudzka, E.; Sałaciak, K.; Sapa, J.; Pytka, K., Serotonin receptors in depression and anxiety: Insights from animal studies. *Life Sciences* **2018,** *210*, 106-124.

183. Pazos, A.; Palacios, J. M., Quantitative autoradiographic mapping of serotonin receptors in the rat brain. I. Serotonin-1 receptors. *Brain Research* **1985,** *346* (2), 205-230.

184. Pazos, A.; Cortés, R.; Palacios, J. M., Quantitative autoradiographic mapping of serotonin receptors in the rat brain. Ii. Serotonin-2 receptors. *Brain Research* **1985,** *346* (2), 231-249.

185. Carhart-Harris, R.; Nutt, D., Serotonin and brain function: A tale of two receptors. *Journal of Psychopharmacology* **2017,** *31* (9), 1091-1120.

186. Alexander, L.; Young, A. H., Recent advances in the psychopharmacology of major depressive disorder. *BJPsych Advances* **2022**, 1-14.

187. Goldberg, S. B.; Pace, B. T.; Nicholas, C. R.; Raison, C. L.; Hutson, P. R., The experimental effects of psilocybin on symptoms of anxiety and depression: A meta-analysis. *Psychiatry Research* **2020,** *284*, 112749.

188. Shao, L.-X.; Liao, C.; Gregg, I.; Davoudian, P. A.; Savalia, N. K.; Delagarza, K.; Kwan, A. C., Psilocybin induces rapid and persistent growth of dendritic spines in frontal cortex in vivo. *Neuron* **2021,** *109* (16), 2535-2544.e4.

189. De Vos, C. M.; Mason, N. L.; Kuypers, K. P., Psychedelics and neuroplasticity: A systematic review unraveling the biological underpinnings of psychedelics. *Frontiers in psychiatry* **2021**, 1575.

190. Olson, D. E., Biochemical mechanisms underlying psychedelic-induced neuroplasticity. *Biochemistry* **2022,** *61* (3), 127-136.

191. Zanos, P.; Gould, T. D., Mechanisms of ketamine action as an antidepressant. *Molecular Psychiatry* **2018,** *23* (4), 801-811.

192. Aleksandrova, L. R.; Phillips, A. G., Neuroplasticity as a convergent mechanism of ketamine and classical psychedelics. *Trends in Pharmacological Sciences* **2021,** *42* (11), 929-942.

193.Https://www.Accessdata.Fda.Gov/drugsatfda_docs/label/2022/215430orig1s000correctedlbl.Pdf.

194. Wilkinson, S. T.; Sanacora, G., A new generation of antidepressants: An update on the pharmaceutical pipeline for novel and rapid-acting therapeutics in mood disorders based on glutamate/gaba neurotransmitter systems. *Drug Discovery Today* **2019,** *24* (2), 606-615.

195. Dagher, M.; Perrotta, K. A.; Erwin, S. A.; Hachisuka, A.; Iyer, R.; Masmanidis, S. C.; Yang, H.; Andrews, A. M., Optogenetic stimulation of midbrain dopamine neurons produces striatal serotonin release. *ACS Chemical Neuroscience* **2022,** *13* (7), 946-958.

196. Monge-Acuña, A. A.; Fornaguera-Trías, J., A high performance liquid chromatography method with electrochemical detection of gamma-aminobutyric acid, glutamate and glutamine in rat brain homogenates. *Journal of Neuroscience Methods* **2009,** *183* (2), 176-181.

197. Hu, Y.; Mitchell, K. M.; Albahadily, F. N.; Michaelis, E. K.; Wilson, G. S., Direct measurement of glutamate release in the brain using a dual enzyme-based electrochemical sensor. *Brain Research* **1994,** *659* (1), 117-125.

198. Zeynaloo, E.; Yang, Y.-P.; Dikici, E.; Landgraf, R.; Bachas, L. G.; Daunert, S., Design of a mediator-free, non-enzymatic electrochemical biosensor for glutamate detection. *Nanomedicine: Nanotechnology, Biology and Medicine* **2021,** *31*, 102305.

199. Viana, R. R.; Pego, A. M. F.; de Oliveira, T. F.; Dallegrave, E.; Eller, S., Liquid chromatography–tandem mass spectrometry method for simultaneous quantification of neurotransmitters in rat brain tissue exposed to 4′-fluoro-α-php. *Biomedical Chromatography* **2022,** e5487.

200. Zangen, A.; Nakash, R.; Overstreet, D. H.; Yadid, G., Association between depressive behavior and absence of serotonin–dopamine interaction in the nucleus accumbens. *Psychopharmacology* **2001,** *155* (4), 434-439.

201. Conio, B.; Martino, M.; Magioncalda, P.; Escelsior, A.; Inglese, M.; Amore, M.; Northoff, G., Opposite effects of dopamine and serotonin on resting-state networks: Review and implications for psychiatric disorders. *Molecular Psychiatry* **2020,** *25* (1), 82-93.

202. Hjorth, O. R.; Frick, A.; Gingnell, M.; Hoppe, J. M.; Faria, V.; Hultberg, S.; Alaie, I.; Månsson, K. N. T.; Wahlstedt, K.; Jonasson, M.; Lubberink, M.; Antoni, G.; Fredrikson, M.; Furmark, T., Expression and co-expression of serotonin and dopamine transporters in social anxiety disorder: A multitracer positron emission tomography study. *Molecular Psychiatry* **2021,** *26* (8), 3970-3979.

203. Michaelides, A.; Zis, P., Depression, anxiety and acute pain: Links and management challenges. *Postgraduate Medicine* **2019,** *131* (7), 438-444.

204. Rink, L.; Adams, A.; Braun, C.; Bschor, T.; Kuhr, K.; Baethge, C., Dose-response relationship in selective serotonin and norepinephrine reuptake inhibitors in the treatment of major depressive disorder: A meta-analysis and network meta-analysis of randomized controlled trials. *Psychotherapy and Psychosomatics* **2022,** *91* (2), 84-93.

205. Pham, T. H.; Gardier, A. M., Fast-acting antidepressant activity of ketamine: Highlights on brain serotonin, glutamate, and gaba neurotransmission in preclinical studies. *Pharmacology & Therapeutics* **2019,** *199*, 58-90.

206. Xia, G.; Han, Y.; Meng, F.; He, Y.; Srisai, D.; Farias, M.; Dang, M.; Palmiter, R. D.; Xu, Y.; Wu, Q., Reciprocal control of obesity and anxiety–depressive disorder via a gaba and serotonin neural circuit. *Molecular Psychiatry* **2021,** *26* (7), 2837-2853.

207. Lüscher, B.; Möhler, H., Brexanolone, a neurosteroid antidepressant, vindicates the gabaergic deficit hypothesis of depression and may foster resilience. *F1000Res* **2019,** *8*.

208. Rafi, H.; Zestos, A. G., Multiplexing neurochemical detection with carbon fiber multielectrode arrays using fast-scan cyclic voltammetry. *Analytical and Bioanalytical Chemistry* **2021,** *413* (27), 6715-6726.

CHAPTER II

Simultaneous Serotonin and Dopamine Monitoring Across Timescales by Rapid Pulse Voltammetry with Partial Least Squares regression

The information in this chapter is reproduced with permission from Analytical and Bioanalytical Chemistry, Copyright 2021.

Simultaneous serotonin and dopamine monitoring across timescales by rapid pulse voltammetry with partial least squares regression

Release. Movassaghi, C. S.; Perrotta, K. A.; Yang, H.; Iyer, R.; Cheng, X.; Dagher, M.; Fillol, M. A.; Andrews, A. M., *Anal Bioanal Chem* 2021, 413 (27), 6747-6767. DOI: 10.1007/s00216-021-03665-1

Introduction

The idea that neurotransmitters function *via* coordinated activities to shape behavior is becoming increasingly supported by *in vivo* studies. [4-12] We recently found that optogenetic stimulation of midbrain dopamine neurons, which drives reward-related behavior, [13] produces serotonin release in striatum. [14] Dopamine and serotonin neurons directly and indirectly form circuits with one another. [15-17] Both systems exhibit developmental, functional, and clinical interplay. [18, 19] The dopamine and serotonin systems are implicated in diverse behaviors of relevance to neuropsychiatric and neurological disorders, including major depressive and anxiety disorders, [20, 21] schizophrenia, [22, 23] substance use disorder, [24, 25] and Parkinson's disease. [26, 27] These and other findings support the overarching hypothesis that multiple neurochemical systems, and particularly, the dopamine and serotonin systems, function (or dysfunction) concertedly. [28-30]

Neurochemical signaling encodes biologically relevant information across multiple timescales. [31] Tonic (basal) neurotransmitter levels arise from clocklike neural firing over minutes to hours to days. Phasic (transient) changes in neurotransmitter levels are rapid (tens of milliseconds to seconds) and are hypothesized to result from synchronized bursts of neural firing in response to evoked or naturally occurring stimuli. [32-36] The ability to monitor transitory neurochemical events, in conjunction with changes in tonic signaling, will enable a more comprehensive understanding of how chemical neurotransmission encodes behaviorally relevant information. [37, 38]

A variety of techniques are available for *in vivo* neurochemical monitoring with various advantages and disadvantages. [39-42] Here, we focus on voltammetry methods, including fast-scan cyclic voltammetry (FSCV), to detect electroactive neurotransmitters. The use of small carbon-fiber microelectrodes (5-30 μm diameter) [43, 44] and high sampling rates (10-100 Hz) [45, 46] in FSCV can be used to differentiate release *vs*. reuptake processes. [47]

While widely employed, FSCV suffers from poor analyte specificity. Overlapping oxidation (and reduction) profiles of structurally similar neurochemicals, many of which occur at low concentrations, make *in vivo* measurements of transmitters other than dopamine difficult with FSCV [48]. Moreover, FSCV is limited by the need for background subtraction of large capacitive currents generated during voltage sweeps at fast scan rates. Background subtraction precludes tonic (basal) neurotransmitter determinations and measurements over longer time frames, (*e.g.*, minutes-hours), due to current drift. [49, 50]

Several novel waveforms have been developed that improve and expand various aspects of sweep-wave voltammetry. [45, 51] Fast-scan controlled absorption voltammetry (FSCAV) enables determination of basal dopamine or serotonin levels. [37,52,53] Other adsorption waveforms and accumulation electrodes have been reported. [54,55] Sombers and coworkers devised a waveform that allowed prediction and subtraction of electrochemical drift for measurements of dopamine, adenosine, and H_2O_2, [56] as well as sweep waveforms to detect the opioid peptide met-enkephalin, H_2O_2, and pH. [57, 58]

Complex waveforms that combine sweeps or staircases with square-wave pulses have been reported. Multiple cyclic square-wave voltammetry was used to quantify tonic dopamine *in vivo* with 10-s resolution. [59] Improvements in selectivity and sensitivity were made using fast-cyclic square-wave voltammetry (FCSWV) [60] and N-FCSWV [61] for monitoring dopamine and serotonin *in vivo*, respectively. Multiplexing has not yet been achieved with square-wave voltammetry—two different waveforms were needed to measure dopamine [60] *vs.* serotonin. [61] Additionally, capacitive current simulation, which relies on assumptions about exponential current decay, was needed for background subtraction. Venton and coworkers used single-walled carbon nanotube electrodes with FSCV to measure simultaneous changes in dopamine and serotonin *in vivo.* [62] The carbon nanotube coating reduced the formation of oxidative byproducts of serotonin and increased the cathodic currents of dopamine and serotonin, improving analyte discrimination *via* more distinct reduction profiles. [63]

Principal components analysis (PCA) [64] and principal components regression (PCR) [65, 66] have been used for multiplexing *via* dimensionality reduction in FSCV, with PCR capable of quantitative predictions. Another dimensionality reduction method widely used in chemometrics is partial least squares regression (PLSR). [67] The PLSR approach is a supervised machine learning technique (*i.e.*, it models input and output); PCA and PCR are considered unsupervised (*i.e.*, only input data is modeled). The use of PLSR was shown to improve predictive accuracy over PCR when analyzing FSCV data for mixtures of neurochemicals. [68] Other uses included prediction and correction of FSCV background drift and pH changes. [56, 58] Kishida and colleagues pioneered combining FSCV with regularized linear regression (*i.e.,* elastic net electrochemistry) for sub-second monitoring of evoked dopamine [69, 70] and serotonin [71, 72] in human striatum during decision making tasks.

While newer waveforms and data processing methods have advanced neurochemical measurements, no single voltammetry technique yet enables tonic and phasic levels of multiple neurotransmitters to be determined simultaneously. To address this, we demonstrate a two-pronged approach to improve waveform design and data analysis. We gained inspiration from the voltammetric electronic tongue (VET), [73] used to measure analytes in food, [74, 75] beverages, [76, 77] and wastewater. [78] Rather than using conventional pulse waveforms, 'smart' pulse waveforms are designed for VET sensing. These pulse trains are initially constructed based on the electrochemical characteristics of the analytes of interest. [79] Pulse widths and amplitudes, as well as pulse train frequencies, among other factors, are optimized to extract distinguishing electrochemical characteristics for data processing. [80, 81] Smart pulse design has been shown to outperform conventional [79] and random [74] pulse waveforms using the VET method.

Data generated by the VET method have been analyzed using a multivariate technique, commonly PLSR. [75, 77] As PLSR models covariance, the model prioritizes variations in input (current response) that correspond to qualitative and quantitative changes in output (analyte classification and concentration). [67] As such, differences in the Helmholtz double layer, mass transport, analyte concentrations and adsorption, and other dynamic electrode surface properties occurring during an applied pulse are considered as potential sources of analyte specific information. This information is encoded in the transient responses of faradaic and non-faradaic currents. By including faradaic and non-faradaic current responses as input to the model (*i.e.,* not background subtracting), the PLSR model selects aspects of the current response that covary with analyte identity and concentration. This is opposed to background subtracted methods, where some information is discarded prior to model input to increase signal-to-noise. Potentially relevant information in the background is then lost.

An appropriately trained model can handle voltammetry data without the need for background subtraction, noise filtering/removal, or drift subtraction. In addition to VET studies, regularized regression applied to FSCV has been used to demonstrate that appropriately trained models benefit from information beyond analyte redox potentials when background subtraction is avoided. [70, 72] The use of regularized regression accounted for drift and noise, similar to PLSR.

Here, we report on the initial development of rapid pulse voltammetry coupled with PLSR (RPV-PLSR) using a smart pulse approach. By avoiding background subtraction, RPV-PLSR utilizes faradaic and nonfaradaic current to improve analyte identification and quantification power. Inclusion of the background current also enables tonic and phasic concentration predictions in a single experiment at fast timescales (*i.e.*, limited only by waveform frequency).

Materials and Methods

Chemicals

Dopamine hydrochloride (#H8502) and serotonin hydrochloride (#H9523) were purchased from Sigma Aldrich (St. Louis, MO). Artificial cerebrospinal fluid (aCSF) for *in vitro* experiments consisted of 147 mM NaCl (#73575), 3.5 mM KCl (#05257), 1.0 mM NaH_2PO_4 (#17844), 2.5 mM $NaHCO_3$ (#88208) purchased from Honeywell Fluka (Charlotte, NC), and 1.0 mM $CaCl_2$ (#499609) and 1.2 mM $MgCl_2$ (#449172) purchased from Sigma Aldrich. The aCSF solution was adjusted to pH 7.3 ± 0.03 using HCl (Fluka, #84415). The phosphate-buffered mobile phase for high performance liquid chromatography (HPLC) consisted of 96 mM NaH_2PO_4, 3.8 mM Na_2HPO_4 (Fluka #71633), pH 5.4, 2-2.8% MeOH (EMD #MX0475), 50 mg/L EDTA $\cdot Na_2$ (Sigma #03682), and 500 mg/L sodium decanesulfonate (TCI #I0348) in water. All aqueous solutions were made using ultrapure water (Milli-Q, Millipore, Billerica, MA).

In vitro Experiments

For *in vitro* training data used for preliminary method validation, carbon fiber microelectrodes were fabricated as described previously [44] with minor modifications. Single 7-µm diameter carbon fibers (Specialty Materials, Lowell, MA) were vacuum-aspirated into borosilicate glass capillaries (Sutter Instrument Company, Novato, CA). Each capillary was pulled to produce two electrodes by tapering and sealing using a micropipette puller (P-1000, Sutter Instrument Company, Novato, CA). Electrode tips were cleaned with 100% isopropanol (Fisher A416P, for electronic use) for 10 min and dried at 90-100 °C for 10-20 min. Electrode tips were then sealed by dipping in non-conductive epoxy (Epoxy Technology Inc., Billerica, MA) for 7-10 min twice at a 1 h interval at room temperature. Epoxied electrodes were dried at 90-100 °C overnight. Prior to testing, electrode tips were blunt-cut using a surgical scalpel under a microscope to create 7-µm diameter disk shaped conducting surfaces. Bare silver wire (0.010-inch diameter, A-M Systems, Sequim, WA) was cleaned using a polishing cloth and inserted into working electrode capillaries to serve as the electrical connection (**Fig. II.S1**). The electrodes were backfilled with 2 M aqueous NaCl for electrical connection. Reference electrodes (RE-5B Ag/AgCl, BASi, West Lafayette, IN) used for all *in vitro* experiments were maintained in oversaturated aqueous KCl. Fresh aCSF was delivered to a flow cell at a constant flow rate of 2.5-2.7 mL/min by a peristaltic pump. (**Fig. II.S1**). Standards (180 µL) of dopamine, serotonin, and their mixtures were injected *via* an autoinjector (VICI E60 Actuator, Valco Instruments Co. Inc., Houston, TX) in pseudo-random order at >5 min intervals.

In vivo Experiments

Animals

Subjects were virgin female mice generated at the University of California, Los Angeles (UCLA) from a DAT^{IREScre} lineage (Jackson Laboratory, stock no. 006660) on a C57Bl/6J background *via* heterozygote mating. All surgeries were carried out under aseptic conditions with isoflurane anesthesia (5% isoflurane for induction, 1.5-2% for maintenance) on a KOPF Model 1900 Stereotaxic Alignment System (KOPF, Tujunga, CA). After each surgery, mice were administered the analgesic carprofen (5 mg/kg, 1 mg/mL, sc) for the first three days, and an antibiotic (amoxicillin, 0.25 mg/mL) and analgesic (ibuprofen, 0.25 mg/mL) in drinking water for 14 days post-surgery.

RPV-PLSR

Three mice first underwent a surgical procedure for head-bar implantation. A pair of rectangular head-bars (9 mm × 7 mm × 0.76 mm, 0.6 g each, laser cut from stainless steel at Fab2Order) were attached to the sides of the skull by C&B-METABOND (**Fig. II.S1**; Parkell, Edgewood, NY). The Cre-dependent adeno-associated viral vector (AAV) was obtained from the

University of North Carolina Vector Core (Chapel Hill, NC). A nanoinjector was used to deliver 600 nL of 7.8 × 10^{12}/mL AAV5/Syn-Flex-ChrimsonR-tdT unilaterally into the ventral tegmental area (VTA)/substantia nigra (SN) area (AP -3.08 mm, ML ±1.20 mm, DV -4.00 mm from Bregma). Then, a 200 μm diameter ferrule-coupled optical fiber (0.22 NA, Thorlabs, Newton, NJ) was implanted (AP -3.08 mm, ML ±1.20 mm, DV -3.80 mm from Bregma via the same path of viral vector injection) to deliver optical stimulation during experiments.

After surgery, mice were pair-housed with cagemates to recover for at least 2-3 weeks and to allow for expression of genes of interest before an additional craniotomy surgery. During this time, subjects were trained to acclimate to the head-fixed testing condition for 15-30 min/session × 6-10 sessions. Two craniotomies were carried out 24 h ahead of testing days. A piece of skull (2.0 mm width × 2.0 mm length, centered at AP +1.0 mm, ML ±1.0 mm from Bregma) above the striatum (STR) of the same hemisphere as the AAV injection site was removed for working electrode insertion. For the Ag/AgCl reference electrode, a 0.4 mm diameter hole (centered AP +2.8 mm, ML ±2.0 mm from Bregma) was made in the skull on the side contralateral to the AAV injection site. The dura remained intact for both surgical areas. All surgery areas were first sealed with a thin layer of Kwik-Cast & Kwik-Sil (World Precision Instruments, Sarasota, FL) and then covered with a thin layer of C&B-METABOND. Animals were allowed to recover for 24 h.

On the testing day, each mouse was transferred and mounted to the head-fixed stage *via* its head-bars (**Fig. II.S1**). After a 10 min habituation period, the C&B-METABOND cover, Kwik-Cast & Kwik-Sil seal, and dura above the recording and reference electrode sites were carefully removed. A Ag/AgCl reference electrode made from bleached silver wire was lowered into the brain. An optical fiber was calibrated to 10 mW/mm^2 daily prior to fiber coupling. Optical stimulation was generated *via* a 532 nm MGL-III-532 laser (Changchun New

Industries Optoelectronics Tech. Col, Ltd, Changchun, P. R. China). Square pulses of 50% duty at 30 or 40 Hz for 20 s were used to deliver optical stimulation at >5 min intervals. One subject received a dose of escitalopram (20 mg/kg, sc). Basal and optically stimulated responses were collected before and beginning 1 h after drug administration.

The working electrode (PEDOT:Nafion carbon fiber microelectrode) was sterilized using 70% ethanol, rinsed with saline, and lowered into the striatum for voltammetry measurements *via* a 1 µm-precision motorized digital micromanipulator (MP-225, Sutter Instrument, Novato, CA). The PEDOT:Nafion coated electrodes were fabricated as per published protocols. [82] Each electrode had a cylindrical conducting surface that was 5-µm in diameter and ~75 µm in length. When lowered to a new recording depth, the electrode baseline was restabilized for at least 10 min before continuing stimulations.

During testing, sweetened milk diluted with water was delivered to the subject every 2 hr. Subject behavior was monitored for signs of distress. After the experiment, each subject was prepared for histological verification of Chrimson expression, recording electrode position, and the position of the optical fiber. At the end of each *in vivo* experiment, electrodes were removed and post-calibrated using standards of dopamine, serotonin, and their mixtures in physiological saline to generate the training set data.

Microdialysis

Mice (N=3) at 3-6 months of age were Chrimson-transfected, had an optical fiber implanted, and were trained to be head-fixed, as described above. Two-three weeks after Chrimson-transfection, a second surgery was carried out first to implant a CMA/7 guide cannula for a microdialysis probe aimed at the dSTR (AP+1.00 mm, ML±1.75 mm, DV-3.10 mm from Bregma) into the same hemisphere as the viral delivery and fiber implant site (see above). The guide cannula was secured to the skull with C&B-METABOND. Animals recovered from the surgery for at least three days before microdialysis.

Subjects underwent online microdialysis testing for one day. Following testing, the microdialysis probe was removed and the brain of each mouse was prepared for histology to verify the microdialysis probe and optical fiber placements, and Chrimson expression. Microdialysis probe and optical fiber tracks were visualized using light microscopy.

On the night before microdialysis (ZT10-12), each mouse was briefly anesthetized with isoflurane (1-3 min) for insertion of a CMA/7 microdialysis probe (1 mm length, 6 kDa cutoff, CMA8010771; Harvard Apparatus, Holliston, MA) into the guide cannula. Subjects were returned to their home cages after insertion and aCSF was continuously perfused through the probe at 2-3 µL/min for 30-60 min followed by a 0.3 µL/min flow rate for an additional 12-14 h to allow stabilization of the brain tissue surrounding the probe.

On the testing day, subjects were relocated to the head-stage recording set-up and allowed to habituate for at least 30 min before basal data collection. Optical stimulation was performed as described above, except the pulses were delivered at 10 Hz for 5 min. The first stimulation was delivered at ~ZT-2 after 6-18 basal dialysate samples were collected and analyzed. Prior to reverse dialysis of escitalopram (10 µM), three optical stimulations were delivered at 1-h intervals. After 90-120 min of intrastriatal drug perfusion, an additional three optical stimulations were delivered at 1-h intervals while drug perfusion was continued.

High performance liquid chromatography was performed using an Amuza HTEC-500 integrated system (Amuza Corporation [formally known as Eicom], San Diego, CA). An Eicom Insight autosampler was used to inject standards and Eicom EAS-20s online autoinjectors were used to collect and inject microdialysis dialysates. [83] Chromatographic separation was achieved using an Eicom PP-ODS II column (4.6 mm ID x 30 mm length, 2 µm particle diameter). The column temperature was maintained at 21 °C. The volumetric flow rate was

450-500 µL/min. Electrochemical detection was performed using an Eicom WE-3G graphite working electrode with an applied potential of +450 mV *vs.* a Ag/AgCl reference electrode.

Standard curves encompassed physiological concentration ranges of serotonin and dopamine in dialysates (0-10 nM). The limit of detection was ≤302 amol (6.05 pM) for each analyte; the practical limit of quantification was ≤916 amol (18.3 pM). Dialysate samples were collected online at 5-min intervals using a dialysate flow rate of 1.8 µL/min and injected immediately onto the HPLC system for analysis.

Voltammetry Data Acquisition and Analysis

Measurement Hardware

Voltammetry measurements were carried out using a two-electrode configuration via a Ag/AgCl reference electrode and a carbon fiber microelectrode working electrode. Waveforms were generated using a PC with a PCI-6221 data acquisition card (National Instruments (NI), Austin, TX) to control an EI-400 potentiostat (Cypress Systems, USA) and a custom 'headstage' analog pre-amplifier. Potentials were applied to the reference electrode while the working electrode was tied to the zero-potential terminal (virtual ground) of the pre-amplifier circuit. The pre-amplifier was designed to output an analog voltage proportional to electrode current. Detailed information on the custom headstage design is in the Supplemental Information (**Fig. II.S2**). The output voltage was amplified by the EI-400, then sampled and quantified by an analog-to-digital converter on the NI PCI-6221 data acquisition card.

Measurement Software

An in-house software program was developed for this study. The software was programmed in MATLAB (R2016a; The MathWorks, Inc., Natick, MA) and consisted of three modules. (1) The signal generation module enabled the design of multi-step waveforms at user-specified potentials, scan rates, sampling and fundamental frequencies, and numbers of sampled points per waveform period. (2) The

MATLAB Data Acquisition Toolbox enabled event-driven communication during the measurement process. Waveforms were loaded from the signal generation module while the user specified the measurement start and stop points, along with optional parameters for stimulation or injection events. The data acquisition card generated the analog potential signal and the stimulation signal and digitized the resulting current. Voltammograms for each measurement cycle and the temporal evolution of current at potentials of interest were plotted in real-time. At the end of each measurement, digitized current measurement data were stored in MATLAB files. (3) The data processing module displayed the acquired data in a variety of user-specified formats, allowed for user-defined background subtraction, digital filtering and signal averaging, and generated MATLAB or Excel files to be extracted for machine learning models.

Waveforms

Three different waveforms were used herein. (1) A four-step rapid pulse waveform consisting of -0.4 V to +0.2 V to +0.8 V to -0.1 V to -0.4 V at 2 ms per step applied at 10 Hz for *in vitro* RPV to investigate differentiating serotonin from dopamine (**Fig. II.1a**). (2) A triangle waveform [44] for FSCV from -0.4 V to +1.2 V to -0.4 V at a scan rate of 400 ms/V delivered at 10 Hz for *in vitro* comparisons with the RPV waveform (**Fig. II.1b**). (3) A combination of the four-step rapid pulse and triangle waveforms described above. Each waveform was delivered in an alternating manner at 5 Hz *in vivo* and during post calibration (**Fig. II.1c**).

Machine Learning

Data were extracted from raw MATLAB files into Excel and imported into Python using Pandas 0.25.1 and Jupyter 6.0.1 notebooks. All models were built using the Python 3.7.4 programming language in Jupyter notebooks using NumPy 1.16.5, SciPy 1.3.1, and scikit-learn 0.22.1. [84] Data visualization was *via* matplotlib 3.1.1. Per each model built, data were normalized unless otherwise noted using either the ℓ_1, ℓ_2 or maximum norm, as chosen by grid search. [84]

Statistics

Statistical analyses for *in vivo* data (two-tailed *t*-tests; Table S1) were carried out using Prism, v.9.1.0 (GraphPad Inc., La Jolla, CA). Basal data over six timepoints just prior to the first optical stimulation were averaged for $N=3$ microdialysis mice and $N=1$ RPV mouse. The areas under the curve for microdialysis stimulation peaks were calculated using four dialysate samples after the onset of stimulation. Due to faster sampling, the areas under the curve for RPV stimulation peaks were calculated using fifty-two points post stimulation onset. Data are expressed as means ± standard errors of the mean (SEMs). Throughout, $P<0.05$ was considered statistically significant.

Results and Discussion

We designed and evaluated an initial rapid pulse waveform *in vitro* for dopamine and serotonin co-detection (**Fig. II.1a**) and to compare with a triangle waveform [44] (**Fig. II.1b**). For *in vivo* experimentation, we alternated the rapid pulse and triangle waveforms (RPV-FSCV; **Fig. II.1c**). Experimental paradigms utilizing these waveforms are shown in **Fig. II.2.** The RPV-FSCV waveform was used to facilitate within-subjects' comparisons (**Fig. II.2a**). For experiments in mice, electrodes were post-calibrated *in vitro* to produce training set data (**Fig. II.2b**). Training set data for each waveform were used to build machine learning regression models to classify and to quantify dopamine and serotonin (**Fig. II.2c**). Multiple waveform-model combinations were compared in the context of cross-validation accuracy and predicted *in vivo* responses.

Rapid Pulse Waveform Design

We designed an initial rapid pulse waveform (**Fig. II.1a**) based on potentials characteristic of commonly used dopamine or serotonin FSCV waveforms (**Fig. II.1b**). The rapid pulse waveform employed a starting potential of -0.4 V, similar to a commonly used dopamine FSCV waveform [85] (**Fig. II.1b**), but with steps to +0.2 V and -0.1 V, similar to the voltages scanned during the N-FSCV waveform used for preventing serotonin adsorption on electrode surfaces and to promote reduction of serotonin, respectively. [86] A step to +0.8 V was included to ensure the oxidation of serotonin and dopamine, while preventing capacitive currents from reaching the maximum current limits of our hardware, which occurs with large potential steps. Employing intermediate pulses (*e.g.,* +0.2 V and -0.1 V) has been shown to increase analyte discrimination and precision for VETs. [80] Both faradaic and non-faradaic currents at intermediate steps contribute analyte-specific information more so than a single, large amplitude pulse step directly to the redox potential of interest (*i.e.*, from -0.4 V directly to +0.8 V), which would be dominated by capacitive current. In the future, intermediate steps can be added to reach +1.3 V, the upper potential commonly used for dopamine detection and recently optimized for serotonin detection. [51] This high upper potential was not used for this proof-of-concept experiment for simplification and to keep the pulse duration short. Employing a counter pulse completes the redox cycle and generates additional information on analyte identity, as demonstrated in electronic tongue pulse design. [79]

In Vitro Model Construction

Data preprocessing is critical to the training and use of machine learning models, such as PLSR. Here, we use the terms 'feature' or 'variable' interchangeably to refer to the current response at a given time point in a voltammogram. We refer to a voltammogram as a 'sample' determined using a particular combination of analyte concentrations (*in vitro*) or at a particular time relative to a stimulation event (*in vivo*).

Preprocessing typically involves mean-centering (setting means across all samples at each feature equal to zero) and either standardization (scaling the data to have unit variance at each feature across all samples) or normalization (scaling the input features to unit length). Mean-centering is done to simplify the computation process and should not affect model output. [67] Standardization is commonly used to remove magnitude-related effects, while normalization is used to preserve them. All are commonly accepted practices in the machine learning field, as well as for PLSR in chemometrics. [67]

Previous implementations of FSCV with PCR or PLSR did not employ mean-centering or data standardization. By forgoing these procedures, the magnitudes of the original current responses were preserved. This caused the PCR or PLSR models to weigh regions of larger current amplitude (*i.e.,* redox peaks) more heavily compared to low amplitude regions (*i.e.,* noise). For techniques like FSCV, which rely mainly on variations in peak current responses for classification and quantification of analytes, non-standardized data make sense. The model should focus mostly on the variances at the highest peak magnitudes to correlate current magnitudes with concentration. However, pulse techniques, such as the VET and RPV, are explicitly designed *not* to rely solely on peak currents for quantification. Instead, the entire voltammogram is treated as a holistic source of predictive data. Thus, data are standardized, as the model should not treat larger current responses with greater importance.

To investigate the effects of standardization on RPV data, we used a variable selection technique. The *in vitro* raw RPV voltammograms are shown in **Figure II.3a.** The samples obtained (1000 data points or 'features') were then represented in 1000 dimensions or principal components (PCs), each of which described some amount of variance in the data. The PCs were formed *via* a linear combination of the original variables and weighted projection coefficients, known as loadings. [87] Loading vectors of greatest magnitude and similar direction in the factor space represented greater correlation.

Variable selection is the process of determining the features to present to the model as input. The relevance of different features can be examined through various methods based on the algorithm used. For PLSR, a variable importance in the projection (VIP) score can be mathematically calculated for each feature. [88] Generally, VIP scores >1 indicate variables that are important for the model to learn from the training data; features with scores <1 are considered less important. Thus, VIP scores can be used to evaluate waveform responses and serve three purposes. First, the VIP scores allow us to evaluate if RPV-PLSR is truly using current responses (features) not just from faradaic currents, but also from noise or capacitive currents. Second, the VIP scores allow us to evaluate how preprocessing affects feature importance (*e.g.*, standardized *vs.* non-standardized data). And third, areas of the pulse response that are consistently more important for the model can be considered for more frequent sampling in future pulse designs, whereas areas of the current response that consistently have low VIP scores can be excluded by either reducing their sampling or removing that part of the pulse train. The VIP scores can be used as another metric to systematically optimize waveforms for a given analyte panel.

Preliminary analyses demonstrated that RPV-PLSR with standardized data are not dominated by magnitude-related effects and use areas of current response that historically have been discarded (**Fig. II.3b**). For standardized data, the number of features with VIP scores >1 was 518 out of a possible 1000 features. For non-standardized data, the VIP scores clearly mimicked the magnitude of the current response. Moreover, the number of VIP scores >1 was only 231/1000. Standardizing the data allowed for a more than doubling of 'important' features and these features spanned areas of the voltammogram dominated by non-faradaic current.

The use of non-faradaic current by the model is further supported by an analysis of the PLSR loadings (**Fig. II.3c**). The magnitude of the projection of the **X** loading vectors onto the **Y** loading vectors was calculated as a mathematical representation of the strength of the correlation that each data point had with different combinations of dopamine and serotonin. To visualize regions of the voltammograms most informative for the model, a moving average kernel was applied to map each variable to low, medium, or high correlation (no shading, 50% shading, or 100% shading, respectively). Areas of the voltammograms with the highest shaded heights were most useful for that analyte (regardless of sign; positive or negative values are arbitrary). For example, the current response of the second pulse step (points 250-500) had high red-shaded areas during capacitive charging illustrating non-faradaic contributions to modeling dopamine. Meanwhile, the majority of the decay of the second pulse step, which would include faradic and non-faradaic contributions, was heavily used for modeling serotonin.

Similar to the VIP scores (**Fig. II.3b**), **Figure II.3c** demonstrates that RPV pulses can be optimized using PLSR analyses (*e.g.*, the last two pulses could be shortened to improve temporal resolution as the tail-ends of each decay are not shaded). These findings support the theory behind intelligent (and iterative) pulse design in RPV and the key idea that background subtracted methods, like FSCV, are likely to be inferior in terms of generating information needed to specify analytes and their concentrations, particularly in complex mixtures, because key information in capacitive current decay is removed. Instead, the VET-based approach used for RPV is a 'soft' technique, agnostically collecting information across the entire pulse train. [89] The capacitive current increases transiently and then decays exponentially due to the presence of charged and polar compounds. Concurrently, faradaic current approaches a limiting value based on the diffusion and adsorption rates of electroactive species. Using multivariate analysis, and specifically, dimensionality reduction, the model is trained on trends across the pulse train, not the response of individual currents, such as in univariate calibration. [90]

Our findings are further supported by similar results for elastic net electrochemistry, [91] in which the authors used non-background subtracted voltammograms obtained using a FSCV triangular waveform to train an elastic net model, a regularized linear regression technique with some similarities to supervised dimensionality reduction techniques like PLSR. [92] The large magnitude (*i.e.,* important) regularization coefficients, similar to the large magnitude loadings and VIP scores discussed above, were found to span areas of the voltammogram outside of the expected peak faradaic responses of dopamine and serotonin [69, 72].

A key difference between RPV and FSCV is that RPV is a pulse method having current decay across each pulse step. Since faradaic and capacitive currents evolve at different rates, each point in the decay provides unique information that is potentially useful for distinguishing analytes. That is, a stepped pulse approach is more information rich when coupled with a regression model compared to a sweep method, even if background subtraction is bypassed in the latter. Further, because RPV uses a bespoke pulse design, which can increase sensitivity when combined with electrode surface modifications, [93] temporal resolution can be maximized by changing the pulse parameters. The waveform parameters in **Figure II.1a** are simply a starting point.

In Vivo Model Construction & Deployment

Based on our preliminary *in vitro* RPV findings and the availability of suitable animal subjects from an ongoing study, [14] we conducted a pilot *in vivo* study with RPV-PLSR. This small study was designed to compare the feasibility of an RPV waveform (that was admittedly unoptimized) with a commonly used FSCV waveform, early in our development of RPV and before continuing with the validation and creation of larger and more complex *in vitro* RPV training sets. We have found that advancing to *in vivo* experiments sooner in methods development helps to guide our *in vitro* efforts (sometimes in unexpected and fruitful ways). [94, 95]

We designed a combined rapid pulse-triangle waveform (RPV-FSCV) for use in conjunction with an optogenetic stimulation paradigm. The red-shifted opsin Chrimson was virally transfected into midbrain dopamine neurons in DAT$^{\mathrm{IRES}\mathit{cre}}$ mice. Four weeks later, carbon-fiber microelectrodes coated with PEDOT:Nafion [82] were used to measure dopamine and serotonin in the striatum (STR). Optical stimulation (532 nm, 30 or 40 Hz, 20 s) was delivered to dopamine cell bodies in the substantia nigra/ventral tegmental area (SN/VTA) while the combined waveform (**Fig. II.1c**) was applied to the carbon fiber microelectrode with each alternating waveform at 5 Hz. After several stimulations, the selective serotonin reuptake inhibitor (SSRI) escitalopram was administered, and stimulation continued one-hour post administration. Similar paradigms have been used to examine dopamine in STR. [96] Electrodes were then removed and used to obtain post-calibration training data for PLSR analysis (**Table II.1**).

Training set samples (one normalized, non-background subtracted voltammogram per standard) were used to train and to cross-validate the PLSR model. While our hypothesis that standardization allows the model to place emphasis on response areas unrelated to magnitude was supported by our *in vitro* data (**Fig. II.3b**), initial analyses of *in vivo* data using standardization resulted in negative predicted basal concentrations for dopamine, serotonin, or both. Nonetheless, dopamine and serotonin showed the expected qualitative and quantitative (nanomolar) responses to stimulation.

By removing magnitude related effects *via* standardization, identification of analytes was possible, but quantitation became less reliable. We attributed this to the limited size and concentration range of the training set; standardization emphasizes variability. For accurate quantitation, standardization requires large data sets to train the model adequately on small-magnitude variations. Conversely, the VIP scores for the normalized data mimicked the non-standardized data in **Figure II.3b**, meaning that lower magnitude responses were still considered by the model due to inclusion of the background, but not as heavily as in standardization. Thus, normalization was used as the preprocessing method for the *in vivo* data to retain current amplitudes associated with a small training set size and for comparison to previous studies. [66, 68]

After training the PLSR model, the number of components was optimized. The variance explained by the model is a function of the number of components included. For

PLSR, the first component always explains the maximal covariance in the data, with successive decreases in covariance explained by additional components (*i.e.,* the first component explains more covariance than the second, which explains more than the third, and so on). The total number of components equals the number of samples, at which the data set is fully reconstructed (the cumulative variance explained reaches 100%). The model is then deployed with an *a priori* number of components such that only the most relevant features that lead to accurate analyte identification and quantification are used to make predictions, while the less relevant features (unrelated noise) are not utilized. Notably, 'noise' as defined by background subtraction may differ from 'noise' as defined by a PLSR model, meaning the background must be included to allow the PLSR model to discern in the number of components. The number of components can be estimated based on training set conditions and domain knowledge (*i.e.,* if the degrees of freedom of the system under study are known), or determined empirically, commonly by hyperparameter tuning during cross-validation.

To determine the variance in the *Y* variable (concentration) explained by the model, R^2Y scores were calculated (**Table II.2**). To estimate the generalizability of the model, Q^2Y scores were calculated (*i.e.,* cross-validated R^2Y scores that serve as a proxy for predictive accuracy) using leave-one-out cross-validation because of the small training set size. [97] Given the known two-component calibration and variability of cross-validation errors for small training sets, [98-100] we opted to deploy the two-component PLSR model *in vivo* at the expense of a lower *in vitro* cross-validation score ($Q^2Y = 0.1$ for two components *vs.* $Q^2Y = 0.6$ for three components). Although ostensibly detrimental to the model, selecting a model with higher cross validation error can prevent overfitting, especially in the case of noisy training data. [101] The two-component model was used to predict *in vivo* concentrations of dopamine and serotonin simultaneously across time in a single subject.

As input to the RPV-PLSR model, for each stimulation, 300 scans (120 s total) were extracted that included 150 scans prior to stimulation (60 s) and 150 scans after the onset of stimulation (60 s). As output, the model predicted dopamine and serotonin concentrations for each scan based on the post-calibration training set. A moving average filter was applied to smooth and to align concentration *vs.* time plots. Basal concentrations were calculated as pre-stimulation baseline averages of the first 100 scans. Stimulated concentrations were defined as the areas under the curve for the stimulation peaks. Representative concentration-time plots are shown in **Figure II.4**.

During the experiment, the carbon fiber microelectrode was lowered from the dorsal striatum to the ventral striatum (dSTR and vSTR, respectively). Multiple stimulations were delivered at each position relative to the surface of the brain The average predicted basal concentration increased for dopamine and decreased for serotonin moving from dSTR to vSTR (**Fig. II.4a,b,** respectively). These trends are in general agreement with previously reported dorsoventral dopamine and serotonin gradients in striatum, [102] which is known to be neurochemically diverse. [103] To investigate the effects of stimulation strength, we applied a 40 Hz stimulation in the dorsal striatum and after ~5 min, applied a 30 Hz stimulation at the same electrode position. Higher frequency stimulation produced greater stimulated dopamine [104, 105] and serotonin release (**Fig. II.4c,d**).

The predicted basal concentrations are most likely overestimates of actual concentrations given that we biased our *in vivo* training set towards higher dopamine and serotonin concentrations in this proof-of-concept study. Given this limitation, the relative differences of the simultaneous dopamine and serotonin levels under varying stimulation paradigms and model-waveform combinations are more important than absolute concentrations. Optical stimulation of dopamine neurons expressing the excitatory opsin Chrimson produced dopamine release detected by RPV-PLSR (**Fig. II.4a,c**). The RPV-PLSR model, which was trained to differentiate dopamine and serotonin, also predicted serotonin release (**Fig. II.4b,d**). Our recent microdialysis findings support the idea that optical stimulation of midbrain dopamine neurons produces serotonin release [14]. Linked dopamine and serotonin in the striatum has been reported elsewhere. [63]

To increase our confidence in RPV-PLSR predictions, we compared the effects of serotonin transporter inhibition on basal and stimulated serotonin and dopamine using RPV-PLSR *vs.* microdialysis. The latter is a 'gold standard' neurochemical monitoring method that relies on chromatographic separations for analyte identification and quantification. [95, 106] Similar to RPV, DAT^{irescre} mice were transfected with Chrimson for optical excitation of midbrain dopamine neurons during microdialysis. [14] Dialysis samples were collected at 5 min intervals and analyzed immediately online by HPLC with electrochemical detection. The optical stimulation was 5 min to match the dialysate sampling time. For RPV, we optically stimulated dopamine neurons for 20 s and sampled at 5 Hz.

Following administration of the selective serotonin reuptake inhibitor (SSRI) escitalopram, we observed potentiation of optically evoked serotonin (*i.e.*, greater area under the curve) determined by RPV-PLSR and microdialysis (**Fig. II.5a,b**). Administration of an SSRI increases stimulated serotonin overflow due to reduced reuptake of serotonin by high affinity serotonin transporters. [61,107,108] Serotonin reuptake inhibition also led to a 60% increase in basal serotonin levels [94] observed *via* microdialysis (**Fig. II.5b**). By contrast, RPV-PLR predicted a small relative decrease in basal extracellular serotonin (2%) (**Fig. II.5a**).

One factor contributing to the RPV-PLSR prediction of lower basal serotonin following escitalopram involves the high concentration and limited number of standards used in the PLSR training set, which may result in insensitivity to modest changes. The RPV training set employed low micromolar concentration standards, whereas the predicted reduction in serotonin basal levels after escitalopram was only ~20 nM. Another factor potentially contributing to the discrepant effects of escitalopram on basal serotonin levels is the difference in the routes of drug administration. Mice in the microdialysis study received intrastriatal infusion of escitalopram, whereas mice in the RPV study were administered a subcutaneous drug injection. Systemic injection of an SSRI activates inhibitory 5HT1A autoreceptors on serotonin cell bodies. [109, 110] This negative feedback reduces serotonin neuron firing, which acutely results in reduced serotonin release in terminals regions like the striatum. Local infusion of escitalopram circumvents activation of somatodendritic 5HT1A receptors and produces an increase in terminal region serotonin levels. [94]

Like serotonin, we observed escitalopram-induced potentiation of optically evoked dopamine by RPV-PLSR and microdialysis (**Fig 5c,d**). Local perfusion of escitalopram did not affect basal dopamine levels determined by microdialysis (**Fig 5d**), while subcutaneous injection of escitalopram was associated with a small (5%) increase in predicted basal dopamine levels by RPV-PLSR (**Fig 5c**). As discussed, limitations of the training set used for RPV-PLSR, as well as the different routes of escitalopram administration may underlie variations in the basal dopamine outcomes.

Despite the high selectivity of escitalopram for serotonin transporters and low affinity for dopamine transporters [111], the serotonin and dopamine systems are linked. Serotonin neurons innervate the SN and VTA, and both systems project to subcortical and cortical regions (*e.g.,* striatum, frontal cortex, dorsomedial thalamus, cerebral cortex). [112,113] Serotonin receptors expressed on dopamine neurons in the striatum mediate dopamine release. [114,115] Moreover, human imaging studies suggest that citalopram and/or escitalopram increase striatal dopamine levels [116] and dopamine transporter binding (as a compensatory response), [117, 118] presumably *via* increases in extracellular serotonin. Regardless of differences in absolute concentrations, microdialysis acts as external validation to confirm that optogenetic stimulation of dopamine neurons releases striatal serotonin and escitalopram potentiates optically stimulated dopamine. Overall, these findings indicate that RPV can be used to detect pharmacologically induced changes in the stimulated release of two neurotransmitters simultaneously *in vivo*.

Waveform-model Combination Comparisons

To compare waveforms and analyses, R^2Y and Q^2Y scores were generated for different model/waveform/background subtracted combinations using the *in vivo* post-calibration training set data (**Table II.1**). In addition to two-component models, R^2Y and Q^2Y values were computed for three- and five-component models (**Table II.2**) due to literature precedent. [68] Greater numbers of components were expected and found to produce erroneous results (negative concentrations, noisy oscillations), likely due to model overfitting. This supported our choice of the two-component model to analyze the *in vivo* results, rather than models with higher cross validation scores. [101] However, due to the large increase in both R^2Y and Q^2Y moving from two to three components (an 'elbow' point; see **Fig. II.S3**), three-component models were chosen to compare cross-validation scores across models. In all cases, training data were pre-processed with mean-centering and normalization.

We sought to answer three questions regarding RPV-PLSR in the context of the current training set data and to guide future studies. 1) How does RPV-PLSR compare, in terms of prediction, with previously developed FSCV-PCR (*i.e.,* background-subtracted voltammograms obtained *via* a triangle waveform (**Fig. II.1b**) and analyzed by PCR)? 2) Does including background current data in RPV-PLSR result in a benefit over background subtracted RPV-PLSR, as suggested by **Fig. II.3c**? 3) Does RPV-PLSR provide more information about analyte identification/quantification than FSCV-PCR or other possible combinations (*e.g.*, why not use FSCV-PLSR?). We discuss various combinations below and find that each step of RPV-PLSR is needed to result in the optimal combination. For each combination, only the voltammograms for the relevant waveform were extracted to build the model (*i.e.,* voltammograms from the triangle waveform were extracted when referring to FSCV; voltammograms from the pulse waveform were extracted when referred to RPV).

Comparing RPV-PLSR to FSCV-PCR

Having demonstrated the non-background subtracted RPV-PLSR waveform-model combination, the effects of striatal recording electrode position, optical stimulation frequency, and SSRI administration were examined using background subtracted FSCV data and PCR analysis (**Fig. II.6**). The FSCV-PCR model has been used for dopamine or serotonin monitoring. [65] Because background currents, which contain information about tonic neurotransmitters levels, are removed, the 'basal' levels predicted by the FSCV-PCR model are not meaningful and thus, were not considered.

Optically stimulated release of dopamine (**Fig. II.6a,c**) and serotonin (**Fig. II.6b,d,e**) were predicted by a two component FSCV-PCR model. However, the stimulated concentrations were predicted to be much larger (~1 μM) than by RPV-PLSR and on the high end of literature reported values. [37,119,120] No increases in optically evoked release were detected in association with higher frequency stimulation for either dopamine or serotonin for FSCV-PCR analyses (**Fig. II.6c,d**) or for serotonin following SSRI administration (**Fig. II.6e**).

To ensure the model had enough components included to pick up on these differences, we tried increasing the number of components in the FSCV-PCR model from three to five. These additional components did not cause the serotonin traces to be distinguished by stimulation paradigm (data not shown; *i.e.,* the concentration traces looked the same for both 30 and 40 Hz stimulation frequency regardless of the number of components beyond two). This suggests that the model did have enough degrees of freedom, but was undertrained and consistently predicting a response that was not related to serotonin. Meanwhile, dopamine traces began to lose noticeable stimulation responses and showed increased noise as the number of components was increased from three to five, indicating that for this data set, two or three components appear to be better.

The results thus far support the notion that PLSR can deal more efficiently with noise and interferents when trained *in vitro* and used *in vivo* because PLSR models covariation of input and output, rather than just input, as in PCR. We did notice similarities in predicted responses for FSCV-PCR and FSCV-PLSR suggesting that overall, more training data and training across common interferents was needed. Further, RPV-PCR produced similar traces in the same concentration range for dopamine compared to RPV-PLSR (1.8 to 2.3 μM). Serotonin traces showed more variation (larger SEMs) and slightly larger predicted concentrations (1.05 to 1.10 μM) but remained responsive to the stimulation paradigms. In both cases, stimulated responses were on the same order of magnitude as RPV-PLSR (10-100 nM). This is despite the low cross-validation score, again supporting the need to cautiously interpret these scores when small training sets are used. For these reasons, we could not state definitively the necessity for PLSR over PCR, other than to state that previous methods support the use of supervised learning over PCR for FSCV. [69] Because PLSR has been compared to PCR elsewhere, [68, 87, 92] we do not compare results further here.

The Need for Including Background Current.

We hypothesized that avoiding background subtraction would result in information gain for the RPV-PLSR model. We indeed observed greater cross validation scores for nonbackground-subtracted compared to background-subtracted RPV-PLSR models (**Table II.2**). However, this trend was not consistent across waveform-model combinations. The FSCV-PLSR and RPV-PCR analyses showed worse cross-validation accuracy without background subtraction (0.48 compared to 0.44 and 0.40 compared to -0.05, respectively), while the FSCV-PCR cross-validation score improved without background subtraction (0.27 compared to 0.41). Because no clear trend in cross-validation was present when background current was subtracted *vs.* not, we suspect that information gain may be waveform and model dependent. Regardless, nonbackground-subtracted voltammograms obtained by our smart pulse waveform and analyzed by PLSR (*i.e.*, RPV-PLSR) resulted in the highest three-component R^2Y (0.82) and Q^2Y (0.57) scores of all background/waveform/model combinations examined (**Table II.2**). These variation and accuracy metrics suggest that RPV-PLSR may be better at modelling and predicting dopamine and serotonin concentrations, at least based on the limited training data.

Comparisons of Further Waveform/Model Combinations

Other waveform/model/background subtraction combinations were explored (**Table II.2**). Two, three, and five component models were trained and used to analyze the *in vivo* post-calibration training set data. While RPV-PCR and FSCV-PLSR behaved somewhat similarly to RPV-PLSR and FSCV-PCR (**Fig. II.S4, II.S5**), in all other cases, except those discussed above, we did not find consistent, biologically relevant responses to stimulation paradigms (optical or pharmacological). Although it is possible these models would begin to produce meaningful results with more training data, we note that only the RPV-PLSR method worked reasonably well for this small data set. The RPV-PLSR method, compared to other waveform/model combinations, predicted the most reasonable relative differences when monitoring dopamine and serotonin across stimulation and pharmacologic paradigms. The absolute concentrations, however, should always be regarded as estimates, especially when using dimensionality reduction models. [121] Nonetheless, we attribute the success of RPV-PLSR to the wealth of information in the pulse and the parsimony of the PLSR model. When combined, our findings support the idea that RPV-PLSR can be used to extract maximally relevant information, even with small training set sizes.

Study Limitations and Future Directions

We note the following limitations of this proof-of-concept study. The first is training set size. While increased training set size should improve model generalizability, [91, 122] training sets with similar sizes to ours (**Table II.1**; N=18) have been used in previous studies. [69, 70] The second limitation is the robustness of our training set. Notably, we did not train for responses to interferents (*e.g.,* 5-hydroxyindoleacetic acid, 3,4-dihydroxyphenylacetic acid, ascorbic acid), changes in pH or ionic salt concentrations (*e.g.,* Na^+, K^+, Ca^{2+}, Mg^{2+}), any of which could conflate capacitive current responses in the PLSR model. This is a potential reason for the likely overestimated basal concentrations. [123] While our findings *in vivo* correspond with previously reported biological phenomena and relative trends, our basal concentrations are outside of what is expected for dopamine and serotonin based on previous voltammetry and microdialysis studies (~10–1000 nM and ~1–100 nM, respectively). [37, 59, 106, 124]

In the future, we plan to design more robust training sets that include interferents, pH changes, and ionic strength changes to investigate their influence on RPV-PLSR. However, most metabolites of dopamine and serotonin are not expected to change extracellularly (at least over short time frames) during stimulation because they are metabolized intracellularly. [125-127] Further, because the RPV-PLSR model was trained using data across a four-step (*i.e.,* intermediate) pulse voltammogram, it is less likely for the dimensionality reduction to confound interferents across multiple potential steps and time points. While varying pH was not considered in this training set, similar approaches have demonstrated pH insensitivity for dopamine and serotonin when using supervised learning, as opposed to unsupervised techniques (*i.e.,* PCR). [69, 72]

Artifacts from ionic and pH changes during stimulated neurotransmitter release occur regardless of background subtraction. [123,128] Some literature suggests that physiological changes in pH and divalent cationic salt concentrations may pose less of an interference problem for biogenic amines when using pulsed voltammetry, [129] as opposed to FSCV, especially with Nafion-coated electrodes, [130] potentially due to different surface binding mechanisms. The PEDOT:Nafion electrodes used here provide some selectivity against the anionic interferents mentioned above and reduce acute (6 h) biofouling, [82] bolstering confidence in our predictions of cationic neurotransmitters.

Long term (chronic) recordings can lead to variability in electrode responses due to biofouling. We will continue to calibrate multiple electrodes post-fouling (that is, after *in vivo* recording), which should account for some variability introduced over the course of brain implantation. We plan to increase the training size in future training sets, such that the model is trained on artifacts of fouling and other confounding factors mentioned above. We hypothesize that with increased training data, nonspecific signals can be parsed out by PLSR, or another supervised model. In theory, we could add short, highly anodic pulses (*i.e.*, 1.3 V *vs.* Ag/AgCl) to try to renew electrode surfaces (electrochemical cleaning as employed in VETs [89] and FSCV [121]). Larger, historical training sets may also require ensemble weighting schemes to account for electrode variation. [122]

At present, we do not directly compare RPV-PLSR to elastic net electrochemistry, [91] another supervised learning technique. Theoretical comparisons of their underlying statistical approaches can be found elsewhere. [92] Instead, we note that dimensionality reduction techniques usually require less computation time than regularized techniques, suggesting the RPV-PLSR should scale well for larger training sets, which is a long-term goal of both techniques. However, both dimensionality reduction (PLSR) and regularization (elastic net) seek to prevent overfitting in some manner, whether by introducing sparsity in the latter case or by projecting data to a lower-dimension feature space in the former. Thus, both methods improve robustness of predictions. The two methods can be combined as a form of variable selection due to their supervised nature (*i.e.,* EN-PLS). [131, 132] In fact, the RPV approach can theoretically be combined with any appropriate supervised regression technique that enables feature selection, representing a paradigm shift in design and analysis of waveform-model combinations.

Based on the initial findings arising from the non-background-subtracted, supervised machine learning regression model (RPV-PLSR), we plan to optimize the pulse waveforms presented here, guided by feature selection as discussed earlier. Supervised learning techniques can enable iterative construction and optimization of fit-for-purpose waveforms to expand measurements to diverse sets of electroactive neurotransmitters (*e.g.*, dopamine, serotonin, norepinephrine, *etc.*). We will also explore other pre-processing and feature selection techniques, as well as more advanced supervised regression models. Larger training sets across many electrodes with more diverse analyte/interferent panels will be needed [121]. Further validation and alternatives to *in vitro* training (*i.e.,* relying on domain knowledge and stimulation paradigms, in addition to cross-validation metrics) should be explored to bolster confidence for *in vivo* predictions when using dimensionality reduction and regularization models that are trained and validated *in vitro*, but applied *in vivo*. Indeed, other areas of the physical sciences are currently working to address model generalizability through embeddings, representations, and domain knowledge. [133] Based on the current findings, future *in vivo* experiments can be designed more robustly to continue to investigate whether data processing models can distinguish and identify analytes in the complex brain matrix (*e.g.,* validation using DAT inhibitors, dopamine and serotonin synthesis inhibitors, and *in vivo* standard addition). Overall, we foresee a new paradigm in which fit-for-purpose pulses are iteratively constructed with feature selection feedback (**Scheme II.1**).

The coupling of voltammetry with more sophisticated pattern recognition and statistical tools is part of a global shift in scientific data analysis. Applications of machine learning in the physical sciences have skyrocketed over the last decade. [134] Other chemistry disciplines, such as materials, physical, and organic chemistry, were early adopters, but modern machine learning techniques have been underutilized in electrochemistry, specifically voltammetry. [135, 136] While advanced techniques, such as deep learning, have been used for classification of voltammograms, [137, 138] its counterpart (regression) is less often reported. [91, 122] The development of this novel voltammetric technique (RPV) coupled with fit-for-purpose machine learning (ML) pipelines (broadly defined as RPV-ML) represents a new paradigm for electroanalytical classification and quantitation of multiplexed neurochemical responses across timescales. This single, customizable technique allows for multiplexed neurotransmitter measurements in real-time in behaving animals, representing a step towards decoding neurotransmission at the molecular scale.

Conclusions

All three aspects of RPV appear essential for its success: intelligent pulse design, avoiding background subtraction, and supervised regression (*i.e.*, PLSR). We have demonstrated that the RPV-PLSR combined paradigm can identify and quantify two neurotransmitters *in vitro*. When dopamine neurons were optically stimulated, the RPV-PLSR model detected serotonin release *in vivo*, which corroborates a novel finding by microdialysis using the same experimental paradigm (*i.e.*, opsin, transfection and stimulation location, and recording location). [14] Compared to FSCV-PCR and other waveform/model combinations, RPV-PLSR was better equipped to detect changes induced by different stimulation frequencies. When an SSRI was administered, RPV-PLSR detected increases in stimulated serotonin levels. Overall, our experimental pipeline demonstrates proof-of-concept for a reliable new technique that can detect biologically relevant (*i.e.,* nM) changes in basal and stimulated levels of multiple neurotransmitters simultaneously across biologically relevant timescales (*i.e.,* stimulated and basal levels over ms to h).

Figures

Figure II.1

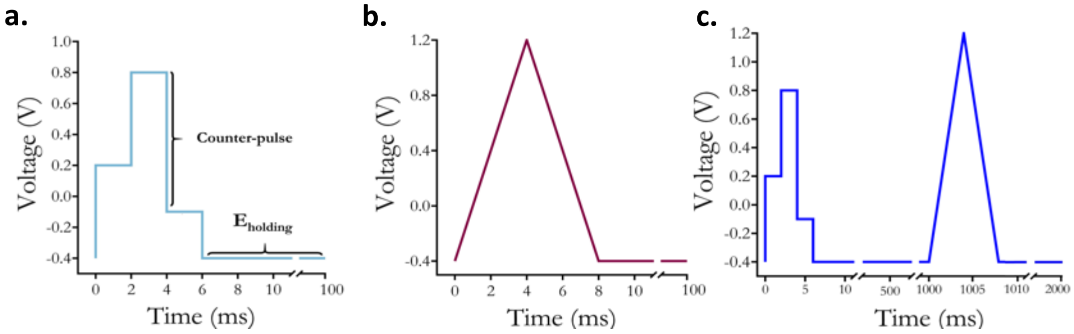

Figure II.1. Voltammetry waveforms used in this study. (**a**) Four-step rapid pulse voltammetry (RPV) pulsed waveform. (**b**) Fast-scan cyclic voltammetry (FSCV) triangle waveform. (**c**) Combined RPV-FSCV waveform.

Figure II.2

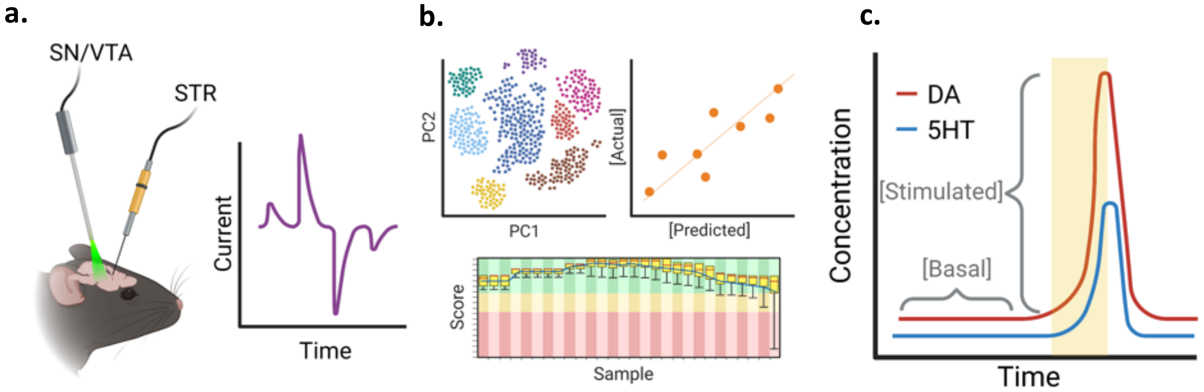

Figure II.2. General scheme for rapid pulse voltammetry-principle least squares regression (RPV-PLSR). (**a**) Dopamine neurons in the substantia nigra and ventral tegmental area (SN/VTA) of DAT^{IREScre} mice were transfected with the excitatory opsin Chrimson. Basal and optically stimulated dopamine and serotonin levels were recorded from the striatum (STR) using the alternating RPV-fast-scan cyclic voltammetry waveform (Fig. II.1c). (**b**) Electrodes used for *in vivo* measurements were then post-calibrated to provide data to build a PLSR model for analyte identification and quantification. (**c**) The *in vivo* data were analyzed using the model. Aspects of this figure were created using Biorender.com.

Figure II.3

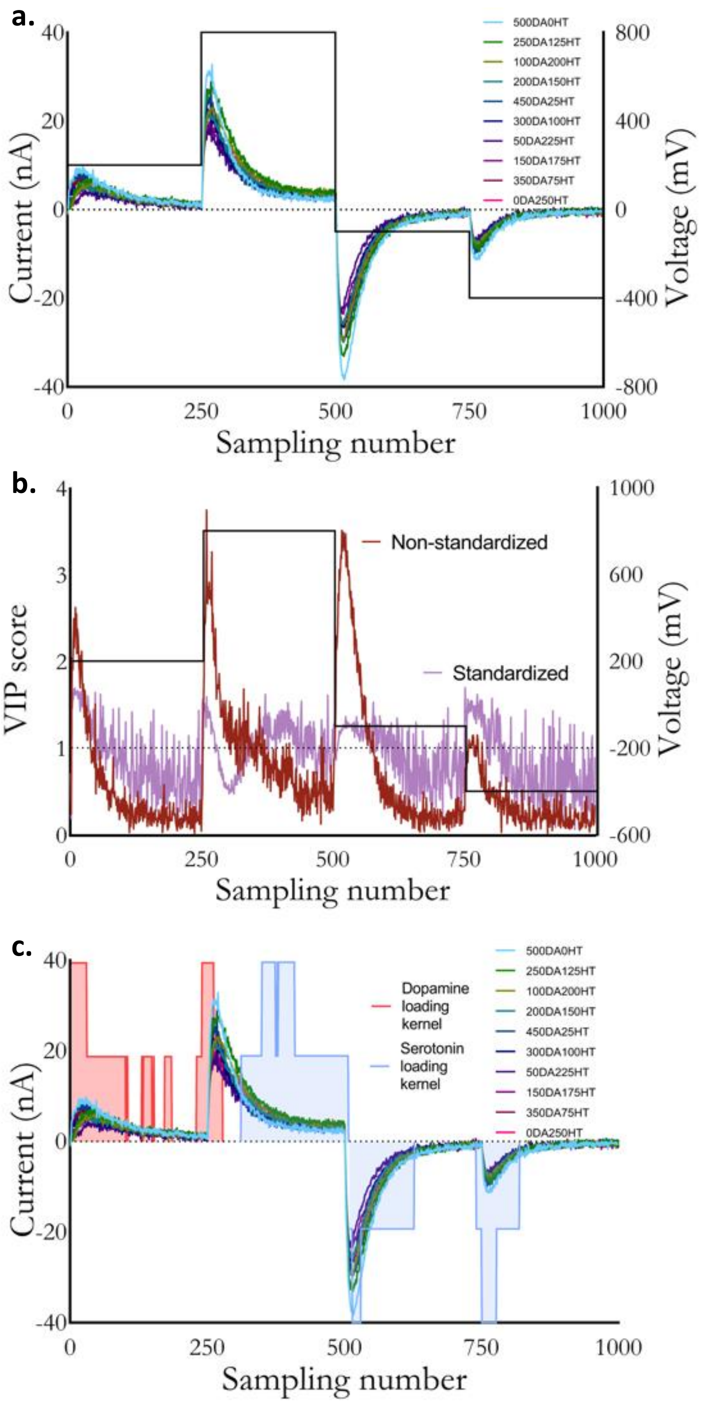

Figure II.3. **(a)** Rapid pulse voltammograms of varying dopamine (DA) and serotonin (5HT) combinations (nM). The pulse waveform is overlaid. **(b)** Variable importance in the projection (VIP) scores for non-standardized *vs.* standardized data obtained from Fig. II3a. **(c)** Loadings analysis overlaid with Fig. II.3a.

Figure II.4

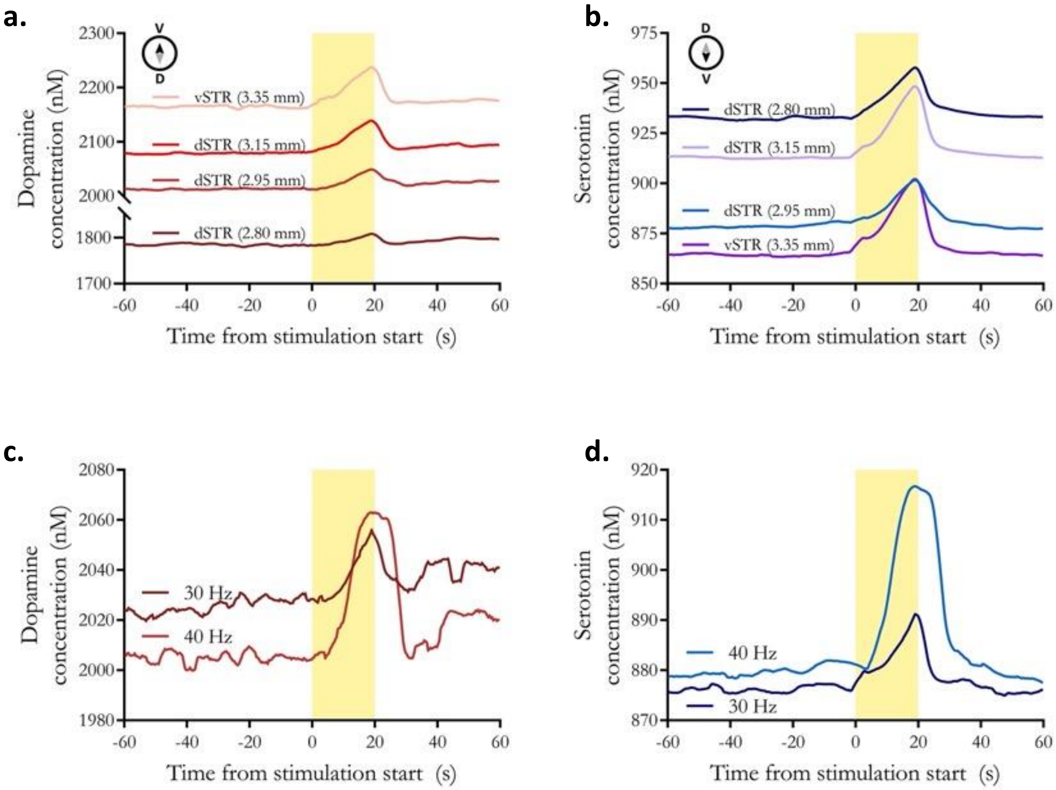

Figure II.4. *In vivo* dopamine and serotonin monitoring using rapid-pulse voltammetry with partial least squares regression (RPV-PLSR) analysis (a,b) Time courses of dopamine or serotonin at various dorsoventral striatal positions measured with RPV-PLSR (*n*=3 at 2.80 mm, *n*=5 at 2.95 mm, *n*=7 at 3.15 mm, and *n*=3 at 3.35 mm for a total of 18 recordings in a single representative mouse). **(c.d)** Time courses of dopamine or serotonin measured in dorsal striatum (dSTR) in response to representative sequential 40 Hz and 30 Hz optical stimulations of midbrain dopamine neurons (*n*=1).

Figure II.5

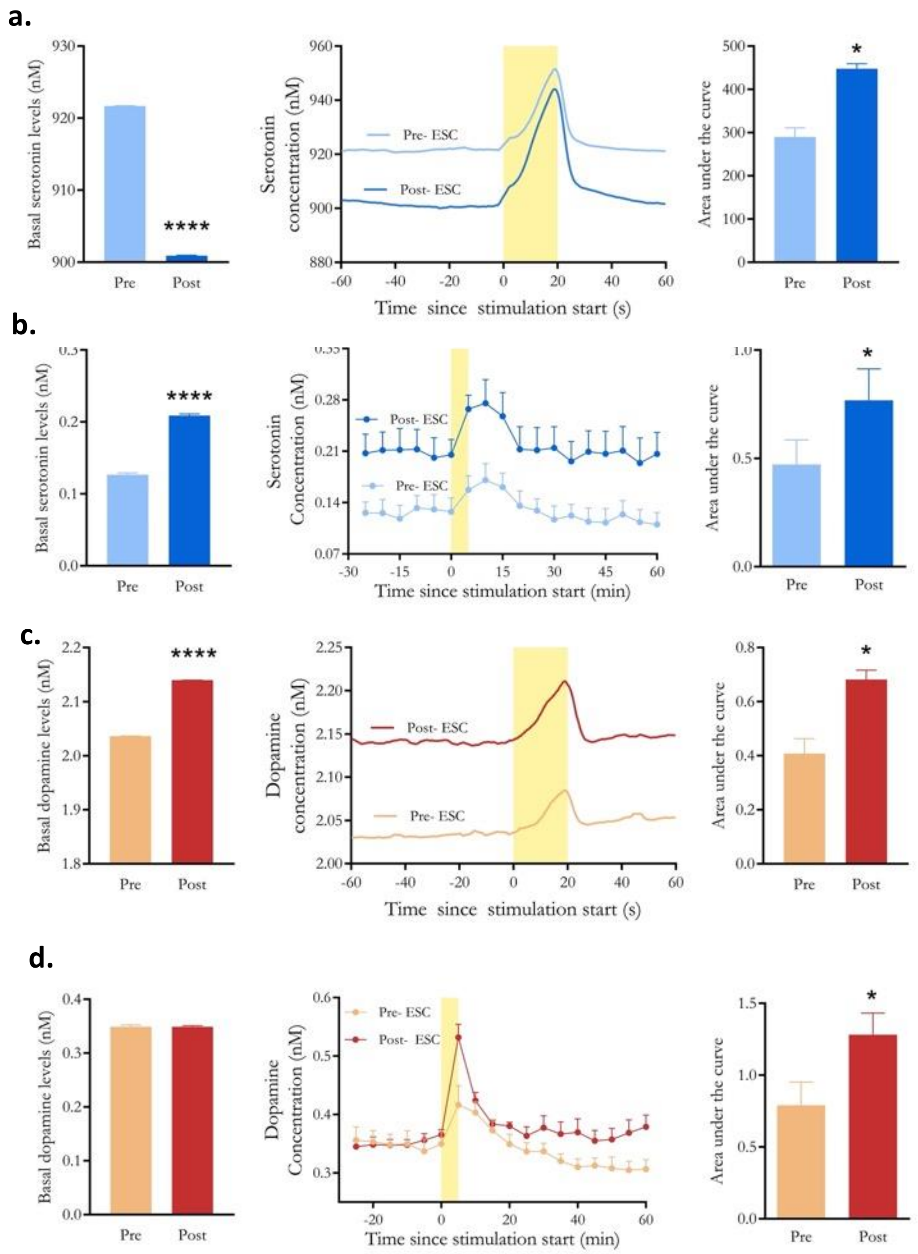

Figure II.5. Responses to the selective serotonin reuptake inhibitor escitalopram by rapid pulse voltammetry with partial least squares regression analysis (RPV-PLSR) *vs.* microdialysis. Time courses are shown in the center panels for serotonin determined by **(a)** RPV-PLSR or **(b)** microdialysis and dopamine by **(c)** RPV-PLSR or **(d)** microdialysis. Escitalopram (20 mg/kg) was administered subcutaneously at t=-60 min for RPV-PLSR or perfused continuously into the dorsal striatum (10 µM) for microdialysis beginning at t=-90 min. Optical stimulation of Chrimson-transfected dopamine neurons occurred during the time periods marked by yellow bars. Basal serotonin or dopamine concentrations before and after/during escitalopram administration are shown in the left bar graphs. Stimulation-induced increases in serotonin or dopamine before *vs.* after/during escitalopram are shown in the right bar graphs and are calculated as areas under the curve. *P<0.05, **P<0.01, and ***P<0.001 (See Table S1 and Methods for statistical details).

Figure II.6

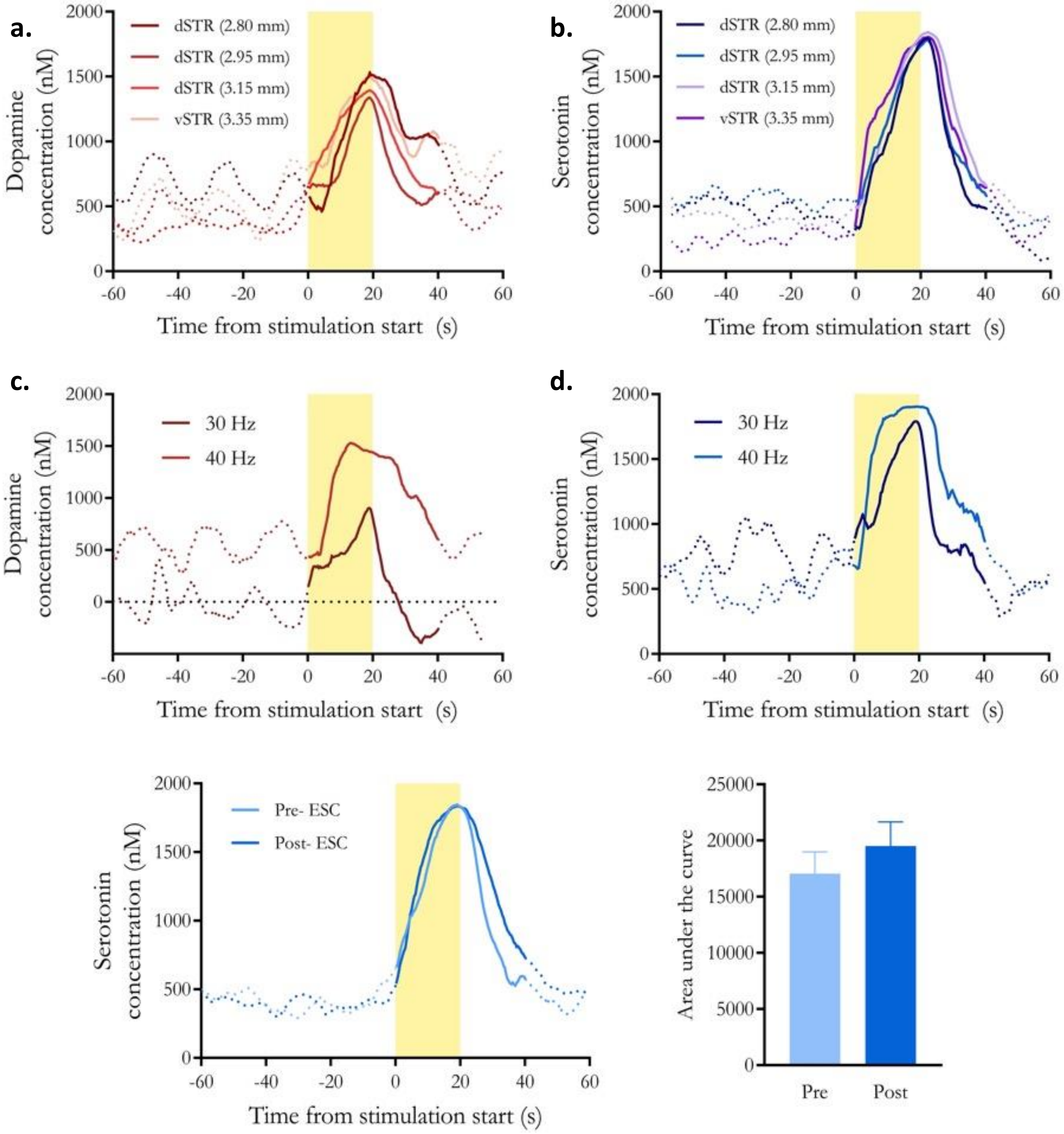

Figure 6. Predictions using a two component fast-scan cyclic voltammetry-principle components (FSCV-PCR) model for dopamine and serotonin *in vivo* (a,b) Time courses of dopamine and serotonin, respectively, at various dorsoventral striatal recording electrode positions determined by FSCV-PCR. **(c,d)** Time courses of dopamine and serotonin, respectively in response to 40 Hz *vs.* 30 Hz stimulations predicted by FSCV-PCR. **(e)** Time course (left) and area under the curve (right) of serotonin for pre- and post- escitalopram administration using FSCV-PCR.

Table II.1

Mouse	Injection	Dopamine (µM)	Serotonin (µM)
1	1	0.0	0.0
		5.0	0.0
	2	0.0	0.0
		0.0	4.0
	3	0.0	0.0
		2.0	2.0
2	1	0.0	0.0
		4.0	0.0
	2	0.0	0.0
		0.0	3.0
	3	0.0	0.0
		1.5	1.5
3	1	0.0	0.0
		5.0	0.0
	2	0.0	0.0
		0.0	5.0
	3	0.0	0.0
		2.0	2.0

Table II.1. Training set concentrations for *in vivo* post-calibration.

Table II.2

Model	Waveform	Background Subtraction	*Components*	R^2Y			Q^2Y		
				2	*3*	*5*	*2*	*3*	*5*
PLSR	Pulse	N		0.408	0.823	0.857	0.072	0.574	0.662
		Y		0.754	0.821	0.874	0.550	0.548	0.555
	Triangle	N		0.720	0.760	0.880	0.420	0.439	0.582
		Y		0.653	0.770	0.844	0.386	0.478	0.034
PCR	Pulse	N		0.356	0.421	0.876	0.033	-0.053	0.651
		Y		0.545	0.563	0.571	0.369	0.396	0.364
	Triangle	N		0.415	0.667	0.784	0.112	0.405	0.430
		Y		0.413	0.490	0.566	0.170	0.273	0.265

Table II.2. Training (R^2Y) and cross-validation (Q^2Y) accuracy metrics for each background subtracted (no (N)/yes (Y))/waveform/model combination.

Scheme II.1

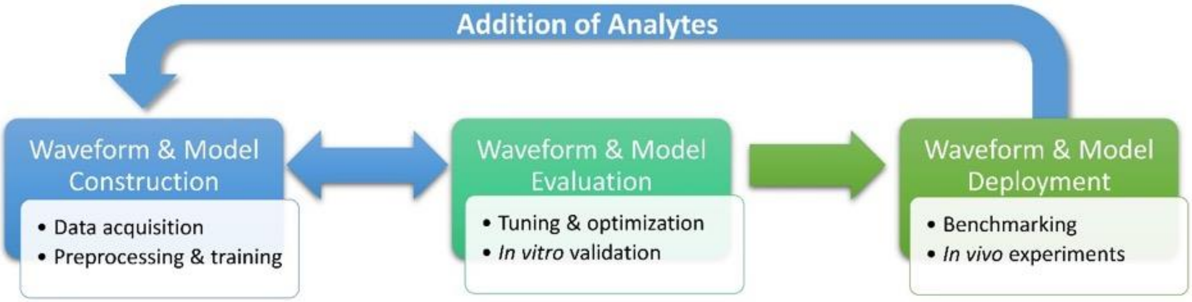

Scheme II.1. Rapid pulse voltammetry-machine learning optimization scheme.

Figure II.S1

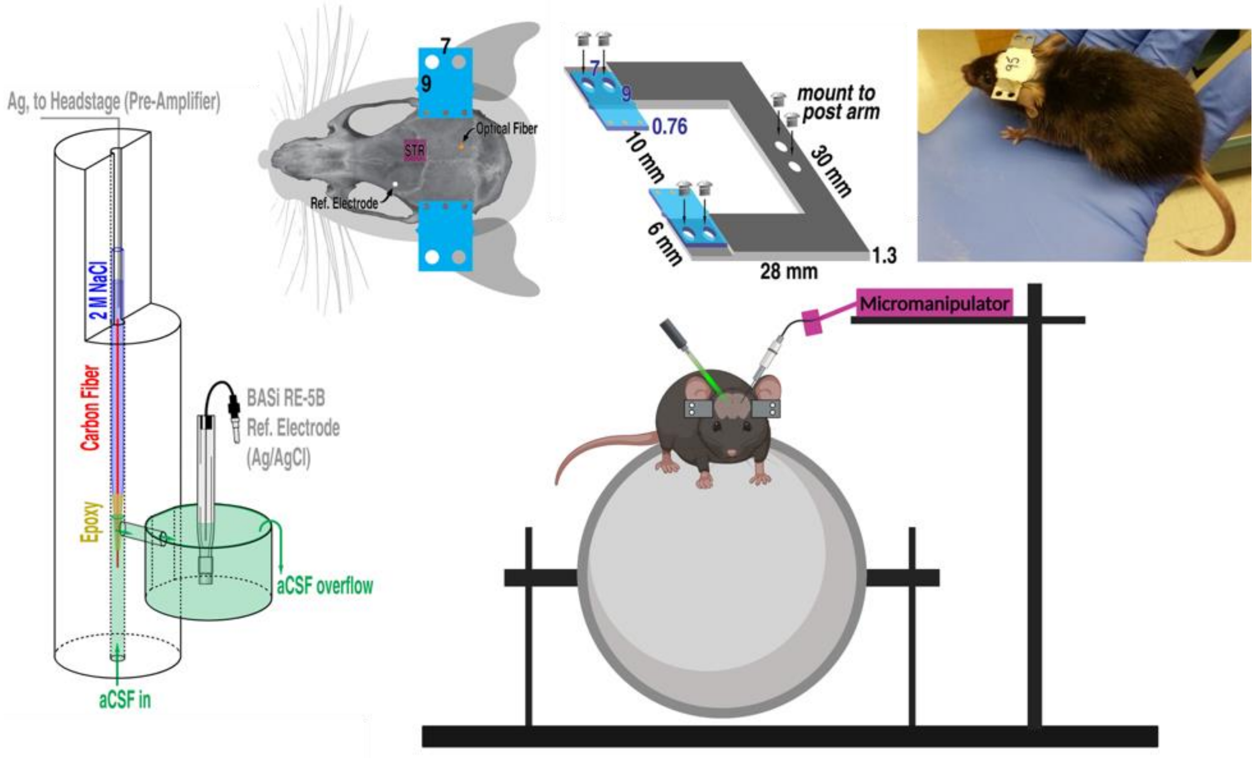

Figure II.S1. Experimental set-up for *in vitro* carbon-fiber microelectrode calibration (flow cell, left) and *in vivo* experiments (right). Photograph courtesy of Wesley Smith. Aspects of this figure were created using Biorender.com.

Figure II.S2

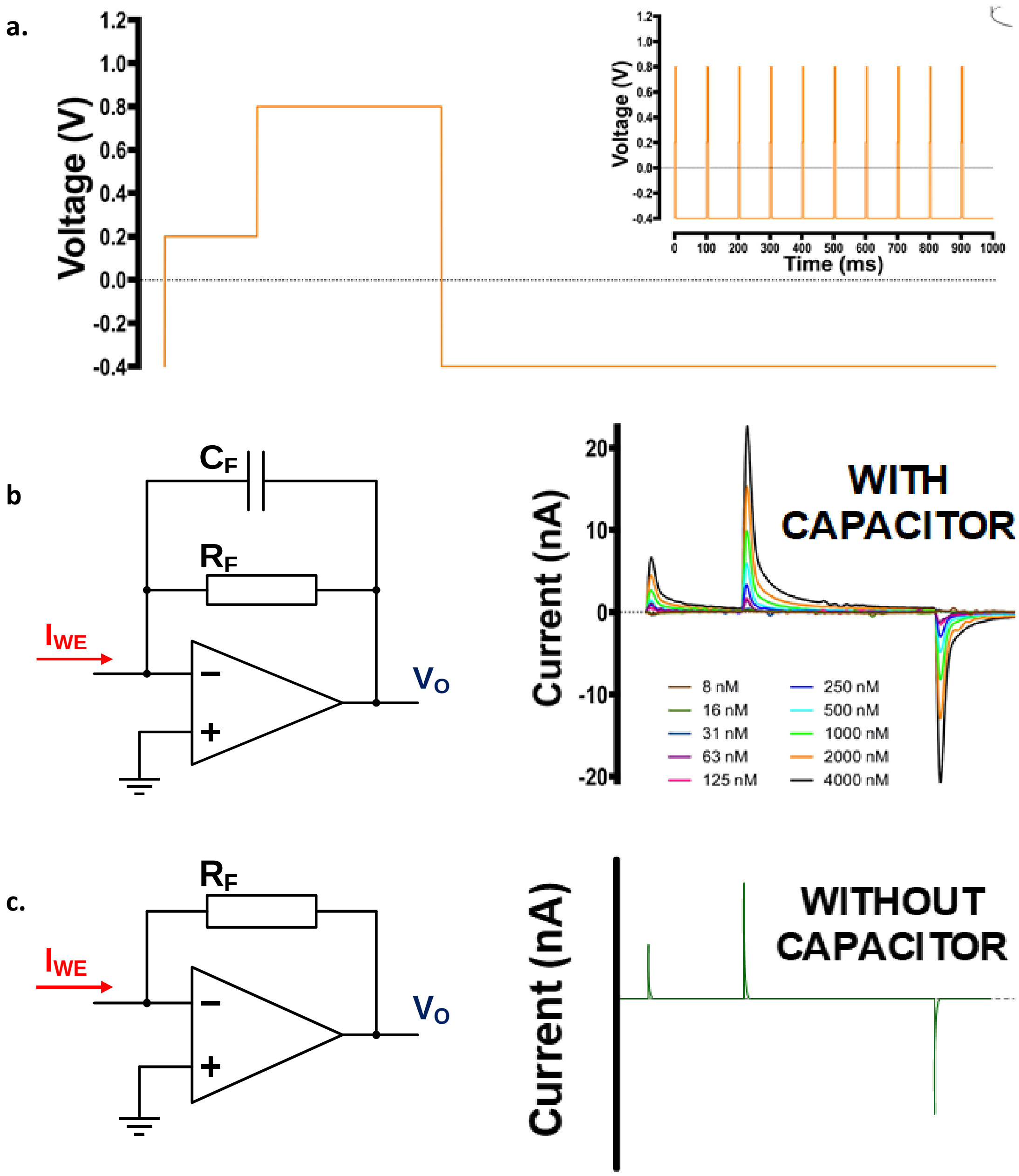

Figure II.S2. Effect of the transimpedance amplifier used in the custom headstage
(a) Representative pulse applied to the electrochemical system. **(b)** Circuit diagram for the transimpedance amplifier (amplifier with feedback resistor R_F in parallel with feedback capacitor C_F) to convert current from the working electrode (I_{WE}) into output voltage (V_O) (left). Representative voltammograms with the capacitor in parallel (right). **(c)** Circuit diagram for amplifier without feedback capacitor (left). Representative voltammogram (right).

The rapid pulse voltammetry (RPV) waveform is shown in **Figure II.S2a**. For this circuit (**Fig. II.S2b**), the relationship between the output voltage and the working electrode current is given by the differential equation:

$$\frac{V_O}{R_F} + C_F \cdot \frac{dV_O}{dt} = -I_{WE} \tag{1}$$

If the feedback capacitor is not present (**Fig. II.S2c**), the relationship is given by:

$$V_O = -R_F \cdot I_{WE} \tag{2}$$

Transimpedance amplifiers often include a feedback capacitor connected in parallel to the feedback resistor for signal stabilization and filtering purposes. The drawback of their use is that the feedback capacitor disrupts the direct proportionality between measured current and output voltage (**Equation 1**). Instead, the output signal will deform (*i.e.,* the exponential current decay will be delayed) according to the differential present in Equation 1 (**Fig. II.S2b**). In most cases, the latter is not desired.

For RPV, we purposefully included a feedback capacitor (**Fig. II.S2b**) to allow a smoother, longer duration of the pulse response. Important electrochemical information is present within the nonfaradaic and faradaic currents immediately after a pulse, on the order of tens of microseconds. Without a feedback capacitor, these currents decay too quickly to be sampled with high enough time resolution by the data acquisition system (8 μs sampling rate; 125 kHz). With a feedback capacitor of appropriate capacitance, the output voltage response is spread out over a longer temporal duration. This additional decay time affords the PLSR model more data points to be sampled from key electrochemical events that would otherwise be missed or under-sampled. While we recognize these electronic components preclude the analysis of an electrochemical system by equivalent circuit analysis, due to the deformation of the original working electrode signal, we note our purpose here is to obtain relevant information for the PLSR model, not to gain mechanistic insights at the electrode surface. Further, the capacitor also helps to stabilize and to reduce the noise of the output signal.

For these reasons, we implemented the feedback capacitor as shown in **Figure II.S2b**. The value of the capacitor was determined empirically to produce the desired smoothing and decay time of the signal, depending on the pulse sequence applied. For our set up, this value was found to be approximately 100 pF.

Figure II.S3

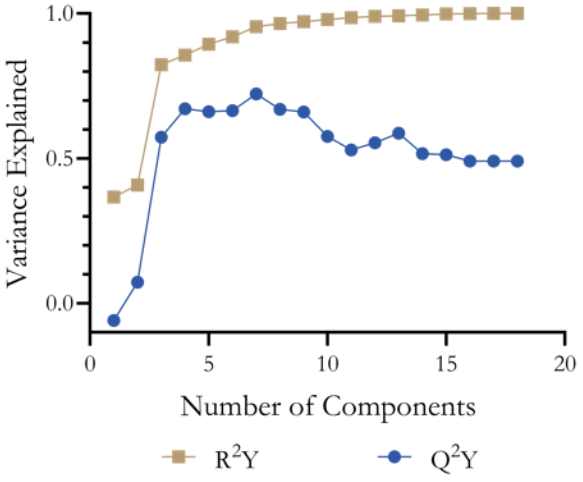

Figure II.S3. Cumulative training (R^2Y) and prediction (Q^2Y) score metrics for the RPV-PLSR model with respect to the number of components.

Figure II.S4

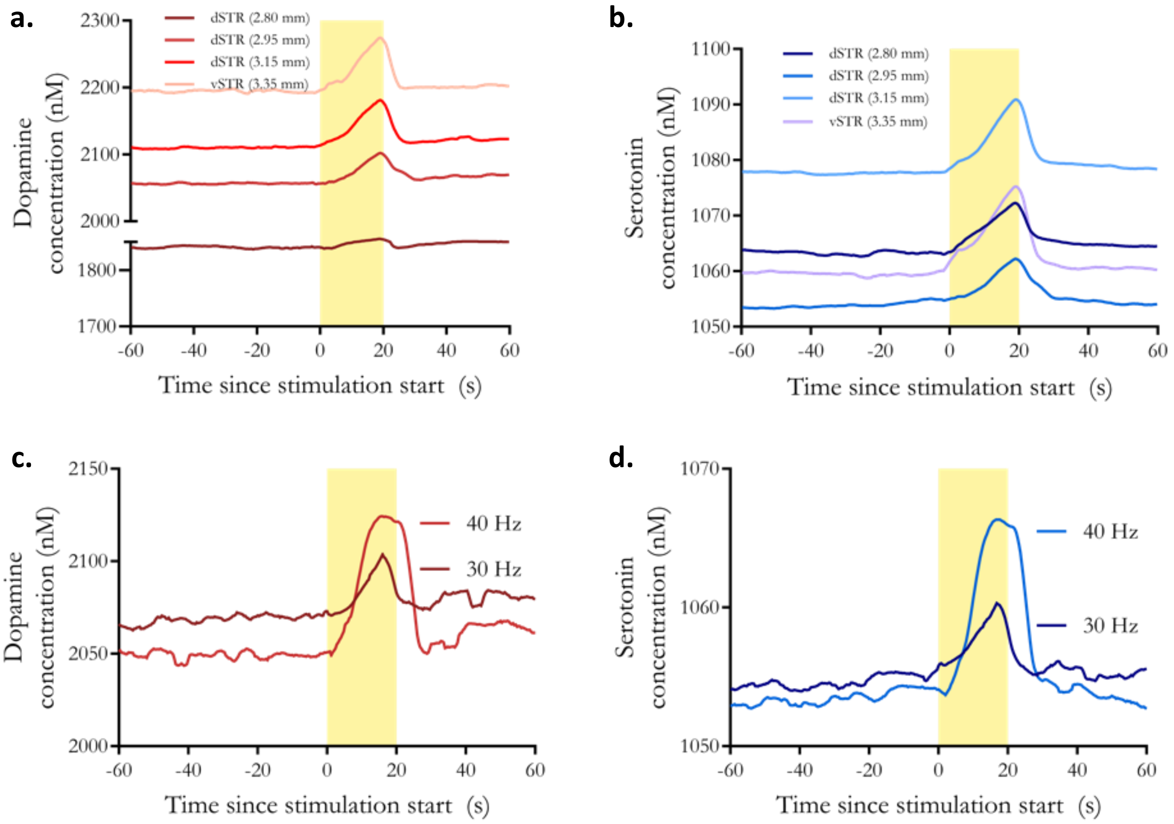

Figure II.S4. *In vivo* dopamine and serotonin monitoring using rapid-pulse voltammetry with principal components regression (RPV-PCR) analysis (a,b) Time courses of dopamine or serotonin at various dorsoventral striatal positions measured with RPV-PCR. **(c.d)** Time courses of dopamine or serotonin measured in dorsal striatum (dSTR) in response to a representative 40 Hz or 30 Hz sequential optical stimulations of midbrain dopamine neurons.

Figure II.S5

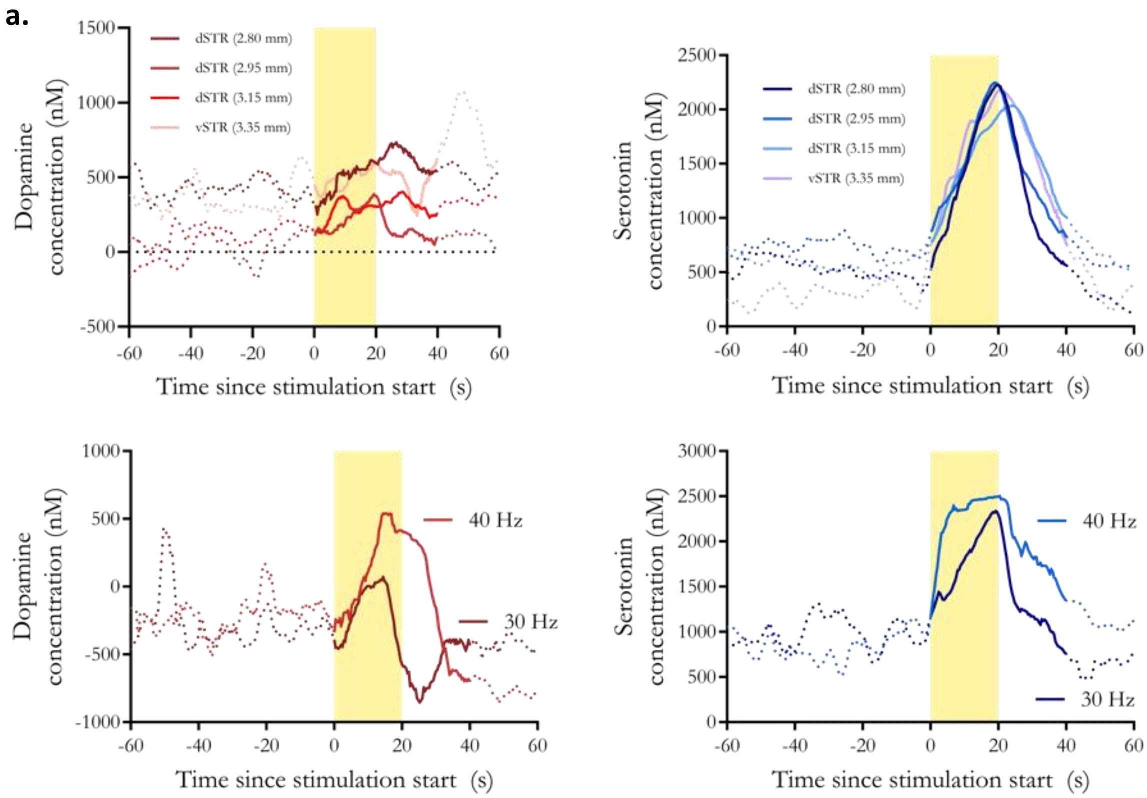

Figure II.S5. Predictions using a FSCV-PLSR model for dopamine and serotonin *in vivo* (a,b) Time courses of dopamine and serotonin, respectively, at various dorsoventral striatal recording electrode positions determined by FSCV-PLSR. **(c,d)** Time courses of dopamine and serotonin, respectively in response to 30 Hz *vs.* 40 Hz stimulations predicted by FSCV-PLSR.

Table II.S1

Figure	Comparison	Test	Statistics	Significant?
5A, left	Basal 5HT RPV: pre- SSRI *vs.* post-SSRI	Paired *t*-test	t(5)=238	*P*<0.001
5A, right	AUC 5HT RPV: pre- SSRI *vs.* post- SSRI	Unpaired *t*-test	t(5)=5.92	*P*<0.01
5B, left	Basal 5HT microdialysis: pre- SSRI *vs.* post- SSRI	Paired *t*-test	t(4)=21.7	*P*<0.001
5B, right	AUC 5HT microdialysis: pre- SSRI *vs.* post- SSRI	Paired *t*-test	t(8)=2.67	*P*<0.05
5C, left	Basal DA RPV: pre- SSRI *vs.* post- SSRI	Paired *t*-test	t(5)=544	*P*<0.001
5C, right	AUC DA RPV: pre- SSRI *vs.* post- SSRI	Unpaired *t*-test	t(5)=3.823	*P*<0.05
5D, left	Basal DA microdialysis: pre- SSRI *vs.* post- SSRI	Paired *t*-test	t(4)=0.030	ns
5D, right	AUC DA microdialysis: pre- SSRI *vs.* post- SSRI	Paired *t*-test	t(8)=2.843	*P*<0.05

Table II.S1 Statistical Summary. The *t*-tests were two-tailed and paired or unpaired depending on whether matching numbers of pre- *vs.* post SSRI samples were available.

References

1. Marcinkiewcz, C. A.; Mazzone, C. M.; D'Agostino, G.; Halladay, L. R.; Hardaway, J. A.; DiBerto, J. F.; Navarro, M.; Burnham, N.; Cristiano, C.; Dorrier, C. E.; Tipton, G. J.; Ramakrishnan, C.; Kozicz, T.; Deisseroth, K.; Thiele, T. E.; McElligott, Z. A.; Holmes, A.; Heisler, L. K.; Kash, T. L., Serotonin engages an anxiety and fear-promoting circuit in the extended amygdala. *Nature* **2016,** *537* (7618), 97-101.

2. Hashemi, P.; Dankoski, E. C.; Lama, R.; Wood, K. M.; Takmakov, P.; Wightman, R. M., Brain dopamine and serotonin differ in regulation and its consequences. *Proc Natl Acad Sci USA* **2012,** *109* (29), 11510-11515.

3. Cheer, J. F.; Heien, M. L. A. V.; Garris, P. A.; Carelli, R. M.; Wightman, R. M., Simultaneous dopamine and single-unit recordings reveal accumbens gabaergic responses: Implications for intracranial self-stimulation. *Proc Natl Acad Sci USA* **2005,** *102* (52), 19150-19155.

4. Ngernsutivorakul, T.; Steyer, D. J.; Valenta, A. C.; Kennedy, R. T., In vivo chemical monitoring at high spatiotemporal resolution using microfabricated sampling probes and droplet-based microfluidics coupled to mass spectrometry. *Anal Chem* **2018,** *90* (18), 10943-10950.

5. Tecuapetla, F.; Patel, J. C.; Xenias, H.; English, D.; Tadros, I.; Shah, F.; Berlin, J.; Deisseroth, K.; Rice, M. E.; Tepper, J. M.; Koos, T., Glutamatergic signaling by mesolimbic dopamine neurons in the nucleus accumbens. *J Neurosci* **2010,** *30* (20), 7105-7110.

6. Amilhon, B.; Lepicard, È.; Renoir, T.; Mongeau, R.; Popa, D.; Poirel, O.; Miot, S.; Gras, C.; Gardier, A. M.; Gallego, J.; Hamon, M.; Lanfumey, L.; Gasnier, B.; Giros, B.; El Mestikawy, S., Vglut3 (vesicular glutamate transporter type 3) contribution to the regulation of serotonergic transmission and anxiety. *J Neurosci* **2010,** *30* (6), 2198-2210.

7. Mingote, S.; Chuhma, N.; Kalmbach, A.; Thomsen, G. M.; Wang, Y.; Mihali, A.; Sferrazza, C.; Zucker-Scharff, I.; Siena, A.-C.; Welch, M. G.; Lizardi-Ortiz, J.; Sulzer, D.; Moore, H.; Gaisler-Salomon, I.; Rayport, S., Dopamine neuron dependent behaviors mediated by glutamate cotransmission. *eLife* **2017,** *6*, e27566.

8. Root, D. H.; Barker, D. J.; Estrin, D. J.; Miranda-Barrientos, J. A.; Liu, B.; Zhang, S.; Wang, H.-L.; Vautier, F.; Ramakrishnan, C.; Kim, Y. S.; Fenno, L.; Deisseroth, K.; Morales, M., Distinct signaling by ventral tegmental area glutamate, gaba, and combinatorial glutamate-gaba neurons in motivated behavior. *Cell Rep* **2020,** *32* (9), 108094.

9. Wang, H.-L.; Zhang, S.; Qi, J.; Wang, H.; Cachope, R.; Mejias-Aponte, C. A.; Gomez, J. A.; Mateo-Semidey, G. E.; Beaudoin, G. M. J.; Paladini, C. A.; Cheer, J. F.; Morales, M., Dorsal raphe dual serotonin-glutamate neurons drive reward by establishing excitatory synapses on vta mesoaccumbens dopamine neurons. *Cell Rep* **2019,** *26* (5), 1128-1142.e7.

10. Lee, K.; Claar, L. D.; Hachisuka, A.; Bakhurin, K. I.; Nguyen, J.; Trott, J. M.; Gill, J. L.; Masmanidis, S. C., Temporally restricted dopaminergic control of reward-conditioned movements. *Nat Neurosci* **2020,** *23* (2), 209-216.

11. Dagher, M.; Perrotta, K. A.; Erwin, S. A.; Hachisuka, A.; Ayer, R.; Masmanidis, S.; Yang, H.; Andrews, A. M., Optogenetic stimulation of midbrain dopamine neurons produces striatal serotonin release. *ACS Chem Neurosci* **In press.**

12. Di Giovanni, G.; Esposito, E.; Di Matteo, V., Role of serotonin in central dopamine dysfunction. *CNS Neurosci Ther* **2010,** *16* (3), 179-194.

13. Aman, T. K.; Shen, R.-Y.; Haj-Dahmane, S., D2-like dopamine receptors depolarize dorsal raphe serotonin neurons through the activation of nonselective cationic conductance. *J Pharmacol Exp Ther* **2007,** *320* (1), 376-385.

14. Lee, E. H. Y.; Geyer, M. A., Dopamine autoreceptor mediation of the effects of apomorphine on serotonin neurons. *Pharmacol Biochem Behav* **1984,** *21* (2), 301-311.

15. Niederkofler, V.; Asher, T. E.; Dymecki, S. M., Functional interplay between dopaminergic and serotonergic neuronal systems during development and adulthood. *ACS Chem Neurosci* **2015,** *6* (7), 1055-1070.

16. Tan, S. K. H.; Hartung, H.; Schievink, S.; Sharp, T.; Temel, Y., High-frequency stimulation of the substantia nigra induces serotonin-dependent depression-like behavior in animal models. *Biol Psychiatry* **2013,** *73* (2), e1-e3.

17. Altieri, S.; Singh, Y.; Sibille, E.; Andrews, A. M., Serotonergic pathways in depression. In *Neurobiology of depression*, CRC Press: 2011; Vol. 20115633, pp 143-170.

18. Nestler, E. J., Role of the brain's reward circuitry in depression: Transcriptional mechanisms. *Int Rev Neurobiol* **2015,** *124*, 151-70.

19. Simpson, E. H.; Kellendonk, C.; Ward, R. D.; Richards, V.; Lipatova, O.; Fairhurst, S.; Kandel, E. R.; Balsam, P. D., Pharmacologic rescue of motivational deficit in an animal model of the negative symptoms of schizophrenia. *Biol Psychiatry* **2011,** *69* (10), 928-935.

20. Sumiyoshi, T.; Kunugi, H.; Nakagome, K., Serotonin and dopamine receptors in motivational and cognitive disturbances of schizophrenia. *Front Neurosci* **2014,** *8*, 395.

21. Rothman, R. B.; Blough, B. E.; Baumann, M. H., Dual dopamine/serotonin releasers as potential medications for stimulante and alcohol addictions. *AAPS J* **2007,** *9* (1), E1-E10.

22. Skowronek, M. H.; Laucht, M.; Hohm, E.; Becker, K.; Schmidt, M. H., Interaction between the dopamine d4 receptor and the serotonin transporter promoter polymorphisms in alcohol and tobacco use among 15-year-olds. *Neurogenetics* **2006,** *7* (4), 239-246.

23. Eskow Jaunarajs, K. L.; George, J. A.; Bishop, C., L-dopa-induced dysregulation of extrastriatal dopamine and serotonin and affective symptoms in a bilateral rat model of parkinson's disease. *Neuroscience* **2012,** *218*, 243-256.

24. Stahl, S. M., Parkinson's disease psychosis as a serotonin-dopamine imbalance syndrome. *CNS Spectr* **2016,** *21* (5), 355-359.

25. Avery, M. C.; Krichmar, J. L., Neuromodulatory systems and their interactions: A review of models, theories, and experiments. *Front Neural Circuits* **2017,** *11*, 108.

26. Zangen, A.; Nakash, R.; Overstreet, D.; Yadid, G., Association between depressive behavior and absence of serotonin-dopamine interaction in the nucleus accumbens. *Psychopharmacology* **2001,** *155* (4), 434-439.

27. Andrews, A. M., The brain initiative: Toward a chemical connectome. *ACS Chem Neurosci* **2013,** *4* (5), 645.

28. Sarter, M.; Kim, Y., Interpreting chemical neurotransmission in vivo: Techniques, time scales, and theories. *ACS Chem Neurosci* **2015,** *6* (1), 8-10.

29. Dreyer, J. K.; Herrik, K. F.; Berg, R. W.; Hounsgaard, J. D., Influence of phasic and tonic dopamine release on receptor activation. *J Neurosci* **2010,** *30* (42), 14273-83.

30. Hajós, M.; Allers, K. A.; Jennings, K.; Sharp, T.; Charette, G.; Sík, A.; Kocsis, B., Neurochemical identification of stereotypic burst-firing neurons in the rat dorsal raphe nucleus using juxtacellular labelling methods. *Eur J Neurosci* **2007,** *25* (1), 119-126.

31. Hajós, M.; Gartside, S. E.; Villa, A. E. P.; Sharp, T., Evidence for a repetitive (burst) firing pattern in a sub-population of 5-hydroxytryptamine neurons in the dorsal and median raphe nuclei of the rat. *Neuroscience* **1995,** *69* (1), 189-197.

32. Hajós, M.; Sharp, T., Burst-firing activity of presumed 5-ht neurones of the rat dorsal raphe nucleus: Electrophysiological analysis by antidromic stimulation. *Brain Res* **1996,** *740* (1), 162-168.

33. Sulzer, D.; Cragg, S. J.; Rice, M. E., Striatal dopamine neurotransmission: Regulation of release and uptake. *Basal Ganglia* **2016,** *6* (3), 123-148.

34. Abdalla, A.; Atcherley, C. W.; Pathirathna, P.; Samaranayake, S.; Qiang, B.; Peña, E.; Morgan, S. L.; Heien, M. L.; Hashemi, P., In vivo ambient serotonin measurements at carbon-fiber microelectrodes. *Anal Chem* **2017,** *89* (18), 9703-9711.

35. Atcherley, C. W.; Wood, K. M.; Parent, K. L.; Hashemi, P.; Heien, M. L., The coaction of tonic and phasic dopamine dynamics. *Chem Comm* **2015,** *51* (12), 2235-2238.

36. Alivisatos, A. P.; Andrews, A. M.; Boyden, E. S.; Chun, M.; Church, G. M.; Deisseroth, K.; Donoghue, J. P.; Fraser, S. E.; Lippincott-Schwartz, J.; Looger, L. L.; Masmanidis, S.; McEuen, P. L.; Nurmikko, A. V.; Park, H.; Peterka, D. S.; Reid, C.; Roukes, M. L.; Scherer, A.; Schnitzer, M.; Sejnowski, T. J.; Shepard, K. L.; Tsao, D.; Turrigiano, G.; Weiss, P. S.; Xu, C.; Yuste, R.; Zhuang, X., Nanotools for neuroscience and brain activity mapping. *ACS Nano* **2013,** *7* (3), 1850-66.

37. Watson, C. J.; Venton, B. J.; Kennedy, R. T., In vivo measurements of neurotransmitters by microdialysis sampling. *Anal Chem* **2006,** *78* (5), 1391-1399.

38. Bucher, E. S.; Wightman, R. M., Electrochemical analysis of neurotransmitters. *Annu Rev Anal Chem* **2015,** *8* (1), 239-261.

39. Su, Y.; Bian, S.; Sawan, M., Real-time in vivo detection techniques for neurotransmitters: A review. *Analyst* **2020,** *145* (19), 6193-6210.
40. Logman, M. J.; Budygin, E. A.; Gainetdinov, R. R.; Wightman, R. M., Quantitation of in vivo measurements with carbon fiber microelectrodes. *J Neurosci Methods* **2000,** *95* (2), 95-102.

41. Singh, Y. S.; Sawarynski, L. E.; Dabiri, P. D.; Choi, W. R.; Andrews, A. M., Head-to-head comparisons of carbon fiber microelectrode coatings for sensitive and selective neurotransmitter detection by voltammetry. *Anal Chem* **2011,** *83* (17), 6658-6666.

42. Puthongkham, P.; Venton, B. J., Recent advances in fast-scan cyclic voltammetry. *Analyst* **2020,** *145* (4), 1087-1102.

43. Bunin, M. A.; Prioleau, C.; Mailman, R. B.; Wightman, R. M., Release and uptake rates of 5-hydroxytryptamine in the dorsal raphe and substantia nigra reticulata of the rat brain. *J Neurochem* **1998,** *70* (3), 1077-1087.

44. Walters, S. H.; Shu, Z.; Michael, A. C.; Levitan, E. S., Regional variation in striatal dopamine spillover and release plasticity. *ACS Chem Neurosci* **2020,** *11* (6), 888-899.

45. Nakatsuka, N.; Andrews, A. M., Differentiating siblings: The case of dopamine and norepinephrine. *ACS Chem Neurosci* **2017,** *8* (2), 218-220.

46. Heien, M. L. A. V.; Khan, A. S.; Ariansen, J. L.; Cheer, J. F.; Phillips, P. E. M.; Wassum, K. M.; Wightman, R. M., Real-time measurement of dopamine fluctuations after cocaine in the brain of behaving rats. *Proc Natl Acad Sci USA* **2005,** *102* (29), 10023-10028.

47. Venton, B. J.; Cao, Q., Fundamentals of fast-scan cyclic voltammetry for dopamine detection. *Analyst* **2020,** *145* (4), 1158-1168.

48. Dunham, K. E.; Venton, B. J., Improving serotonin fast-scan cyclic voltammetry detection: New waveforms to reduce electrode fouling. *Analyst* **2020,** *145* (22), 7437-7446.

49. Atcherley, C. W.; Laude, N. D.; Parent, K. L.; Heien, M. L., Fast-scan controlled-adsorption voltammetry for the quantification of absolute concentrations and adsorption dynamics. *Langmuir* **2013,** *29* (48), 14885-92.

50. West, A.; Best, J.; Abdalla, A.; Nijhout, H. F.; Reed, M.; Hashemi, P., Voltammetric evidence for discrete serotonin circuits, linked to specific reuptake domains, in the mouse medial prefrontal cortex. *Neurochem Int* **2019,** *123*, 50-58.

51. Dengler, A. K.; McCarty, G. S., Microfabricated microelectrode sensor for measuring background and slowly changing dopamine concentrations. *J Electroanal Chem* **2013,** *693*, 28-33.

52. Kim, S. Y.; Oh, Y. B.; Shin, H. J.; Kim, D. H.; Kim, I. Y.; Bennet, K.; Lee, K. H.; Jang, D. P., 5-hydroxytryptamine measurement using paired pulse voltammetry. *Biomed Eng Lett* **2013,** *3* (2), 102-108.

53. Meunier, C. J.; McCarty, G. S.; Sombers, L. A., Drift subtraction for fast-scan cyclic voltammetry using double-waveform partial-least-squares regression. *Anal Chem* **2019,** *91* (11), 7319-7327.

54. Calhoun, S. E.; Meunier, C. J.; Lee, C. A.; McCarty, G. S.; Sombers, L. A., Characterization of a multiple-scan-rate voltammetric waveform for real-time detection of met-enkephalin. *ACS Chem Neurosci* **2019,** *10* (4), 2022-2032.

55. Meunier, C. J.; Mitchell, E. C.; Roberts, J. G.; Toups, J. V.; McCarty, G. S.; Sombers, L. A., Electrochemical selectivity achieved using a double voltammetric waveform and partial least squares regression: Differentiating endogenous hydrogen peroxide fluctuations from shifts in ph. *Anal Chem* **2018,** *90* (3), 1767-1776.

56. Oh, Y.; Heien, M. L.; Park, C.; Kang, Y. M.; Kim, J.; Boschen, S. L.; Shin, H.; Cho, H. U.; Blaha, C. D.; Bennet, K. E.; Lee, H. K.; Jung, S. J.; Kim, I. Y.; Lee, K. H.; Jang, D. P., Tracking tonic dopamine levels in vivo using multiple cyclic square wave voltammetry. *Biosens Bioelectron* **2018,** *121*, 174-182.

57. Park, C.; Oh, Y.; Shin, H.; Kim, J.; Kang, Y.; Sim, J.; Cho, H. U.; Lee, H. K.; Jung, S. J.; Blaha, C. D.; Bennet, K. E.; Heien, M. L.; Lee, K. H.; Kim, I. Y.; Jang, D. P., Fast cyclic square-wave voltammetry to enhance neurotransmitter selectivity and sensitivity. *Anal Chem* **2018,** *90* (22), 13348-13355.

58. Shin, H.; Oh, Y.; Park, C.; Kang, Y.; Cho, H. U.; Blaha, C. D.; Bennet, K. E.; Heien, M. L.; Kim, I. Y.; Lee, K. H.; Jang, D. P., Sensitive and selective measurement of serotonin in vivo using fast cyclic square-wave voltammetry. *Anal Chem* **2020,** *92* (1), 774-781.

59. Swamy, B. E. K.; Venton, B. J., Carbon nanotube-modified microelectrodes for simultaneous detection of dopamine and serotoninin vivo. *Analyst* **2007,** *132* (9), 876-884.

60. Zhou, F.-M.; Liang, Y.; Salas, R.; Zhang, L.; De Biasi, M.; Dani, J. A., Corelease of dopamine and serotonin from striatal dopamine terminals. *Neuron* **2005,** *46* (1), 65-74.

61. Hermans, A.; Keithley, R. B.; Kita, J. M.; Sombers, L. A.; Wightman, R. M., Dopamine detection with fast-scan cyclic voltammetry used with analog background subtraction. *Anal Chem* **2008,** *80* (11), 4040-4048.

62. Heien, M. L. A. V.; Johnson, M. A.; Wightman, R. M., Resolving neurotransmitters detected by fast-scan cyclic voltammetry. *Anal Chem* **2004,** *76* (19), 5697-5704.

63. Keithley, R. B.; Mark Wightman, R.; Heien, M. L., Multivariate concentration determination using principal component regression with residual analysis. *Trends Analyt Chem* **2009,** *28* (9), 1127-1136.

64. Wold, S.; Sjöström, M.; Eriksson, L., Pls-regression: A basic tool of chemometrics. *Chemom Intell Lab Syst* **2001,** *58* (2), 109-130.

65. Kim, J.; Oh, Y.; Park, C.; Kang, Y. M.; Shin, H.; Kim, I. Y.; Jang, D. P., Comparison study of partial least squares regression analysis and principal component analysis in fast-scan cyclic voltammetry. *Int J Electrochem Sci* **2019,** *14* (7), 5924-5937.

66. Kishida, K. T.; Saez, I.; Lohrenz, T.; Witcher, M. R.; Laxton, A. W.; Tatter, S. B.; White, J. P.; Ellis, T. L.; Phillips, P. E. M.; Montague, P. R., Subsecond dopamine fluctuations in human striatum encode superposed error signals about actual and counterfactual reward. *Proc Natl Acad Sci USA* **2016,** *113* (1), 200-205.

67. Kishida, K. T.; Sandberg, S. G.; Lohrenz, T.; Comair, Y. G.; Sáez, I.; Phillips, P. E. M.; Montague, P. R., Sub-second dopamine detection in human striatum. *PLOS ONE* **2011,** *6* (8), e23291.

68. Bang, D.; Kishida, K. T.; Lohrenz, T.; White, J. P.; Laxton, A. W.; Tatter, S. B.; Fleming, S. M.; Montague, P. R., Sub-second dopamine and serotonin signaling in human striatum during perceptual decision-making. *Neuron* **2020,** *108* (5), 999-1010.e6.

69. Moran, R. J.; Kishida, K. T.; Lohrenz, T.; Saez, I.; Laxton, A. W.; Witcher, M. R.; Tatter, S. B.; Ellis, T. L.; Phillips, P. E. M.; Dayan, P.; Montague, P. R., The protective action encoding of serotonin transients in the human brain. *Neuropsychopharmacology* **2018,** *43* (6), 1425-1435.

70. Winquist, F.; Wide, P.; Lundström, I., An electronic tongue based on voltammetry. *Anal Chim Acta* **1997,** *357* (1), 21-31.

71. Campos, I.; Masot, R.; Alcañiz, M.; Gil, L.; Soto, J.; Vivancos, J. L.; García-Breijo, E.; Labrador, R. H.; Barat, J. M.; Martínez-Mañez, R., Accurate concentration determination of anions nitrate, nitrite and chloride in minced meat using a voltammetric electronic tongue. *Sens Actuators B Chem* **2010,** *149* (1), 71-78.

72. Labrador, R. H.; Masot, R.; Alcañiz, M.; Baigts, D.; Soto, J.; Martínez-Mañez, R.; García-Breijo, E.; Gil, L.; Barat, J. M., Prediction of nacl, nitrate and nitrite contents in minced meat by using a voltammetric electronic tongue and an impedimetric sensor. *Food Chem* **2010,** *122* (3), 864-870.

73. Ivarsson, P.; Holmin, S.; Höjer, N.-E.; Krantz-Rülcker, C.; Winquist, F., Discrimination of tea by means of a voltammetric electronic tongue and different applied waveforms. *Sens Actuators B Chem* **2001,** *76* (1), 449-454.

74. Winquist, F.; Krantz-Rülcker, C.; Wide, P.; Lundström, I., Monitoring of freshness of milk by an electronic tongue on the basis of voltammetry. *Meas Sci Technol* **1998,** *9* (12), 1937-1946.

75. Ciosek, P.; Wróblewski, W., Sensor arrays for liquid sensing–electronic tongue systems. *Analyst* **2007,** *132* (10), 963-978.

76. Campos, I.; Alcañiz, M.; Masot, R.; Soto, J.; Martínez-Máñez, R.; Vivancos, J.-L.; Gil, L., A method of pulse array design for voltammetric electronic tongues. *Sens Actuators B Chem* **2012,** *161* (1), 556-563.

77. Fuentes, E.; Alcañiz, M.; Contat, L.; Baldeón, E. O.; Barat, J. M.; Grau, R., Influence of potential pulses amplitude sequence in a voltammetric electronic tongue (vet) applied to assess antioxidant capacity in aliso. *Food Chem* **2017,** *224*, 233-241.

78. Tian, S.-Y.; Deng, S.-P.; Chen, Z.-X., Multifrequency large amplitude pulse voltammetry: A novel electrochemical method for electronic tongue. *Sens Actuators B Chem* **2007,** *123* (2), 1049-1056.

79. Vreeland, R. F.; Atcherley, C. W.; Russell, W. S.; Xie, J. Y.; Lu, D.; Laude, N. D.; Porreca, F.; Heien, M. L., Biocompatible pedot:Nafion composite electrode coatings for selective detection of neurotransmitters in vivo. *Anal Chem* **2015,** *87* (5), 2600-2607.

80. Sampson, M. M.; Yang, H.; Andrews, A. M., Advanced microdialysis approaches resolve differences in serotonin homeostasis and signaling. In *Compendium of in vivo monitoring in real-time molecular neuroscience*, WORLD SCIENTIFIC: 2017; pp 119-140.

81. Pedregosa, F.; Varoquaux, G.; Gramfort, A.; Michel, V.; Thirion, B.; Grisel, O.; Blondel, M.; Prettenhofer, P.; Weiss, R.; Dubourg, V., Scikit-learn: Machine learning in python. *J Mach Learn Res* **2011,** *12*, 2825-2830.

82. Heien, M. L. A. V.; Phillips, P. E. M.; Stuber, G. D.; Seipel, A. T.; Wightman, R. M., Overoxidation of carbon-fiber microelectrodes enhances dopamine adsorption and increases sensitivity. *Analyst* **2003,** *128* (12), 1413-1419.

83. Jackson, B. P.; Dietz, S. M.; Wightman, R. M., Fast-scan cyclic voltammetry of 5-hydroxytryptamine. *Anal Chem* **1995,** *67* (6), 1115-20.

84. Kramer, R., *Chemometric techniques for quantitative analysis*. CRC Press: Boca Raton, FL, 1998.

85. Chong, I.-G.; Jun, C.-H., Performance of some variable selection methods when multicollinearity is present. *Chemom Intell Lab Syst* **2005,** *78* (1), 103-112.

86. Ivarsson, P.; Johansson, M.; Höjer, N.-E.; Krantz-Rülcker, C.; Winquist, F.; Lundström, I., Supervision of rinses in a washing machine by a voltammetric electronic tongue. *Sens Actuators B Chem* **2005,** *108* (1), 851-857.

87. Winquist, F., Voltammetric electronic tongues – basic principles and applications. *Microchim Acta* **2008,** *163* (1), 3-10.

88. Montague, P. R.; Kishida, K. T., Computational underpinnings of neuromodulation in humans. *Cold Spring Harb Symp Quant Biol* **2018,** *83*, 71-82.

89. Hastie, T.; Tibshirani, R.; Friedman, J. H., *The elements of statistical learning: Data mining, inference, and prediction*. 2nd ed.; Springer: New York, NY, 2001.

90. Kawagoe, K. T.; Zimmerman, J. B.; Wightman, R. M., Principles of voltammetry and microelectrode surface states. *J Neurosci Methods* **1993,** *48* (3), 225-240.

91. Yang, H.; Sampson, M. M.; Senturk, D.; Andrews, A. M., Sex- and sert-mediated differences in stimulated serotonin revealed by fast microdialysis. *ACS Chem Neurosci* **2015,** *6* (8), 1487-1501.

92. Yang, H.; Thompson, A. B.; McIntosh, B. J.; Altieri, S. C.; Andrews, A. M., Physiologically relevant changes in serotonin resolved by fast microdialysis. *ACS Chem Neurosci* **2013,** *4* (5), 790-8.

93. O'Neill, B.; Patel, J. C.; Rice, M. E., Characterization of optically and electrically evoked dopamine release in striatal slices from digenic knock-in mice with dat-driven expression of channelrhodopsin. *ACS Chem Neurosci* **2017,** *8* (2), 310-319.

94. Martens, H. A.; Dardenne, P., Validation and verification of regression in small data sets. *Chemom Intell Lab Syst* **1998,** *44* (1), 99-121.

95. Braga-Neto, U. M.; Dougherty, E. R., Is cross-validation valid for small-sample microarray classification? *Bioinformatics* **2004,** *20* (3), 374-380.

96. Isaksson, A.; Wallman, M.; Göransson, H.; Gustafsson, M. G., Cross-validation and bootstrapping are unreliable in small sample classification. *Pattern Recognit Lett* **2008,** *29* (14), 1960-1965.

97. Varoquaux, G., Cross-validation failure: Small sample sizes lead to large error bars. *NeuroImage* **2018,** *180*, 68-77.

98. Ng, A. Y. In *Preventing "overfitting" of cross-validation data*, International Conference on Machine Learning (ICML), Citeseer: 1997; pp 245-253.

99. Zhang, L.; Doyon, W. M.; Clark, J. J.; Phillips, P. E.; Dani, J. A., Controls of tonic and phasic dopamine transmission in the dorsal and ventral striatum. *Mol Pharmacol* **2009,** *76* (2), 396-404.

100. Brimblecombe, K. R.; Cragg, S. J., The striosome and matrix compartments of the striatum: A path through the labyrinth from neurochemistry toward function. *ACS Chem Neurosci* **2017,** *8* (2), 235-242.

101. Hill, D. F.; Parent, K. L.; Atcherley, C. W.; Cowen, S. L.; Heien, M. L., Differential release of dopamine in the nucleus accumbens evoked by low-versus high-frequency medial prefrontal cortex stimulation. *Brain Stimul* **2018,** *11* (2), 426-434.

102. Wightman, R. M.; Amatorh, C.; Engstrom, R. C.; Hale, P. D.; Kristensen, E. W.; Kuhr, W. G.; May, L. J., Real-time characterization of dopamine overflow and uptake in the rat striatum. *Neuroscience* **1988,** *25* (2), 513-523.

103. Mathews, T. A.; Fedele, D. E.; Coppelli, F. M.; Avila, A. M.; Murphy, D. L.; Andrews, A. M., Gene dose-dependent alterations in extraneuronal serotonin but not dopamine in mice with reduced serotonin transporter expression. *J Neurosci Methods* **2004,** *140* (1-2), 169-81.

104. Daws, L. C.; Toney, G. M.; Davis, D. J.; Gerhardt, G. A.; Frazer, A., In vivo chronoamperometric measurements of the clearance of exogenously applied serotonin in the rat dentate gyrus. *J Neurosci Methods* **1997,** *78* (1), 139-150.

105. Wood, K. M.; Hashemi, P., Fast-scan cyclic voltammetry analysis of dynamic serotonin reponses to acute escitalopram. *ACS Chem Neurosci* **2013,** *4* (5), 715-720.

106. Dawson, L. A.; Watson, J. M., Vilazodone: A 5-ht1a receptor agonist/serotonin transporter inhibitor for the treatment of affective disorders. *CNS Neurosci Ther* **2009,** *15* (2), 107-117.

107. Gartside, S. E.; Umbers, V.; Hajós, M.; Sharp, T., Interaction between a selective 5-ht1a receptor antagonist and an ssri in vivo: Effects on 5-ht cell firing and extracellular 5-ht. *Br J Pharmacol* **1995,** *115* (6), 1064-1070.

108. Owens, M. J.; Knight, D. L.; Nemeroff, C. B., Second-generation ssris: Human monoamine transporter binding profile of escitalopram and r-fluoxetine. *Biol Psychiatry* **2001,** *50* (5), 345-50.

109. Conio, B.; Martino, M.; Magioncalda, P.; Escelsior, A.; Inglese, M.; Amore, M.; Northoff, G., Opposite effects of dopamine and serotonin on resting-state networks: Review and implications for psychiatric disorders. *Mol Psychiatry* **2020,** *25* (1), 82-93.

110. Watabe-Uchida, M.; Zhu, L.; Ogawa, Sachie K.; Vamanrao, A.; Uchida, N., Whole-brain mapping of direct inputs to midbrain dopamine neurons. *Neuron* **2012,** *74* (5), 858-873.

111. Alex, K. D.; Pehek, E. A., Pharmacologic mechanisms of serotonergic regulation of dopamine neurotransmission. *Pharmacology & Therapeutics* **2007,** *113* (2), 296-320.

112. Navailles, S.; De Deurwaerdère, P., Presynaptic control of serotonin on striatal dopamine function. *Psychopharmacology (Berl)* **2011,** *213* (2), 213-242.

113. Smith, G. S.; Ma, Y.; Dhawan, V.; Chaly, T.; Eidelberg, D., Selective serotonin reuptake inhibitor (ssri) modulation of striatal dopamine measured with [11c]-raclopride and positron emission tomography. *Synapse* **2009,** *63* (1), 1-6.

114. Warwick, J. M.; Carey, P. D.; Cassimjee, N.; Lochner, C.; Hemmings, S.; Moolman-Smook, H.; Beetge, E.; Dupont, P.; Stein, D. J., Dopamine transporter binding in social anxiety disorder: The effect of treatment with escitalopram. *Metab Brain Dis* **2012,** *27* (2), 151-158.

115. de Win, M. M. L.; Habraken, J. B. A.; Reneman, L.; van den Brink, W.; den Heeten, G. J.; Booij, J., Validation of [123i] β-cit spect to assess serotonin transporters in vivo in humans: A double-blind, placebo-controlled, crossover study with the selective serotonin reuptake inhibitor citalopram. *Neuropsychopharmacology* **2005,** *30* (5), 996-1005.

116. Altieri, S. C.; Yang, H.; O'Brien, H. J.; Redwine, H. M.; Senturk, D.; Hensler, J. G.; Andrews, A. M., Perinatal vs genetic programming of serotonin states associated with anxiety. *Neuropsychopharmacology* **2015,** *40* (6), 1456-70.

117. Hashemi, P.; Dankoski, E. C.; Petrovic, J.; Keithley, R. B.; Wightman, R. M., Voltammetric detection of 5-hydroxytryptamine release in the rat brain. *Anal Chem* **2009,** *81* (22), 9462-71.

118. Rodeberg, N. T.; Sandberg, S. G.; Johnson, J. A.; Phillips, P. E. M.; Wightman, R. M., Hitchhiker's guide to voltammetry: Acute and chronic electrodes for in vivo fast-scan cyclic voltammetry. *ACS Chem Neurosci* **2017,** *8* (2), 221-234.

119. Loewinger, G.; Patil, P.; Kishida, K. T.; Parmigiani, G., Multi-study learning for real-time neurochemical sensing in humans using the "study strap ensemble". *bioRxiv* **2021**, 856385.

120. Johnson, J. A.; Hobbs, C. N.; Wightman, R. M., Removal of differential capacitive interferences in fast-scan cyclic voltammetry. *Anal Chem* **2017,** *89* (11), 6166-6174.

121. Gardier, A. M.; David, D. J.; Jego, G.; Przybylski, C.; Jacquot, C.; Durier, S.; Gruwez, B.; Douvier, E.; Beauverie, P.; Poisson, N.; Hen, R.; Bourin, M., Effects of chronic paroxetine treatment on dialysate serotonin in 5-ht1b receptor knockout mice. *J Neurochem* **2003,** *86* (1), 13-24.

122. Meiser, J.; Weindl, D.; Hiller, K., Complexity of dopamine metabolism. *Cell Commun Signal* **2013,** *11* (1), 34.

123. Mohammad-Zadeh, L. F.; Moses, L.; Gwaltney-Brant, S. M., Serotonin: A review. *J Vet Pharmacol Ther* **2008,** *31* (3), 187-199.

124. Qi, Z.; Miller, G. W.; Voit, E. O., Mathematical models of dopamine metabolism in parkinson's disease. In *Systems biology of parkinson's disease*, Wellstead, P.; Cloutier, M., Eds. Springer New York: New York, NY, 2012; pp 151-171.

125. Takmakov, P.; Zachek, M. K.; Keithley, R. B.; Bucher, E. S.; McCarty, G. S.; Wightman, R. M., Characterization of local ph changes in brain using fast-scan cyclic voltammetry with carbon microelectrodes. *Anal Chem* **2010,** *82* (23), 9892-9900.

126. Yoshimi, K.; Weitemier, A., Temporal differentiation of ph-dependent capacitive current from dopamine. *Anal Chem* **2014,** *86* (17), 8576-8584.

127. Gerhardt, G. A.; Hoffman, A. F., Effects of recording media composition on the responses of nafion-coated carbon fiber microelectrodes measured using high-speed chronoamperometry. *J Neurosci Methods* **2001,** *109* (1), 13-21.

128. Fu, G.-H.; Xu, Q.-S.; Li, H.-D.; Cao, D.-S.; Liang, Y.-Z., Elastic net grouping variable selection combined with partial least squares regression (en-plsr) for the analysis of strongly multi-collinear spectroscopic data. *Appl Spectrosc* **2011,** *65* (4), 402-408.

129. Giglio, C.; Brown, S. D., Using elastic net regression to perform spectrally relevant variable selection. *J Chemom* **2018,** *32* (8), e3034.

130. Vasudevan, R. K.; Ziatdinov, M.; Vlcek, L.; Kalinin, S. V., Off-the-shelf deep learning is not enough, and requires parsimony, bayesianity, and causality. *Npj Comput Mater* **2021,** *7* (1), 16.

131. Carleo, G.; Cirac, I.; Cranmer, K.; Daudet, L.; Schuld, M.; Tishby, N.; Vogt-Maranto, L.; Zdeborová, L., Machine learning and the physical sciences. *Rev Mod Phys* **2019,** *91* (4), 045002.

132. Gundry, L.; Guo, S.-X.; Kennedy, G.; Keith, J.; Robinson, M.; Gavaghan, D.; Bond, A. M.; Zhang, J., Recent advances and future perspectives for automated parameterisation, bayesian inference and machine learning in voltammetry. *Chem Comm* **2021,** *57* (15), 1855-1870.

133. Bond, A. M., A perceived paucity of quantitative studies in the modern era of voltammetry: Prospects for parameterisation of complex reactions in bayesian and machine learning frameworks. *J Solid State Electrochem* **2020,** *24* (9), 2041-2050.

134. Matsushita, G. H. G.; Sugi, A. H.; Costa, Y. M. G.; Gomez-A, A.; Da Cunha, C.; Oliveira, L. S., Phasic dopamine release identification using convolutional neural network. *Comput Biol Med* **2019,** *114*, 103466.

135. Ye, J.-J.; Lin, C.-H.; Huang, X.-J., Analyzing the anodic stripping square wave voltammetry of heavy metal ions via machine learning: Information beyond a single voltammetric peak. *J Electroanal Chem* **2020,** *872*, 113934.

CHAPTER III

Bayesian optimization of RPV-PLSR waveforms for improved serotonin detection

The information in this chapter is in preparation for submission and adapted here.

Cameron S. Movassaghi*, Katie A. Perrotta*, Maya E. Curry, Audrey N. Nashner,
Katherine K. Nguyen, Mila E. Wesely, Chong Lui, Aaron Meyer, Anne M. Andrews

*Co-first author

Introduction

Voltammetry is widely used to characterize and quantify neurotransmitter release and reuptake.[1, 2] While there are now a variety of different voltammetry techniques, fast-scan cyclic voltammetry (FSCV) is most commonly used *in vivo*, particularly for detecting dopamine.[3] Unlike traditional cyclic voltammetry, FSCV uses fast scan rates, *i.e.*, 400-1000 V/s, which cause large and continually evolving capacitive currents.[2, 4, 5] The capacitive current is much larger than the faradaic current produced by electrochemical species in the brain. To maintain a suitable signal-to-noise ratio for faradaic current detection, the capacitive current is typically removed through background subtraction.[6] Background subtraction limits FSCV to detecting stimulated and not basal changes in neurotransmitters. Other related techniques, such as fast-scan controlled absorption voltammetry (FSCAV) have enabled the determination of basal dopamine or serotonin levels.[7-9]

The use of fast scan rates shifts the oxidation and reduction potentials of electroactive neurotransmitters. Oxidation and reduction peaks for different neurotransmitters that are separated using slow-wave cyclic voltammetry converge when using FSCV. For example, peak oxidation potentials for dopamine, serotonin, and norepinephrine are ~0.6 V by FSCV, making these species difficult to distinguish, particularly in a complex matrix such as the brain. The FSCV technique has been used mainly to detect dopamine *in vivo* because dopamine is found at higher concentrations than other electroactive neurotransmitters, principally in the striatum, and because striatal dopamine has been robustly associated with specific behaviors, including locomotion and reward-related behavior, using electrophysiology.[10-13]

Modified waveforms are used to improve serotonin detection. Jackson *et. al.* developed an ‘N-shaped’ waveform that purports to avoid byproducts formed during the oxidation of serotonin.[4] This waveform also does not oxidize dopamine well, which improves relative signals for serotonin. The ‘N-shaped’ waveform was further optimized by Dunham and coworkers by changing the switching potential, scan rate, and hold time at the peak potential.[14] The strategy behind developing these waveforms was to incorporate features of the dopamine triangle waveform into the ‘N-shaped’ waveform to try to improve serotonin detection and fouling. Ultimately, the two new waveforms they developed using this approach outperformed the original ‘N-shaped’ waveform.

Complex waveforms that combine sweeps or staircases with square-wave pulses have also recently been developed.[15] Multiple cyclic square-wave voltammetry was employed to quantify tonic dopamine *in vivo* with 10-s resolution[16] and was recently adapted in a separate application to detect tonic serotonin.[17] Improvements in sensitivity and selectivity were made using fast-cyclic square-wave voltammetry (FCSWV)[18] and N-FCSWV[19] for monitoring dopamine and serotonin, respectively, *in vivo*. Park *et al.* demonstrated that principal components regression (PCR) could be used to identify distinct features of dopamine, serotonin, norepinephrine, and epinephrine when a FCSWV waveform was applied.[18]

While these new cyclic voltammetry waveforms can be used to measure basal neurotransmitter levels or a single neurotransmitter, none can be used to monitor basal *and* stimulated levels simultaneously while also co-detecting multiple neurotransmitters.[20] We recently reported a different voltammetry approach called rapid pulse voltammetry coupled with partial least squares regression (RPV-PLSR).[21] Rather than a sweep waveform, RPV-PLSR utilizes a series of rapid pulses. Additionally, instead of subtracting background current, RPV-PLSR uses all capacitive and faradaic current information to maximize analyte identification, differentiation, and quantification. Pulse waveforms are characterized by rapid decays of capacitive and faradaic currents at different exponential rates after each pulse step, with capacitive current decaying faster. Differences in current decay yield information about specific analytes used by the PLSR model to distinguish one analyte from another. Recent work using random pulse sequences for monoamine neurotransmitter detection supports this claim.[22, 23]

Varying specific parameters of waveforms, from hold times to potential steps to scan rates, can improve analyte-specific currents.[1, 14, 24] However, to our knowledge, a systematic approach to designing analyte-specific, pulsed waveforms has not been reported. Changes to waveform parameters interact in complex ways; hold time impacts peak current, switching potential impacts the electrode surface, and so forth.[3] Intuitive waveform development is inherently a 'guess and check'-like approach, leaving the overall waveform search space relatively unexplored. Our goals are to develop unbiased and generalizable approaches that enable the exploration of large waveform search spaces to discover new, perhaps non-intuitive waveforms, for multiplexed analyte detection. For neurotransmitters, we further aim to enable *in vivo* monitoring across timescales, *i.e.*, quantification of basal and stimulated neurotransmitter levels using the same waveform in the same recording session.

As an example of a generalizable approach, we sought to enhance our original generation (OG) RPV waveform[21] to improve predictions of basal and stimulated serotonin. Serotonin is difficult to detect using voltammetry due to its relatively low physiological concentrations, colocalization with other monoamine neurotransmitters having similar redox profiles, and irreversible oxidation byproducts[25-28] that can foul electrodes. Other waveform optimization pipelines have involved stepwise parameter optimization utilizing prior knowledge from the voltammetry literature and then experimentally evaluating seeing a new waveform compares to either the FSCV triangle or 'N-shaped' waveforms.

In our initial attempts to optimize RPV waveform pulse steps we tried using other pulse techniques (chronoamperometry, differential pulse voltammetry) to gain insight into which step potentials may be better for particular analytes. However, these efforts were not productive because the behavior of single steps or steps in series, did not align with the behavior of an RPV waveform due to the fact that steps are layered in a way that has only been previously used for the electronic tongue application.[29, 30] With no guiding principles and a seemingly infinite number of step combinations that could be used to construct an RPV waveform, we had no way to evaluate new step combinations systematically using a human-centric approach. Therefore, we turned to a statistical optimization model, Bayesian optimization.[31, 32]

Bayesian optimization enables data-driven experimental design to identify global optima in high-dimension search spaces amongst parameters with complex interactions.[33] Bayesian optimization has been widely applied across diverse fields, including automated machine learning,[34] robotics,[35] sensor design,[36] materials discovery,[37, 38] and chemical reaction optimization.[39, 40] In our case, alternative approaches can be used to design waveforms (e.g., first-principles, chemometric screening, experimental design). However, these approaches suffer from limitations associated with computational complexity, an exponential number of experiments required per parameter, and/or the inability to account for confounding waveform parameter interactions.[41]

Bayesian optimization is commonly used for 'black box' problems that are practically difficult to evaluate due to time/resources/lack of theoretical knowledge.[42-44] Black-box problems are solved by constructing probabilistic models that are sequentially updated as data is acquired (*i.e.*, adaptive experimental design).[31, 33] The closed-feedback loop of Bayesian optimization outperforms conventional and other state of-the-art optimization procedures, including expert scientists, in a fraction of the experimental time and resources.[39, 42]

Waveform design is a black box optimization problem. We seek an input (a waveform) that is related to an optimal output objective (*e.g.*, maxima of sensitivity/selectivity, minima of error, etc.) by an unknown objective function (the black box). Evaluating waveforms is expensive (labor, time, materials, etc.) and the search space is vast. Despite its advantages and versatility, applications of Bayesian optimization to analytical chemistry and specifically, electrochemistry are still spare.[45-48] We are not aware of previous applications of Bayesian optimization to voltammetry waveform design.

Here, we introduce novel training set designs and data processing procedures to address the challenging issue waveform optimization in the specific context of generalizing *in vitro* training data to the complex *in vivo* environment of the brain. We show that information contained in voltammograms is dependent on specific potentials that occur in specific orders, confirming the need for a parsimonious search approach. We present an initial proof-of-concept using Bayesian optimization for automated, machine-learning guided, fit-for-purpose voltammetry waveforms. The approach outperforms randomly designed and domain expert designed waveforms. Importantly, our approach can be straightforwardly applied to the design of any voltammetric waveform for any electroactive analyte.

Results and Discussion

Our Bayesian optimization workflow for robust, systematic, and unbiased voltammetric waveform development is shown in **Fig. III.1**. A search is initialized with six randomly generated pulse waveforms, where each waveform x is embedded as a vector in 8 dimensional space such that $x := [E_1, \tau_1, E_2, \tau_2, E_3, \tau_3, E_4, \tau_4]$, where E is the potential step (V) and τ is the step hold time (ms). In this initial design, for eventual comparison with our human-designed four-step waveform (**Fig. III.4a**), we constrained the search space to four steps per waveform, with E_1 and E_2 constrained to 0-1.3 V and E_3 and E_4 constrained to -0.5-0 V. These constraints ensured that waveforms remained inside the solvent window and encoded a 'pulse/counter-pulse' concept. We constrained τ to 0.5-2.0 ms based on our preliminary results showing that capacitive current decays fully after ~2 ms yet important features are contained in as little as ~0.5 ms.[15] Pulses as short as 0.5 ms contain valuable information and do not result in voltage cross talk (*i.e.*, residual capacitive current from successive voltage steps).[11, 14] To limit the number of parameters, hold time was defined as $(100\text{-}\ \sum= \llbracket(\tau))\rrbracket$ ms, so that every pulse was applied at 10 Hz; the holding potential was defined as E_4.

We experimentally produced calibration curve data (**upper left table, Fig. III.1**) for each random waveform in duplicate and on separate days to assist the model in gauging noise/uncertainty. Each generated waveform was trained using the fractional factorial box design laid out in the table in **Figure III.1**. For training, samples A- P the concentrations of dopamine, serotonin, 5-hydroxyindoleacetic acid (5-HIAA), 3,4-dihydroxyphenylacetic acid (DOPAC), and ascorbic acid were altered so that the model could be trained across all of these analytes. The test samples T1- T4 that also had varied levels of serotonin, dopamine, and interferents, were used to assess dopamine and serotonin accuracy and limit of detection (LOD). Repeats of T1-T3 were made in aCSF at pH 7.1, pH 7.2, and in aCSF with altered ion content of Na^+ and K^+, respectively, to assess the accuracy of dopamine and serotonin in the presence of changing H^+, Na^+, and K^+ that it was not trained on. The ability of Bayesian optimization to account for noise and variance of the surrogate model (i.e., uncertainty) is a key strength of this technique.[36] Data for each of the eight random waveforms (**gray boxes, Fig. III.1**) was then processed using PLSR.

The test set results are used to calculate the eight optimization metrics listed. These metrics and corresponding waveform parameters are used to create surrogate models (*i.e.,* Gaussian processes[36]) of the unknown objective functions (*i.e.,* black box functions relating waveform parameters to their optimization metric). An acquisition function (*i.e.*, expected improvement[36]) finds the optima of each surrogate function, and outputs the next most likely waveform that will improve the respective metric. The eight different output metrics/waveform: dopamine and serotonin accuracy (average test set accuracy; mean absolute error of T1-4 predictions), variance at 0 (proxy for LOD) for dopamine and serotonin, ion accuracy for dopamine and serotonin (T3 and blank accuracy with altered cations), and pH accuracy for dopamine and serotonin (T1, T2 and blank accuracy at pH 7.1 and 7.2). This multi-metric approach allows for waveforms with tunable figures of merit (*e.g.*, sensitivity can be preferentially optimized should other metrics be satisfactory).

The eight waveforms output from the first optimization loop of this workflow are shown (**Fig. III.1, right**). For each waveform (a new 'string'), we obtained calibration curve data for the new waveforms, trained the corresponding PLSR model, calculated the optimization metrics using test set results, and predicted the next set of optimal waveforms. We demonstrate that the Bayesian optimizer is covering a wide search space across all the set parameters, mentioned above (**Fig. III.2**). Although the process may seem random, it is exploring the search space parsimoniously. Specific combinations of pulse step potential and τ influence serotonin accuracy as measured by partial dependence plots (**Fig. III.3**). For example, combinations of the second step potential, the third step potential, and third step tau have high-dimensional interactions, as denoted by the yellow shading (location of minima).

We focused first on the results for the second waveform optimized across strings for serotonin prediction accuracy, defined as the mean absolute error in the PLSR model predictions of test samples T1- 4. Across four Bayesian optimization strings, three new waveforms were predicted by the Bayesian optimizer for serotonin accuracy, as the first string was randomly generated to initialize the search space. The evolution of these three waveforms (**Fig III.4b-d**) can be compared to our initial rapid pulse voltammetry waveform (**Fig. III.4a**). We note the similarity of our 'human-in-the-loop' waveform (**Fig. III.1a**) to one of the first-iteration Bayesian optimized overall accuracy waveforms (**Fig. III.1, bottom right, green**). Even in the first iteration, our Bayesian optimization scheme has nearly perfectly predicted our chemical intuition choice for the potentials of the **Figure III.4a** waveform design; they differ only by ~100 mV or less. The Bayesian calculations optimized step length on their own to find optimal temporal resolution (in this case, 5.8 ms rather than 8 ms).

We did not simply 'get lucky' or stumble across a great waveform randomly. A convergence plot (**Fig. III.4e**) shows that for each Bayesian string, the waveform optimized for serotonin accuracy found a new minimum for serotonin prediction error in each iteration, which demonstrates improvement across strings. We compared the predictions of the serotonin waveform from string four (BO4wf2 RPV) to the original RPV waveform (OG RPV) through calculating the accuracy of test samples 1-4 (**Fig. III.5**). We determined that the BO4wf2 RPV waveform increased prediction accuracy for test samples 1-4 by ~20% compared to the OG RPV waveform.

The Bayesian optimization process was repeated from a new set of six random waveforms and carried out for three strings as described above. We noticed that for certain metrics, particularly dopamine and serotonin accuracy, the predicted waveforms between Bayesian optimization one and two looked similar (**Fig. III.6**). For dopamine accuracy the string 3 predicted waveforms resulted in the same high to lower potential step for the oxidative potentials, and a low to higher potential step for the reductive potentials. The serotonin accuracy waveforms share more characteristics with the OG RPV waveform across Bayesian Optimization 1 and 2, falling into a low to high potential step for the oxidative potential steps and a high to low potential step for the reductive potential steps.

Conclusion

Overall, our Bayesian approach provides a closed feedback loop that enables accelerated machine learning-driven design of fit-for-purpose RPV waveforms. We have demonstrated that the model covers a wide portion of the search space and that unique waveform characteristics are combined to predict new waveforms. Additionally, a Bayesian optimization waveform, BO4w2 RPV, has more accurate test sample predictions for serotonin than OG RPV. The Bayesian optimization approach has worked to optimize RPV waveforms but can be generalized to any voltammetry waveform.

Methods

Chemicals

Serotonin standards, dopamine standards, and artificial cerebrospinal fluid (aCSF) solutions were purchased from and prepared as described in previous literature.[15] The standards for 5-HIAA (#H8876), DOPAC (#850217), and ascorbic acid (#A92902) were purchased from Sigma-Aldrich (St. Louis, MO). The aCSF solution was adjusted to pH 7.1, 7.2 or 7.3 ± 0.03 using HCl (Fluka, #84415). High potassium aCSF buffer contained the following ionic composition: 31 mM NaCl (#73575), 120 mM KCl (#05257), 1.0 mM NaH_2PO_4 (#17844), 2.5 mM $NaHCO_3$ (#88208) purchased from Honeywell Fluka (Charlotte, NC), and 1.0 mM CaCl2 (#499609) and 1.2 mM MgCl2 (#449172) purchased from Sigma-Aldrich. All aqueous solutions were made using LC-MS water (Fisher Scientific, W6-4).

Electrode Fabrication and Polymerization

Carbon fiber microelectrodes were fabricated as follows, 7-µm diameter carbon fibers (T650/35, Cytec Carbon Fiber) were vacuum-aspirated into O.D. 1.2 mm, I.D. 0.69 mm, 10 cm length borosilicate glass capillaries (Sutter Instrument Company, Novato, CA, B120-69-10). A micropipette puller (P-1000, Sutter Instrument Company, Novato, CA) was used to pull each capillary into two electrodes by tapering and sealing the glass around the carbon fiber. Four-part epoxy (Sigma Aldrich, Spurr Low Viscosity Embedding Kit- EM0300) was then backfilled into the tip of each electrode and epoxied electrodes were dried at 70 °C for 8-12 hours. Electrode tips were cut to ~100 µm using micro-scissors under an inverted microscope. The electrodes were backfilled with a non-toxic metal alloy of gallium-indium-tin, Galinstan (Alfa Aesar, 14634-18), for electrical conduction. Bare copper wire (0.0253-in. diameter, Archor B22) was polished using a 600-grit polishing disc and inserted into working electrode capillaries to serve as the electrical connection to the potentiostat, epoxy (Loctite

EA 1C) was then put around the top of the electrode to secure the wire in place. The epoxy was cured after 24 hours when left at room temperature.

Electrode tips were cleaned with HPLC-grade isopropanol (Sigma Aldrich #34863) for 10 min. Electrodes were then overoxidized by applying a static 1.4 V potential for 20 min.[37] Low-density EDOT:Nafion solution was made by first creating a 40 mM EDOT stock; 100 µL of this stock was added to 200 µL of Nafion and diluted with 20 mL of acetonitrile.[38] A triangle waveform (1.5V to -0.8V to 1.5V) was applied using a CHI Instruments Electrochemical Analyzer 15x at 100 mV/s to generate a PEDOT:Nafion coating on each electrode.

In vitro Experiments

Reference electrodes were made by placing 0.025-inch silver wire (A-M Systems, 783500) into bleach for 10 minutes. The electrode was rinsed with DI water before being used in experiments. A flow cell (NEC-FLOW-1, Pine Research Instrumentation Inc.) was combined with a VICI air actuated injector (220-0302H) to make *in vitro* measurements. An HPLC pump by Dionex (Sunnyvale, California) was used to move aCSF through the flow cell at a constant flow rate of 1.0 mL/min.

Standards were made using a fractional factorial box design as shown in the table in **Figure III.1**. The fractional factorial box design is a chemometric approach that designs a multi-dimensional 'box' spanning analytes, their concentrations, and experimental conditions of interest.[27, 39] We selected a fractional approach to bias towards low analyte concentrations and small relative changes. High accuracy and precision in the nM range are important for monitoring basal and stimulated neurotransmitter levels using a single technique. The fractional approach avoids a full factorial design, which would require orders of magnitude (and prohibitively) more calibration samples. In contrast, traditional calibration sets are less information-rich and can lead to spurious correlations when training a multiplexed method with overlapping signals arising from analytes and interferents.[27]

Calibration standards were injected (roughly 1 mL sample into a 500 µL loop volume) A- T4 into a flow cell for 20 seconds at 200- 300 second intervals, depending on the waveform. In each string, the calibration curves for the waveforms were completed across multiple days. A different electrode was used for each string. We define a training set (*i.e.*, calibration set) as known concentration analyte mixtures, *i.e.*, 'standards', used to train a PLSR model, while a test set is defined as known concentration analyte mixtures not used during training, but instead used to test how well a model performs.

Voltammetry Hardware and Software

A two-electrode configuration *via* an Ag/AgCl reference electrode and a carbon fiber microelectrode working electrode was used. A PC with a PCIe-6363 data acquisition card (National Instruments (NI), Austin, TX) was used to control a WaveNeuro One FSCV Potentiostat System (NEC-WN-BASIC, Pine Research Instrumentation Inc.) with a 1,000 nA/V headstage amplifier (AC01HS2, Pine Research Instrumentation Inc.). The copper wire of the working electrode and the silver wire reference electrode were inserted into a microelectrode-headstage coupler (AC01HC0315-5, Pine Research Instrumentation Inc.) that connects the electrodes to the potentiostat. These wires must be ~0.025 inches to make a good connection into the coupler.

In-house software was developed for RPV and described in our previous paper.[15] However, the software has since been updated and named Seroware. Details about Seroware and open-source access to the program can be found in another manuscript, titled 'Seroware, part 1: An open source, end-to-end software suite for voltammetric acquisition and analysis of neurotransmitters'.

Waveforms

Bayesian Optimization 1

String 1

	Step 1	Tau 1	Step 2	Tau 2	Step 3	Tau 3	Step 4	Tau 4	Holding Potential
1	0.8 V	0.5 ms	0.5 V	0.5 ms	-0.3 V	1.0 ms	-0.1 V	1.5 ms	96.5 ms
2	0.9 V	0.5 ms	0.7 V	1.0 ms	-0.4 V	0.5 ms	-0.3 V	1.5 ms	96.5 ms
3	0.5 V	2.0 ms	0.2 V	1.5 ms	-0.1 V	1.5 ms	-0.3 V	1.0 ms	94 ms
4	0.6 V	2.0 ms	0.8 V	0.5 ms	-0.2 V	2.0 ms	-0.4 V	0.5 ms	95 ms
5	0.2 V	1.0 ms	0.3 V	1.5 ms	-0.1 V	1.5 ms	0.0 V	0.5 ms	95.5 ms
6	0.7 V	1.5 ms	0.6 V	2.0 ms	-0.3 V	1.0 ms	-0.1 V	2.0 ms	93.5 ms

String 2

	Step 1	Tau 1	Step 2	Tau 2	Step 3	Tau 3	Step 4	Tau 4	Holding Potential
1	0.308 V	1.6 ms	0.385 V	1.0 ms	-0.397 V	1.5 ms	-0.268 V	0.6 ms	95.3 ms
2	0.747 V	1.0 ms	0.499 V	1.9 ms	-0.309 V	0.8 ms	-0.237 V	0.5 ms	95.8 ms
3	0.113 V	0.9 ms	0.930 V	1.7 ms	-0.243 V	1.4 ms	-0.056 V	1.0 ms	95 ms
4	0.291 V	1.7 ms	0.106 V	0.9 ms	-0.165 V	1.6 ms	-0.393 V	0.6 ms	95.2 ms
5	0.815 V	1.0 ms	0.001105 V	1.1 ms	-0.379 V	1.2 ms	-0.137 V	1.5 ms	95.2 ms
6	0.163 V	1.4 ms	0.972 V	1.9 ms	-0.080 V	1.9 ms	-0.051 V	1.5 ms	93.3 ms
7	0.747 V	0.5 ms	0.001251 V	0.5 ms	-0.162 V	0.8 ms	-0.324 V	1.9 ms	96.3 ms
8	0.362 V	0.7 ms	0.524 V	2.0 ms	-0.333 V	1.6 ms	-0.291 V	0.9 ms	94.8 ms

String 3

	Step 1	Tau 1	Step 2	Tau 2	Step 3	Tau 3	Step 4	Tau 4	Holding Potential
1	0.102 V	1.3 ms	0.092 V	0.6 ms	-0.350 V	0.8 ms	-0.321 V	1.8 ms	95.5 ms
2	0.517 V	0.7 ms	0.806 V	1.9 ms	-0.098 V	1.8 ms	-0.493 V	1.3 ms	94.3 ms
3	0.437 V	0.8 ms	0.548 V	1.9 ms	-0.291 V	1.7 ms	-0.282 V	0.9 ms	94.7 ms
4	0.646 V	1.0 ms	0.171 V	1.8 ms	-0.236 V	1.5 ms	-0.218 V	1.7 ms	94 ms
5	0.351 V	1.1 ms	0.784 V	0.9 ms	-0.350 V	0.6 ms	-0.209 V	0.5 ms	96.9 ms
6	0.325 V	1.7 ms	1.255 V	1.2 ms	-0.109 V	1.3 ms	-0.306 V	1.0 ms	94.8 ms
7	0.105 V	0.9 ms	0.303 V	1.8 ms	-0.009 V	0.8 ms	-0.066 V	1.0 ms	95.5 ms
8	0.004 V	2.0 ms	0.598 V	0.9 ms	-0.212 V	2.0 ms	-0.161 V	1.4 ms	93.7 ms

String 4

	Step 1	Tau 1	Step 2	Tau 2	Step 3	Tau 3	Step 4	Tau 4	Holding Potential
1	0.128 V	1.9 ms	1.248 V	1.9 ms	-0.469 V	0.9 ms	-0.109 V	1.9 ms	93.4 ms
2	0.274 V	0.7 ms	0.779 V	1.5 ms	-0.180 V	1.4 ms	-0.425 V	1.4 ms	94.5 ms
3	0.578 V	1.0 ms	0.856 V	0.9 ms	-0.298 V	1.7 ms	-0.141 V	1.7 ms	94.9 ms
4	0.837 V	1.9 ms	1.074 V	0.5 ms	-0.096 V	0.7 ms	-0.300 V	0.7 ms	95 ms
5	0.770 V	0.8 ms	0.945 V	1.5 ms	-0.266 V	1.5 ms	-0.394 V	1.5 ms	94.9 ms
6	0.000 V	1.5 ms	0.560 V	1.8 ms	-0.216 V	1.3 ms	-0.154 V	1.3 ms	94.2 ms
7	0.315 V	1.4 ms	1.289 V	0.5 ms	-0.479 V	1.0 ms	-0.293 V	1.0 ms	96.4 ms
8	0.226 V	0.8 ms	0.286 V	1.8 ms	-0.465 V	0.9 ms	-0.359 V	0.9 ms	95.7 ms

Bayesian Optimization 2

String 1

	Step 1	Tau 1	Step 2	Tau 2	Step 3	Tau 3	Step 4	Tau 4	Holding Potential
1	0.113 V	0.6 ms	1.223 V	0.8 ms	-0.271 V	0.6 ms	-0.420 ms	0.7 ms	97.3 ms
2	0.366 V	0.6 ms	0.860 V	2.0 ms	-0.309 V	0.6 ms	-0.353 ms	0.6 ms	96.2 ms
3	0.363 V	1.8 ms	1.077 V	1.6 ms	-0.192 V	1.5 ms	-0.314 ms	0.9 ms	94.2 ms
4	0.088 V	1.2 ms	1.060 V	1.8 ms	-0.165 V	0.6 ms	-0.458 ms	1.0 ms	95.4 ms
5	0.172 V	0.9 ms	0.045 V	2.0 ms	-0.110 V	1.7 ms	-0.260 ms	1.6 ms	93.8 ms
6	0.580 V	1.4 ms	0.951 V	1.9 ms	-0.482 V	1.9 ms	-0.053 ms	1.6 ms	93.2 ms

String 2

	Step 1	Tau 1	Step 2	Tau 2	Step 3	Tau 3	Step 4	Tau 4	Holding Potential
1	0.543 V	1.7 ms	1.116 V	1.5 ms	-0.217 V	1.6 ms	-0.293 V	1.0 ms	94.2 ms
2	0.200 V	1.8 ms	1.111 V	0.9 ms	-0.191 V	1.5 ms	-0.383 V	0.9 ms	94.9 ms
3	0.119 V	0.6 ms	0.480 V	2.0 ms	-0.006 V	0.6 ms	-0.342 V	1.0 ms	95.8 ms
4	0.129 V	1.2 ms	0.759 V	1.7 ms	-0.397 V	1.1 ms	-0.453 V	1.8 ms	94.2 ms
5	0.230 V	1.2 ms	0.116 V	0.5 ms	-0.082 V	1.5 ms	-0.417 V	1.1 ms	95.7 ms
6	0.410 V	1.6 ms	1.074 V	1.6 ms	-0.197 V	1.3 ms	-0.304 V	1.6 ms	93.9 ms

String 3

	Step 1	Tau 1	Step 2	Tau 2	Step 3	Tau 3	Step 4	Tau 4	Holding Potential
1	0.605 V	1.6 ms	0.505 V	1.5 ms	-0.185 V	1.4 ms	-0.098 V	1.6 ms	93.9 ms
2	0.227 V	1.7 ms	1.174 V	0.6 ms	-0.180 V	1.3 ms	-0.422 V	2.0 ms	94.4 ms
3	0.300 V	1.7 ms	1.122 V	0.9 ms	-0.197 V	0.9 ms	-0.420 V	0.8 ms	95.7 ms
4	0.703 V	0.7 ms	1.123 V	1.2 ms	-0.088 V	1.4 ms	-0.318 V	0.8 ms	95.9 ms
5	0.133 V	1.2 ms	1.083 V	1.7 ms	-0.213 V	0.7 ms	-0.415 V	1.0 ms	95.4 ms
6	1.159 V	1.5 ms	0.887 V	1.0 ms	-0.023 V	2.0 ms	-0.275 V	1.0 ms	94.5 ms

Bayesian Optimization Models

Bayesian optimization was done using the open-source Python package Scikit-Optimize.[40] The software uses an 'ask and tell' interface. First, the search space was constrained as described above. The surrogate model (Gaussian process regressor with a Matérn and white noise kernel) was initialized through the 'tell' interface using vectorized and normalized String 1 waveform parameters (inputs) and optimization metrics (outputs). The acquisition function (negative expected improvement) was then minimized using the 'ask' interface to generate a vectorized waveform to be experimentally queried. After experimental results were obtained with the predicted waveform, the metrics of all previous waveforms were aggregated with the newest metrics, the Bayesian optimizer was updated using the 'tell' interface and used to set new query points using the 'ask' interface.

Data Analysis

Data were extracted using in-house custom acquisition software written in MATLAB 2016a and models built as described in previous literature using open-source Python packages (Scikit-Learn).[15, 41] Briefly, roughly 40-100 voltammograms were extracted per train and test sample injection. All voltammograms were normalized and the number of components was chosen using cross-validation. Test set metrics were then calculated using the final model. The PLSR model was trained to account for drift using voltammograms collected throughout the experiment while aCSF containing interferents was flowed and injections were not occurring (~2 h). Data, in which drift was evident, were extracted from these background epochs and labeled as 'zero' analyte concentrations to teach the model what drifting, as opposed to analyte-containing, voltammograms look like. These 'drift zeroes' were in addition to data from injections of aCSF alone (i.e., blanks) to account for flow cell injection and pump artifacts.

Figures

Figure III.1

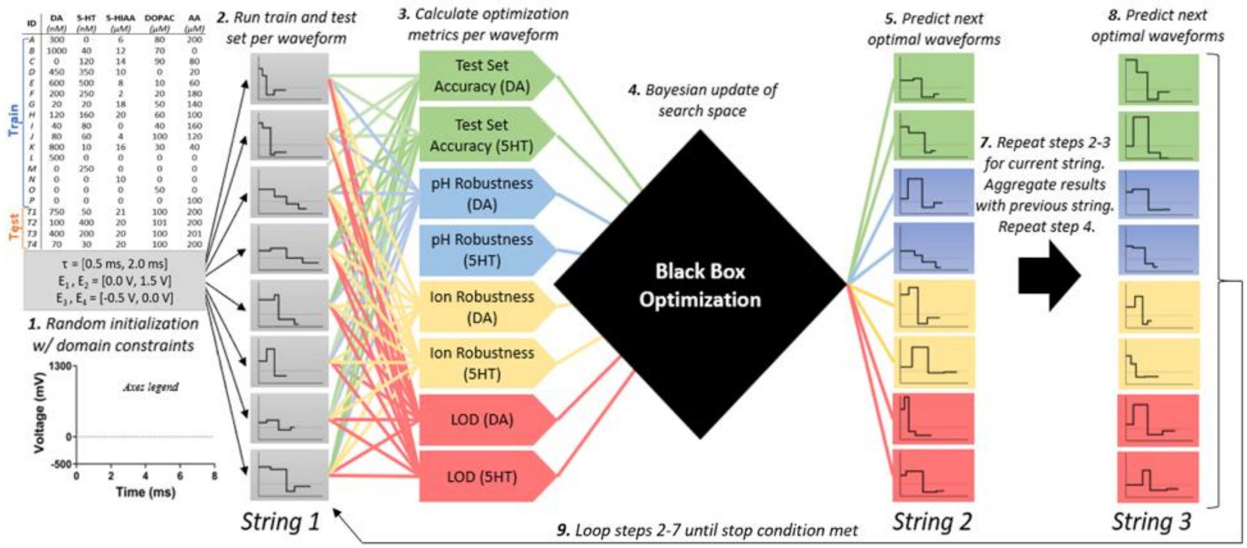

ID	DA (nM)	5-HT (nM)	5-HIAA (μM)	DOPAC (μM)	AA (μM)
A	300	0	6	80	200
B	1000	40	12	70	0
C	0	120	14	90	80
D	450	350	10	0	20
E	600	500	8	10	60
F	200	250	2	20	180
G	20	20	18	50	140
H	120	160	20	60	100
I	40	80	0	40	160
J	80	60	4	100	120
K	800	10	16	30	40
L	500	0	0	0	0
M	0	250	0	0	0
N	0	0	10	0	0
O	0	0	0	50	0
P	0	0	0	0	100
T1	750	50	21	100	200
T2	100	400	20	101	200
T3	400	200	20	100	201
T4	70	30	20	100	200

Figure III.1. Bayesian optimization for machine learning-guided RPV waveform design for serotonin (5HT) and dopamine (DA). Upper left corner is a table showing the fractional factorial calibration (A-R) and test (T1-4) set design. All calibration sets used here encompassed physiologically relevant mixtures of serotonin (0-500 nM, 50 nM increments) and dopamine (0-1000 nM, 100 nM increments), in aCSF, in the presence of interferents (i.e., metabolites, pH, ions) to simulate *in vivo* environments.

Figure III.2

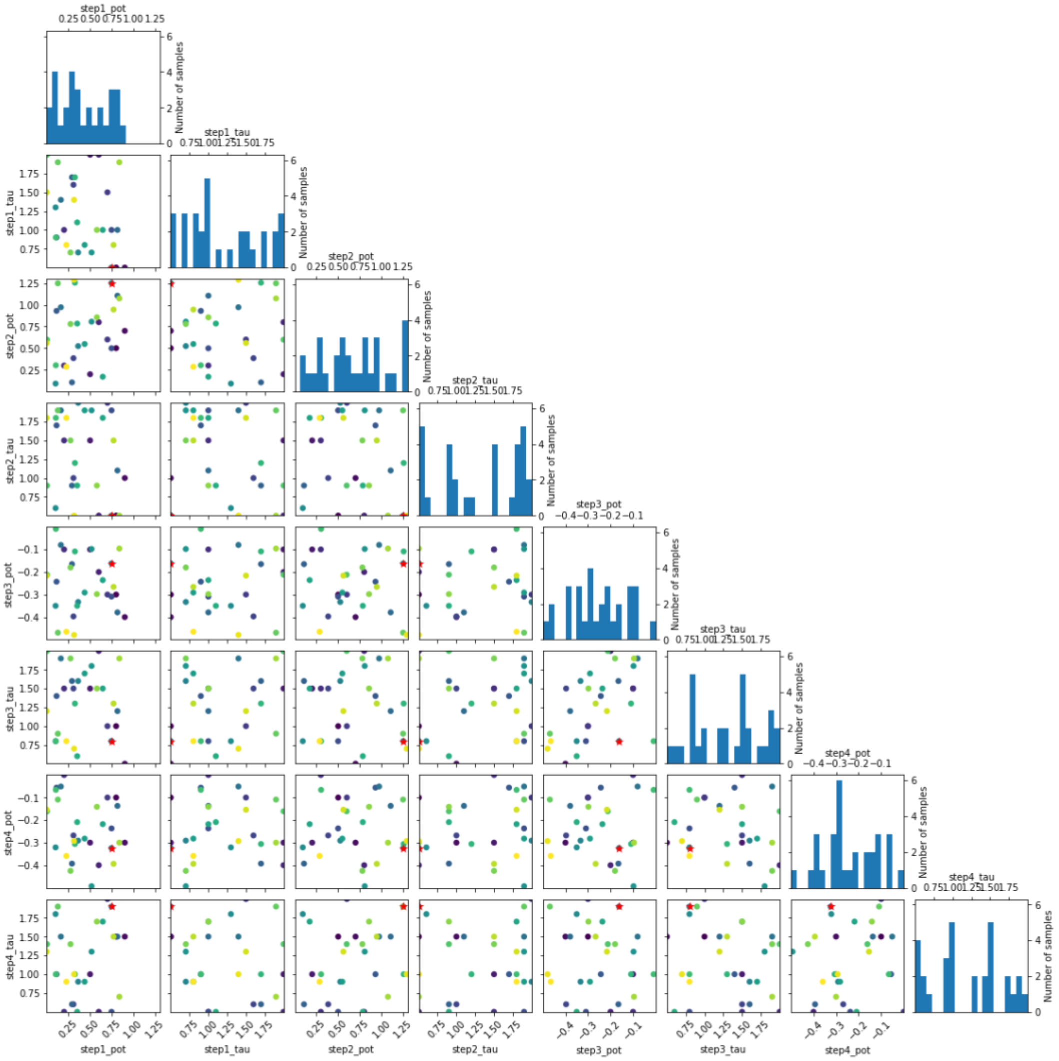

Figure III.2. Parameter distribution plots demonstrating how the Bayesian optimizer is spanning the search space.

Figure III.3

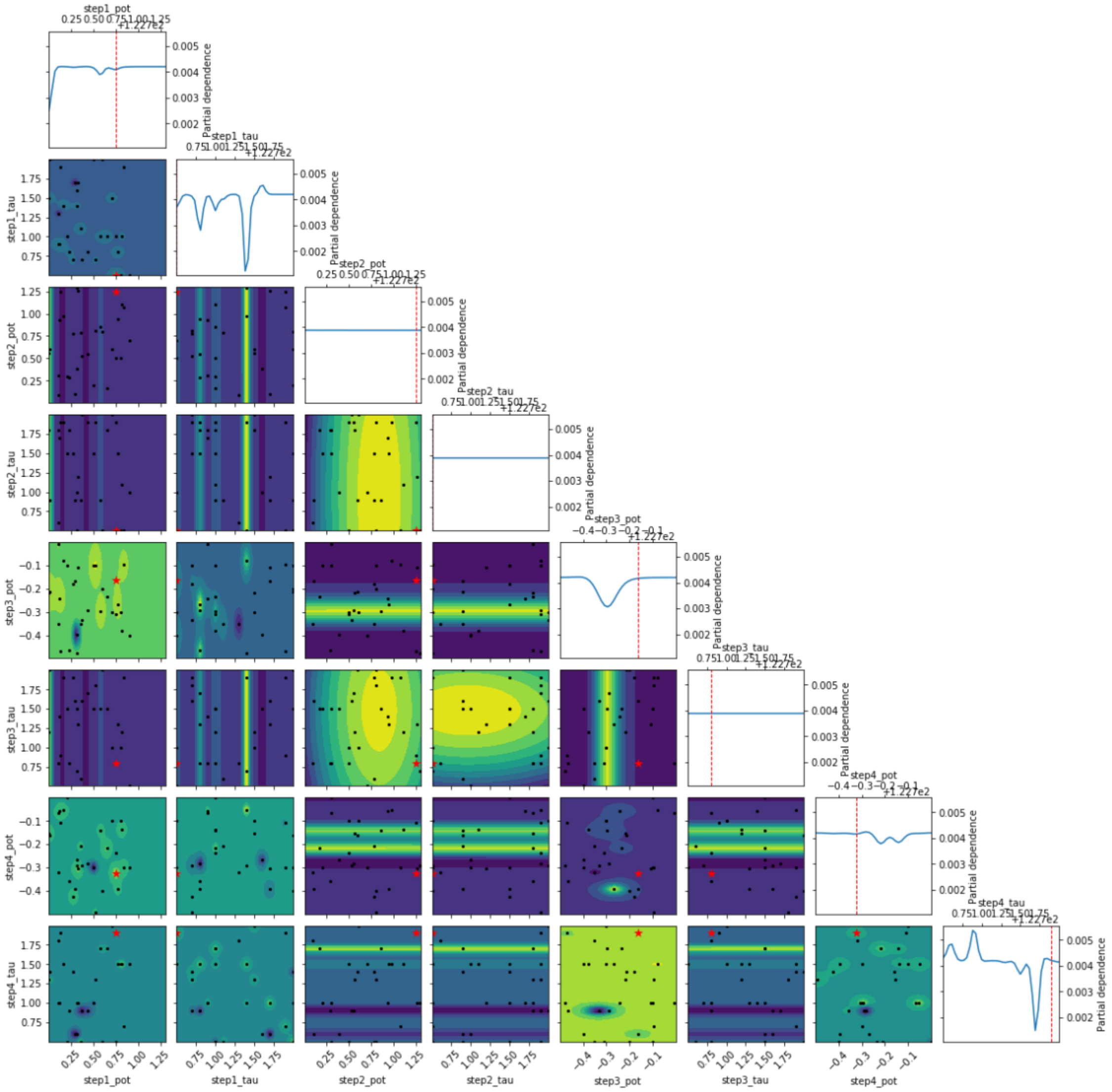

Figure III.3. Partial dependence plots for serotonin accuracy

Figure III.4

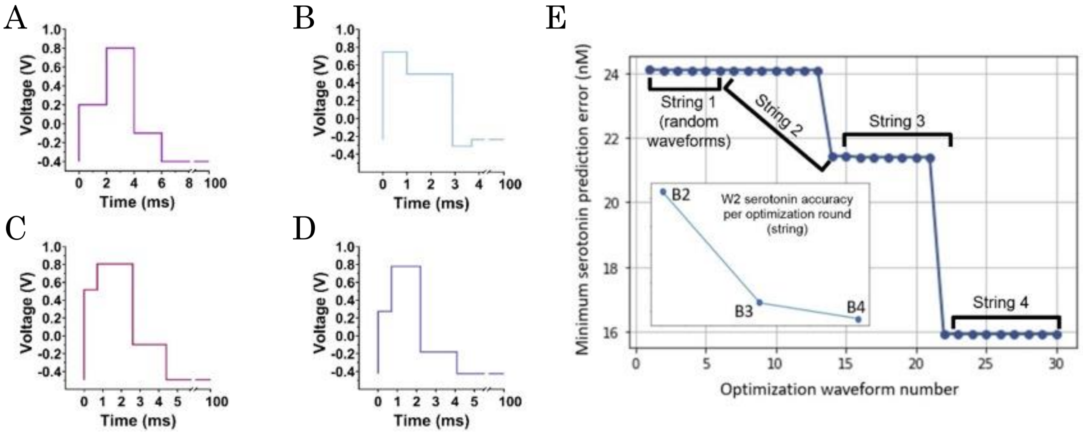

Figure III.4. a) OG RPV waveform, **b-d)** the predicted Bayesian optimization waveforms for the serotonin accuracy metric across strings 2-4, **e)** convergence plot for serotonin accuracy across all Bayesian strings, with serotonin accuracy

Figure III.5

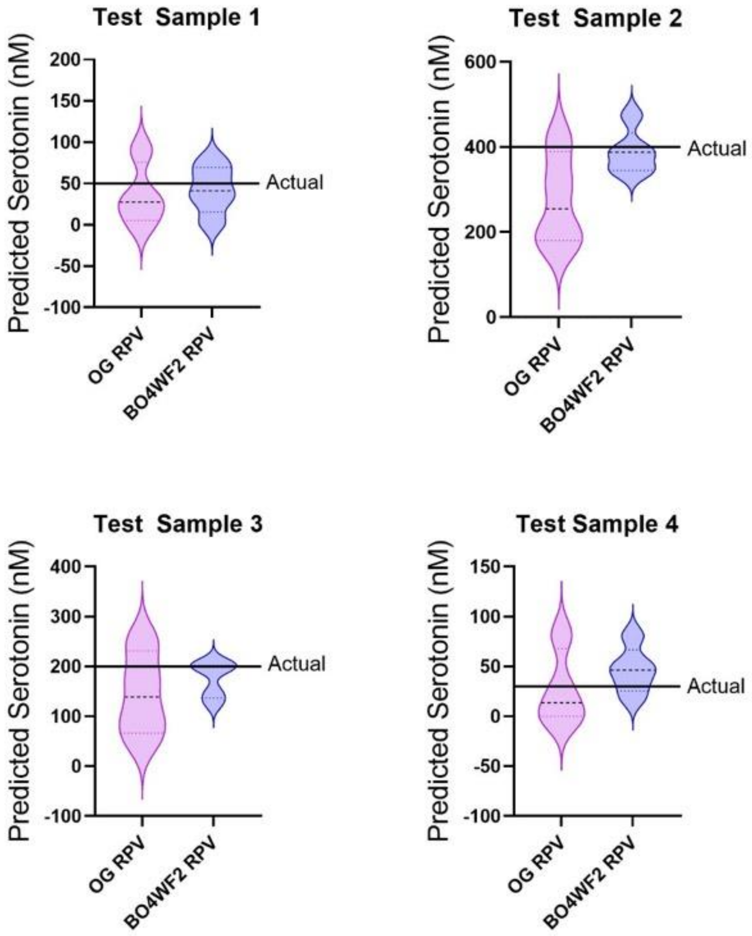

Figure III.5. Violin plots of serotonin predictions for test samples 1-4, comparing the prediction accuracy for the OG RPV waveform and the BO4wf2 waveform.

Figure III.6

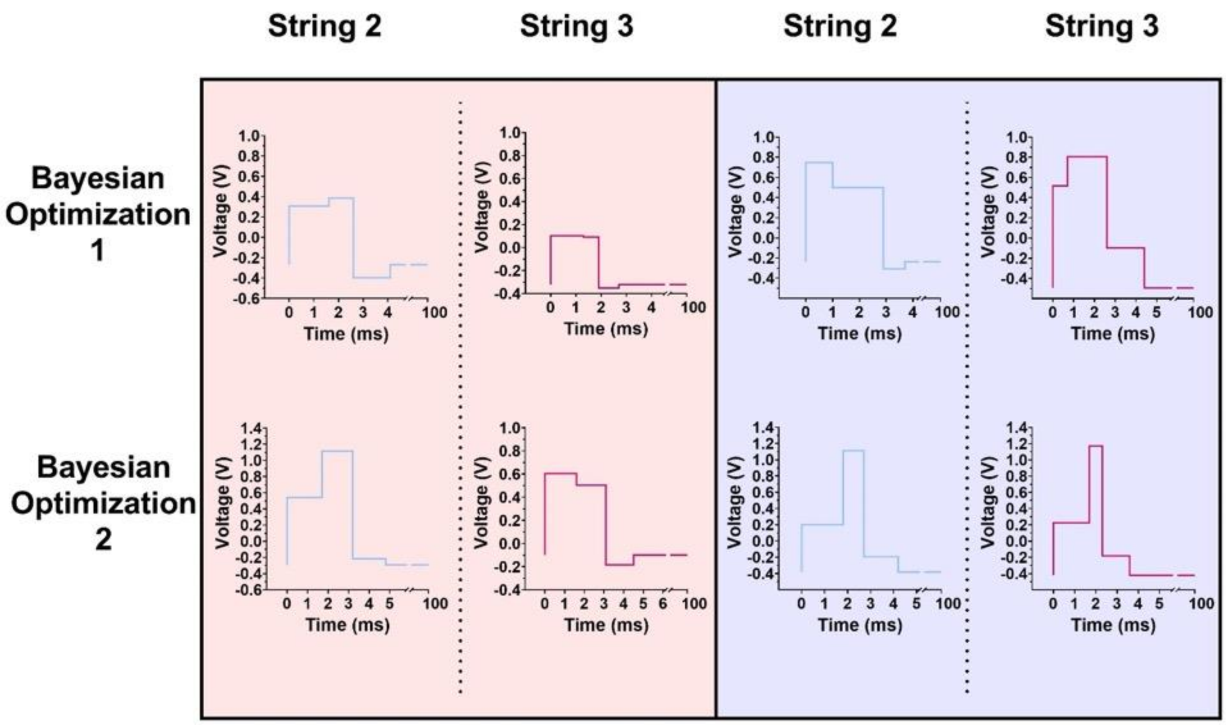

Figure III.6. Predicted Bayesian optimization waveforms across two separate Bayesian optimization experiments. Waveforms for the dopamine accuracy metric are highlighted in red and the serotonin accuracy metric in blue.

References

1. Puthongkham, P.; Venton, B. J., Recent advances in fast-scan cyclic voltammetry. *Analyst* **2020,** *145* (4), 1087-1102.

2. Rodeberg, N. T.; Sandberg, S. G.; Johnson, J. A.; Phillips, P. E. M.; Wightman, R. M., Hitchhiker's guide to voltammetry: Acute and chronic electrodes for in vivo fast-scan cyclic voltammetry. *ACS Chem Neurosci* **2017,** *8* (2), 221-234.

3. Venton, B. J.; Cao, Q., Fundamentals of fast-scan cyclic voltammetry for dopamine detection. *Analyst* **2020,** *145* (4), 1158-1168.

4. Jackson, B. P.; Dietz, S. M.; Wightman, R. M., Fast-scan cyclic voltammetry of 5-hydroxytryptamine. *Anal Chem* **1995,** *67* (6), 1115-20.

5. Hashemi, P.; Dankoski, E. C.; Petrovic, J.; Keithley, R. B.; Wightman, R. M., Voltammetric detection of 5-hydroxytryptamine release in the rat brain. *Anal Chem* **2009,** *81* (22), 9462-71.

6. Howell, J. O.; Kuhr, W. G.; Ensman, R. E.; Mark Wightman, R., Background subtraction for rapid scan voltammetry. *Journal of Electroanalytical Chemistry and Interfacial Electrochemistry* **1986,** *209* (1), 77-90.

7. Abdalla, A.; Atcherley, C. W.; Pathirathna, P.; Samaranayake, S.; Qiang, B.; Peña, E.; Morgan, S. L.; Heien, M. L.; Hashemi, P., In vivo ambient serotonin measurements at carbon-fiber microelectrodes. *Analytical Chemistry* **2017,** *89* (18), 9703-9711.

8. Atcherley, C. W.; Laude, N. D.; Parent, K. L.; Heien, M. L., Fast-scan controlled-adsorption voltammetry for the quantification of absolute concentrations and adsorption dynamics. *Langmuir* **2013,** *29* (48), 14885-92.

9. West, A.; Best, J.; Abdalla, A.; Nijhout, H. F.; Reed, M.; Hashemi, P., Voltammetric evidence for discrete serotonin circuits, linked to specific reuptake domains, in the mouse medial prefrontal cortex. *Neurochem Int* **2019,** *123*, 50-58.

10. Schultz, W., Predictive reward signal of dopamine neurons. *Journal of Neurophysiology* **1998,** *80* (1), 1-27.

11. Schultz, W., Behavioral theories and the neurophysiology of reward. *Annual Review of Psychology* **2006,** *57* (1), 87-115.

12. Lee, K.; Claar, L. D.; Hachisuka, A.; Bakhurin, K. I.; Nguyen, J.; Trott, J. M.; Gill, J. L.; Masmanidis, S. C., Temporally restricted dopaminergic control of reward-conditioned movements. *Nature Neuroscience* **2020,** *23* (2), 209-216.

13. Long, C.; Lee, K.; Yang, L.; Dafalias, T.; Wu, A. K.; Masmanidis, S. C., Physiological constraints on the rapid dopaminergic modulation of striatal reward activity. *bioRxiv* **2022**, 2022.09.16.508310.

14. Dunham, K. E.; Venton, B. J., Improving serotonin fast-scan cyclic voltammetry detection: New waveforms to reduce electrode fouling. *Analyst* **2020,** *145* (22), 7437-7446.

15. Bang, D.; Kishida, K. T.; Lohrenz, T.; White, J. P.; Laxton, A. W.; Tatter, S. B.; Fleming, S. M.; Montague, P. R., Sub-second dopamine and serotonin signaling in human striatum during perceptual decision-making. *Neuron* **2020,** *108* (5), 999-1010.e6.

16. Oh, Y.; Heien, M. L.; Park, C.; Kang, Y. M.; Kim, J.; Boschen, S. L.; Shin, H.; Cho, H. U.; Blaha, C. D.; Bennet, K. E.; Lee, H. K.; Jung, S. J.; Kim, I. Y.; Lee, K. H.; Jang, D. P., Tracking tonic dopamine levels in vivo using multiple cyclic square wave voltammetry. *Biosens Bioelectron* **2018,** *121*, 174-182.

17. Shin, H.; Goyal, A.; Barnett, J. H.; Rusheen, A. E.; Yuen, J.; Jha, R.; Hwang, S. M.; Kang, Y.; Park, C.; Cho, H.-U.; Blaha, C. D.; Bennet, K. E.; Oh, Y.; Heien, M. L.; Jang, D. P.; Lee, K. H., Tonic serotonin measurements in vivo using n-shaped multiple cyclic square wave voltammetry. *Analytical Chemistry* **2021,** *93* (51), 16987-16994.

18. Park, C.; Oh, Y.; Shin, H.; Kim, J.; Kang, Y.; Sim, J.; Cho, H. U.; Lee, H. K.; Jung, S. J.; Blaha, C. D.; Bennet, K. E.; Heien, M. L.; Lee, K. H.; Kim, I. Y.; Jang, D. P., Fast cyclic square-wave voltammetry to enhance neurotransmitter selectivity and sensitivity. *Anal Chem* **2018,** *90* (22), 13348-13355.

19. Shin, H.; Oh, Y.; Park, C.; Kang, Y.; Cho, H. U.; Blaha, C. D.; Bennet, K. E.; Heien, M. L.; Kim, I. Y.; Lee, K. H.; Jang, D. P., Sensitive and selective measurement of serotonin in vivo using fast cyclic square-wave voltammetry. *Analytical Chemistry* **2020,** *92* (1), 774-781.

20. Andrews, A. M., The brain initiative: Toward a chemical connectome. *ACS Chemical Neuroscience* **2013,** *4* (5), 645-645.

21. Movassaghi, C. S.; Perrotta, K. A.; Yang, H.; Iyer, R.; Cheng, X.; Dagher, M.; Fillol, M. A.; Andrews, A. M., Simultaneous serotonin and dopamine monitoring across timescales by rapid pulse voltammetry with partial least squares regression. *Analytical and Bioanalytical Chemistry* **2021,** *413* (27), 6747-6767.

22. Eltahir, A. M.; White, J.; Lohrenz, T. M.; Montague, R., Low amplitude burst detection of catecholamines. *bioRxiv* **2021**.

23. Montague, P. R.; Lohrenz, T.; White, J.; Moran, R. J.; Kishida, K. T., Random burst sensing of neurotransmitters. *bioRxiv* **2019**, 607077.

24. Ross, A. E.; Venton, B. J., Sawhorse waveform voltammetry for selective detection of adenosine, atp, and hydrogen peroxide. *Anal Chem* **2014,** *86* (15), 7486-7493.

25. Wrona, M. Z.; Dryhurst, G., Oxidation chemistry of 5-hydroxytryptamine. 1. Mechanism and products formed at micromolar concentrations. *The Journal of Organic Chemistry* **1987,** *52* (13), 2817-2825.

26. Wrona, M. Z.; Dryhurst, G., Further insights into the oxidation chemistry of 5-hydroxytryptamine. *Journal of Pharmaceutical Sciences* **1988,** *77* (11), 911-917.

27. Wrona, M. Z.; Dryhurst, G., Oxidation chemistry of 5-hydroxytryptamine: Part ii. Mechanisms and products formed at millimolar concentrations in acidic aqueous solution. *Journal of Electroanalytical Chemistry and Interfacial Electrochemistry* **1990,** *278* (1), 249-267.
28. Wrona, M. Z.; Dryhurst, G., Electrochemical oxidation of 5-hydroxytryptamine in aqueous solution at physiological ph. *Bioorganic Chemistry* **1990,** *18* (3), 291-317.

29. Breijo, E. G.; Pinatti, C. O.; Peris, R. M.; Fillol, M. A.; Martínez-Máñez, R.; Camino, J. S., Tnt detection using a voltammetric electronic tongue based on neural networks. *Sensors and Actuators A: Physical* **2013,** *192*, 1-8.

30. Carbó, N.; López Carrero, J.; Garcia-Castillo, F. J.; Tormos, I.; Olivas, E.; Folch, E.; Alcañiz Fillol, M.; Soto, J.; Martínez-Máñez, R.; Martínez-Bisbal, M. C., Quantitative determination of spring water quality parameters via electronic tongue. *Sensors* **2018,** *18* (1), 40.

31. Greenhill, S.; Rana, S.; Gupta, S.; Vellanki, P.; Venkatesh, S., Bayesian optimization for adaptive experimental design: A review. *IEEE Access* **2020,** *8*, 13937-13948.

32. Frazier, P. I., A tutorial on bayesian optimization. *arXiv* **2018.**

33. Brochu, E.; Cora, V. M.; Freitas, N. d., A tutorial on bayesian optimization of expensive cost functions, with application to active user modeling and hierarchical reinforcement learning. *ArXiv* **2010,** *abs/1012.2599.*

34. Klein, A.; Falkner, S.; Bartels, S.; Hennig, P.; Hutter, F., Fast bayesian optimization of machine learning hyperparameters on large datasets. In *Proceedings of the 20th International Conference on Artificial Intelligence and Statistics*, Aarti, S.; Jerry, Z., Eds. PMLR: Proceedings of Machine Learning Research, 2017; Vol. 54, pp 528-536.

35. Calandra, R.; Seyfarth, A.; Peters, J.; Deisenroth, M. P., Bayesian optimization for learning gaits under uncertainty. *Ann Math Artif Intell* **2016,** *76* (1), 5-23.

36. Garnett, R.; Osborne, M. A.; Roberts, S. J., Bayesian optimization for sensor set selection. In *Proceedings of the 9th ACM/IEEE International Conference on Information Processing in Sensor Networks*, Association for Computing Machinery: Stockholm, Sweden, 2010; pp 209–219.

37. Wahl, C. B.; Aykol, M.; Swisher, J. H.; Montoya, J. H.; Suram, S. K.; Mirkin, C. A., Machine learning-accelerated design and synthesis of polyelemental heterostructures. *Sci Adv* **2021,** *7* (52), eabj5505.

38. Liang, Q.; Gongora, A. E.; Ren, Z.; Tiihonen, A.; Liu, Z.; Sun, S.; Deneault, J. R.; Bash, D.; Mekki-Berrada, F.; Khan, S. A.; Hippalgaonkar, K.; Maruyama, B.; Brown, K. A.; Fisher Iii, J.; Buonassisi, T., Benchmarking the performance of bayesian optimization across multiple experimental materials science domains. *Npj Comput Mater* **2021,** *7* (1), 188.

39. Shields, B. J.; Stevens, J.; Li, J.; Parasram, M.; Damani, F.; Alvarado, J. I. M.; Janey, J. M.; Adams, R. P.; Doyle, A. G., Bayesian reaction optimization as a tool for chemical synthesis. *Nature* **2021,** *590* (7844), 89-96.

40. Griffiths, R.-R.; Hernández-Lobato, J. M., Constrained bayesian optimization for automatic chemical design using variational autoencoders. *Chem Sci* **2020,** *11* (2), 577-586.

41. Díaz-Cruz, J. M.; Esteban, M.; Ariño, C., *Chemometrics in electroanalysis*. 1 ed.; Springer: Cham, Switzerland, 2019; p 202.

42. Shahriari, B.; Swersky, K.; Wang, Z.; Adams, R. P.; Freitas, N. d., Taking the human out of the loop: A review of bayesian optimization. *Proc IEEE* **2016,** *104* (1), 148-175.

43. Häse, F.; Roch, L. M.; Kreisbeck, C.; Aspuru-Guzik, A., Phoenics: A bayesian optimizer for chemistry. *ACS Cent Sci* **2018,** *4* (9), 1134-1145.

44. Wang, Y.; Chen, T.-Y.; Vlachos, D. G., Nextorch: A design and bayesian optimization toolkit for chemical sciences and engineering. *J Chem Inf Model* **2021,** *61* (11), 5312-5319.

45. Gundry, L.; Guo, S.-X.; Kennedy, G.; Keith, J.; Robinson, M.; Gavaghan, D.; Bond, A. M.; Zhang, J., Recent advances and future perspectives for automated parameterisation, bayesian inference and machine learning in voltammetry. *Chem Comm* **2021,** *57* (15), 1855-1870.

46. Bond, A. M., A perceived paucity of quantitative studies in the modern era of voltammetry: Prospects for parameterisation of complex reactions in bayesian and machine learning frameworks. *J Solid State Electrochem* **2020,** *24* (9), 2041-2050.

47. Puthongkham, P.; Wirojsaengthong, S.; Suea-Ngam, A., Machine learning and chemometrics for electrochemical sensors: Moving forward to the future of analytical chemistry. *Analyst* **2021,** *146* (21), 6351-6364.

48. Fenton Jr, A. M.; Brushett, F. R., Using voltammetry augmented with physics-based modeling and bayesian hypothesis testing to identify analytes in electrolyte solutions. *J Electroanal Chem* **2022,** *904*, 115751.

49. Mitchell, E. C.; Dunaway, L. E.; McCarty, G. S.; Sombers, L. A., Spectroelectrochemical characterization of the dynamic carbon-fiber surface in response to electrochemical conditioning. *Langmuir* **2017,** *33* (32), 7838-7846.

50. Vreeland, R. F.; Atcherley, C. W.; Russell, W. S.; Xie, J. Y.; Lu, D.; Laude, N. D.; Porreca, F.; Heien, M. L., Biocompatible pedot:Nafion composite electrode coatings for selective detection of neurotransmitters in vivo. *Anal Chem* **2015,** *87* (5), 2600-2607.

51. Hibbert, D. B., Experimental design in chromatography: A tutorial review. *J Chromatogr B* **2012,** *910*, 2-13.

52. Https://scikit-optimize.Github.Io/stable/index.Html.

53. Pedregosa, F.; Varoquaux, G.; Gramfort, A.; Michel, V.; Thirion, B.; Grisel, O.; Blondel, M.; Prettenhofer, P.; Weiss, R.; Dubourg, V., Scikit-learn: Machine learning in python. *J Mach Learn Res* **2011,** *12*, 2825-2830.

CHAPTER IV

Optogenetic Stimulation of Midbrain Dopamine Neurons Produces Striatal Serotonin Release

The information in this chapter is reproduced with permission from ACS Chemical Neuroscience, Copyright 2022.

Optogenetic Stimulation of Midbrain Dopamine Neurons Produces Striatal Serotonin Release. Merel Dagher*, Katie A. Perrotta*, Sara A. Erwin, Ayaka Hachisuka, Rahul Iyer, Sotiris C. Masmanidis, Hongyan Yang, and Anne M. Andrews. *ACS Chemical Neuroscience* 2022 *13* (7), 946-958.DOI: 10.1021/acschemneuro.1c00715.

*Co-first author

Introduction

Optogenetics entails expressing light-driven ionotropic receptors in neurons or other excitable cells to enable spatially and temporally restricted activation or inhibition.[139-142] Gene constructs for microbial or engineered rhodopsins packaged in viruses are used to transduce brain-region-specific gene expression following local delivery. Gene expression can be further targeted using Cre recombinase under the control of cell-type-specific promotors, in combination with Cre-activated opsin constructs.[143] Opsins produce excitatory (*e.g.,* channelrhodopsin-2, Chrimson) or inhibitory (*e.g.,* halorhodopsin, archaerhodopsin) effects on neural activity.[144-146] The discovery and use of opsins have enabled the identification of neural pathways involved in the modulation of behavior.[13, 147-149]

Opsin-targeted cell types, however, do not operate autonomously. Dopamine and serotonin are examples of functionally interconnected neurotransmitter systems. For instance, while dopamine signaling is often associated with reward prediction error, serotonin transmission also plays a role in processing reward-associated information.[150-152] Moreover, while widely used therapeutics for mood disorders target the serotonin system,[153] the dopamine system encodes information associated with anhedonia, a core symptom of major depressive disorder.[5, 18, 151, 154-157] Interactions between the dopamine and serotonin systems are evident in drug mechanisms of action, *e.g.,* cocaine, methamphetamine, and 3,4-methylenedioxymethamphetamine.[158-161] Thus, these systems act in concert to modulate subjective states.[29, 162]

Microdialysis is a tissue sampling technique. When combined with chemical separation and detection methods, microdialysis enables the identification and quantification of neurotransmitters, metabolites, and drugs in the extracellular space.[163] Several groups, including ours, have optimized microdialysis to monitor brain extracellular dopamine or serotonin levels *via* online coupling with fast separations by high performance liquid chromatography (HPLC) and electrochemical detection in awake mice and rats.[83, 94, 95, 119, 164-166] Dopamine and serotonin can be resolved in the same dialysate samples enabling biologically relevant changes in basal and stimulated levels of these neurotransmitters to be simultaneously monitored.[95, 167]

Here, we set out to determine the magnitude of extracellular dopamine release in the dorsal striatum (dSTR) upon optogenetic stimulation of midbrain dopaminergic neurons. The excitatory opsin Chrimson was expressed under the control of the dopamine transporter promoter in mice. Optical activation of dopamine neurons has been used to study dopaminergic encoding of reward and movement.[13, 168] In addition to dopamine, we observed optically induced increases in the dopamine metabolite 3-methoxytyramine (3-MT) and in serotonin levels. These findings demonstrate a functional link between the dopamine and serotonin systems in the basal ganglia. They illustrate the importance of monitoring multiple neurotransmitters simultaneously. And they suggest that opsin-induced behavioral changes may not be attributable solely to the neurotransmitter system or cell type targeted by opsin expression. That is to say, while optogenetics imparts highly selective control of specific types of neurons, brain function and behavior arise from distributed and interconnected networks.

Materials and Methods

Animal Procedures

Mice were generated at the University of California, Los Angeles (UCLA) from a DAT$^{\mathrm{IRES}cre}$ line (The Jackson Laboratory, stock no. 006660) on a C57Bl/6J background *via* heterozygous matings. Mice were housed in groups of 2-5 same-sex siblings prior to surgery, same-sex-sibling pairs after the first surgery to deliver viral vectors and to implant optical fibers and head bars, and singly after the second surgery to implant a microdialysis guide cannula. Food and water were available *ad libitum* throughout, with the exception of microdialysis testing days where mice were hand-fed a 2:1 sweetened condensed milk:water solution *via* pipette every 2 h.

The light-dark cycle (12/12 h) in the animal colony room was set to lights on at 0730 h (ZT0). The same light schedule was maintained in the room where microdialysis was performed. The Association for Assessment and Accreditation of Laboratory Animal Care International has fully accredited UCLA. All animal care and use met the requirements of the NIH Guide for the Care and Use of Laboratory Animals, 2011. The UCLA Chancellor's Animal Research Committee (Institutional Animal Care and Use Committee) preapproved all animal procedures.

Surgeries were carried out under aseptic conditions with isoflurane anesthesia on a KOPF Model 1900 Stereotaxic Alignment System (KOPF, Tujunga, CA). A pair of rectangular stainless steel head-bars (9 mm × 7 mm × 0.76 mm, 0.6 g each, Fab2Order, Brownsburg, IN) were attached to the sides of the skull by C&B Metabond (Parkell, Edgewood, NY) for head fixation (**Fig. IV.S1A,B**). Viral vectors, 600 nL of 7.8×10^{12}/mL AAV5/Syn-Flex-ChrimsonR-tdTomato (for experimental groups) or 4.4×10^{12}/mL AAV5/EF1a-DIO-eYFP or 3.3×10^{12}/mL AAV5/EF1a-DIO-mcherry (for control subjects), were delivered unilaterally into the SN/VTA

(AP-3.08 mm, ML ±1.20 mm, DV -4.00 mm from Bregma) using a Nanoject II (Drummond Scientific, Broomall, PA). A 200 µm diameter optical fiber (0.22 NA, Thorlabs, Newton, NJ) with a total length of 1 cm was lowered *via* the same track to reach the AAV injection site for optogenetic stimulation. Optical fibers were secured on the skull with C&B Metabond. The top of each optical fiber outside the skull was covered by a sleeve until coupling to a laser device for testing. All AAV Cre-dependent adeno-associated viral vectors were obtained from the University of North Carolina Vector Core (Chapel Hill, NC).

After the first surgery, animals recovered for 2-3 weeks (**Fig. IV.1B**) to allow for viral vector expression prior to guide cannula implantation for microdialysis. During recovery, subjects were acclimated to being head-fixed over the course of 6-10 training sessions, each lasting 15-30 min. A second surgery was carried out on each mouse to implant a CMA/7 guide cannula for a microdialysis probe aimed at the dSTR (AP+1.00 mm, ML±1.75 mm, DV-3.10 mm from Bregma) in the same hemisphere as the viral delivery and fiber implant site. Each guide cannula was secured to the skull with C&B Metabond. Animals recovered from the second surgery for at least three days before microdialysis. Following each surgery, mice were given daily carprofen injections (5 mg/kg, 1 mg/mL, subcutaneously) for the first three days and a combination of an antibiotic (amoxicillin, 0.25 mg/mL) and a second analgesic (ibuprofen, 0.25 mg/mL) in their drinking water for 14 days postoperatively.

Microdialysis

Virgin female mice (*N*=23) underwent microdialysis at 3-6 months of age. Microdialysis was carried out over two consecutive days for Chrimson-transfected mice (*N*=14) and one day for control mice (*N*=9). On the night before the first testing day (ZT10-12), each mouse was transferred to the testing room in its home cage and briefly anesthetized with isoflurane (1-3 min) for insertion of a CMA/7 microdialysis probe (1 mm length, 6 kDa cutoff, CMA8010771) into the guide cannula. Subjects were returned to their home cages and aCSF was continuously perfused through the probe *via* a liquid swivel (375/D/22QM, Instech Laboratories Inc., Plymouth Meeting, PA) at 2-3 µL/min for 30-60 min followed by a 0.3 µL/min flow rate for an additional 12-14 h to allow the tissue surrounding the probe to recover from acute changes associated with probe insertion. Subjects were tethered to the liquid swivel but otherwise could move freely in their home cages.

Prior to microdialysis, the tubing connecting the microdialysis probe to the liquid swivel was disconnected. The mouse was transferred from its home cage and mounted to the head-fixed stage *via* its head-bars in the same testing room. The microdialysis probe was connected between the microdialysis syringe pump and the online autoinjector. The aCSF was perfused at 1.8 uL/min throughout each testing day, and samples were collected at 5-min intervals. Subjects were habituated for at least 10-min before the optical fiber was coupled for stimulation delivery.

An MGL-III-532 or MGL-III-589 laser (Opto Engine LLC, Ltd, Changchun, P. R. China) was used to deliver light pulses. The excitation spectrum of Chrimson has a λ_{max} at 590 nm. Due to the broad excitation spectrum, either 532 nm (green) or 589 nm (yellow) light were used to excite this opsin.[145] The output of the optical fiber was calibrated to deliver 10 mW/mm^2 immediately before coupling on each testing day.

The stimulation pulse width (50 ms), frequency (10 Hz), and train duration (5 min) were selected to generate neurotransmitter release detectable by microdialysis using a 5-min dialysate sampling time. In preliminary experiments, we investigated stimulation pulse widths that varied from 5-2500 ms. We also investigated laser powers ranging from 5-20 mW/mm^2. Longer pulse widths were ultimately favored over higher laser power with shorter pulses to avoid tissue damage over longer stimulation times needed for microdialysis. There were no significant differences in stimulation output for frequencies over 10-30 Hz using 50% duty cycle and a 5-min train duration. A longer train duration was used previously by Correia *et al.* to investigate the role of serotonin transmission in locomotion.[169]

The first stimulation was delivered at ~ZT2 after 6-18 basal dialysate samples were collected and analyzed. Prior to reverse dialysis of drugs, three optical stimulations were delivered at 1-h intervals (**Fig. IV.1B**). After 90-120 min of intrastriatal drug perfusion, an additional three optical stimulations were delivered at 1-h intervals while drug perfusion continued. On day 1, four Chrimson-transfected mice were perfused with the D1-like antagonist SCH-23390 (100 µM) through the dialysis probe. On day 2, the same four Chrimson-transfected mice were perfused with 100 µM eticlopride (D2-like antagonist).

Eleven mice not receiving D1- or D2-like antagonists underwent brief (5 min) perfusion with 120 mM K^+ (KCl substituted isotonically for NaCl in aCSF) to stimulate neurochemical overflow[94, 95, 106] for peak identification. In **Fig. IV.S2,** data from a representative K^+-stimulated mouse are shown. Three Chrimson-transfected mice were perfused with an SSRI (10 µM escitalopram) on day one to confirm serotonin peak identity (**Fig. IV.3A, B**). Four mice (three control and one Chrimson-transfected) were administered the COMT inhibitor tolcopone (10 mg/kg, intraperitoneal) to identify the 3-MT peak (**Fig. IV.2C**).

Dialysate Analysis

High performance liquid chromatography was performed using an Amuza HTEC-500 integrated system (Amuza Corporation [formally known as Eicom], San Diego, CA). An Eicom Insight autosampler was used to inject standards and Eicom EAS-20s online autoinjectors were used to collect and inject dialysate samples online.[83] Chromatographic separation was achieved using an Eicom PP-ODS II column (4.6 mm ID x 30 mm length, 2 µm particle diameter) and a phosphate-buffered mobile phase (96 mM NaH_2PO_4 (Fluka #17844), 3.8 mM Na_2HPO_4 (Fluka #71633), pH 5.4, 2-2.8% MeOH (EMD #MX0475), 50 mg/L EDTA·Na_2 (Sigma #03682), and 500 mg/L sodium decanesulfonate (TCI #I0348) in water purified *via* a Milli-Q Synthesis A10 system (EMD Millipore Corporation, Billerica, MA). The column temperature was maintained at 21 °C. The volumetric flow rate was 450-500 µL/min. Electrochemical detection was performed using an Eicom WE-3G graphite working electrode with an applied potential of +450 mV *vs.* a Ag/AgCl reference electrode.

Dopamine (Sigma #H8502), 3-MT (Sigma #65390), and serotonin (Sigma #H9523) standards were prepared in ice-cold 1:1 mobile phase/aCSF (147 mM NaCl (Fluka #73575), 3.5 mM KCl (Fluka #05257), 1.0 mM $CaCl_2$ (Aldrich #499609), 1.0 mM NaH_2PO_4, 2.5 mM $NaHCO_3$ (Fluka #88208), 1.2 mM $MgCl_2$ (Aldrich #449172), pH 7.3 ± 0.03. (See supplemental information in Liu et al., 2020 for detailed information on formulating aCSF).[170] Standard curves encompassed physiological concentration ranges (0-10 nM; **Fig. IV.S5**). The limit of detection was ≤300 amol (6 pM) for each analyte; the practical limit of quantification was ≤900 amol (18 pM). Dialysate samples were collected online at 5-min intervals using a dialysate flow rate of 1.8 µL/min and injected immediately onto the HPLC system for analysis.

In situ Hybridization

We used RNAscope® technology (Advanced Cell Diagnostics Inc., Newark, CA) for *in situ* hybridization to colocalize mRNAs for D1 receptors in dorsal raphe neurons expressing SERT, VGLUT3, or both.[1, 2, 171, 172] A DAT$^{\mathrm{IRES}cre}$ mouse not transfected with Chrimson was sacrificed by cervical dislocation without isoflurane and the brain was removed, cryoprotected, and frozen. Coronal sections were cut at 16-µm on a cryostat at -15-20 °C and mounted on polylysine-coated slides.

In situ hybridization was conducted using the RNAscope® fresh-frozen V2 protocol. Briefly, sections were incubated in freshly prepared 4% paraformaldehyde (Sigma-Aldrich Cat#441244) in phosphate buffered saline for 15 min followed by sequential dehydration in 50% EtOH, 70% EtOH, and 100% EtOH for 5 min each. Sections were then incubated with the necessary reagents from the Multiplex Fluorescent Reagent Kit V2 (ACD #323110) in a HybEZ® oven. Probes were as follows: *Sert* (Mm-Slc6a4 Cat#315851) channel 1, *Vglut3* (Mm-Slc32a1 Cat#319191-C2) channel 2, and *Drd1* (Mm-Drd1a-C3 Cat# 406491-C3) channel 3. Opal dyes 520, 570, and 690 were paired with each probe, respectively (Cat#FP1487A, FP1488A, FP1497A). ProLong™ Diamond Antifade Mountant with DAPI (Molecular Probes P36966) was added to stain cell bodies.

Visualization was carried out using a Leica DMI8 or Zeiss LSM800 microscope and images were processed with LAS X and Zen software. Cell nuclei in each field of view were identified *via* DAPI staining. The DAPI labeled nuclei associated with puncta for one or more mRNA probes were then counted. Data are reported as percent positive cells calculated by dividing the number of cells labeled with *Sert*, *Drd1*, and/or *Vglut3* by the total number of *Sert* labeled cells.

Histology

At the end of each experiment, the microdialysis probe was removed and the brain of each mouse was prepared for histology to verify probe and optical fiber placements, and Chrimson, mCherry, or eYFP expression. Subjects were exsanguinated with an overdose of 100 mg/kg pentobarbital (2 mL/kg administered at 50 mg/mL, ip) followed immediately by transcardial perfusion with 4% paraformaldehyde in PBS. Sections from the midbrain and dSTR were cut using a vibratome and mounted on microscope slides. Images were acquired using a Zeiss Axio Examiner microscope as follows: tdTomato and mCherry (550 nm excitation/605 nm emission), or eYFP (470 nm excitation/525 nm emission). Microdialysis probe and optical fiber tracks were visualized *via* light microscopy. Three of the 23 microdialysis subjects failed histology verification for probe or fiber placement. Data for these subjects were excluded from analyses.

Data Analysis and Statistics

The microdialysis time-course data were analyzed in terms of absolute neurochemical concentrations (nM) and as percents of mean pre-stimulation basal neurochemical levels (%basal). Overflow peaks following optical stimulation were identified and analyzed individually using the following criteria and procedures. (1) For each control mouse, the concentrations of six dialysate samples for each neurochemical immediately preceding the onset of the first optical stimulation were averaged (nM) and converted to mean 100% basal levels. (2) For Chrimson-expressing mice on experimental days 1 and 2, basal levels of individual neurochemicals were determined separately by day. The concentrations of the six dialysate samples immediately preceding the onset of the first pre-drug or post-drug optical stimulation were averaged (nM) and converted to mean 100% basal levels. (3) The AUC for each stimulation peak, defined by the four dialysate samples after the onset of stimulation, was calculated by trapezoidal integration and is reported in nM or as a percent of mean pre-stimulation basal levels.

Statistical analyses were carried out using Prism, v.9.0.2 (GraphPad Inc., La Jolla, CA). Data are expressed as group means ± SEMs. Two-tailed *t*-tests (either unpaired or ratio paired, as appropriate) were used for two-group comparisons. Throughout, $P<0.05$ was considered statistically significant. Detailed statistics are summarized in **Table IV.S1**.

Results and Discussion

Using microdialysis,[83, 94, 95] we quantified extracellular dopamine in a dopamine-rich projection region—the dSTR—during optical stimulation of midbrain dopamine cell bodies (**Fig. IV.1, Fig. IV.S1**). To induce dopamine release, we applied 50-ms square pulses at 10 Hz and 10 mW/mm^2 laser power. Stimulation pulse train durations were 5 minutes to match dialysate sampling times. These parameters were optimized to produce reproducible neurotransmitter release detectable *via* microdialysis. Activation of the excitatory opsin Chrimson[145] produced temporally specified increases in striatal extracellular dopamine levels (**Fig. IV.2A**). Control mice expressing mCherry or yellow fluorescent protein (YFP) in dopamine cell bodies showed no detectable changes in dopamine upon optical stimulation (**Fig. IV.2B**).

Basal (unstimulated) dialysate dopamine levels were not statistically different in Chrimson-expressing *vs.* control mice (**Fig. IV.2C**; see **Table IV.S1** for detailed statistics). Basal dopamine levels for control animals were normally distributed around the mean. In contrast, basal dopamine levels for Chrimson-expressing animals were not normally distributed. Individual dopamine concentrations fell mostly below the mean, apart from three animals, one of which was an outlier. Notably, this outlier is not the same animal that is an outlier for basal serotonin levels in Chrimson-transfected mice (**Fig. IV.4A** *vide infra*). As such, we chose to not to exclude outliers from analysis, although exclusion would have led to a statistically significant reduction in basal dopamine levels in Chrimson-transfected *vs.* control mice. Stimulated dopamine overflow, quantified as area under the curve (AUC), was greater in Chrimson-expressing *vs.* control mice (**Fig. IV.2D**; t_{18}=3.0, P<0.01). Dopamine levels were increased ~200 pM by optical stimulation.

In addition to dopamine, optical activation appeared to lead to increases in two other chromatographic peaks (**Fig. IV.S2**). We initially hypothesized that the larger peak (peak 2) was serotonin. However, since retention times commonly shift between standards and brain dialysate samples, we could not definitively identify peak 2 using serotonin-containing standards. We perfused a selective serotonin reuptake inhibitor (SSRI) through the dialysis membrane during intracerebral dialysis to investigate peak identity. Increases in peak areas in response to serotonin transporter inhibition identified a small, later eluting peak (peak 3) as serotonin (**Fig. IV.3A, B**; $t_2=5.7$, $P<0.05$).

Previous experience analyzing striatal tissue samples then led us to suspect that the remaining optically responsive peak was 3-methoxytyramine (3-MT). Dopamine is metabolized by catechol-*O*-methyltransferase (COMT) to produce 3-MT, which is hypothesized to function as a neuromodulator.[173, 174] We administered the COMT inhibitor tolcapone systemically[175] and found that peak 2 was selectively decreased (**Fig. IV.3C**; $t_3=9.6$, $P<0.01$). We also perfused 3-MT through the dialysis membrane into dSTR, *i.e.*, *in vivo* standard addition, and observed a retention time match confirming the identity of peak 2 as 3-MT and ruling out the possibility that this peak was serotonin (**Fig. IV.3D**).

Having identified two optically (*i.e.*, biologically) responsive neurochemicals, in addition to dopamine, we quantified their basal dialysate levels. We found no differences in basal 3-MT or serotonin levels in Chrimson-expressing *vs.* control mice (**Fig. IV.4A**). Optogenetic stimulation of midbrain dopaminergic neurons evoked reproducible increases in 3-MT and serotonin in Chrimson-expressing but not control mice (**Fig. IV.4B,C**; $t_{18}=3.1$, $P<0.01$, $t_{15}=4.4$, $P<0.001$, respectively). Since basal neurochemical levels varied across individual mice (**Fig. IV.2C, 4A**), we also analyzed optically stimulated neurochemical levels normalized to mean pre-stimulation basal levels (**Fig. IV.S3**). Concentration and %basal analyses similarly indicated that in addition to dopamine, 3-MT and serotonin overflow were increased in response to optogenetic stimulation of Chrimson-transfected dopamine neurons.

Optical stimulation of control mice lacking opsin expression showed no nonspecific increases in neurochemicals associated with light-induced arousal.

We parsimoniously hypothesized that the increased overflow of serotonin associated with optical stimulation of dopamine neurons was mediated by activation of dopamine receptors on serotonin terminals in striatum. The mRNAs for DRD2 and DRD3 receptors (*i.e.*, D2-like) were previously identified in dorsal raphe.[176, 177] Ren *et al.*[171] and Spaethling *et al.*[178] used single-cell transcriptomics to localize *Drd2* transcripts to serotonergic neurons. Using RNAseq, Dymecki and colleagues identified *Drd2* mRNA in dorsal raphe serotonin neurons specified by *Pet1* expression.[179]

A small number of DRN serotonin neurons has also been reported to contain *Drd1a* mRNA.[171, 179] We carried out *in situ* hybridization to investigate colocalization of D1 receptor (*Drd1*) and serotonin transporter (*Sert*) mRNAs in the dorsal raphe nucleus (**Fig. IV.5A,B**). We included a probe for the vesicular glutamate transporter type 3 (VGLUT3) because a subpopulation of serotonergic neurons co-expresses VGLUT3[180] and projects to the striatum.[12, 180] We found that ~25% of total *Sert*-positive cells in the dorsal raphe were positive for *Sert* mRNA alone (**Fig. IV.5C**). Approximately 10% of total *Sert*-positive cells showed colocalization of *Sert* and *Drd1* mRNA, while an additional 35% of *Sert*-positive cells showed *Drd1* and *Vglut3* mRNA colocalization. Positive and negative *in situ* hybridization controls are shown in Figure SIV.4.

Since our data suggested that almost half of dorsal raphe serotonin neurons may express heterologous D1 receptors, we investigated whether blocking striatal D1-like receptors prevents optically stimulated serotonin overflow. We perfused SCH 23390, a D1-like receptor antagonist, into the dSTR. Basal dopamine (t_3=4.4, P<0.05) and serotonin (t_3=3.5, P<0.05) levels were increased by local D1-like receptor inhibition (**Fig. IV.6A,B**). Stimulated dopamine (t_3=6.2, P<0.01), 3-MT (t_3=4.8, P<0.05), and serotonin (t_3=4.5, P<0.05) levels were also increased by local perfusion of SCH 23390 (**Fig. IV.6B,C**). Elevations in striatal dopamine levels in response to SCH-23390 have been previously reported.[181] In addition to serotonin neurons, medium spiny neurons (MSNs) in striatum express D1 receptors. Blocking D1-receptors on MSNs disinhibits dopamine neurons causing an increase in dopamine levels.[182, 183]

To focus on optically stimulated neurochemical levels, we normalized the SCH 23390 time-course data. Data prior to drug perfusion were normalized to pre-drug/pre-stimulation basal neurochemical levels determined in each mouse (**Fig. IV.7A**). Data collected during drug perfusion were normalized to post-drug/pre-simulation basal neurochemical levels. When normalized to the respective basal levels, elevation of stimulated 3-MT (t_3=3.7; P<0.05) remained (**Fig. IV.7A,B**). In contrast, potentiation of optically stimulated dopamine and serotonin levels were no longer evident during striatal SCH 23390 perfusion (**Fig. IV.7A,B**). Thus, increases in the stimulated AUC for serotonin calculated using dialysate concentrations (**Fig. IV.6C**) was largely the result of SCH 29930-induced increases in basal dialysate concentrations.

The D1-like receptor inhibitory increase in basal serotonin levels (**Fig. IV.6A**) can be explained by a circuit connecting dSTR to the DRN.[1] Approximately, 95% of projections from the dSTR to the DRN are D1-expressing MSNs,[1] which tonically inhibit DRN (and presumably serotoninergic) neurons. Blocking D1-like receptors on MSNs dendritic spines[184] could reduce tonic inhibition of DRN cell populations leading to increased serotonin levels in the dSTR. Regardless, local inhibition of D1 heteroreceptors on serotonin terminals and/or MSNs did not *prevent* optically evoked striatal serotonin.

Mice that received the D1-like inhibitor on day 1 of microdialysis were perfused with eticlopride (ETC), a D2-like receptor antagonist, on day 2 (**Fig. IV.1A**). Inhibition of D2-like receptors, which are expressed as dopaminergic heteroreceptors and autoreceptors in striatum,[185] was not associated with changes in basal levels of dopamine, 3-MT, or serotonin (**Fig. IV.8A**). Though not statistically significant due to small sample sizes, eticlopride perfusion into the dSTR potentiated optically evoked dopamine and 3-MT analyzed either as basal (nM) concentrations (**Fig. IV.8B,C**) or %basal levels normalized to pre-stimulation basal (**Fig. IV.9A,B**). Previous studies have shown that extracellular dopamine is increased upon inhibition of presynaptic D_2 receptors.[186, 187] Importantly, in the context of our current hypothesis, and similar to striatal D1-like receptor inhibition, D2-like inhibition did *not* block serotonin overflow associated with optically evoked dopamine release.

Functional interactions between the dopamine and serotonin systems have been investigated for more than 50 years.[188-190] In prefrontal cortex, dopamine receptor activation by the nonselective agonist apomorphine, local dopamine perfusion, or D2 autoreceptor inhibition by haloperidol each produced increases in serotonin levels in rats.[191] Systemic administration of apomorphine was also shown to increase extracellular serotonin in striatum and hippocampus.[192] Our findings indicate that optogenetic activation of midbrain dopamine neurons expressing the excitatory opsin Chrimson produces temporally specified increases in striatal serotonin, as well as an active dopamine metabolite, 3-MT.

We tested hypotheses linking striatal dopamine and serotonin based on the idea that these neurotransmitters are released from different terminals in striatum. We found that serotonin overflow was not prevented by inhibition of striatal D1-like or D2-like receptors (**Figs. IV.6-9**). Our findings suggest that optically evoked dopamine does not produce serotonin release by stimulating dopamine receptors on striatal serotonin terminals (or direct/indirect pathway MSNs).

Our findings contrast with those of Jacobs and coworkers where apomorphine-induced or behaviorally evoked increases in striatal extracellular serotonin were inhibited by systemic and intrastriatal D2-like receptor inhibition.[192, 193] Differences in species (rats *vs.*

mice), drug (raclopride *vs.* eticlopride) and/or perfusion concentration (10 uM *vs.* 100 uM) might account for the discrepancies between studies. Jacobs and colleagues did not report on striatal dopamine levels in their studies, *i.e.*, apomorphine and the tail-pinch and light-dark-transition behaviors may have direct receptor/serotonin system effects that are different from those mediated by evoked dopamine.[194] Artigas and colleagues reported that reverse dialysis of D1-like or D2-like agonists into striatum in rats did not alter serotonin levels supporting the idea that dopamine-serotonin interactions are not mediated by striatal dopamine receptors.[167]

Another possibility is that serotonin is released from dopaminergic terminals *via* co-transmission or co-release. Co-transmission involves release of different neurotransmitters from different vesicle populations within the same neurons; co-release entails release of two or more neurotransmitters from the same vesicles.[195] Anatomical, genetic, and functional evidence shows that neurons can have mixed neurochemical phenotypes (for review see[195-198] among others) and argues specifically for a serotonin/glutamate mixed phenotype.[12, 180]

Regarding serotonin/dopamine interactions, under conditions where serotonin transporters are genetically or pharmacologically inactivated, serotonin appears to be taken up by dopamine transporters into dopamine neurons, indicated by double serotonin/tyrosine hydroxylase immunoreactivity in the substantia nigra pars compacta and ventral tegmental area.[199] Thus, SSRI treatment may result in serotonin being used as a 'false' transmitter by dopamine neurons. Studies on chronic SSRI administration using *in vivo* neurochemical monitoring are needed to test this hypothesis further. In any case, mice with wildtype serotonin transporter expression did not show serotonin colocalization in midbrain dopamine neurons suggesting that under typical circumstances, such as those investigated here, evidence is lacking for serotonin co-transmission or co-release by dopaminergic neurons.[199]

Beyond striatum, a dopaminergic pathway connects the substantia nigra to the dorsal raphe, which contains a majority of forebrain-projecting serotonin cell bodies (**Fig. IV.10**). Mesostriatal serotonergic afferents project from the dorsal raphe to the striatum.[2] In addition to striatum, optical activation of dopamine neurons could increase extracellular dopamine in the vicinity of midbrain dopamine cell bodies. Substantia nigra dopamine neurons exhibit activity-dependent somatodendritic dopamine release and D2-mediated autoinhibition.[3, 200-202] Activation of nigral D2 autoreceptors might increase extracellular serotonin in the dorsal raphe *via* disinhibition.[203] Furthermore, optical stimulation of dopamine cell bodies could activate dopamine projections to the dorsal raphe (**Fig. IV.10**). Both scenarios produce dopamine interactions with dorsal raphe serotonin neurons and ostensibly, could increase release of serotonin in striatum (and other brain regions).

Alternately, indirect mechanisms involving SNr-thalamus-cortex-dSTR and/or SNr-thalamus-cortex-DRN pathways cannot be ruled out.[204-207] Moreover, recent reports describe the presence of dopamine neurons in the rostral dorsal raphe nucleus.[208, 209] Future experiments to parse out specific contributions from dopamine neurons in the SNr, SNc, VTA and DRN to dopamine-induced serotonin release will be informative. It is also possible that optical stimulation of dopamine neurons in Chrimson-transfected mice, in addition to releasing dopamine, is interoceptively detected by mice.[210] The perception, increased arousal, and/or reward associated with dopaminergic activity could lead to increases in extracellular serotonin by complex mechanisms not involving direct connections between the dopamine and serotonin systems.

Regardless of mechanism, the present findings indicate that optogenetic stimulation of midbrain dopamine neurons evokes striatal serotonin release. We recently reported similar findings elucidated by rapid-pulse voltammetry.[211] Dopamine-serotonin coupling is likely to be of importance to the facilitation of reward prediction, locomotor control, habit formation, and anhedonia.

Figures

Figure IV.1

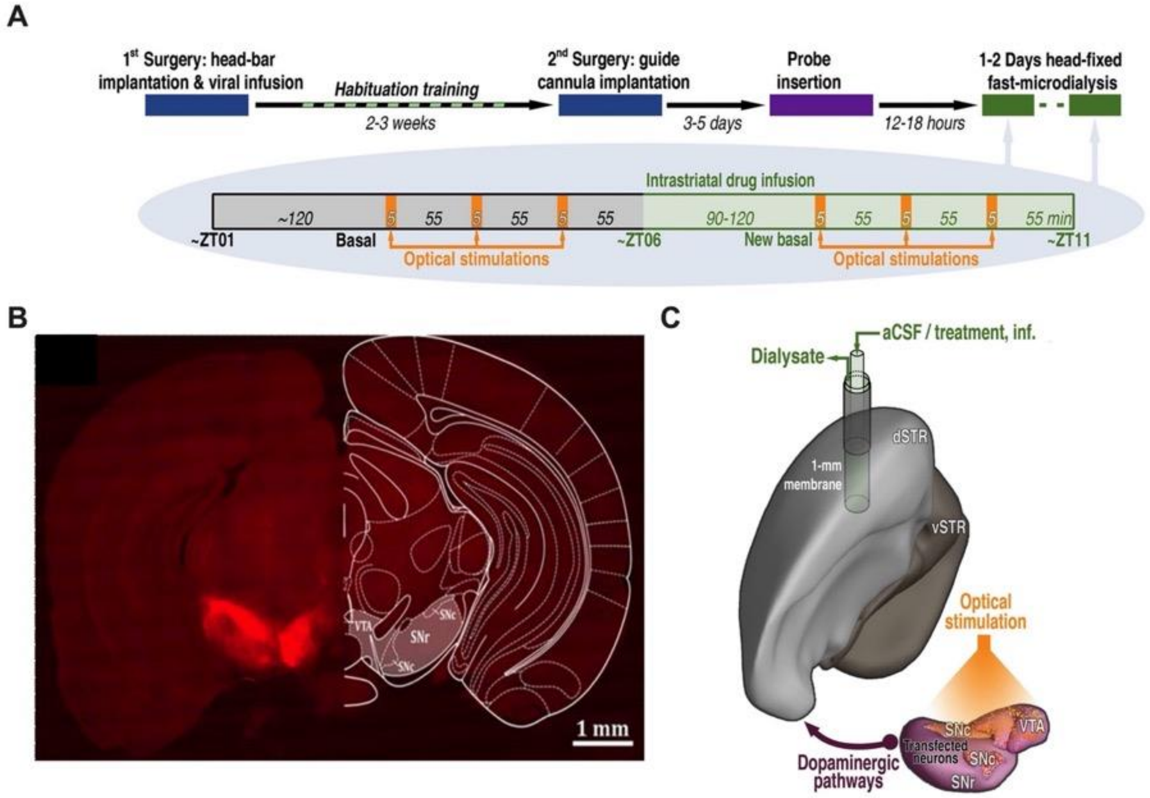

Figure IV.1: Optogenetic stimulation of dopamine cell bodies. A. Experimental paradigm and timelines. Chrimson-expressing mice underwent microdialysis over two consecutive days. Control mice (transfected with mCherry or eYFP) were dialyzed only on Day 1. **B.** Representative optical microscopy image of unilateral Chrimson-positive neurons in the substantia nigra and ventral tegmental area. The coronal brain atlas plate 58, adapted from *The Mouse Brain in Stereotaxic Coordinates,* Paxinos and Franklin, *2nd edition (2001) Academic Press*, is overlaid on the hemisphere contralateral to transfection. Ventral tegmental area (VTA), substantia nigra pars compacta (SNc), and substantia nigra pars reticulata (SNr) **C.** Model showing the location of the microdialysis probe in the dorsal striatum (dSTR) relative to Chrimson transfection and optical stimulation in the ipsilateral VTA, SNc, and SNr. Ventral striatum (vSTR), artificial cerebrospinal fluid (aCSF).

Figure IV.2

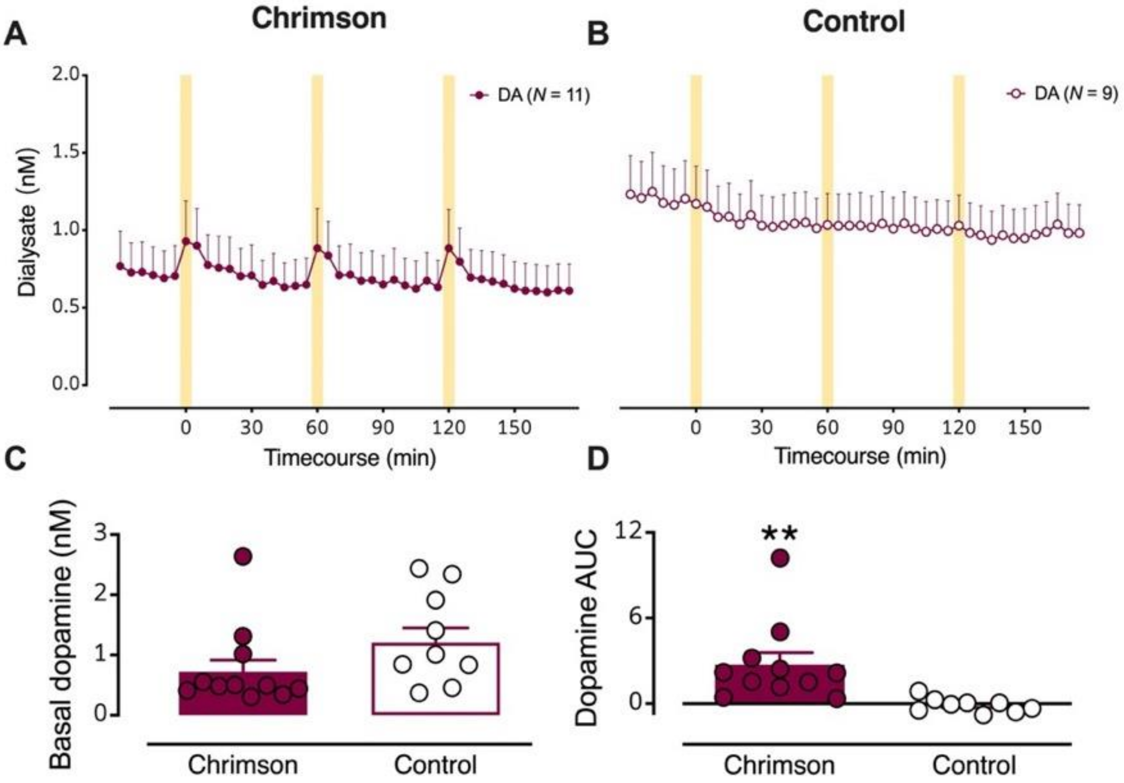

Figure IV.2: Optical stimulation of dopaminergic cell bodies produces dopamine release in striatal terminal regions. **A.** Dialysate dopamine levels were increased in response to optical stimulation in mice expressing Chrimson (*N*=11) **B.** but not in control mice (*N*=9). The yellow bars indicate optical stimulations (10 mw/mm^2, 50 ms pulse width @ 10 Hz for 5 min). **C.** Basal dopamine levels in mice transfected with Chrimson relative to control mice. **D.** Dopamine overflow, quantified by area under the curve, was increased in Chrimson expressing but not control mice. Data are means ± SEMs. **$P<0.01$.

Figure IV.3

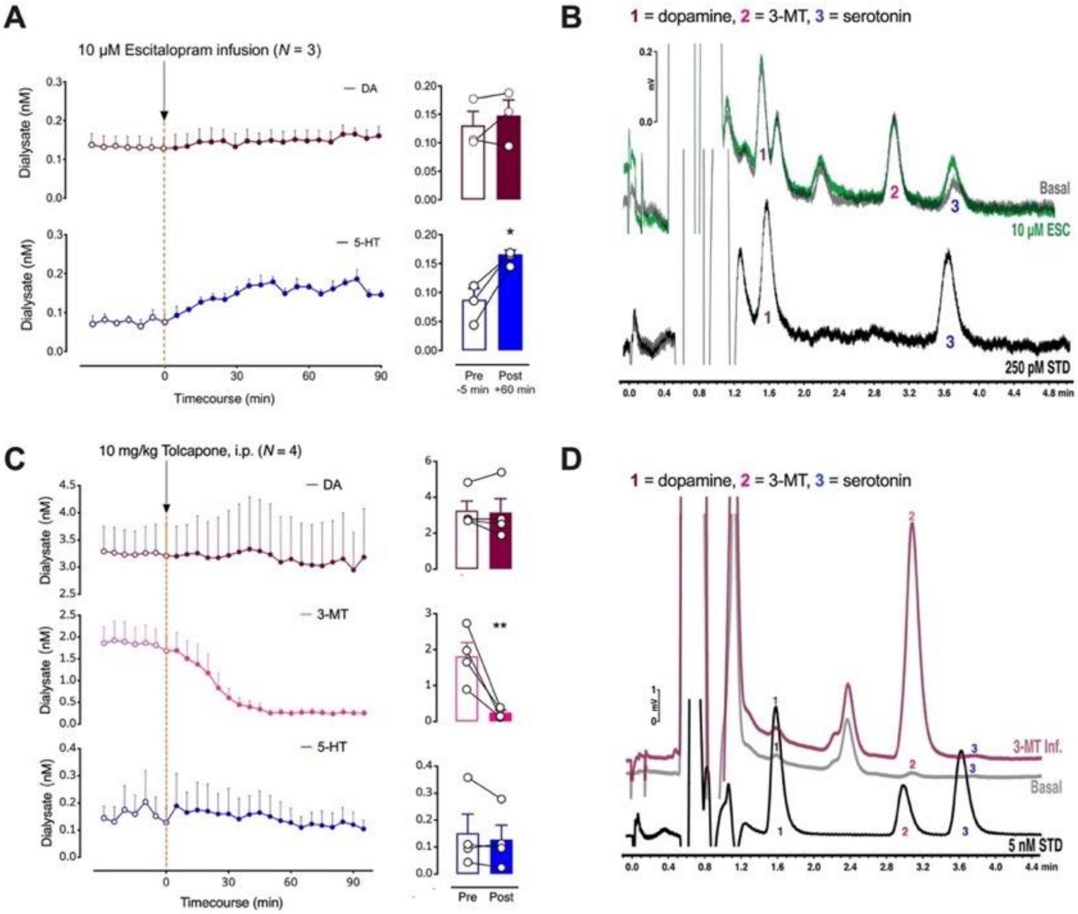

Figure IV.3: A. The left panel shows the effects of intrastriatal perfusion of 10 µM escitalopram on dopamine (DA; top, red) and serotonin levels (5-HT; bottom, blue). Basal serotonin levels were significantly increased after escitalopram administration (right). **B.** Representative chromatograms showing dopamine (peak 1), 3-MT (peak 2), and serotonin (peak 3) from a control mouse under basal conditions (gray) and during perfusion of the selective serotonin reuptake inhibitor (SSRI) escitalopram (green). Peak 3 showed a large increase in response to local delivery of the SSRI suggesting that this peak was serotonin. A standard containing 500 pM dopamine (peak 1) and serotonin (peak 3) is overlaid in black. **C.** The left panel shows the effects of systemic administration of tolcapone, a catechol-*O*- methyltransferase (COMT) inhibitor on dopamine (DA; top, red), 3-methyltyramine (3-MT; middle, pink), and serotonin levels (5-HT; bottom, blue). The enzyme COMT converts dopamine to 3-MT. Only 3-MT (pink) was significantly reduced after tolcapone administration (right). **D.** Representative chromatograms showing dopamine (peak 1), 3-MT (peak 2), and serotonin (peak 3) after the intrastriatal perfusion of 50 nM 3-MT (red) *vs.* a basal dialysate sample from the same control mouse (gray). Reverse dialysis of 3-MT confirms peak 2 as 3-MT. A standard containing 5 nM dopamine (peak 1), 3-MT (peak 2), and serotonin (peak 3) is overlaid in black. Data in A and C are means ± SEMs. $^{*}P<0.05$, $^{**}P<0.01$. A peak sometimes appearing between peaks 1 and 2 was not responsive to optical stimulation or high K^+ perfusion, therefore, we did not attempt to identify this peak.

Figure IV.4

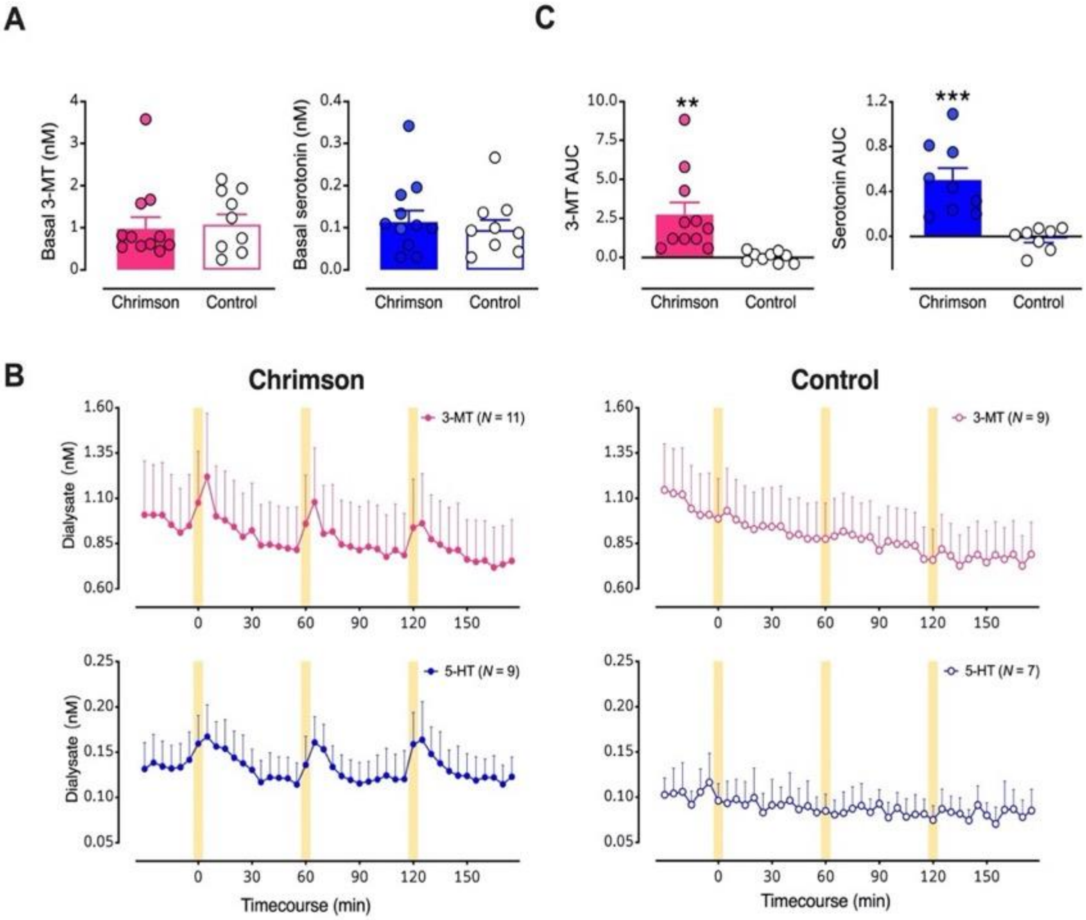

Figure IV.4: Optical stimulation of midbrain dopamine neurons evokes overflow of 3-methyltyramine (3-MT) and serotonin in dorsal striatum (dSTR). A. Basal dialysate levels of 3-MT (left, pink) and serotonin (right, blue) in mice with *vs.* without Chrimson transfection. **B.** Time course of stimulated 3-MT (pink) and serotonin (blue) in mice transfected with Chrimson (left) compared to mice transfected with a control protein (right). Yellow bars indicate 5-min optical stimulations. **C.** Comparisons of areas under the curve (AUC) for the overflow of 3-MT or serotonin produced by optical stimulation of dopamine neurons expressing Chrimson with respect to control mice. Data are means ± SEMs. $^{**}P<0.01$, $^{***}P<0.001$. In two mice per group, data for serotonin were below the detectable limit.

Figure IV.5

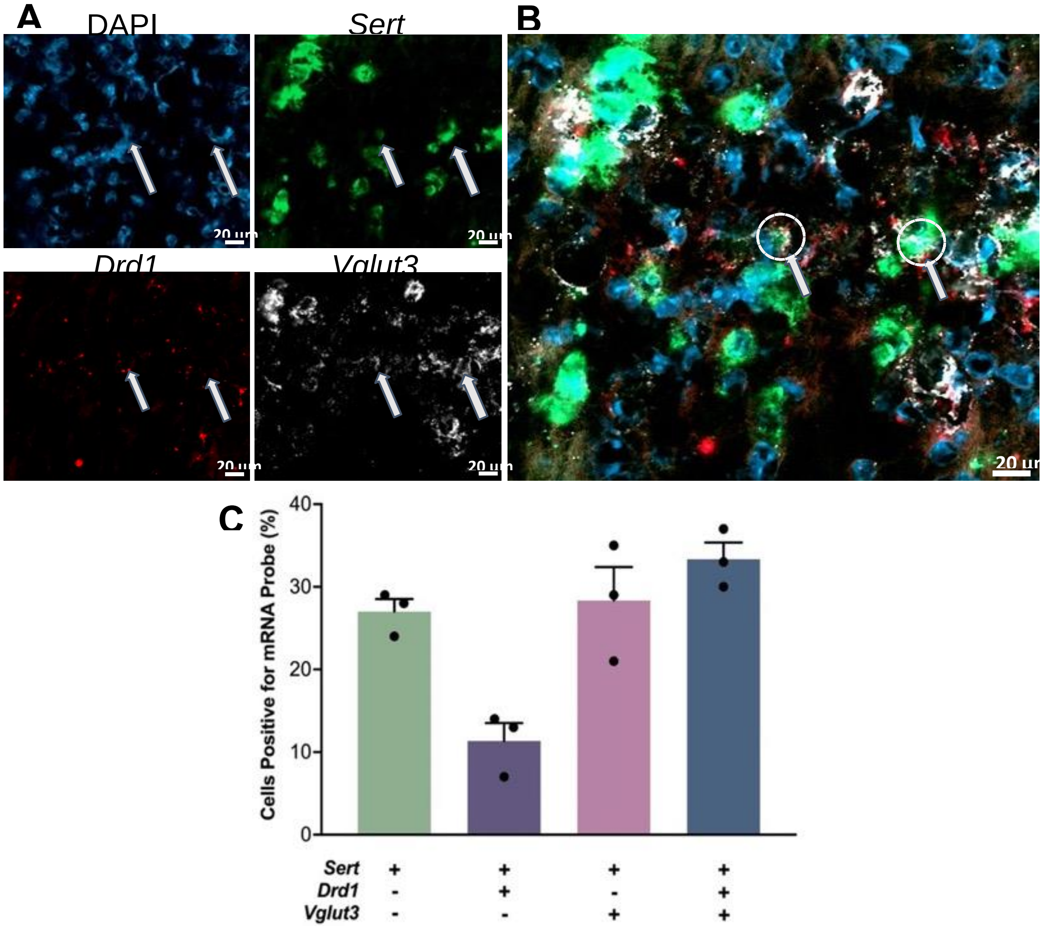

Figure IV.5: Co-localization of serotonin transporter (*Sert*), D1 dopamine receptor (*Drd1*), and vesicular glutamate transporter 3 (*Vglut3*) mRNA in the dorsal raphe nucleus. A. Cell nuclei were stained with DAPI (top left, blue). Antisense probes to localize *Sert* (top right, green), *Drd1* (bottom left, red), and *Vglut3* (bottom right, white) mRNA were visualized. Puncta for each mRNA were colocalized in some nuclei but did not necessarily overlap. **B.** Overlay of images in A. Arrows indicate examples of the three mRNAs colocalized in the same nuclei. **C.** Relative quantification of cells containing *Sert*, *Drd1*, and *Vglut3* mRNA with respect to the total number of *Sert* expressing cell bodies. (SEMs are for *n*=3 z-stack planes in a single mouse. A total of 248 cells were counted).

Figure IV.6

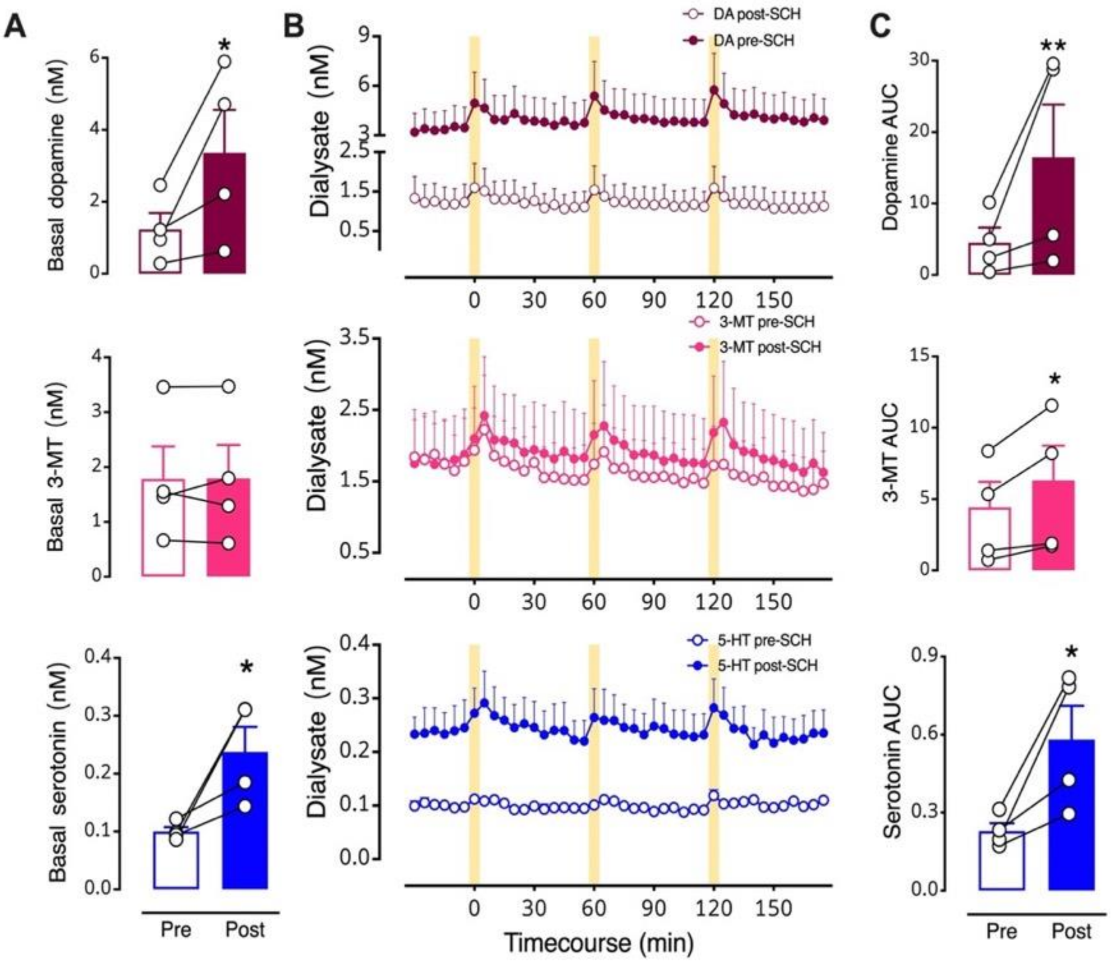

Figure IV.6: Intrastriatal perfusion of a D1-like receptor inhibitor. A. Basal levels for the three neurochemicals pre- *vs.* post-SCH 23390. **B.** Time courses before and during intrastriatal perfusion of 100 µM SCH 23390 showing optically stimulated increases in dopamine (red, top), 3-methyltyramine (3-MT; pink, middle), and serotonin (blue, bottom). **C.** Area under the curve (AUC) comparisons of overflow induced by optical stimulation prior to (Pre) and during (Post) SCH 23390 striatal perfusion. Following three pre-drug stimuli, SCH 23390 was perfused for 90-120 min in each mouse prior to the first post-drug stimulation (see Fig. III.1A for timeline). The data 30 min prior to the first post-drug stimulus were used to calculate post-drug basal levels. The drug was continuously perfused throughout the post-drug stimulation period. Data are means ± SEMs. Some error bars in B cannot be seen due to scale. $^{*}P<0.05$, $^{**}P<0.01$ pre- *vs.* post-initiation of drug perfusion. $N=4$ mice. Each basal data point in A represents the mean of six measurements taken just prior to the first pre- or post-drug stimulation (errors not shown). The AUC data points in C are means of each of the three stimuli (errors not shown).

Figure IV.7

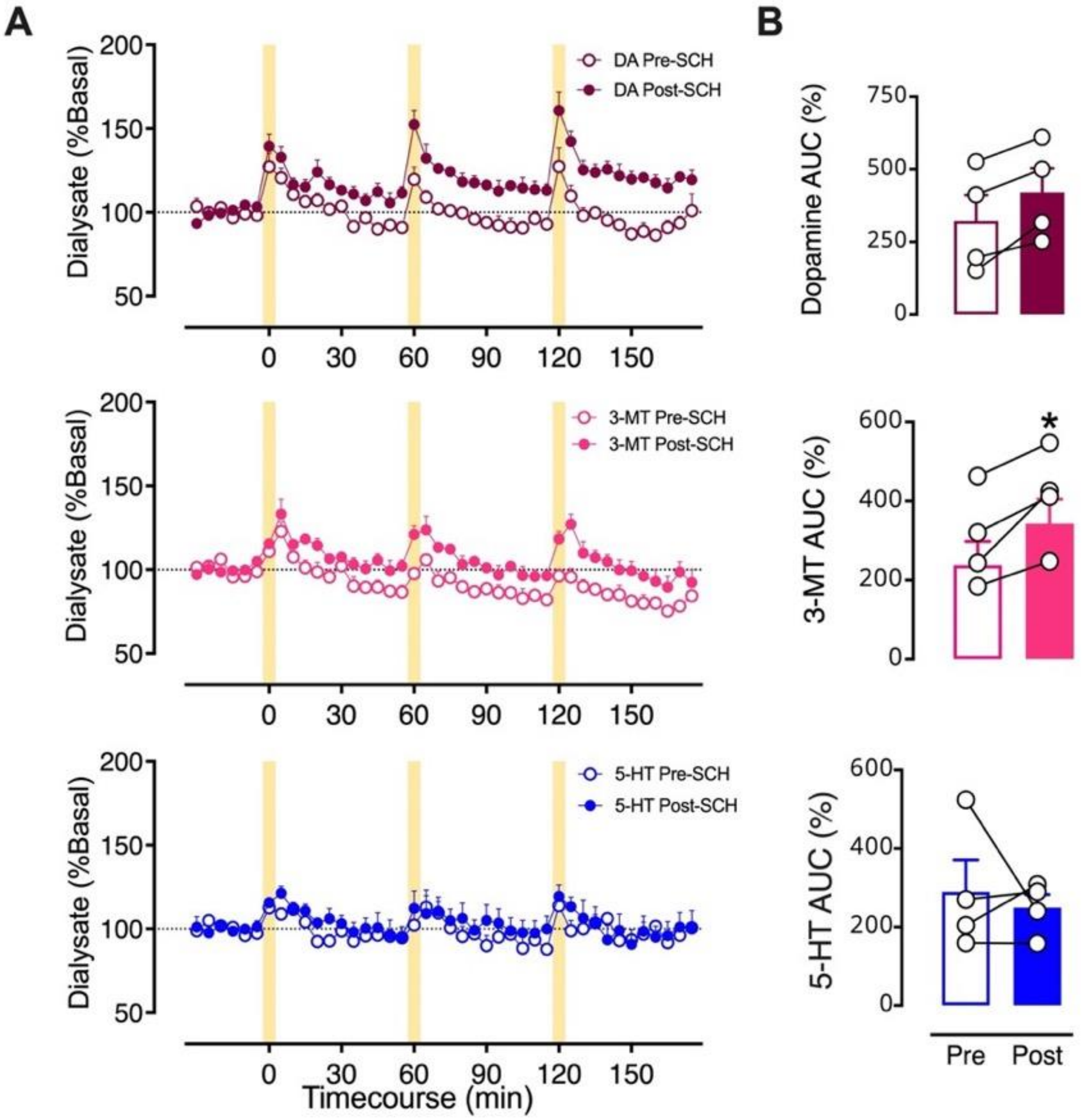

Figure IV.7: Effects of intrastriatal perfusion of a D1-like receptor inhibitor analyzed with respect to pre-stimulation basal levels. A. Time courses of optically stimulated neurochemical levels before and during intrastriatal perfusion of SCH 23390 (100 µM). **B.** Optically evoked overflow expressed as area under the curve for data normalized to pre-stimulation basal levels (AUC (%)). Data are means ± SEMs. *N*=4 mice. $*P<0.05$. The AUC datapoints in C are means of the three stimuli for each mouse (errors not shown).

Figure IV.8

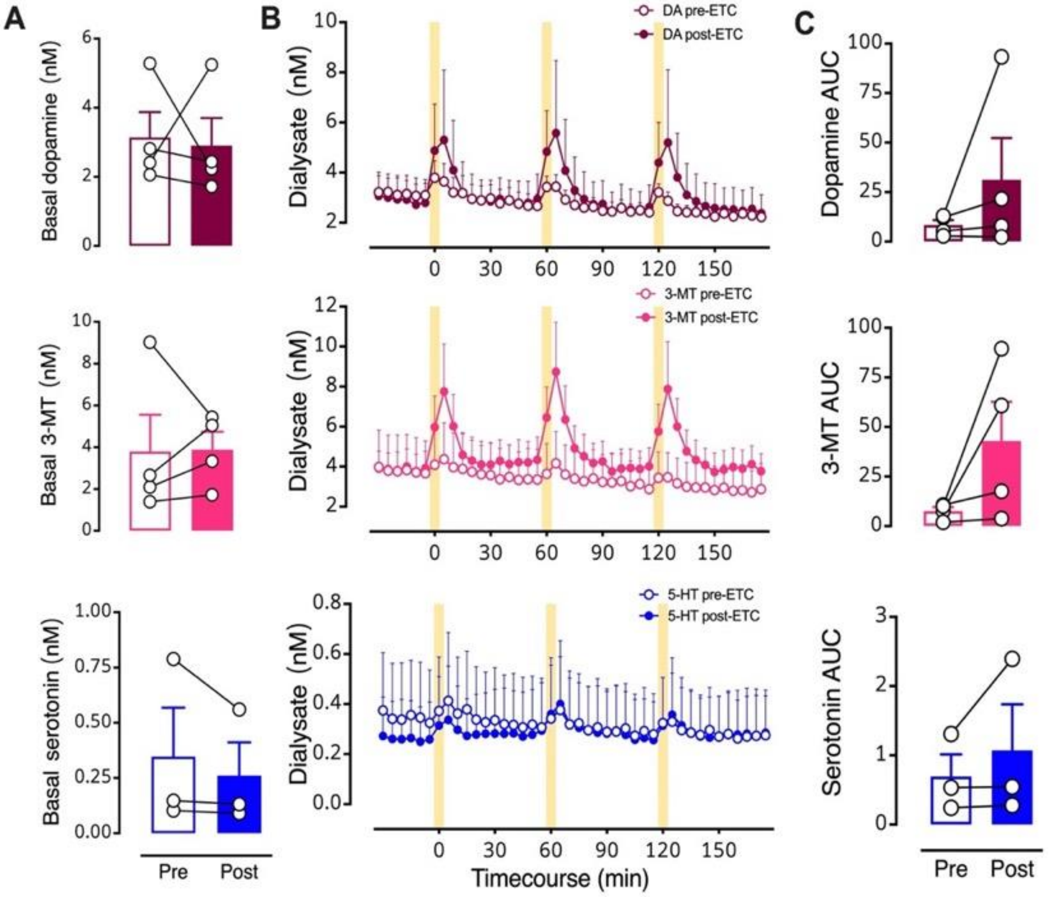

Figure IV.8: Intrastriatal perfusion of a D_2 antagonist does not prevent optically evoked serotonin. A. Pre- *vs.* post-eticlopride basal levels of all three neurochemicals. **B.** Time course before and during intrastriatal infusion of the D2-like receptor inhibitor eticlopride (100 μM). **C.** Areas under the curve (AUC) for optically stimulated neurochemical release prior to (Pre) and during (Post) eticlopride perfusion into striatum. Data are means ± SEMs for N=4 mice. Serotonin levels for one mouse were not detectable. Basal data points in A represent the means of six measurements just prior to the first stimulation (errors not shown). The AUC datapoints in C represent the means of three stimuli (errors not shown).

Figure IV.9

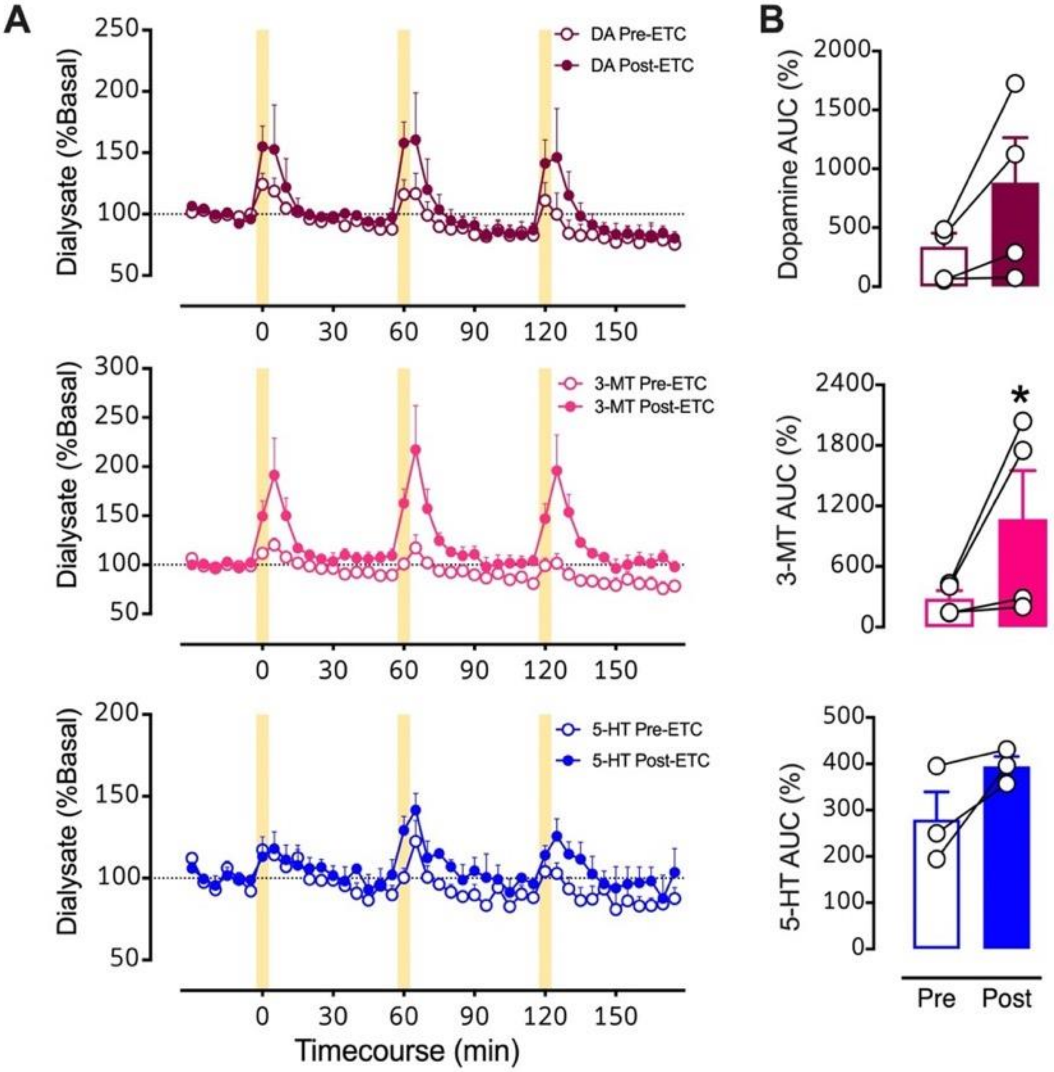

Figure IV.9: Effects of intrastriatal perfusion of a D_2 antagonist analyzed with respect to pre-stimulation basal levels. A. Time courses before and during intrastriatal perfusion of eticlopride (100 µM) showing basal and stimulated neurochemical levels expressed as percents of respective pre-stimulation basal levels. **B.** Optically evoked overflow expressed as area under the curve for data normalized to pre-stimulation basal levels (AUC (%)). Data are means ± SEMs for *N*=4 mice. Serotonin levels for one mouse were not detectable. **P*<0.05 *vs.* pre-drug. %Basal data points in A represent the means of six measurements just prior to the first stimulation (errors not shown). The AUC datapoints in C are the means of the three stimuli (errors not shown).

Figure IV.10

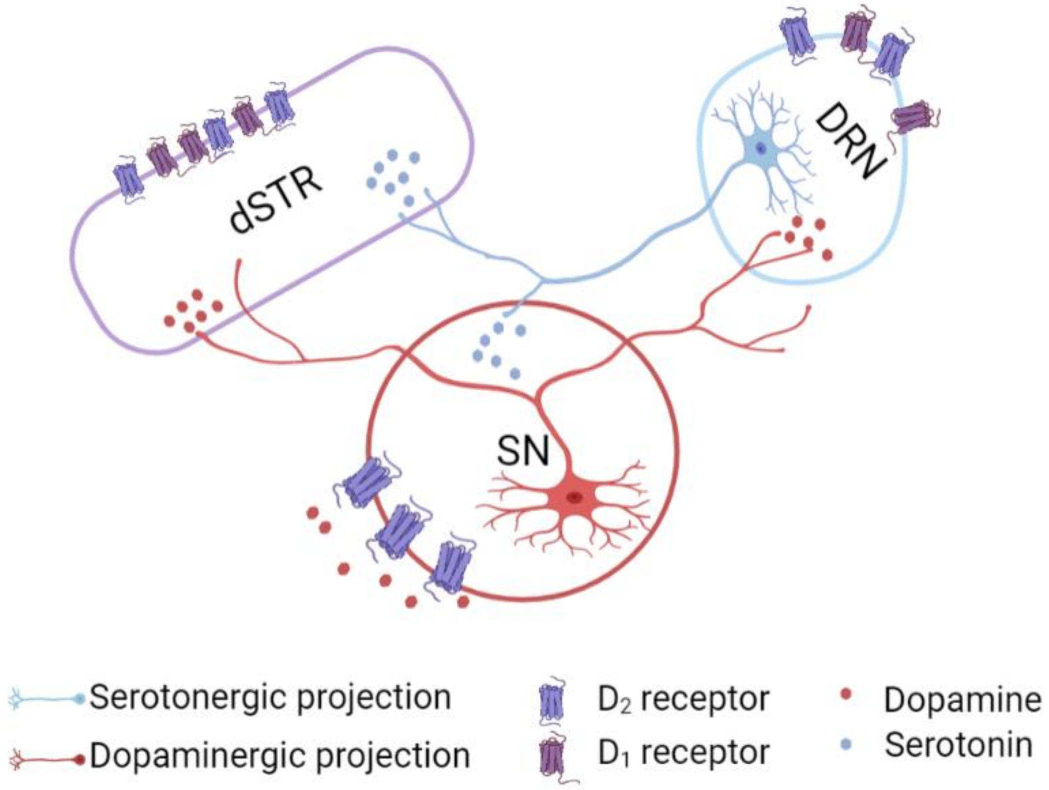

Figure IV.10: Proposed mechanisms of dopamine-mediated serotonin release. The substantia nigra (SN) sends dense dopaminergic projections to the striatum (nigrostriatal pathway) and to the dorsal raphe nucleus (DRN).[1] The DRN sends serotonergic projections to dopaminergic cell bodies in the SN and to the striatum.[2] We found that optical activation of midbrain dopamine neurons produces striatal serotonin release that was not blocked by striatal D1- or D2-like receptor inhibition. Another possible mechanism for dopamine-mediated serotonin release is that an optogenetically induced increase in dopamine in the SN, which promotes D2 somatodendritic autoreceptor activation[3] and subsequent disinhibition of serotonin cell bodies in the DRN, produces serotonin release in the striatum. Alternately, optically induced dopamine release in DRN could act *via* local D1 or D2-like receptors to increase the probability of firing of DRN serotonin neurons projecting to dSTR.

Figure IV.S1

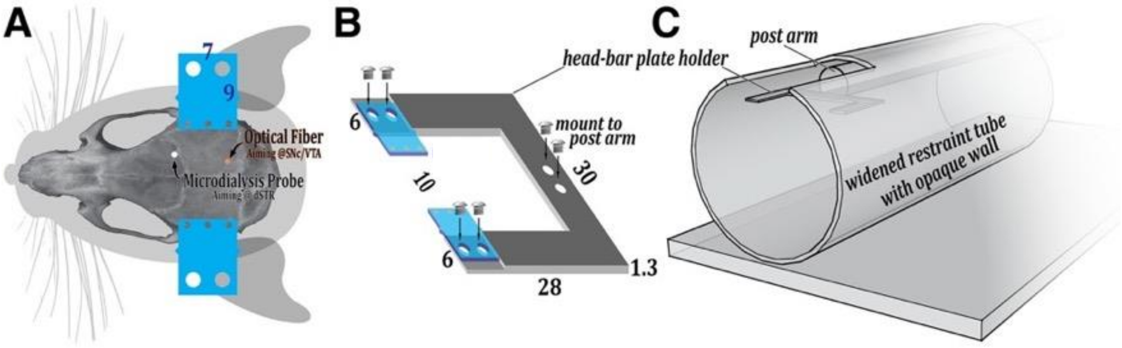

Figure IV.S1: Head-fixed recording set-up. A. Schematic showing the locations of the head-bar implants (in blue and to scale) and the stimulation (stim) and recording (dSTR) site craniotomies relative to a mouse skull. **B.** Schematic of the head-bar plate holder (in gray and to scale). The head-bar plate holder was 30 mm long, 28 mm wide, and 1.3 mm thick. The mini-plates, which attach the holder to the head bars, were 9 mm long, 7 mm wide, and 0.65 mm thick, with a 10 mm gap between them. **C.** Schematic of the custom head-fixed tube used for fast microdialysis recordings with optical stimulation. The restraint tube (2” diameter), constructed of opaque (black) plexiglass, provided loose restraint to reduce spontaneous and stimulated physical movement, which can evoke movement-induced dopamine release artifacts in dorsal striatum.

Figure IV.S2

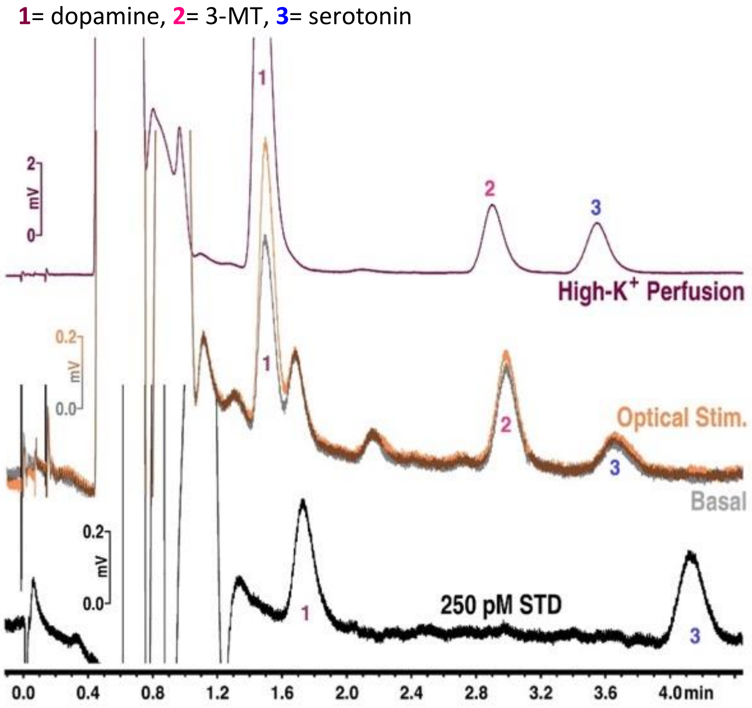

Figure IV.S2: Optical stimulation of midbrain dopamine neurons increases in striatal serotonin and 3-methoxytyramine. Representative chromatograms from a Chrimson-transfected mouse under basal conditions (gray), and in response to optical stimulation (orange) or high-K^+ perfusion (red). Both optical stimulation and high-K^+ perfusion induced increases in neurochemicals (peaks 2 and 3), in addition to dopamine (peak 1). Chromatogram of a standard containing 250 pM dopamine (peak 1) and serotonin (peak 3) is shown in black. Peaks 2 and 3 in the dialysate samples could not be definitively identified based on comparison with retention times in the standard chromatogram.

Figure IV.S3

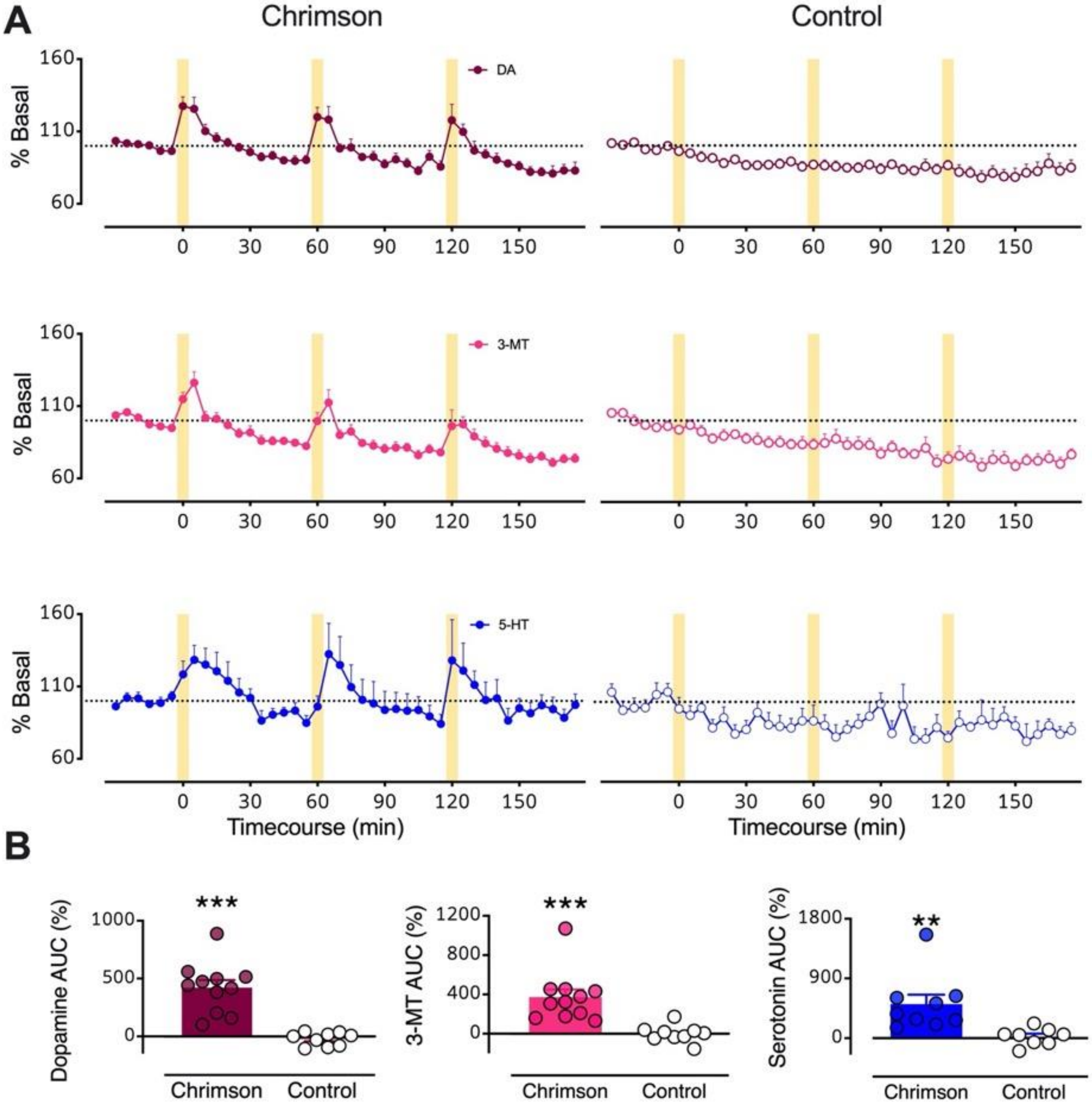

Figure IV.S3: Normalized responses to optical stimulation. A. Time courses of %basal dialysate levels for DA (top, red), 3-MT (middle, pink), and serotonin (5-HT; bottom, blue) in mice expressing Chrimson (left) *vs.* mice transfected with a control protein (right). Optically induced overflow of dopamine, 3-MT, and serotonin were only detected in the Chrimson animals. **B.** The magnitudes of overflow are represented as areas under the curve percent (AUC (%)). Dialysate serotonin concentrations were below the detectable threshold in 2/11 Chrimson mice and 2/9 control mice. The yellow bars indicate optical stimulations (5 min). **P<0.01 and ***P<0.001.

Figure IV.S4

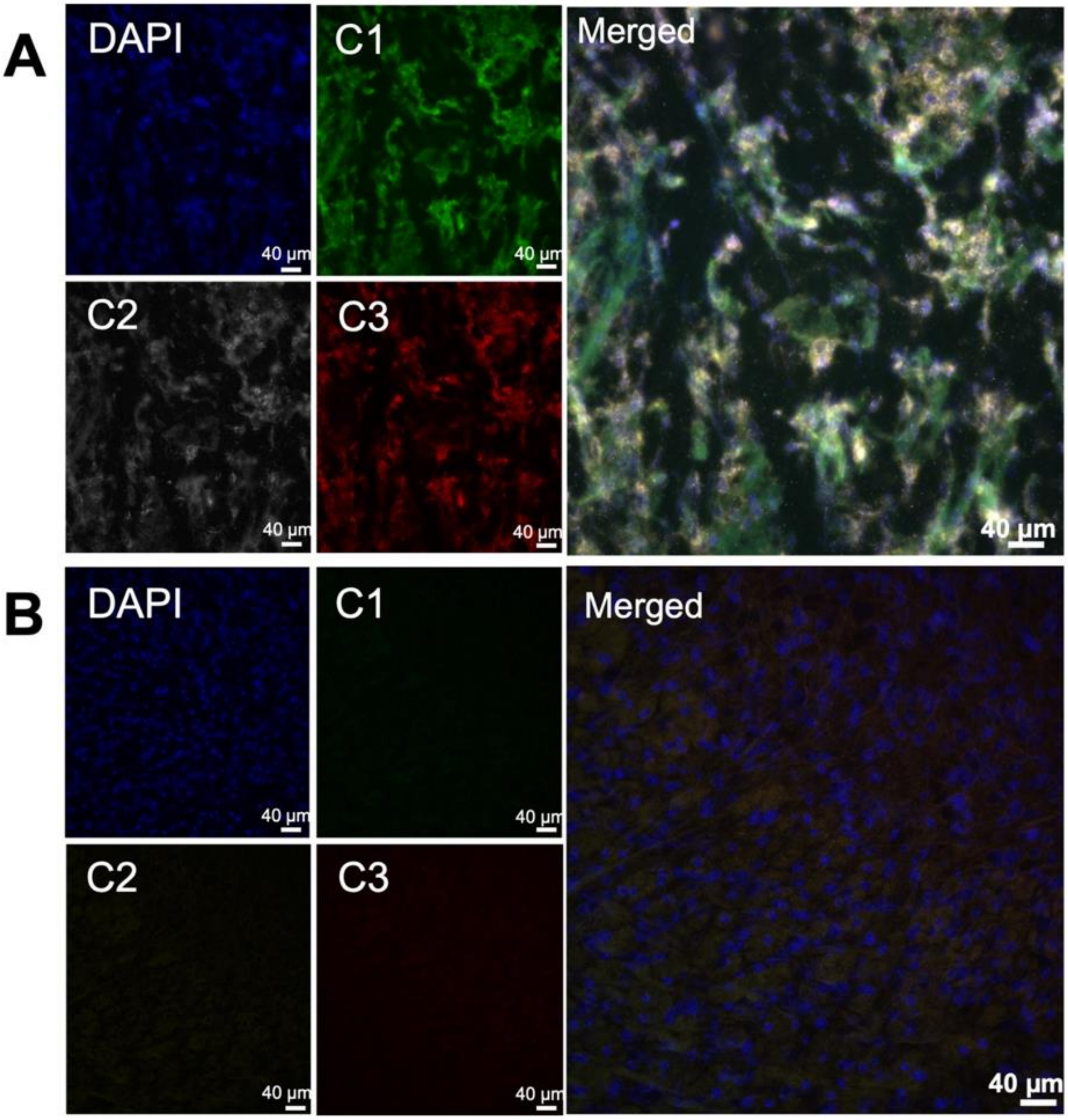

Figure IV.S4: RNAscope *in situ* hybridization controls in dorsal raphe. A.The RNAscope® Multiplex Fluorescent Assay as a 3-plex positive control. The RNA polymerase II subunit RPB1 (Polr2a, C1 channel), cyclophilin B (PPIB, C2 channel), and ubiquitin C (UBC, C3 channel) are mRNAs found in all mouse cells. Cell nuclei stained by DAPI are shown in blue. The overlay is shown on the right **B.** The RNAscope® Multiplex Fluorescent Assay as a 3-plex negative control. A probe for DapB, an mRNA that codes for a reductase enzyme from *Bacillus subtilis*, was used in all three channels with each of the opal dyes to evaluate background staining.

Figure IV.S5

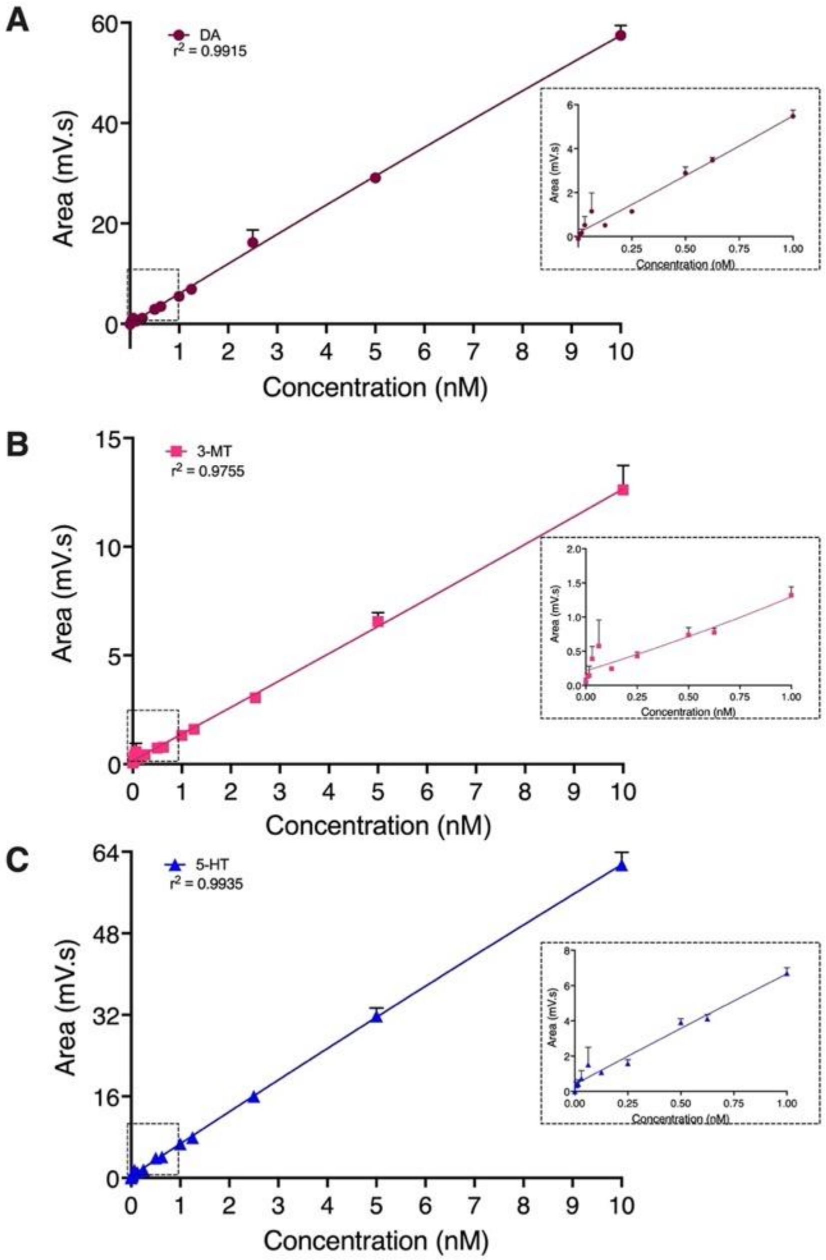

Figure IV.S5: Standard curves for dopamine, 3-methyltyramine 3-MT), and serotonin. Fourteen standards (0 nM, 0.008 nM, 0.016 nM, 0.032 nM, 0.063 nM, 0.125 nM, 0.250 nM, 0.500 nM, 0.625 nM, 1 nM, 1.25 nM, 2.5 nM, 5 nM, and 10 nM) were injected into the HPLC (20 µL volumes) to create standard curves. Insets are zoomed in on the lower concentrations ranging from 0-1 nM. Quadratic curve-fits were applied to **A.** dopamine, **B.** 3-MT, and **C.** serotonin standards. Each point represents *N*=3 replicates measured on different days. Error bars (standard errors of the means) are too small to be visualized in some cases.

Table IV.S1

Table S1: Statistical summary

Figure	Comparison	Test	Results	Significant?
2C	Basal DA: control *vs.* Chrimson	Unpaired two-tailed t-test	t (18)=1.6; *P*>0.1	No
2D	**AUC DA: control *vs.* Chrimson**	**Unpaired two-tailed t-test**	**t (18)=3.0; *P*<0.01**	**
3A	DA: 5 mins pre- *vs.* 60 mins post-ESC	Paired two-tailed t-test	t (2)=0.92; *P*>0.4	No
3A	**5HT: 5 mins pre- *vs.* 60 mins post-ESC**	**Paired two-tailed t-test**	**t (2)=5.7; *P*<0.05**	*
3C	DA: 5 mins pre vs. 60 mins post TOL	Ratio paired two-tailed t-test	t (3) = 0.83; *P*>0.46	No
3C	**3MT: 5 mins pre vs. 60 mins post TOL**	**Ratio paired two-tailed t-test**	**t (3) = 9.6; *P*<0.01**	**
3C	5HT: 5 mins pre vs. 60 mins post TOL	Ratio paired two-tailed t-test	t (3) = 1.3; *P*>0.29	No
4A	Basal 3MT: control *vs.* Chrimson	Unpaired two-tailed t-test	t (18)=0.27; *P*>0.7	No
4A	Basal 5HT: control *vs.* Chrimson	Unpaired two-tailed t-test	t (18)=0.52; *P*>0.6	No
4C	**AUC 3MT: control vs. Chrimson**	**Unpaired two-tailed t-test**	**t (18)=3.1; *P*<0.01**	**
4C	**AUC 5HT: control vs. Chrimson**	**Unpaired two-tailed t-test**	**t (15)=4.4; *P*<0.001**	***
6A	**Basal DA: pre- *vs.* post-SCH**	**Ratio paired two-tailed t-test**	**t (3)=4.4; *P*<0.05**	*
6A	Basal 3MT: pre- *vs.* post-SCH	Ratio paired two-tailed t-test	t (3) = 0.17; *P*>0.87	No
6A	**Basal 5HT: pre- *vs.* post-SCH**	**Ratio paired two-tailed t-test**	**t (3) = 3.5; *P*<0.05**	*
6C	**AUC DA: pre- *vs.* post-SCH**	**Ratio paired two-tailed t-test**	**t (3) = 6.2; *P*<0.05**	**
6C	**AUC 3MT: pre- *vs.* post-SCH**	**Ratio paired two-tailed t-test**	**t (3) = 4.8; *P*<0.05**	*
6C	**AUC 5HT: pre- v*s.* post-SCH**	**Ratio paired two-tailed t-test**	**t (3) = 4.5; *P*<0.05**	*
7B	AUC (%) DA: pre vs. post SCH	Ratio paired two-tailed t-test	t (3) = 2.4; *P*<0.1	Trend
7B	**AUC (%) 3MT: pre vs. post SCH**	**Ratio paired two-tailed t-test**	**t (3) = 3.7; *P*<0.05**	*
7B	AUC (%) 5HT: pre vs. post SCH	Ratio paired two-tailed t-test	t (3) = 0.41; *P*>0.71	No

8A	Basal DA: pre vs. post ETC	Ratio paired two-tailed t-test	t (3) = 0.31; *P*>0.78	No
8A	Basal 3MT: pre vs. post ETC	Ratio paired two-tailed t-test	t (3) = 0.81; *P*>0.47	No
8A	Basal 5HT: pre vs. post ETC	Ratio paired two-tailed t-test	t (2) = 2.7; *P*>0.11	No
8C	AUC DA: pre vs. post ETC	Ratio paired two-tailed t-test	t (3) = 1.5; *P*<0.23	No
8C	AUC 3MT: pre vs. post ETC	Ratio paired two-tailed t-test	t (3) = 3.1; *P*<0.06	Trend
8C	AUC 5HT: pre vs. post ETC	Ratio paired two-tailed t-test	t (2) = 1.4; *P*>0.28	No
9B	AUC (%) DA: pre vs. post ETC	Ratio paired two-tailed t-test	t (3) = 2.6; *P*<0.08	Trend
9B	**AUC (%) 3MT: pre vs. post ETC**	**Ratio paired two-tailed t-test**	**t (3) = 4.4; *P*<0.05**	*****
9B	AUC (%) 5HT: pre vs. post ETC	Ratio paired two-tailed t-test	t (2) = 1.8; *P*>0.21	No
S3B	**AUC (%) DA: control vs. chrimson**	**Unpaired two-tailed t-test**	**t (18) = 5.9; *P*<0.001**	*******
S3B	**AUC (%) 3MT: control vs. chrimson**	**Unpaired two-tailed t-test**	**t (18) = 4.1; *P*<0.001**	*******
S3B	**AUC (%) 5HT: control vs. chrimson**	**Unpaired two-tailed t-test**	**t (15) = 3.1; *P*<0.01**	******

References

1. Pollak Dorocic, I.; Fürth, D.; Xuan, Y.; Johansson, Y.; Pozzi, L.; Silberberg, G.; Carlén, M.; Meletis, K., A whole-brain atlas of inputs to serotonergic neurons of the dorsal and median raphe nuclei. *Neuron* **2014,** *83* (3), 663-678.

2. Muzerelle, A.; Scotto-Lomassese, S.; Bernard, J. F.; Soiza-Reilly, M.; Gaspar, P., Conditional anterograde tracing reveals distinct targeting of individual serotonin cell groups (b5-b9) to the forebrain and brainstem. *Brain Structure and Function* **2016,** *221* (1), 535-61.

3. Hikima, T.; Lee, C. R.; Witkovsky, P.; Chesler, J.; Ichtchenko, K.; Rice, M. E., Activity-dependent somatodendritic dopamine release in the substantia nigra autoinhibits the releasing neuron. *Cell Reports* **2021,** *35* (1), 108951.

4. Bernstein, J. G.; Boyden, E. S., Optogenetic tools for analyzing the neural circuits of behavior. *Trends in Cognitive Science* **2011,** *15* (12), 592-600.

5. Boyden, E. S., Optogenetics: Using light to control the brain. *Cerebrum* **2011,** *2011*, 16.

6. Kim, C. K.; Adhikari, A.; Deisseroth, K., Integration of optogenetics with complementary methodologies in systems neuroscience. *Nat Rev Neurosci* **2017,** *18* (4), 222-235.

7. Entcheva, E.; Kay, M. W., Cardiac optogenetics: A decade of enlightenment. *Nature Reviews Cardiology* **2020**.

8. Han, X., In vivo application of optogenetics for neural circuit analysis. *ACS Chemical Neuroscience* **2012,** *3* (8), 577-84.

9. Deisseroth, K., Optogenetics. *Nature Methods* **2011,** *8* (1), 26-29.

10. Klapoetke, N. C.; Murata, Y.; Kim, S. S.; Pulver, S. R.; Birdsey-Benson, A.; Cho, Y. K.; Morimoto, T. K.; Chuong, A. S.; Carpenter, E. J.; Tian, Z.; Wang, J.; Xie, Y.; Yan, Z.; Zhang, Y.; Chow, B. Y.; Surek, B.; Melkonian, M.; Jayaraman, V.; Constantine-Paton, M.; Wong, G. K.; Boyden, E. S., Independent optical excitation of distinct neural populations. *Nature Methods* **2014,** *11* (3), 338-46.

11. Madisen, L.; Mao, T.; Koch, H.; Zhuo, J. M.; Berenyi, A.; Fujisawa, S.; Hsu, Y. W.; Garcia, A. J., 3rd; Gu, X.; Zanella, S.; Kidney, J.; Gu, H.; Mao, Y.; Hooks, B. M.; Boyden, E. S.; Buzsaki, G.; Ramirez, J. M.; Jones, A. R.; Svoboda, K.; Han, X.; Turner, E. E.; Zeng, H., A toolbox of cre-dependent optogenetic transgenic mice for light-induced activation and silencing. *Nature Neuroscience* **2012,** *15* (5), 793-802.

12. Johansen, J. P.; Hamanaka, H.; Monfils, M. H.; Behnia, R.; Deisseroth, K.; Blair, H. T.; LeDoux, J. E., Optical activation of lateral amygdala pyramidal cells instructs associative fear learning. *Proceedings of the National Academy of Sciences* **2010,** *107* (28), 12692-12697.

13. Ohmura, Y.; Tanaka, K. F.; Tsunematsu, T.; Yamanaka, A.; Yoshioka, M., Optogenetic activation of serotonergic neurons enhances anxiety-like behaviour in mice. *The International Journal of Neuropsychopharmacology* **2014,** *17* (11), 1777-1783.

14. Chaudhury, D.; Walsh, J. J.; Friedman, A. K.; Juarez, B.; Ku, S. M.; Koo, J. W.; Ferguson, D.; Tsai, H.-C.; Pomeranz, L.; Christoffel, D. J.; Nectow, A. R.; Ekstrand, M.; Domingos, A.; Mazei-Robison, M. S.; Mouzon, E.; Lobo, M. K.; Neve, R. L.; Friedman, J. M.; Russo, S. J.; Deisseroth, K.; Nestler, E. J.; Han, M.-H., Rapid regulation of depression-related behaviours by control of midbrain dopamine neurons. *Nature* **2013,** *493* (7433), 532-536.

15. Lee, K.; Claar, L. D.; Hachisuka, A.; Bakhurin, K. I.; Nguyen, J.; Trott, J. M.; Gill, J. L.; Masmanidis, S. C., Temporally restricted dopaminergic control of reward-conditioned movements. *Nature Neuroscience* **2020,** *23* (2), 209-216.

16. Moran, R. J.; Kishida, K. T.; Lohrenz, T.; Saez, I.; Laxton, A. W.; Witcher, M. R.; Tatter, S. B.; Ellis, T. L.; Phillips, P. E.; Dayan, P.; Montague, P. R., The protective action encoding of serotonin transients in the human brain. *Neuropsychopharmacology* **2018,** *43* (6), 1425-1435.

17. Fischer, A. G.; Ullsperger, M., An update on the role of serotonin and its interplay with dopamine for reward. *Frontiers in Human Neuroscience* **2017,** *11*, 484.

18. Browne, C. J.; Abela, A. R.; Chu, D.; Li, Z.; Ji, X.; Lambe, E. K.; Fletcher, P. J., Dorsal raphe serotonin neurons inhibit operant responding for reward via inputs to the ventral tegmental area but not the nucleus accumbens: Evidence from studies combining optogenetic stimulation and serotonin reuptake inhibition. *Neuropsychopharmacology* **2019,** *44* (4), 793-804.

19. Altieri, S.; Singh, Y.; Sibille, E., Serotonergic pathways in depression. In *Neurobiology of depression*, CRC Press: 2011; Vol. 20115633, pp 143-170.

20. Niederkofler, V.; Asher, T. E.; Dymecki, S. M., Functional interplay between dopaminergic and serotonergic neuronal systems during development and adulthood. *ACS Chemical Neuroscience* **2015,** *6* (7), 1055-1070.

21. Dremencov, E.; Gispan-Herman, I.; Rosenstein, M.; Mendelman, A.; Overstreet, D. H.; Zohar, J.; Yadid, G., The serotonin–dopamine interaction is critical for fast-onset action of antidepressant treatment: In vivo studies in an animal model of depression. *Progress in Neuro-Psychopharmacology and Biological Psychiatry* **2004,** *28* (1), 141-147.

22. de Abreu, M. S.; Maximino, C.; Cardoso, S. C.; Marques, C. I.; Pimentel, A. F. N.; Mece, E.; Winberg, S.; Barcellos, L. J. G.; Soares, M. C., Dopamine and serotonin mediate the impact of stress on cleaner fish cooperative behavior. *Hormones and Behavior* **2020,** *125*, 104813.

23. Hashemi, P.; Dankoski, E. C.; Lama, R.; Wood, K. M.; Takmakov, P.; Wightman, R. M., Brain dopamine and serotonin differ in regulation and its consequences. *Proceedings of the National Academy of Sciences* **2012,** *109* (29), 11510-11515.

24. Daw, N. D.; Kakade, S.; Dayan, P., Opponent interactions between serotonin and dopamine. *Neural Networks* **2002,** *15* (4-6), 603-616.

25. Di Giovanni, G.; Esposito, E.; Di Matteo, V., Role of serotonin in central dopamine dysfunction: 5ht modulation of da function. *CNS Neuroscience & Therapeutics* **2010,** *16* (3), 179-194.

26. Bengel, D.; Murphy, D. L.; Andrews, A. M.; Wichems, C. H.; Feltner, D.; Heils, A.; Mossner, R.; Westphal, H.; Lesch, K. P., Altered brain serotonin homeostasis and locomotor insensitivity to 3, 4-methylenedioxymethamphetamine ("ecstasy") in serotonin transporter-deficient mice. *Mol Pharmacol* **1998,** *53* (4), 649-55.

27. Dunlap, L. E.; Andrews, A. M.; Olson, D. E., Dark classics in chemical neuroscience: 3,4-methylenedioxymethamphetamine. *ACS Chemical Neuroscience* **2018,** *9* (10), 2408-2427.

28. Drake, L. R.; Scott, P. J. H., Dark classics in chemical neuroscience: Cocaine. *ACS Chemical Neuroscience* **2018,** *9* (10), 2358-2372.

29. Abbruscato, T. J.; Trippier, P. C., Dark classics in chemical neuroscience: Methamphetamine. *ACS Chemical Neuroscience* **2018,** *9* (10), 2373-2378.

30. Avery, M. C.; Krichmar, J. L., Neuromodulatory systems and their interactions: A review of models, theories, and experiments. *Front. Neural Circuits* **2017,** *11*.

31. Zangen, A.; Nakash, R.; Overstreet, D.; Yadid, G., Association between depressive behavior and absence of serotonin-dopamine interaction in the nucleus accumbens. *Psychopharmacology* **2001,** *155* (4), 434-439.

32. *Microdialysis techniques in neuroscience*. Humana Press: Totowa, NJ, 2013; Vol. 75.

33. Sampson, M. M.; Yang, H.; Andrews, A. M., Advanced microdialysis approaches resolve differences in serotonin homeostasis and signaling. In *Compendium of in vivo monitoring in real-time molecular neuroscience*, WORLD SCIENTIFIC: 2017; pp 119-140.

34. Altieri, S. C.; Yang, H.; O'Brien, H. J.; Redwine, H. M.; Senturk, D.; Hensler, J. G.; Andrews, A. M., Perinatal vs genetic programming of serotonin states associated with anxiety. *Neuropsychopharmacology* **2015,** *40* (6), 1456-70.

35. Ngo, K. T.; Varner, E. L.; Michael, A. C.; Weber, S. G., Monitoring dopamine responses to potassium ion and nomifensine by in vivo microdialysis with online liquid chromatography at one-minute resolution. *ACS Chemical Neuroscience* **2017,** *8* (2), 329-338.

36. Zhang, J.; Jaquins-Gerstl, A.; Nesbitt, K. M.; Rutan, S. C.; Michael, A. C.; Weber, S. G., In vivo monitoring of serotonin in the striatum of freely moving rats with one minute temporal resolution by online microdialysis-capillary high-performance liquid chromatography at elevated temperature and pressure. *Anal Chem* **2013,** *85* (20), 9889-97.

37. Liu, Y.; Zhang, J.; Xu, X.; Zhao, M. K.; Andrews, A. M.; Weber, S. G., Capillary ultrahigh performance liquid chromatography with elevated temperature for sub-one minute

separations of basal serotonin in submicroliter brain microdialysate samples. *Anal Chem* **2010,** *82* (23), 9611-6.

38. Yang, H.; Sampson, M. M.; Senturk, D.; Andrews, A. M., Sex- and sert-mediated differences in stimulated serotonin revealed by fast microdialysis. *ACS Chemical Neuroscience* **2015,** *6* (8), 1487-1501.

39. Yang, H.; Thompson, A. B.; McIntosh, B. J.; Altieri, S. C.; Andrews, A. M., Physiologically relevant changes in serotonin resolved by fast microdialysis. *ACS Chemical Neuroscience* **2013,** *4* (5), 790-8.

40. Ferre, S.; Cortes, R.; Artigas, F., Dopaminergic regulation of the serotonergic raphe-striatal pathway: Microdialysis studies in freely moving rats. *The Journal of Neuroscience* **1994,** *14* (8), 4839-4846.

41. Shin, G.; Gomez, A. M.; Al-Hasani, R.; Jeong, Y. R.; Kim, J.; Xie, Z.; Banks, A.; Lee, S. M.; Han, S. Y.; Yoo, C. J.; Lee, J. L.; Lee, S. H.; Kurniawan, J.; Tureb, J.; Guo, Z.; Yoon, J.; Park, S. I.; Bang, S. Y.; Nam, Y.; Walicki, M. C.; Samineni, V. K.; Mickle, A. D.; Lee, K.; Heo, S. Y.; McCall, J. G.; Pan, T.; Wang, L.; Feng, X.; Kim, T. I.; Kim, J. K.; Li, Y.; Huang, Y.; Gereau, R. W. t.; Ha, J. S.; Bruchas, M. R.; Rogers, J. A., Flexible near-field wireless optoelectronics as subdermal implants for broad applications in optogenetics. *Neuron* **2017,** *93* (3), 509-521 e3.

42. Correia, P. A.; Lottem, E.; Banerjee, D.; Machado, A. S.; Carey, M. R.; Mainen, Z. F., Transient inhibition and long-term facilitation of locomotion by phasic optogenetic activation of serotonin neurons. *Elife* **2017,** *6*.

43. Mathews, T. A.; Fedele, D. E.; Coppelli, F. M.; Avila, A. M.; Murphy, D. L.; Andrews, A. M., Gene dose-dependent alterations in extraneuronal serotonin but not dopamine in mice with reduced serotonin transporter expression. *The Journal of Neuroscience Methods* **2004,** *140* (1-2), 169-81.

44. Liu, Q.; Zhao, C.; Chen, M.; Liu, Y.; Zhao, Z.; Wu, F.; Li, Z.; Weiss, P. S.; Andrews, A. M.; Zhou, C., Flexible multiplexed in2o3 nanoribbon aptamer-field-effect transistors for biosensing. *iScience* **2020,** *23* (9), 101469.

45. Ren, J.; Isakova, A.; Friedmann, D.; Zeng, J.; Grutzner, S. M.; Pun, A.; Zhao, G. Q.; Kolluru, S. S.; Wang, R.; Lin, R.; Li, P.; Li, A.; Raymond, J. L.; Luo, Q.; Luo, M.; Quake, S. R.; Luo, L., Single-cell transcriptomes and whole-brain projections of serotonin neurons in the mouse dorsal and median raphe nuclei. *Elife* **2019,** *8*.

46. Huang, K. W.; Ochandarena, N. E.; Philson, A. C.; Hyun, M.; Birnbaum, J. E.; Cicconet, M.; Sabatini, B. L., Molecular and anatomical organization of the dorsal raphe nucleus. *eLife* **2019,** *8*.

47. Saller, C. F.; Salama, A. I., 3-methoxytyramine accumulation: Effects of typical neuroleptics and various atypical compounds. *Naunyn-Schmiedeberg's Archives of Pharmacology* **1986,** *334* (2), 125-132.

48. Sotnikova, T. D.; Beaulieu, J.-M.; Espinoza, S.; Masri, B.; Zhang, X.; Salahpour, A.; Barak, L. S.; Caron, M. G.; Gainetdinov, R. R., The dopamine metabolite 3-methoxytyramine is a neuromodulator. *PLoS ONE* **2010,** *5* (10), e13452.

49. Kaakkola, S.; Wurtman, R. J., Effects of comt inhibitors on striatal dopamine metabolism: A microdialysis study. *Brain Research* **1992,** *587* (2), 241-249.

50. Mansour, A.; Meador-Woodruff, J. H.; Bunzow, J. R.; Civelli, O.; Akil, H.; Watson, S. J., Localization of dopamine d2 receptor mrna and d1 and d2 receptor binding in the rat brain and pituitary: An in situ hybridization-receptor autoradiographic analysis. *J Neurosci* **1990,** *10* (8), 2587-600.

51. Suzuki, M.; Hurd, Y. L.; Sokoloff, P.; Schwartz, J. C.; Sedvall, G., D3 dopamine receptor mrna is widely expressed in the human brain. *Brain Research* **1998,** *779* (1-2), 58-74.

52. Spaethling, J. M.; Piel, D.; Dueck, H.; Buckley, P. T.; Morris, J. F.; Fisher, S. A.; Lee, J.; Sul, J. Y.; Kim, J.; Bartfai, T.; Beck, S. G.; Eberwine, J. H., Serotonergic neuron regulation informed by in vivo single-cell transcriptomics. *FASEB J* **2014,** *28* (2), 771-80.

53. Niederkofler, V.; Asher, T. E.; Okaty, B. W.; Rood, B. D.; Narayan, A.; Hwa, L. S.; Beck, S. G.; Miczek, K. A.; Dymecki, S. M., Identification of serotonergic neuronal modules that affect aggressive behavior. *Cell Rep* **2016,** *17* (8), 1934-1949.

54. Belmer, A.; Beecher, K.; Jacques, A.; Patkar, O. L.; Sicherre, F.; Bartlett, S. E., Axonal non-segregation of the vesicular glutamate transporter vglut3 within serotonergic projections in the mouse forebrain. *Frontiers in Cellular Neuroscience* **2019,** *13*, 193.

55. Wang, H.-L.; Zhang, S.; Qi, J.; Wang, H.; Cachope, R.; Mejias-Aponte, C. A.; Gomez, J. A.; Mateo-Semidey, G. E.; Beaudoin, G. M. J.; Paladini, C. A.; Cheer, J. F.; Morales, M., Dorsal raphe dual serotonin-glutamate neurons drive reward by establishing excitatory synapses on vta mesoaccumbens dopamine neurons. *Cell Reports* **2019,** *26* (5), 1128-1142.e7.

56. Bourne, J. A., Sch 23390: The first selective dopamine d1-like receptor antagonist. *CNS Drug Reviews* **2006,** *7* (4), 399-414.

57. Cameron, D. L.; Williams, J. T., Dopamine d1 receptors facilitate transmitter release. *Nature* **1993,** *366* (6453), 344-347.

58. Burke, D. A.; Rotstein, H. G.; Alvarez, V. A., Striatal local circuitry: A new framework for lateral inhibition. *Neuron* **2017,** *96* (2), 267-284.

59. Nishi, A.; Kuroiwa, M.; Shuto, T., Mechanisms for the modulation of dopamine d(1) receptor signaling in striatal neurons. *Frontiers in Neuroanatomy* **2011,** *5*, 43.

60. Ford, C. P., The role of d2-autoreceptors in regulating dopamine neuron activity and transmission. *Neuroscience* **2014,** *282*, 13-22.

61. Jenkins, B. G.; Sanchez-Pernaute, R.; Brownell, A. L.; Chen, Y. C.; Isacson, O., Mapping dopamine function in primates using pharmacologic magnetic resonance imaging. *The Journal of Neuroscience* **2004,** *24* (43), 9553-60.

62. Martelle, J. L.; Nader, M. A., A review of the discovery, pharmacological characterization, and behavioral effects of the dopamine d2-like receptor antagonist eticlopride. *CNS Neuroscience & Therapeutics* **2008,** *14* (3), 248-262.

63. Samanin, R.; Garattini, S., The serotonergic system in the brain and its possible functional connections with other aminergic systems. *Life Sciences* **1975,** *17* (8), 1201-9.

64. Kostowski, W., Interactions between serotonergic and catecholaminergic systems in the brain. *Pol J Pharmacol Pharm* **1975,** *27* (Suppl), 15-24.

65. Waldmeier, P. C.; Delini-Stula, A. A., Serotonin--dopamine interactions in the nigrostriatal system. *Eur J Pharmacol* **1979,** *55* (4), 363-73.

66. Petty, F.; Kramer, G.; Moeller, M., Does learned helplessness induction by haloperidol involve serotonin mediation? *Pharmacol Biochem Behav* **1994,** *48* (3), 671-6.

67. Mendlin, A.; Martin, F. J.; Jacobs, B. L., Involvement of dopamine d2 receptors in apomorphine-induced facilitation of forebrain serotonin output. *Eur J Pharmacol* **1998,** *351* (3), 291-8.

68. Mendlin, A.; Martin, F. J.; Jacobs, B. L., Dopaminergic input is required for increases in serotonin output produced by behavioral activation: An in vivo microdialysis study in rat forebrain. *Neuroscience* **1999,** *93* (3), 897-905.

69. Martin-Ruiz, R.; Ugedo, L.; Honrubia, M. A.; Mengod, G.; Artigas, F., Control of serotonergic neurons in rat brain by dopaminergic receptors outside the dorsal raphe nucleus. *Journal of Neurochemistry* **2001,** *77* (3), 762-75.

70. Vaaga, C. E.; Borisovska, M.; Westbrook, G. L., Dual-transmitter neurons: Functional implications of co-release and co-transmission. *Curr Opin Neurobiol* **2014,** *29*, 25-32.

71. Nusbaum, M. P.; Blitz, D. M.; Marder, E., Functional consequences of neuropeptide and small-molecule co-transmission. *Nature Reviews Neuroscience* **2017,** *18* (7), 389-403.

72. Granger, A. J.; Wallace, M. L.; Sabatini, B. L., Multi-transmitter neurons in the mammalian central nervous system. *Curr Opin Neurobiol* **2017,** *45*, 85-91.

73. Hnasko, T. S.; Edwards, R. H., Neurotransmitter corelease: Mechanism and physiological role. *Annu Rev Physiol* **2012,** *74*, 225-43.

74. Zhou, F. C.; Lesch, K. P.; Murphy, D. L., Serotonin uptake into dopamine neurons via dopamine transporters: A compensatory alternative. *Brain Research* **2002,** *942* (1-2), 109-19.

75. Kalivas, P. W.; Duffy, P., A comparison of axonal and somatodendritic dopamine release using in vivo dialysis. *J Neurochem* **1991,** *56* (3), 961-7.

76. Cheramy, A.; Leviel, V.; Glowinski, J., Dendritic release of dopamine in the substantia nigra. *Nature* **1981,** *289* (5798), 537-42.

77. Geffen, L. B.; Jessell, T. M.; Cuello, A. C.; Iversen, L. L., Release of dopamine from dendrites in rat substantia nigra. *Nature* **1976,** *260* (5548), 258-60.

78. Lee, E. H.; Geyer, M. A., Dopamine autoreceptor mediation of the effects of apomorphine on serotonin neurons. *Pharmacology Biochemistry and Behavior* **1984,** *21* (2), 301-11.

79. Silkis, I., Mutual influence of serotonin and dopamine on the functioning of the dorsal striatum and motor activity (hypothetical mechanism). *Neurochemical Journal* **2014,** *8*, 149-161.

80. Pollak Dorocic, I.; Fürth, D.; Xuan, Y.; Johansson, Y.; Pozzi, L.; Silberberg, G.; Carlén, M.; Meletis, K., A whole-brain atlas of inputs to serotonergic neurons of the dorsal and median raphe nuclei. *Neuron* **2014,** *83* (3), 663-78.

81. Gerfen, C. R.; Bolam, J. P., Chapter 1 - the neuroanatomical organization of the basal ganglia. In *Handbook of behavioral neuroscience*, Steiner, H.; Tseng, K. Y., Eds. Elsevier: 2016; Vol. 24, pp 3-32.

82. Mathur, B. N.; Lovinger, D. M., Serotonergic action on dorsal striatal function. *Parkinsonism Relat Disord* **2012,** *18 Suppl 1*, S129-31.

83. Cho, J. R.; Chen, X.; Kahan, A.; Robinson, J. E.; Wagenaar, D. A.; Gradinaru, V., Dorsal raphe dopamine neurons signal motivational salience dependent on internal state, expectation, and behavioral context. *The Journal of Neuroscience* **2021,** *41* (12), 2645-2655.

84. Lin, R.; Liang, J.; Luo, M., The raphe dopamine system: Roles in salience encoding, memory expression, and addiction. *Trends Neurosci* **2021,** *44* (5), 366-377.

85. Luis-Islas, J.; Luna, M.; Floran, B.; Gutierrez, R., Optoception: Perception of optogenetic brain stimulation. *bioRxiv* **2021**, 2021.04.22.440969.

86. Movassaghi, C. S.; Perrotta, K. A.; Yang, H.; Iyer, R.; Cheng, X.; Dagher, M.; Fillol, M. A.; Andrews, A. M., Simultaneous serotonin and dopamine monitoring across timescales by rapid pulse voltammetry with partial least squares regression. *Anal Bioanal Chem* **2021,** *413* (27), 6747-6767.

CHAPTER V

Optimizing Methods for ICP-MS Analysis of Mercury in Fish: An Upper-Division Analytical Chemistry Laboratory Class

The information in this chapter is reproduced with permission from ACS Journal of Chemical Education, Copyright 2022.

Optimizing Methods for ICP-MS Analysis of Mercury in Fish: An Upper-Division Analytical Chemistry Laboratory Class

Release. Wonhyeuk Jung, Christopher S. Dunham, Katie A. Perrotta, Yu Chen, James K. Gimzewski, and Joseph A. Loo. Journal of Chemical Education 2022 99 (10), 3566-3572.DOI: 10.1021/acs.jchemed.2c00429

Introduction

Government regulatory bodies such as the Food and Drug Administration (FDA) and the Environmental Protection Agency (EPA) routinely oversee the administration and enforcement of regulations governing hazardous compounds that can enter the food supply.[1] Screening mercury (Hg) in commercial fish products is of particular importance because seafood is the main source of this toxin for the general public.[2] Mercury toxicity can lead to brain damage including psychological disturbance, impaired hearing, loss of sight, ataxia, loss of motor control, and general debilitation.[3] Moreover, Hg exposure during the embryonic phase can lead to severe abnormalities in psychomotor development.[4]

Thus, the FDA closely monitors total Hg levels in commercial fish, provides guidelines on its consumption, and prohibits the sale of fish that have total mercury levels higher than an action level of 1 ppm.[5-9] Action levels represent the limit at which the FDA will take legal action to remove products from the market. The FDA regularly updates the elemental analysis manual for food and related products and inductively coupled plasma-mass spectrometry (ICP-MS) is one of the primary methods for the quantification of total Hg in fish.[10]

ICP-MS is a sensitive tool for elemental quantification with diverse applications, e.g. environmental sample analysis, water quality control, and food analysis.[11-14] This technique utilizes a plasma to achieve ionization and atomization of molecular species into their elemental components and is well suited for sensitive quantitative analysis, as it can detect analytes at concentrations well into the parts-per-trillion (ppt) range.[15] These traits make ICP-MS a particularly powerful technique for trace metal analysis in commercial products.

The prevalence of ICP-MS in real-world analytical chemistry applications has led to a number of proposed student lab exercises using ICP-MS over the last decade.[16-20] Such protocols are of great pedagogical value and introduce students to foundational concepts of

ICP-MS and the practical application of the technique. However, important analytical chemistry concepts such as the impact of matrix effects on the accuracy of ICP-MS analysis and parameter optimization via the usage of a standard reference material (SRM), which should closely mimic the composition of the sample , have not been extensively explored in previously published student-led ICP-MS experiments.[17-20] Here, we introduce a hands-on lab exercise for an upper-division, undergraduate analytical chemistry course that mimics industry- and government-level ICP-MS protocols.

This undergraduate lab exercise was tested during the Winter 2020 quarter and fully implemented during the Winter 2022 quarter at the University of California, Los Angeles (UCLA) for a chemical instrumentation/analytical chemistry class. Students were tasked with optimizing experimental and instrument parameters with fish samples that were digested with two different acid matrices, Digestion A (5.6% HNO_3 and 1.2%H_2O_2) or Digestion B (5.6% HNO_3, 0.74%HCl and 1.2%H_2O_2). In order to analyze these samples in an acid composition appropriate for the ICP-MS analysis, students diluted these samples 3.5-fold with water. The resulting two matrices for the samples were denoted as Matrix A (1.62% HNO_3 and 0.34% H_2O_2) and Matrix B (1.62% HNO_3,0.21% HCl, and 0.34% H_2O_2).

Furthermore, students were introduced to the concept of kinetic energy discrimination (KED) as a means of suppressing polyatomic interfering species.[21] Polyatomic interference is caused by polyatomic species that are isobaric with the target element. KED takes advantage of the fact that isobaric polyatomic species will lose more kinetic energy relative to the target ions as they travel through a cell filled with a non-reactive gas such as helium (**Figure V.1**).

The SRM 1947 (Lake Michigan Fish Tissue) from the National Institute of Standards and Technology (NIST) was used for method validation.[22] Students analyzed each sample/matrix combination across multiple lab periods. Each lab section investigated a different KED voltage. Students pooled their data across lab sections together into a centralized cloud repository for analysis. Using their data, students determined an optimal matrix and KED voltage combination for their analysis. Finally, students used the optimized parameter dataset to assess the safety of the fish sample for potential human consumption.

This experiment aimed to achieve the following learning outcomes:

1. Students will learn how to validate a method with standard reference material (SRM)
2. Students will investigate how different acid matrix compositions affect accuracy of the analysis.
3. Students will learn how to optimize instrument parameters. In this case, students observed how varying the KED voltage affected the analysis.

Experimental Procedure

Reagents

Hydrochloric acid (37%, ≥99.999% trace metal grade, Sigma-Aldrich, Cat. no. 339253), nitric acid (70%, ≥99.999% trace metal grade, Sigma-Aldrich, Cat. no. 225711), hydrogen peroxide 30% (trace metal grade, Sigma-Aldrich, Cat. no. 95321), and water (high performance liquid chromatography (HPLC)-grade, Fisher, Cat. no. W9-1) were used to generate matrices for digestion and analysis. Scandium stock solution (100 µg/mL, 7% HNO_3, Inorganic Ventures, part no. CGSC10-125ML) and yttrium stock solution (100 µg/mL, 2% HNO_3, Inorganic Ventures, part no. MSY-100PPM-125ML) were diluted to 8 ng/mL and 4 ng/mL, respectively, with either Matrix A (1.62% HNO_3 and 0.34% H_2O_2) or Matrix B (1.62% HNO_3,0.21% HCl, and 0.34% H_2O_2) to generate internal standard (ISTD) solutions. Mercury standard (10 µg/mL, 5% HNO_3, Agilent, part no. 5190-8575) was diluted with either Matrix A or Matrix B to generate a 10 ng/mL stock solution, which was used to make calibration solutions. ICP-MS tuning solution (10 mg/mL Ce, Co, Li, Mg, Tl, and Y, Agilent, part no. 5190-0465) was diluted to 1 µg/L with 2% HNO_3 to conduct instrument warm-up and auto-tuning. SRM 1947 (Lake Michigan Fish Tissue, certification date 9/3/2020, expiration date 12/31/2026) was purchased from NIST.[21] Various fish (canned Skipjack tuna, Chilean sea bass filet, swordfish filet) were purchased from local supermarkets. Following digestion (see the Microwave Digestion & Sample Preparation section for details), the samples were stored in acid-resistant Nalgene™ Narrow-Mouth Bottles Made of Teflon™ PFA (Fisher, Cat. no. DS1630-0001).

Microwave Digestion and Sample Preparation

All samples were digested via microwave digestion. Microwave digestion was performed by teaching assistants (TAs) and staff at the ICP-MS facility within the UC Center for

Environmental Implications of Nanotechnology at UCLA. Samples (method blank, approx. 1 g SRM, approx. 1 g fish) were measured into clean Teflon vessels for acid digestion (the exact masses are reported in the Experimental Protocol document). The digestion was carried out using either a mixture of 4 mL 70% HNO_3, 2 mL 30% H_2O_2, and 1 mL H_2O (called Digestion A), or 4 mL 70% HNO_3, 2 mL 30% H_2O_2, and 1 mL 37% HCl (Digestion B) at 190°C for 20 minutes in a microwave digestion system (Titan MPS, PerkinElmer). Once the samples were cooled to room temperature, they were subsequently diluted to the final volume of 50 mL by adding filtered deionized water. In later steps detailed in "Teaching Methods", Digestion A is further diluted to 1.62% HNO_3 and 0.34% H_2O_2 (matching the composition of "Matrix A"). Digestion B is diluted to 1.62% HNO_3, 0.21% HCl, and 0.34% H_2O_2 (matching the composition of "Matrix B").

ICP-MS Instrument Parameters

An 8800 QQQ ICP-MS system (Agilent) equipped with an SPS 4 Autosampler (Agilent) was used for the experiment. ^{201}Hg isotope was targeted for the analysis. MassHunter Workstation 4.1 software (Agilent) was used to control the system and to process the data. The key parameters for ICP-MS are listed in **Table V.1** and were consistent throughout all experiments.

Teaching Assistant Responsibilities and Classroom Organization

The TAs held several responsibilities both preceding and following the lab period. Teaching assistants were tasked with preparing stock solutions of Matrix A and Matrix B solvents for calibration curves, preparing working solutions of internal standards, preparing sample microwave digestions, performing instrument warm-ups and pre-run maintenance (e.g. rinsing the probe, and sample and internal standard inlet tubes), and consolidating and uploading student data to the course's cloud storage repository. The average additional time commitment from the TAs for these tasks was approximately 6 hours per week.

This exercise was performed alongside and independent of several distinct mass spectrometry laboratory exercises during the Winter 2022 quarter of the Chemical Instrumentation class. The 42 students participating in the class either had limited or no prior analytical chemistry lab experience. The class maintained three distinct laboratory sections of approximately 14 students per section. Each section operated two distinct, four-hour lab periods per week (e.g. Tuesday/Thursday morning, Tuesday/Thursday afternoon, Wednesday/Friday afternoon) for 10 weeks (i.e. the duration of classroom instruction for the academic quarter). Students from each section worked in groups of 3-4 during the week in which they were assigned to this experiment to minimize crowding around the instrument while accommodating a relatively large laboratory class size. A full breakdown of the class structure is laid out in **Figure V.2**.

Hazards

The handling of mercury samples described in this protocol was approved by and in accordance with UCLA Environmental Health and Safety (EH&S) guidelines. Students should always wear protective goggles, gloves, and lab coats during the experiment. 70% HNO_3 and 37% HCl used for mercury extraction are caustic and should be handled with care. The calibration solutions that contain HNO_3, HCl, and mercury should be generated with care in a well-ventilated fume hood and should be disposed of properly following data acquisition. Finally, it is highly recommended that the autosampler chamber be ventilated during and after the experiment to minimize build-up of mercury-containing vapor.

Results and Discussion

Students were instructed on the fundamental concepts of quantitative analytical chemistry and selected concepts of ICP-MS (instrumentation, application) during the lecture, in addition to assigned reading for the course. For the laboratory exercise, students were provided with the protocol accessible in the Experimental Protocol. During the ICP-MS experiment, each of the three sections were assigned their own KED voltage to investigate (ranging from 0-12 V). Students then compiled their raw data into the central data repository to compare KED and matrix effects across the 3 sections.

Each "Lab Period 1" began with a TA-guided question-and-answer session to ensure students completed the pre-lab exercises (see Experimental Protocol), followed by guided inquiry and a discussion of experimental methods. These discussions covered: conical tube rinse protocols (see Experimental Protocol), sample preparation and dilution, calibration curve preparation, and kinetic energy discrimination voltage. During this period, students were instructed on how to use serological- and/or micro-pipettes. The TAs prepared the 10 ng/mL working stock Hg solution, from which students generated their calibration curves in Matrix A. Students calculated the calibration curve concentrations in the pre-lab assignment. Water was then used to dilute the method blank, SRM, and fish sample 3.5-fold to match the matrix composition of Matrix A. After the completion of solution preparation, students vortexed all containers and loaded their samples into the autosampler.

Next, students were instructed on how to use the instrument software and received guidance on basic principles of sample batch design. The final batch parameters were approved by the TAs before batch submission to the instrument queue for analysis. Representative calibration curves, produced by the MassHunter software using student data, are shown in **Figure V.3**. All student data presented herein are done with the explicit consent of the students who produced the data.

During "Lab Period 2", students repeated the procedures followed during lab period 1, except now using Matrix B. As above, calibration standards were made in Matrix B from the 10 ng/mL working stock Hg solution. Water was used to dilute the method blank, SRM, and fish sample 3.5-fold to match the composition of Matrix B. Following sample preparation and batch submission to the instrument software queue, students engaged in a TA-led discussion about data analysis. Students examined data collected during the previous lab period by both themselves and the groups in other lab sections. They were asked to first calculate the percent error of the average SRM concentrations of each run (Equation 1). Sample and SRM masses from the microwave digestion were provided in a shared README file. Using this data, students calculated the expected mercury concentration for the SRM in each matrix and compared these values to the acquired data.

Equation 1: $((\text{expected } [\text{SRM}] - \text{observed } [\text{SRM}]) / \text{expected } [\text{SRM}]) * 100$

A review of recently published literature that involves ICP-MS-based analysis of Hg shows that recovery rates around 90 to 95% are accepted as sufficient for method validation.[23-25] Students validated the method by checking whether the percent error calculated from Equation 1 is within 10%. Students were asked to determine which matrix performed better in combination with other parameters by comparing expected and observed SRM mercury concentrations. Then, students assessed which KED voltage was the most optimal by comparing the datasets from several different KED voltages (e.g. 0V, 2V, 6V). For the final phase of the experiment, students were asked to use the data obtained from the optimal set of method parameters to evaluate whether their fish sample would be safe to consume according to FDA guidelines.

Educational outcomes for this exercise were assessed through a combination of pre- and post-lab surveys and a written lab report assignment. All students were provided with a short list of questions to address in their report concerning method validation and optimization, results, and interpretation. Students from all groups determined that Matrix B, with its hydrochloric acid component, served as a superior matrix for mercury analysis. Students determined that the choice in optimal gas mode could vary based on the applied KED. In many cases, students found that the no gas mode and helium gas mode with a KED of 6V to be the optimal method based on SRM error (%). An example of parameter optimization analysis as performed by the students is shown in **Table V.2**.

Pedagogical Evaluation and Student Outcomes

The pedagogical benefits of this experiment were evaluated through student laboratory reports, student surveys, and anecdotal communication from students throughout and following the exercise.

Student lab reports were structured similar to scientific papers in the Journal of Analytical Chemistry. A detailed rubric was used by the TAs to grade each report. This rubric outlined strict criteria outlined with the aforementioned learning outcomes that must be met by the students in order to achieve a high grade. The discussion and conclusion section of the lab report required students to successfully address the following items:

- Is the method valid? Justify your answer. What does having a valid method allow you to do?
- Which matrix performs best? Explain your selection.
- Do you notice any effects of KED? Is there a KED voltage that performs best?

- Which combination of parameters would you use to achieve optimal results? How did you come to this conclusion?

The discussion and conclusion section was worth a total of 27 points and the scores were distributed as shown in **Figure V.4**. The majority of students performed exceptionally well, scoring above 25 points out of 27 (above an A-). Only 5 students out of the 38 who submitted the report scored below a C. These lab report scores indicate that this laboratory exercise successfully taught the students the desired learning goals.

Below is an example conclusion from a student lab report that demonstrates student understanding of the laboratory exercise.

> "With this study, an accurate measurement was able to be made of store-bought Skipjack tuna. Utilizing varying experimental conditions such as different matrices, KED, and gas modes, an optimal condition was able to be found and used. Matrix B, containing 1.6% HNO_3, 0.34% H_2O_2, and 0.21% HCl, 6V of KED and a No Gas mode yielded the lowest deviations from a NIST-Certified SRM at roughly 1.59%. The concentration of mercury in this sample was found to be roughly 43ppb in comparison the FDA reported 95% confidence intervals of 120 ppb to 140 ppb. Therefore, this method of analysis can verify that the mercury contents of the store-bought Skipjack tuna is within safe ranges for human consumption which is essential due to mercury being a potent toxin in high quantities."

Anecdotally, students expressed a significant amount of enthusiasm and engagement throughout the lab exercise. Several students provided unprompted feedback expressing appreciation for the overall rigor, robustness, and practical nature of the exercise. Perhaps most importantly, a number of students informed the TAs that this exercise significantly improved their perception of analytical chemistry and led to a greater interest in the field.

Surveys were administered prior to and after the conclusion of the lab exercise to gauge the educational benefits of the class. Students were asked to rate their understanding on a scale of 1-10, 10 being the greatest understanding. The surveys assessed students' general understanding of ICP-MS, how a SRM is used for method verification, polyatomic interference, the purpose of using different gas modes, and the application of KED (**Figure V.5**). The students' understanding increased after the lab in all areas. The class also resulted in the students feeling more confident in their ability to explain the concept of KED to a colleague. In the post-lab survey, there was an additional question that asked, "Did this lab help to improve your understanding of ICP-MS and undergraduate-level analytical chemistry techniques and data analysis?", to which 98% of students responded "yes".

Our objective in this lab exercise was to use the methodology employed by the FDA to teach advanced method development and parameter optimization skills. Students were able to successfully select the most optimal ICP-MS method by comparing the experimentally determined and expected values of mercury in the SRM. Using this information, students could inform the report reader about whether the fish was safe for human consumption according to FDA standards. Overall, the real-world relevance of the experiment kept students engaged and interested in the lab exercise.

Conclusions

This laboratory exercise was successfully incorporated into an analytical chemistry class at UCLA. For this exercise, mercury concentration determination with ICP-MS was performed on consumer-grade fish samples. However, this exercise can be adjusted accordingly to be implemented into any course curriculum that aims to teach the concept of optimizing instrument parameters for measuring real world samples. The utilization of FDA-approved practices introduces students to real-life applications of government-level analytical chemistry techniques for food safety analysis. The class provides students with hands-on practical lab work experience and discussion-focused data interpretation which promotes development of analytical skills essential for aspiring analytical chemists. The pre- and post- lab surveys and laboratory reports highlight student growth in ICP-MS data acquisition, method optimization, and data analysis.

Figures

Figure V.1

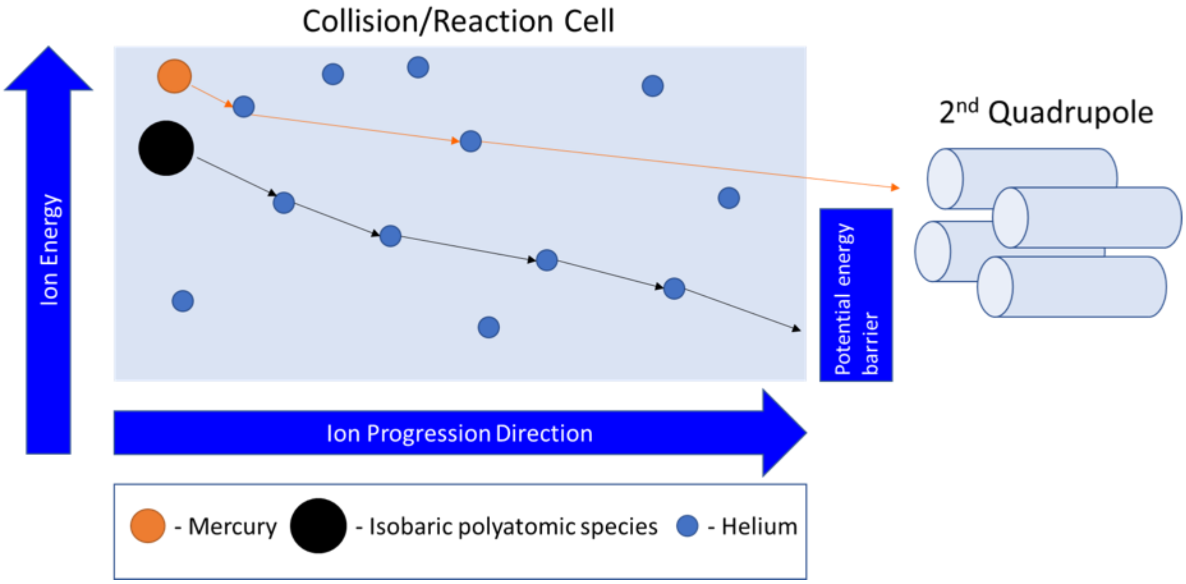

Figure V.1. Kinetic energy discrimination can be used to suppress polyatomic interference (or isobaric interference). Isobaric polyatomic species have larger collision cross sectional areas compared to the target molecule (^{201}Hg, orange spheres) and experience more collisions as they travel through the helium (blue spheres)-filled collision/reaction cell. The resulting kinetic energy difference between the target atoms of interest and the isobaric polyatomic species (black spheres) can be taken advantage of by utilizing an energy filter between the cell and the 2nd quadrupole, ensuring that only the analytes enter the quadrupole analyzer. By adjusting the energy difference between the cell and the quadrupole, the potential energy barrier that ions need to overcome (depicted as KED voltages in this experiment) can be varied.

Figure V.2

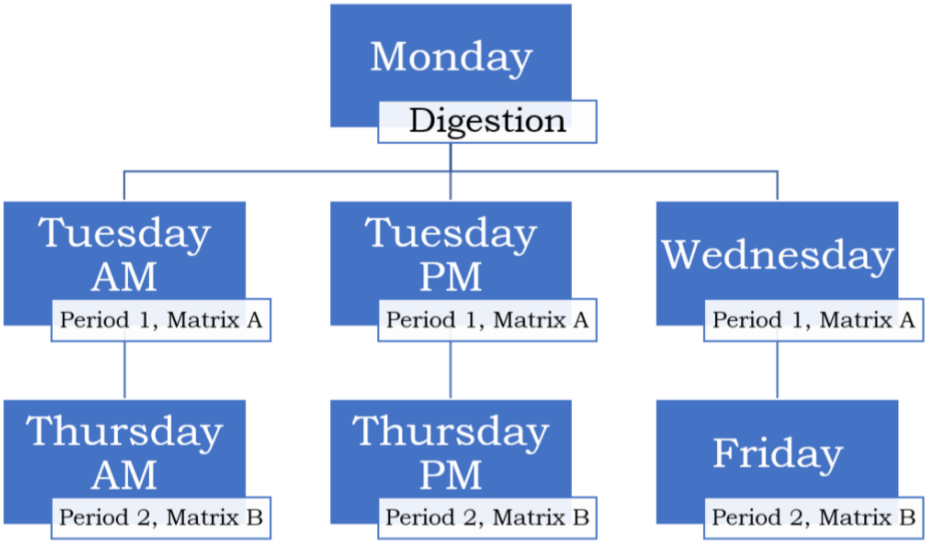

Figure V.2. Laboratory section timelines. On Monday samples were delivered to the ICP-MS core at the California NanoSystems Institute by the TAs. These samples were digested following the methods described above by the core staff and picked up by the TAs the following morning prior to the Tuesday AM section. During Period 1 samples were analyzed using Matrix A. Period 2 followed a similar protocol to Period 1 but instead used Matrix B. Data from each of the three sections was compiled in a central repository to compare data across periods.

Figure V.3

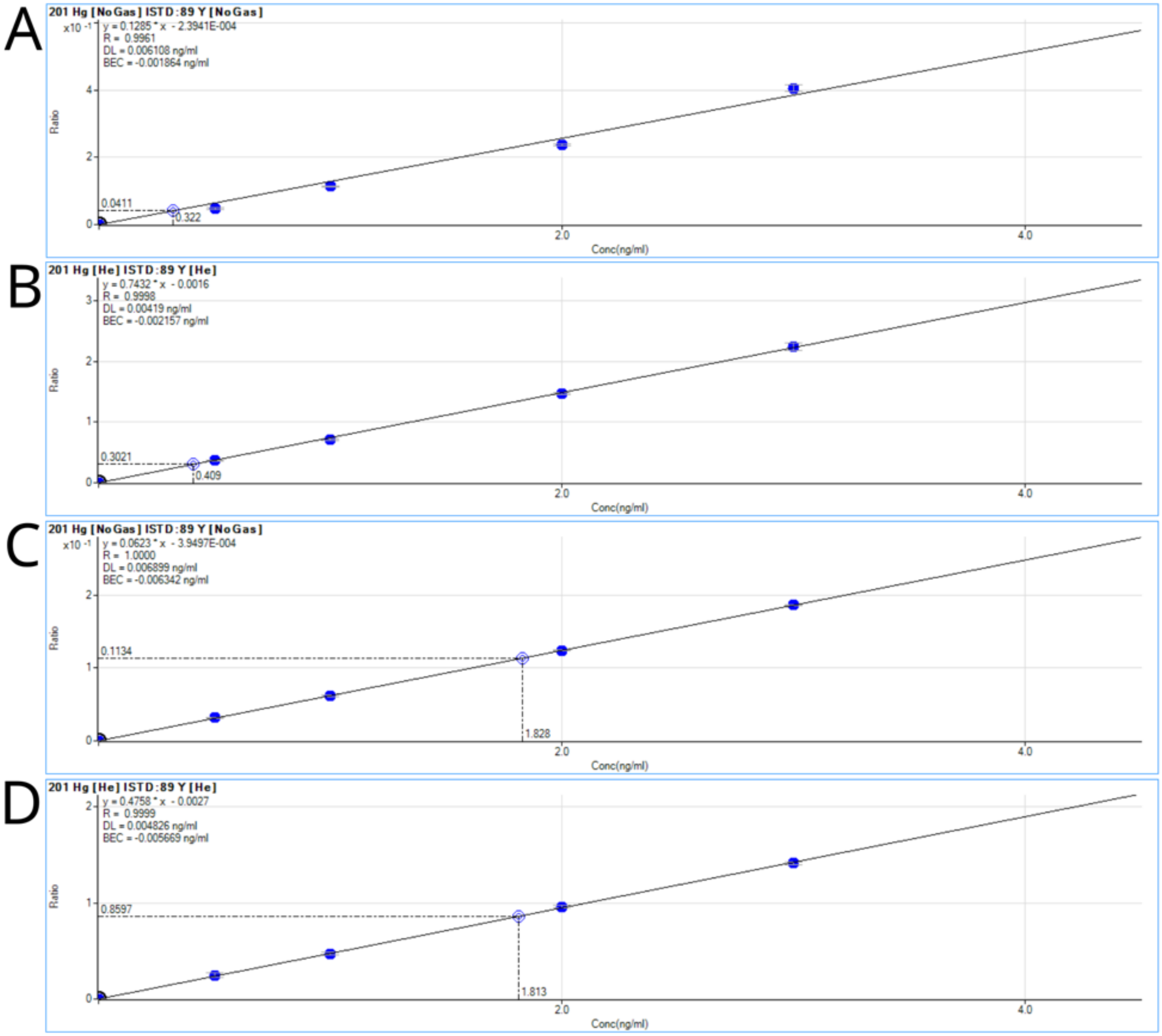

Figure V.3. Calibration curves produced from student data. The y-axis is expressed as the ratio between analyte signal (Hg) to internal standard (Y). A) Matrix A in no gas mode, B) Matrix A in helium mode, C) Matrix B in no gas mode, and D) Matrix B in helium mode. Overall linearity was excellent with R^2 values ranging from 0.980 to 1.000.

Figure V.4

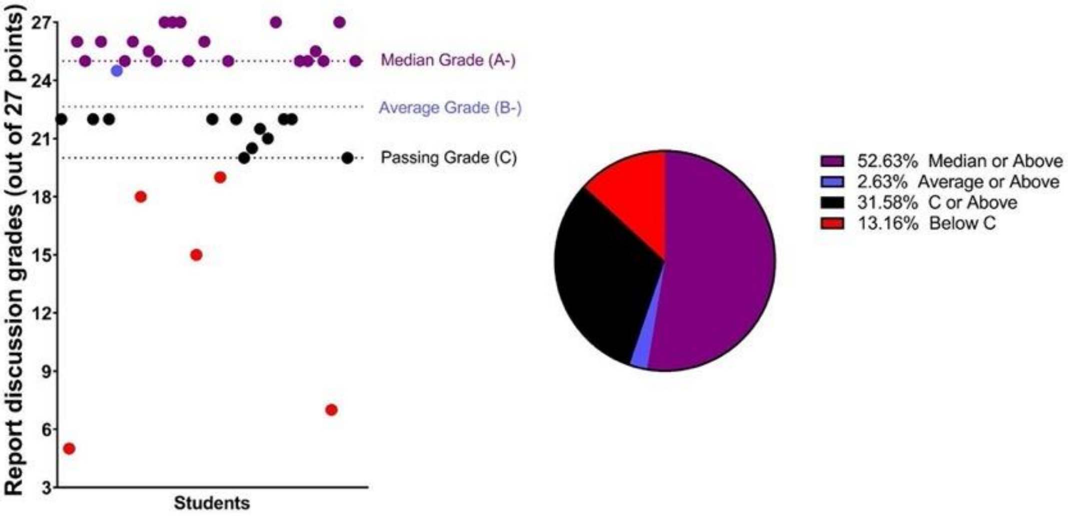

Figure 4. The score distribution of the discussion section of the reports. Each point represents an individual student. This section specifically evaluates whether the learning objectives stated above were achieved.

Figure V.5

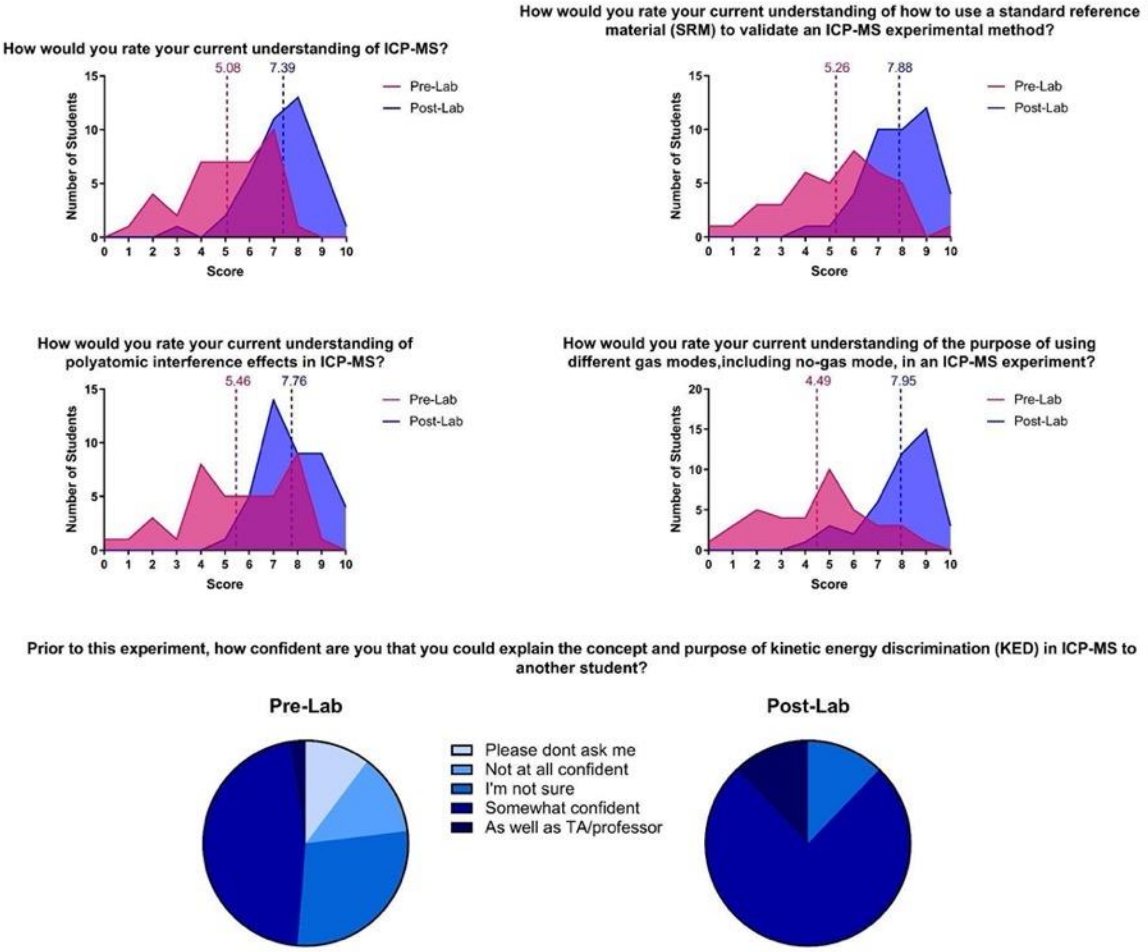
How would you rate your current understanding of ICP-MS?

How would you rate your current understanding of how to use a standard reference material (SRM) to validate an ICP-MS experimental method?

How would you rate your current understanding of polyatomic interference effects in ICP-MS?

How would you rate your current understanding of the purpose of using different gas modes,including no-gas mode, in an ICP-MS experiment?

Prior to this experiment, how confident are you that you could explain the concept and purpose of kinetic energy discrimination (KED) in ICP-MS to another student?

Pre-Lab

Post-Lab

Figure 5. Student responses to pre- and post-lab surveys. The numbers listed above the dashed lines are the mean of the probability distributions.

Table V.1

.

RF Power	1550 W	*Nebulizer Pump*	0.10 revolutions per second
RF Matching	1.80 V	*S/C Temp*	2°C
Sampling Depth	8.0 mm	*Gas Switch*	Dilution Gas
Carrier Gas	1.00 L/min	*Makeup/Dilution Gas*	0.20 L/min
Option Gas	0.0%		

Table 1. Instrument parameters

Table V.2

Matrix	*Mode*	*KED (V)*	*Fish (ng/mL)*	*Mean SRM (ng/mL)*	*SRM error (%)*	*Error within 10% Y/N*
A	No Gas	0V	0.180	2.140	21.64	NO
A	He Gas	0V	0.179	2.060	17.12	NO
A	No Gas	2V	0.180	2.051	16.60	NO
A	He Gas	2V	0.179	1.873	6.453	YES
A	No Gas	6V	0.194	2.233	26.93	NO
A	He Gas	6V	0.230	2.024	15.03	NO
B	No Gas	0V	0.284	1.959	7.423	YES
B	He Gas	0V	0.274	1.912	4.849	YES
B	No Gas	2V	0.266	1.976	8.367	YES
B	He Gas	2V	0.280	1.955	7.236	YES
B	No Gas	6V	0.268	1.852	1.589	YES
B	He Gas	6V	0.237	1.784	-2.147	YES

Table 2. Student-generated summary of data for determining the optimal parameter combination.

References

1. Metals and Your Food | FDA. https://www.fda.gov/food/chemicals-metals-pesticides-food/metals-and-your-food. Accession date: 7/4/2022

2. Storelli, M. M., Barone, G., Piscitelli, G. & Marcotrigiano, G. O. Mercury in fish: Concentration vs. fish size and estimates of mercury intake. *Food Additives and Contaminants.* **24**, 1353–1357 (2007).

3. Fernandes Azevedo, B., Barros Furieri, L., Peçanha, F. M. I., Wiggers, G. A., Frizera Vassallo, P., Ronacher Simões, M., Fiorim, J., Rossi De Batista, P., Fioresi, M., Rossoni, L., Stefanon, I., Alonso, M. J., Salaices, M., & Valentim Vassallo, D. Toxic effects of mercury on the cardiovascular and central nervous systems. *J. Biomed. Biotechnol.* **2012**, (2012).

4. Storelli, M. M., Giacominelli Stuffler, R., Marcotrigiano, G. O. & Marcotrigian, G. O. Total and methylmercury residues in tuna-fish from the Mediterranean Sea. *Food Additives and Contaminants.* **19**, 715-720 (2002).

5. Mercury Concentrations in Fish from the FDA Monitoring Program (1990-2010) | FDA. https://www.fda.gov/food/metals/mercury-concentrations-fish-fda-monitoring-program-1990-2010. Accession date: 3/26/2022

6. Mercury Levels in Commercial Fish and Shellfish (1990-2012) | FDA. https://www.fda.gov/food/metals-and-your-food/mercury-levels-commercial-fish-and-shellfish-1990-2012. Accession date: 3/26/2022

7. Advice about Eating Fish. | FDA. https://www.fda.gov/food/consumers/advice-about-eating-fish. Accession date: 3/26/2022

8. Public Health Statement: Mercury | ATSDR. https://www.atsdr.cdc.gov/PHS/PHS.asp?id=112&tid=24. Accession date: 3/26/2022

9. Guidance for Industry: Action Levels for Poisonous or Deleterious Substances in Human Food and Animal Feed | FDA. https://www.fda.gov/regulatory-information/search-fda-guidance-documents/guidance-industry-action-levels-poisonous-or-deleterious-substances-human-food-and-animal-feed. Accession date: 3/26/2022

10. Elemental Analysis Manual for Food and Related Products. Version 1.2 (2020) | FDA. https://www.fda.gov/media/87509/download. Accession date: 3/26/2022

11. Pröfrock, D., Leonhard, P., Wilbur, S. & Prange, A. Sensitive, simultaneous determination of P, S, Cl, Br and I containing pesticides in environmental samples by GC hyphenated with collision-cell ICP-MS. *J. Anal. At. Spectrom.* **19**, 623–631 (2004).

12. Allibone, J., Fatemian, E. & Walker, P. J. Determination of mercury in potable water by ICP-MS using gold as a stabilising agent. *J. Anal. At. Spectrom.* **14**, 235–239 (1999).

13. Nardi, E. P., Evangelista, F. S., Tormen, L., SaintṔierre, T. D., Curtius, A. J., Souza, S. S. d., & Barbosa, F. The use of inductively coupled plasma mass spectrometry (ICP-MS) for the determination of toxic and essential elements in different types of food samples. *Food Chem.* **112**, 727–732 (2009).

14. Maione, C., De Paula, E. S., Gallimberti, M., Batista, B. L., Campiglia, A. D., Barbosa, F., & Barbosa, R. M. Comparative study of data mining techniques for the authentication of organic grape juice based on ICP-MS analysis. *Expert Syst. Appl.* **49**, 60–73 (2016).

15. Ammann, A. A. Inductively coupled plasma mass spectrometry (ICP MS): a versatile tool. *J. Mass Spectrom.* **42**, 419–427 (2007).

16. Sanders, J. K. Inductively Coupled Plasma-Mass Spectrometry: Practices and Techniques (Taylor, Howard E.). *J. Chem. Educ.* **78**, 1465 (2001).

17. Donnell, A. M., Nahan, K., Holloway, D. & Vonderheide, A. P. Determination of Arsenic in Sinus Wash and Tap Water by Inductively Coupled Plasma–Mass Spectrometry. *J. Chem. Educ.* **93**, 738–741 (2016).

18. He, P., Colón, L. A. & Aga, D. S. Determination of Total Arsenic and Speciation in Apple Juice by Liquid Chromatography–Inductively Coupled Plasma Mass Spectrometry: An Experiment for the Analytical Chemistry Laboratory. *J. Chem. Educ.* **93**, 1939–1944 (2016).

19. Duedahl-Olesen, L., Holmfred, E., Niklas, A. A., Nielsen, I. K. & Sloth, J. J. Case Study Teaching for Active Learning on Analytical Quality Assurance Concepts in Relation to Food Safety Exposure Assessment. *J. Chem. Educ.* **98**, 3776–3783 (2021).

20. Neu, H. M., Lee, M., Pritts, J. D., Sherman, A. R. & Michel, S. L. J. Seeing the 'Unseeable,' A Student-Led Activity to Identify Metals in Drinking Water. *J. Chem. Educ.* **97**, 3690–3696 (2020).

21. Yamada, N. Kinetic energy discrimination in collision/reaction cell ICP-MS: Theoretical review of principles and limitations. *Spectrochimica Acta - Part B Atomic Spectroscopy.* **110**, 31–44 (2015).

22. SRM 1947 - Lake Michigan Fish Tissue | NIST. https://www-s.nist.gov/srmors/view_detail.cfm?srm=1947 Accession date: 3/26/2022

23. Djedjibegovic, J., Larssen, T., Skrbo, A., Marjanović, A. & Sober, M. Contents of cadmium, copper, mercury and lead in fish from the Neretva river (Bosnia and Herzegovina) determined by inductively coupled plasma mass spectrometry (ICP-MS). *Food Chem.* **131**, 469–476 (2012).

24. Kenduzler, E., Ates, M., Arslan, Z., McHenry, M. & Tchounwou, P. B. Determination of mercury in fish otoliths by cold vapor generation inductively coupled plasma mass spectrometry (CVG-ICP-MS). *Talanta.* **93**, 404–410 (2012).

25. Zhu, S., Chen, B., He, M., Huang, T. & Hu, B. Speciation of mercury in water and fish samples by HPLC-ICP-MS after magnetic solid phase extraction. *Talanta.* **171**, 213–219 (2017).

CHAPTER VI

Conclusion

Development and Validation of RPV-PLSR

I worked on a variety of projects throughout my graduate research. My focus, however, was on developing a new voltammetry method called rapid pulse voltammetry coupled with partial least squares regression analysis (RPV-PLSR). The published or soon to be published work on RPV-PLSR was covered in chapters 2 and 3. This chapter covers unpublished work done that provided foundations and validation of the RPV-PLSR technique. I worked on the RPV-PLSR project with Cameron Movassaghi. We both designed and carried out *in vitro* experiments. I optimized surgeries for and performed *in vivo* experiments. Cameron coded the RPV software, PLSR models, and Bayesian optimization models.

The RPV-PLSR technique uses faradaic and capacitive current to identify and quantify neurotransmitters *in vivo* across phasic and tonic timescales. The initial waveform for dopamine and serotonin co-detection[1] (**Fig. VI.1a**) was developed by former group members using an intelligent pulse design approach inspired by VETs[2, 3] and was based on analyte peak potentials in fast scan cyclic voltammetry (FSCV) waveforms traditionally used to detect dopamine[4] or serotonin.[5] Employing counter pulses (*e.g.*, E_3 in **Fig. VI.1a**) completes the redox cycle and generates additional information to confirm analyte identity, as demonstrated in voltammetric electronic tongue (VET) pulse design.[2, 3] Calibration curves (**Fig. VI.1b**) were produced in the presence of the physiologically relevant interferents 3,4-dihydroxyphenylacetic acid (DOPAC; 100 μM) and 5-hydroxyindoleacetic acid (5HIAA; 20 μM). Using six principal components, the R2 value of calibration (*i.e.*, R2Y; goodness of fit) was 0.98, while the cross-validated R2 value (*i.e.*, Q2Y; proxy for predictive accuracy) was 0.90 (**Fig. VI.1c**).

Faradaic and Nonfaradaic Currents in Preprocessing & Feature Selection

The use of non-faradaic current by the PLSR model was supported by an analysis of the PLSR loadings (**Fig. VI.2**), which are linear combinations of the original variables and weighted projection coefficients.[6] Loading vectors with the greatest absolute magnitude in the factor space represent greater correlation. To visualize regions of the voltammograms most informative for the model, a moving average kernel was applied to map each variable to low, medium, or high correlation (*i.e.*, 0%, 50%, or 100% shading, respectively). Areas with the highest shading heights were most useful for that analyte. As an example, the current response of the second pulse (points 250-500) has high red shading during capacitive charging, illustrating non-faradaic contributions to modeling dopamine during this pulse. Meanwhile, most of the decay of the second pulse, which included faradaic and non-faradaic contributions, was heavily used for modeling serotonin. The shading of all four capacitive current regions supports the key idea that non-background subtracted methods like RPV generate relevant information needed to specify analytes and their concentrations through the inclusion of capacitive current at each step. To confirm these findings, a variable importance in the projection (VIP) score was calculated for each feature. Variable (feature) selection is the process of selecting features to present to the model as input; VIP scores are PLSR-specific feature-selection metrics.[7] The VIP score calculations confirmed the findings of the loadings analysis by spanning non-faradaic areas of the voltammogram. The VIP scores also demonstrated that preprocessing can be used a priori to emphasize certain areas of the pulse response before the model sees the data; normalization resulted in magnitude-related importance (231/1000 points>1 for VIP scores), while standardization resulted in variance-related importance (518/1000 points>1 for VIP scores).

Multi-electrode Training and Comparison to Conventional Methods

As a proof of concept for training across multiple electrodes, three PEDOT:Nafion-coated electrodes were used to obtain training, cross-validation, and test data (**Fig. VI.3**). To account for intra-sample variability, ±10 voltammograms were extracted from the maximum temporal evolution of post-injection anodic current, resulting in 21 voltammograms per sample (roughly 730 voltammograms total). Data were analyzed by PLSR or principle component regression (PCR). Background subtraction (BGS) prior to analysis is denoted as BGS or non-BGS. Our proposed method is RPV-PLSR (non-BGS). For comparison, we included the historically used FSCV-PCR (BGS)[8] and recently introduced FSCV-PCR (non-BGS),[9] along with several other combinations. For direct comparison of these methods, all samples were mean centered and normalized.

The R2Y and Q2Y scores (**Fig VI.3a**) are highest for RPV-PLSR (non-BGS), followed by RPV-PCR (non-BGS). The RPV models outperformed all other combinations. All PLSR models required the fewest components during hyperparameter tuning (7). Of the PCR methods, non-BGS methods required fewer components (8 or 9) compared to BGS (10), supporting the parsimony of PLSR (*i.e.*, a "quicker learner"). Fewer components were required for non-BGS methods, suggesting that the background currents contain useful, covariate information. We compared learning curves for RPV-PLSR *vs.* FSCV-PCR under background[8] *vs.* non-background[9] subtracted conditions (BGS and non-BGS, respectively; **Fig. VI.3b**). Avoiding background subtraction resulted in delayed but rapid increases in bootstrapped Q2Y, suggesting that non-BGS models learn from low magnitude, non-faradaic information when provided sufficient training data (*i.e.*, more evidence for generalizability of larger training sets[9]). Notably, RPV-PLSR (non-BGS) had the most rapid Q2Y learning curve, required less training data, and had the highest R2Y, indicating it converges first. For this small training set, RPV-PLSR (non-BGS) best predicted the test set (*i.e.*, 1 μM dopamine/0 μM serotonin and 1 μM serotonin/0 μM dopamine; **Fig. VI.3c, d**).

In vitro Validation of RPV-PLSR Waveforms

Below, I describe how the initial RPV waveform (**Fig. VI.1a**) was evaluated in the context of multiple challenges to mimic dynamic *in vivo* matrices. A training set (*i.e.*, calibration set) is defined as known concentrations of analyte mixtures, *i.e.*, "standards", used to train a PLSR model. A test set was defined as known concentrations of analyte mixtures not used during training but instead used to test how well a model performs. All calibration sets encompassed physiologically relevant mixtures of serotonin (0-500 nM, 50 nM increments) and dopamine (0-1000 nM, 100 nM increments), in artificial cerebrospinal fluid (aCSF) and in the presence of interferents (*i.e.*, metabolites, pH, ions) to simulate *in vivo* environments.

For more robust training sets in the future, a fractional factorial box design (**Table VI.1**) will be used. This chemometric approach involves a multi-dimensional 'box' spanning analytes, their concentrations, and experimental conditions of interest.[10, 11] A fractional approach was biased towards low analyte concentrations and small relative changes because high accuracy and precision in the nM range are important for monitoring basal and stimulated neurotransmitter levels *in vivo* using a single technique. A fractional approach further avoids a full factorial design, which would require orders of magnitude (and prohibitively) more calibration samples. In contrast, traditional calibration sets are less information-rich and can lead to spurious correlations when training a method with overlapping signals arising from multiple analytes and interferents.[10]

As a general procedure, calibration standards were injected in pseudo-random order (the order was randomized, but the same randomized order was injected each time) into a flow cell. Replicate injections accounted for inter-run variability (repeatability). Accruing training data over multiple days and electrodes accounted for intra-run variability (reproducibility).[9, 11, 12] The long-term goal is to accumulate training sets over the course of the project.

RPV-PLSR Can Be Trained to Account for Changes in pH

Decreases in pH occur *in vivo* in response to coordinated neural activity, which increases carbonic acid[13] and can affect capacitive current.[14] The effects of pH on RPV-PLSR were tested, choosing first to explore transient decreases in pH also known to occur as neurotransmitters are released extracellularly through presynaptic membrane fusion, which releases vesicular protons.[15] Calibration standards sets were prepared in full at three physiologically relevant pH values (7.1, 7.2, 7.3) and injected into a flow cell with continuous delivery of aCSF (pH 7.3) to simulate small bursts of pH change associated with tonic acitivity.[16-18] A single PLSR model was trained by combining the calibration sets obtained at the three pH values. This model predicted serotonin and dopamine levels in the test set with 12% and 33% error, respectively (**Fig. VI.4a**). The precision (standard deviation; 10 nM and 26 nM for serotonin and serotonin, respectively; or ~5% relative standard deviation in each case) of the predictions across pH was consistent meaning that pH changes were not being confused with analyte predictions. I suspect that dopamine accuracy was lower systematically due to dopamine oxidation (predicted dopamine levels were ~200 nM less than expected) associated with lengthy experiments. In the future, dopamine stability can be increased using nitrogen purging or adding (and training on) physiological ascorbate levels.[19] Regardless, these preliminary results show that RPV-PLSR models can be trained across physiologically relevant pH changes to improve the robustness of dopamine and serotonin predictions.

Cation Interferents Can Be Identified

Cationic interferent concentrations (*e.g.*, Na^+, K^+, Ca^{2+}) fluctuate in the extracellular space upon neuronal stimulation due to the generation and recovery from action potentials. Cationic gradient can affect double-layer capacitance.[20-22] I generated training sets in aCSF with 3.5 mM KCl and 147 mM NaCl +(normal) and isotonic 120 mM KCl and 31 mM NaCl (altered cation (AC)) buffers.[22] When the PLSR model was trained using only normal aCSF calibration standards, but used to predict test samples in AC aCSF, serotonin was predicted with high accuracy (8% error) but not dopamine (240% error) (**Fig. VI.4b**). When the model was trained with both normal and AC aCSF calibration sets, test samples containing either normal or AC aCSF for serotonin (10% error) and dopamine (4% error) were both predicted with high accuracy (**Fig. VI.4c**). Together, the pH and AC experiments demonstrated that when PLSR models encounter interferents, they can correct for interferent effects with more information-rich training data.

Increases in capacitive current were evident when AC aCSF was injected compared to normal aCSF. Nonetheless, the accuracy of serotonin predictions in varying [K^+] and [Na^+] without explicit training demonstrated that pulse waveforms can predict analyte-specific information even in the presence of interferents that affect capacitive current. Using Bayesian optimization detailed in Chapter 3, the aim is to identify 'interferent agnostic' waveforms (*i.e.*, waveforms that accurately predict serotonin and dopamine regardless of physiological changes in interferents.) We have serendipitously found that the initial RPV-PLSR is agnostic for K^+ and Na^+ (**Fig. VI.4b,c**). The effects of interferents whose concentrations change during and after a stimulus are not corrected for by conventional FSCV background subtraction because backgrounds are determined in a static manner prior to stimulation; the dynamic effects of interferants on capacitive and Faradaic current remain.[4, 21, 23] Nonetheless, the literature suggests that physiological changes in pH and divalent cation concentrations pose less of an interference problem for biogenic amines when using pulse voltammetry,[24] as opposed to FSCV,[25] especially when electrodes include Nafion surface coatings.[1, 26]

Simulation of Phasic and Tonic Detection

I used RPV-PLSR to predict stimulated and basal serotonin and dopamine concentrations, simultaneously, *in vivo*.[1] The RPV-PLSR approach avoids background subtraction enabling basal neurotransmitter predictions. However, our initial prediction accuracies for basal serotonin and dopamine levels were not very accurate.[1] Using an expanded calibration set, we collected preliminary data using our lead RPV waveform to predict small increases in serotonin and dopamine (simulated phasic concentrations *via* flow cell injections), as well as changes in background dopamine and serotonin levels (simulated tonic changes *via* changes in mobile phases containing 60 nM and 110 nM serotonin and dopamine, respectively) (**Fig. VI.4d**).[27, 28] Predicted "basal" and "stimulated" dopamine levels showed <10% prediction errors. However, predicted "basal" and "stimulated" serotonin levels had >10% errors. While we still have room for improvement, these preliminary data illustrate the approach for testing subsequent models for their ability to predict low basal levels and small stimulated increases in dopamine and serotonin.

Structurally Similar Interferents and Electrode Drift

Neurotransmitter metabolites with structures similar to serotonin and dopamine pose the greatest challenge for voltammetry because of highly overlapping electrochemical characteristics.[29] In preliminary experiments, we used our lead RPV waveform and PLSR to predict test samples containing 1000 nM serotonin and dopamine in the presence of 500 nM additions of 5-HIAA, DOPAC, ascorbic acid (AA), or uric acid (UA) (**Fig. VI.5a,b**). The calibration set contained concentrations of serotonin and dopamine that varied; metabolite and interferent levels were held constant at a relevant background level (100 μM DOPAC, 20 μM 5-HIAA, 200 μM AA, and 100 μM UA), unless denoted by 500 nM additions, to simulate metabolite concentration changes, as expected *in vivo*.[30-32]

The above experiments were also used to test different and novel data processing and drift training methods. The PLSR model was trained to account for drift using voltammograms collected throughout the experiment while aCSF containing interferents was flowed and injections were not occurring (~2 h). Data, in which drift was evident, were extracted from these background epochs and labeled as 'zero' analyte concentrations to teach the model what drifting, as opposed to analyte-containing, voltammograms look like. These 'drift zeroes' were in addition to data from injections of aCSF alone (*i.e.*, blanks) to account for flow cell injection and pump artifacts. Our 'drift training' procedure reduced test set prediction errors from as much as 93% to 5% for serotonin and 23% to 6.7% for dopamine (**Fig. VI.5c, d**). The drift voltammograms were taken only from the training data, but were able to correct the drift present in the test data obtained much later in the day, suggesting this procedure is generalizable.

Notably, dopamine predictions were confounded by the presence of DOPAC when not trained on varying concentrations of DOPAC (**Fig. VI.5d**). To improve dopamine/DOPAC differentiation, the model was calibrated using different concentrations of dopamine and DOPAC. This greatly improved dopamine test set prediction accuracy (3% error), suggesting that metabolites should be included in calibration sets as needed (**Fig. VI.5e**). These preliminary data illustrate that, like the pH and cation experiments, experiments can be designed to identify and quantify the effects of specific interferents—DOPAC in this case.

Analyte prediction accuracy was further improved using calibration set “bracketing”. That is, the calibration set was injected before and after the test set to account for calibration changes occurring over the course of the experiment (*i.e.*, drift, fouling). This is essentially the concept of using both ‘pre-calibration’ *vs.* ‘post-calibration’ fouled electrodes to obtain training data.[33, 34] When using calibration bracketing combined with drift training, the precision and accuracy of dopamine predictions improved (**Fig. VI.5e-g**).

Pre- and Post-Calibration *in vivo*

It was observed empirically that electrode responses were altered in mins to ~1 h after *in vivo* implantation, making pre-fouling data most different from *in vivo* and post-fouling data (**Fig. VI.6a**).[35] This presented difficulties for generalizing *in vitro* training data to *in vivo* analysis. The *in vitro* test sets obtained before and after an electrode was implanted *in vivo* were used to investigate the merit of combining pre- and post-fouled calibration data into a single model (**Fig. VI.6b**). When the RPV-PLSR model contained only pre-fouled calibration data, it could only accurately predict test data obtained using an electrode that had not been implanted in tissue, and not test data obtained on the same electrode after fouling (*i.e.*, after *in vivo* implantation for ~6 h). Similarly, when the model was trained on post-fouled calibration data, it could only accurately predict test data acquired from an electrode that had been placed in brain tissue. However, when we combined pre- and post-fouled calibration data into a single PLSR model, the model predicted both the pre- and post-test data with high accuracy. Taken together with the bracketing approach (**Fig. VI.5g**), this finding supports the combined use of pre- and post-fouled training data to quantify *in vivo* data (**Fig. VI.6b**). This training approach for a generalizable model *in vivo* is an advantage for acute animal work over human work, where collecting post-implantation calibration data on the implanted electrode is not possible.[36] For future RPV-PLSR *in vivo* experiments done by our group, we will wait ~1 h post-implantation before collecting data since the greatest electrochemical effects of biofouling occurred within the first hour of *in vivo* experiments (**Fig. VI.6c,d**).

Conclusions and Future Directions

The RPV-PLSR technique can be calibrated *in vitro* with a high degree of goodness of fit. The loadings plots representing contributions from both serotonin and dopamine demonstrated that both Faradaic and capacitive currents are being used by the model to make analyte predictions. Recent literature using electrochemical impedance spectroscopy also suggests that there are analyte-specific contributions to capacitive current, which supports our reasoning for not background subtracting.[37] We compared RPV-PLSR to RPV or FSCV with PCR and FSCV with PLSR *in vitro*. Much like our findings *in vivo*, an RPV-PLSR non-background subtracted approach outperformed all other variations. The model not only performed the best but also learned the fastest, as shown by R2Y and Q2Y scores and learning curves.

When challenged, RPV-PLSR could not ignore changes in pH and cationic buffer composition *in vitro*. However, the model predicted dopamine and serotonin accurately when standards were made in these environments and then used to train the model. An advantage of RPV-PLSR is that basal and stimulated levels of neurotransmitters can be measured. Thus, we simulated basal and stimulated levels *in vitro* using the flow cell. Dopamine was predicted with ~10% error, while, serotonin predictions had ~ 20% error. We believe that if this experiment was repeated with our more robust training set described in **Table VI.1** that serotonin would be predicated with higher accuracy.

We developed a 'drift training' protocol that allowed serotonin and dopamine to be predicted accurately in the presence of their metabolites. To train for background current drift, portions of the background were labeled as 'zero' and added to the model. Using this method, we significantly improved predictions for serotonin and dopamine. Prediction accuracy was further improved by using 'bracketing' *in vitro.* To improve prediction accuracy *in vivo,* pre- and post-fouled training sets should be implemented and the experimenter should let the RPV waveform equilibrate for ~1 h post-implantation before starting measurements.

Developing a Picospritzing Method for in vivo Validation: *in vivo* Standard Addition

In future experiments, the RPV-PLSR waveforms will be initially validated *in vivo* by delivering serotonin, dopamine, and their mixtures directly into the brain near recording electrodes. This method allows for the control of the identity of the species producing electrode responses. Picospritzing (pressure ejection) and microiontophoresis have been used to deliver exogenous substances into the brain. Picospritzing, however, requires lower pipette concentrations and minimizes leak current.[38, 39] It controls the amount of substance ejected better than microiontophoresis and can deliver uncharged substances (*e.g.*, drugs); iontophoresis requires charge. Picospritzing has been used extensively to deliver serotonin or dopamine to study *in vivo* transporter function with no evidence of contributions from endogenously released neurotransmitter.[40-42]

This *in vivo* standard addition method will be carried out essentially as practiced by Daws and coworkers.[43] For picospritzing, each CFM will be coupled to a pulled four-barrel borosilicate glass pipette (~300 μM tip-tip separation) and implanted into the striatum. Pipettes will be calibrated to deliver serotonin, dopamine, or mixtures in aCSF with 100 μM ascorbate (200 μM concentrations of analyte; mixtures to mimic *in vivo* ratios). Neurotransmitters will be pressure ejected at 10 min intervals in pseudo-random order. The CFMs will be calibrated pre- and post-fouling for model training to account for changes in electrode sensitivity over the course of experiments in a within subjects' design.

Pilot experiments have been done in which 120 mM K^+ solution was picospritzed into the striatum. While the settings of the picospritzer need to be optimized, it was clear that RPV-PLSR can detect high K^+-induced increases in neurotransmitter release (**Fig. VI.7**). For future experiments, the settings 5-25 psi for 0.25-3.0 s are suggested.[44-46]

Pharmacological *in vivo* Validation

Here, DAT-Cre mice will be transfected with the excitatory opsin Chrimson. Previous literature from our group demonstrates that selective optical stimulation of dopamine cell bodies results in the release of dopamine and serotonin in the striatum.[47] To selectively release dopamine optogenetically, mice will be pretreated with *para*-chlorophenylalanine (PCPA) for three days to deplete serotonin levels. Two groups of mice will be used in the experiments. The first group will be transfected with Chrimson in dopamine cell bodies and undergo optogenetics. In this group, both dopamine and serotonin are expected to increase with optical stimulation. The second group will be pretreated with PCPA, transfected with Chrimson in dopamine cell bodies, and undergo optogenetic stimulation of dopamine cell bodies. In the second group, only dopamine release will be increased with optical stimulation. The relative concentrations of dopamine and serotonin release will be compared across groups to test whether the PLSR model does or does not confuse dopamine with serotonin when predicting the identity and concentration of analytes.

Prenatal Citalopram Exposure Promotes Resilience in Male Offspring Exposed to Maternal Stress

In addition to RPV, I worked on developing HPLC and microdialysis methods for a project on the effects of maternal stress. I assisted during the dissection of offspring brains at P7, P14, and P21. Dr. Sara Erwin and Dr. Merel Dagher carried out all of the chronic unpredictable stress, behavior experiments, and surgeries. They assisted in running HPLC and microdialysis experiments once I set up and tested the methods. Sara, Merel, and I designed the microdialysis experimental paradigms together. A manuscript detailing this project in its entirety is in preparation.

Mood and anxiety disorders are highly prevalent during pregnancy and can lead to adverse maternal and offspring outcomes. Selective serotonin reuptake inhibitors are the most common medications used to treat mood and anxiety disorders. Both human and animal studies suggest that serotonin signaling plays an important role in the vulnerability to and manifestation of stress-associated affective disorders. Moreover, the serotonin system is an early orchestrator of brain development. In this study, pregnant mice underwent chronic, unpredictable stress during the latter two-thirds of their pregnancies using ethologically relevant and/or mild stressors. Some of the mice received the serotonin-selective reuptake inhibitor antidepressant citalopram (Celexa) concomitantly in their drinking water. After birth, brain tissue serotonin levels at three developmentally relevant time points for serotonin system maturation were measured in the offspring. A subset of the adult offspring was assessed for long-term behavioral effects of *in utero* exposure to stress and/or citalopram. Finally, male adult offspring underwent microdialysis in the ventral hippocampus to investigate neurochemical effects.

The offspring of stressed mothers had higher serotonin tissue levels and protein concentrations in the forebrain at postnatal day seven compared to control animals. Adult male adult offspring displayed greater anxiety-like behavior and stress responsiveness than sex-matched control mice. These effects were rescued in male mice whose mothers were administered citalopram concomitant with stress. No changes were observed in basal or stimulated ventral hippocampal extracellular serotonin levels during adulthood. Yet, male adults exposed to *in utero* stress had increased kappa opioid receptor agonist-induced serotonin release in the presence of serotonin transporter inhibition, which was attenuated by *in utero* exposure to citalopram. These findings suggest that prenatal stress negatively impacts neurochemical and behavioral outcomes in offspring that persist into adulthood. These outcomes can be reversed with SSRI treatment during pregnancy.

Methods

Animals

Timed-pregnant CD 1 mice (N=75 purchased, 73 pregnant) were purchased from Charles River Laboratories (Hollister, CA) and studied. The dams were 12-24 weeks of age at the beginning of pregnancy. Dams were either singly housed (stressed groups) or housed in groups of 2-4 mice per cage until embryonic day 17 (E17). All dams were singly housed at E18 until their offspring were weaned at postnatal day 21 (P21).

Dams that received citalopram were dosed *via* drinking water. Citalopram hydrobromide (TCI America Cat#2370) was dissolved in 1.5% sucrose (260 mg/L).[48] Oral concentrations were based on concentrations that produced antidepressant-like effects in mice.[49, 50] This dose was found to produce blood serum levels of citalopram that fall within the human therapeutic range (30-200 ng/mL)[51] that crosses the placental barrier to fetus.[48] Each water bottle was filled with ~200 mL citalopram solution and was changed every three days. Control and stress only groups received plain drinking water. Water bottles for all groups were weighed daily to monitor liquid intake. Food and water were available *ad libitum* throughout the study, except for E16, when all dams were food-deprived for 22-24 h for the novelty suppressed feeding (NSF) test.

After weaning, offspring were housed in 2-5 same-sex siblings per cage. The light-dark cycle (12/12 h) was set to lights on at 0730 h (ZT0) in the colony room. The same light schedule was maintained in the rooms where behavior tests and microdialysis were carried out. The Association for Assessment and Accreditation of Laboratory Animal Care International has fully accredited UCLA. All animal care and use met the requirements of the NIH Guide for the Care and Use of Laboratory Animals, revised 2011. The UCLA Chancellor's Animal Research Committee (Institutional Animal Care and Use Committee) preapproved all procedures.

Chronic Unpredictable Stress Paradigm During Pregnancy

Experiments were carried out in six different cohorts of mice over four years. In the first cohort, only control and maternal chronic unpredictable stress (CUS) groups were studied. Later cohorts included control, CUS, CUS plus citalopram (CUS+CIT), and CIT. The initial cohorts only contained control and CUS groups to determine if stress-induced embryonic changes in serotonin[48] persisted in postnatal development. Some animals from each cohort were used for postnatal offspring tissue analysis, while remaining mice were used for adult offspring behavior testing and microdialysis.

Timed pregnant female mice arrived on E7 and were exposed to chronic unpredictable stress from E8 through E14, the developmental equivalent of post-conception day 22-64 in humans.[52] On E8, pregnant females in the stress groups were restrained, their ears were clipped for identification, and they were given an intraperitoneal (ip) saline injection as initial stressors. The maternal CUS paradigm was carried out as previously described[48] and is detailed in **Table VI.2**. Mice in the stressed groups were singly housed throughout the duration of the stress paradigm. On E9, stress dams were exposed to 1% 2,4,5-trimethylthiazole (Sigma Aldrich #W332518) in water (v/v), a volatile component of fox urine, which was placed on a nestlet square (200 μL) on the wire lid of their cage for 15 min. On E10, dams in the stress group were exposed to constant light overnight from ZT12-24. On E11, stressed dams were placed in a 3.8 cm diameter plastic restraint tube for 30 min.[53] On E12, they were exposed to constant white noise (70 dB) overnight from ZT12-24. The cage of each stressed dam was tilted at a 45° angle on E13 for the duration of the light cycle (ZT0-12).

On E14, stress dams were exposed overnight to ~85 g of sani-chip cage bedding saturated with 400 mL water from ZT12-24. On E15-17, all pregnant females, irrespective of group, underwent the following behavior tests, which were also stressors: open field test (OFT; E15), forced swim test (FST; E16), and the novelty suppressed feeding test (NSF; E17).

Postnatal Dissections and Tissue Collection

Offspring brains for neurochemical analyses were collected on P7, P14, and P21. At each postnatal developmental timepoint, 1-3 pups were randomly selected from each litter with fewer pups taken from smaller litters. The random selection process involved spreading out the pile of pups to pick animals in different areas of the nest to not introduce bias based on litter dynamics, *i.e.*, only picking pups from the top of the pile. The pups were weighed, their sex was identified, if possible, and they were transported individually to the procedure room. Pups were immediately sacrificed *via* decapitation without anesthesia. Their brains were rapidly removed and placed briefly in deionized water. The following brain regions were collected at P7: forebrain, midbrain, and hindbrain.[48] At P14 and P21, frontal cortex, hypothalamus, hippocampus, brain stem, striatum, and the intact remaining hemisphere were collected. Brain tissue samples were placed in Eppendorf tubes and immediately frozen on dry ice before storage in a -80° C freezer.

Tissue Sample Analysis

All analyses were performed using an Amuza HTEC-500 integrated HPLC system (Amuza Corporation, San Diego, CA) with an Amuza Insight autosampler for injecting standards and brain tissue extracts. Chromatographic separation for monoamine neurotransmitters and metabolites was attained using an Agilent Poroshell 120 column (SB C18, 3.0 mm, 100 mm, 2.7 µm particle size). The mobile phase for neurotransmitters consisted of 0.1 M monochloroacetic Acid (Sigma #402923), 0.2-0.4 g/L octanesulfonic acid

(Acros #41636), pH 2.6, 50 mg/L EDTA·Na_2 (Sigma #03682), 0.01% triethylamine (EMD TX1200), and 5-10% acetonitrile (EMD AX0145) in water purified *via* a Milli-Q Synthesis A10 system (EMD Millipore Corporation, Billerica, MA).

The amino acid separation employed a Phenomenex Kinetex LC Column (C18, 100 mm, 3 mm, 2.6 µm particle size, #00D 4462 Y0) column. The amino acid mobile phase consisted of 0.05-0.2 M sodium phosphate monobasic (Fluka #17844), 50 mg/L EDTA·Na_2 (Sigma #03682), pH 7.3-7.5, and 20-25% MeOH (EMD #MMX04751) in water purified *via* a Milli-Q Synthesis A10 system.

Column temperatures were maintained at 21-35 °C. The volumetric flow rates were 300-525 µL/min. Electrochemical detection was performed using an Amuza pure graphite (PG) working electrode with an applied potential of +600 mV *vs.* a Ag/AgCl reference electrode. Standards were prepared for serotonin (Sigma #H9523), 5-hydroxyindoleacetic acid 5-HIAA (Sigma # H8876), norepinephrine (Sigma # A9512), dopamine (Sigma # H8502), 3,4-dihydroxyphenylacetic acid (DOPAC) (Sigma #850217), homovanillic acid (HVA) (Sigma # H1252), phenylalanine (Sigma #78019), tryptophan (Sigma #51145), tyrosine (Sigma #93829), valine (Sigma #94619), isoleucine (Sigma #12752), and leucine (Sigma #L8000) in ice-cold sonication solution (0.1M glacial acetic acid and 1mg/mL EDTA-Na_2). Standard curves, which were run with each group of samples, encompassed analyte physiological concentration ranges (31-500 nM). Chromatographic run times were 12-18 min for neurotransmitters and 20-25 min for amino acids.

Microdialysis

Male offspring (N=25) undergoing microdialysis were implanted with guide cannulas at 3-6 months of age. Surgeries were carried out under aseptic conditions with isoflurane anesthesia, and carprofen and bupivacaine as systemic and local analgesics, respectively, on a KOPF Model 1900 Stereotaxic Alignment System (KOPF, Tujunga, CA). A CMA/7 guide cannula (Harvard Apparatus #CMAP000138) for a microdialysis probe was implanted with the tip in the vHPC (AP 3.6 mm, ML ±3.2 mm, DV 1.5 mm from Bregma). Each guide cannula was secured to the skull with Bosworth Trim II adhesive (Henry Schein #2509679). Animals recovered from surgery for at least three days before microdialysis. Following surgery, mice were given twice daily carprofen injections (5 mg/kg, 1 mg/mL, sc) for the first three days.

On the night before the first day of microdialysis (ZT10-12), each mouse was transferred to the testing room in its home cage where a CMA/7 microdialysis probe (2 mm length, 6 kDa cutoff, metal-free, CMA8010772) was inserted into the guide cannula. Subjects were placed into a new, smaller cage that had bedding from their home cage. Artificial cerebrospinal fluid (aCSF) (147 mM NaCl (Fluka #73575), 3.5 mM KCl (Fluka #05257), 1.0 mM $CaCl_2$ (Aldrich #499609), 1.0 mM NaH_2PO_4 (Fluka #17844), 2.5 mM $NaHCO_3$ (Fluka #88208), 1.2 mM $MgCl_2$ (Aldrich #449172), pH 7.3 ± 0.03 was continuously perfused through the probe *via* a liquid swivel (375/D/22QM, Instech Laboratories Inc., Plymouth Meeting, PA) at 0.3 µL/min for 14-16 h to stabilize the tissue around the probe. Subjects were tethered to the liquid swivel but otherwise could move freely in their home cages during the entirety of the microdialysis experiments.

Microdialysis experiments were carried out between ZT1-8 as previously described.[47, 54, 55] Basal dialysate samples were collected from ZT1-2, followed by three high K^+ stimulations each lasting 5 min, separated by an hour of aCSF infusion from ZT2-5. After the last high K^+ stimulation, animals were either (1) perfused with 10 µM citalopram into the vHPC for 2 h, (2) systemically injected with 10 mg/kg, ip, U50,588H (Sigma-Aldrich #D8040) or U69,593 (Sigma-Aldrich #U103), then perfused with 10 µM citalopram into the vHPC for 2 h, or (3) perfused with 10 µM citalopram into the vHPC for 2 h followed by an ip injection of 10 mg/kg U50,588 or U69,593.

Doses for citalopram, U50,588, and U69,593 were determined empirically through pilot experiments. The U50,588 dose was determined in a conditioned place aversion behavioral assay, where 10 mg/kg ip was found to induce the greatest aversion to the drug-paired side in male mice. Due to issues with manufacturer availability of U50,588, the kappa opioid agonist U69,593 at 10 mg/kg ip was substituted for U50,588 in the last seven mice.

Analysis of microdialysis samples was performed immediately after collection of each sample, *i.e.*, online,[54] using an Amuza HTEC 500 integrated HPLC system (Amuza Corporation, San Diego, CA) equipped with an Amuza Insight autosampler used for injecting standards and an Amuza EAS 20s online autoinjector for collecting and injecting dialysate samples. Chromatographic separation was achieved using an Amuza PP ODS III column (4.6 mm ID × 30 mm length, 2 µm particle diameter) and a phosphate-buffered mobile phase with 14.89 g/L NaH_2PO4 (Fluka #17844), 1.02 g/L Na_2HPO_4 (Thermo Scientific AC448160050), 2% MeOH (EMD #MX0475), 50 mg/L $EDTA \cdot Na_2$ (Sigma #03682), and 600 mg/L sodium decanesulfonate (TCI #I0348) in Optima LC/MS grade water (Fisher Scientific CAS# 7732 18 5).

The column temperature was maintained at 25 °C. The volumetric flow rate was 500 µL/min. Electrochemical detection was performed using an Amuza WE 3G graphite working electrode with an applied potential of +450 mV *vs.* an Ag/AgCl reference electrode. Dopamine (Sigma #H8502) and serotonin (Sigma #H9523) standards were prepared in a 1:1 mixture of mobile phase and aCSF. Standard curves, which were verified weekly, encompassed physiological concentration ranges (31 pM-10 nM). All online dialysate samples were collected at 5 min intervals at a dialysate flow rate of 2.5 µL/min and injected immediately onto the HPLC system for analysis. The ES280 PowerChrom Chromatography

Data System (CDS) Software (eDAQ, Denistone East, Australia) was used to collect, display, and analyze all chromatographic peaks.

Statistical Analysis

Statistical analyses were carried out using Prism, v.9.3.0 (GraphPad Inc., La Jolla, CA). Data are expressed as group means ± SEMs, with $P<0.05$ considered to be statistically significant.

Postnatal Tissue Analysis

One or two mice per treatment group were randomly selected for tissue neurotransmitter analysis at three different early postnatal timepoints (**Fig. VI.8A**). Brain regions from postnatal day 7, 14, and 21 (P7, P14, and P21, respectively) pups were analyzed. At P7, brains were sectioned into forebrain, midbrain, and hindbrain due to their small size. At P14 and P21, larger brains enabled dissection of frontal cortex, hypothalamus, hippocampus, brain stem, striatum, and the intact remaining hemisphere were collected. Only the frontal cortex, hippocampus, and striatum were analyzed *via* HPLC, the other regions were saved for future analysis. At P7, serotonin, norepinephrine, and dopamine levels normalized for tissue protein levels determined in forebrain, midbrain, and hindbrain showed no significant differences in control *vs.* CUS groups (**Fig. VI.9A-C**).

When tissue protein concentrations used to normalize neurotransmitter levels (as a proxy for tissue wet weight) were examined in greater detail, we found increases in forebrain but not midbrain or hindbrain protein levels in CUS mice compared to controls at P7 (**Fig. VI.9D-F**). Analysis of neurotransmitters without considering protein levels revealed that pups exposed to prenatal stress had increased serotonin and norepinephrine concentrations only in the forebrain (**Fig. VI.9G-I**). Concomitant treatment of stressed dams with CIT rescued the prenatal stress-induced increases in serotonin in the forebrain of P7 offspring

(**Fig. VI.9J**). No differences were observed in regional tissue neurotransmitter concentrations in P14 or P21 brains (data not shown).

Adult Offspring Neurochemistry

To assess the effects of prenatal stress with and without maternal SSRI treatment on adult offspring neurochemistry, male offspring underwent microdialysis. Only male mice were included as behavior data (not shown) pointed to males as more susceptible to the effects of prenatal stress than female mice in the tests carried out here. To probe potential mechanisms of stress-induced behavioral changes, 8-OH-DPAT injections were given to male and female adult offspring to determine differences in 5HT1A receptor activity. No differences were seen and thus not probed further in microdialysis experiments (**Fig. VI.12**).

Three microdialysis paradigms were explored where the order of the pharmacological agents administered was varied to test different hypotheses (**Fig. VI.8B**). The ventral hippocampus (vHPC) was targeted due to dense innervation from serotonin neurons[56, 57] that undergoes terminal arborization during the postnatal period targeted by the maternal stress paradigm. Moreover, the vHPC is involved in encoding emotion-related memories[58] and anxiety-related behavior[59] (**Fig. VI.10A**). Chromatographic peaks were identified and quantified based on standard curves (**Fig. VI.10B**); peak identity was confirmed by *in vivo* perfusion (standard addition) of serotonin or dopamine (**Fig. VI.10C, D**). No differences in basal or K^+-stimulated dialysate vHPC serotonin levels were observed with respect to maternal treatment group in adult male offspring (**Fig. VI.11A-C**). Additionally, no differences in vHPC basal dialysate dopamine levels were observed (**Fig. VI.11D, E**). However, the CUS group had higher stimulated dopamine levels compared to control and CUS+CIT groups (**Fig. VI.11F**).

After basal and K+-stimulated serotonin and dopamine levels were determined, a subset of mice was perfused with citalopram in the vHPC to investigate differences in tonic serotonin levels. In a second subset of mice, KOR agonists were injected systemically to investigate the effects of KOR activation on serotonin levels. Kappa opioid receptors have been implicated in mediating responses to stress.[60-63] As in the first subset, citalopram (10 uM) was first perfused for 2 h. Then, a KOR-agonist was administered systemically (U50,488 or U69,593, 10 mg/kg, i.p.) and dialysate samples were collected for an additional 1.5 h while CIT continued to be perfused (**Fig. VI.13A, D**).

Stress potentiated the increase in serotonin levels induced by KOR activation (**Fig. VI.13B**). This effect was rescued in the CUS+CIT group (**Fig. VI.13C**). To determine whether serotonin levels continued to rise over prolonged periods of CIT perfusions, we infused CIT for more than 3 h (**Fig. VI.14**). While we did observe a significant correlation between serotonin concentration over the longer perfusion period, the increase was less than 1 nM, confirming that larger increases in serotonin levels were the result of KOR agonist injection. As expected, KOR activation decreased dopamine levels (**Fig. VI.13E, F**). Unexpectedly, however, CIT perfusion also decreased dopamine levels.

To test if whether the findings regarding the treatment group associated effects of KOR activation depended on SERT inhibition, in a third subset of mice, a KOR agonist was administered prior to CIT perfusion. Decreases in dopamine levels were seen, however, no differences in serotonin levels were observed post KOR administration in the absence of SERT inhibition (**Fig. VI.15**).

Conclusions

The results of this study point to possible long-term benefits of SSRI treatment during stressful pregnancies. As such, the effects of concomitant SSRI treatment might mitigate the adverse effects of maternal stress on offspring behavior and underlying serotonin system function. We found that stress induced developmental changes in offspring protein, neurotransmitter, and amino acid (data not shown) tissue levels in early postnatal development. Stress induced increases in serotonin levels were rescued in offspring whose mothers also received citalopram during their pregnancies. While these postnatal effects on brain development were no longer observed by postnatal day 14 or 21, their impact on behavior were seen in adulthood. We found that male, but not female, mice born to stressed mothers displayed increased anxiety- and depressive-like behavior. Moreover, we found that male mice experiencing the effects of stress *in utero* were more susceptible to stress challenges, *i.e.*, overnight fasting, than female mice. These behavioral phenotypes were reversed in animals whose mothers were concomitantly treated with citalopram *in utero*.

Lastly, we assayed serotonin and dopamine transmission in adult male mice. While we did not see changes in basal or stimulated serotonin release, we did find pharmacologically induced changes in neurochemistry. Male mice born to stressed mothers showed higher serotonin concentrations in the vHPC in response to citalopram administration with and without the presence of kappa opioid receptor activation. These effects were rescued in the male mice whose mothers had been treated with citalopram *in utero*.

Our results add to the existing literature on the adverse effects of maternal stress during pregnancy. Importantly, they suggest long-term benefits of pharmacological treatments of stress experienced by pregnant mothers. The decision to take medication during pregnancy is influenced by many factors that include severity of maternal disorder, type of medication, and other complications. However, contrary to social perception that all medications during pregnancy are harmful to the developing fetus, our results show that SSRIs do not cause changes litter size, fetal birth weight, or viability, and are efficacious in mitigating the trans-generational effects of maternal stress in a mouse model.

While we probed the vHPC, other brain regions are implicated in the adverse effects of stress, particularly cortical regions including the prefrontal cortex (PFC).[64, 65] Moreover, KOR receptor expression and localization in cell populations, *i.e.*, dopaminergic neurons, and involvement of the kappa system in stress responses point to a system with much to be uncovered. Future experiments should focus on probing serotonergic pathways, *i.e.*, MRN → vHPC and MRN → PFC, to understand how the brain adapts to prenatal stress exposure. Moreover, future experiments should be designed to dissociate the effects of prenatal stress from postnatal maternal care, as maternal care is an important influencer of offspring development.[66, 67]

In sum, we showed that untreated maternal stress during pregnancy has prolonged developmental effects that impacts long-term offspring health. This study fills an important gap in the previous literature in answering how long-term behavioral and neurochemical effects are impacted given adverse *in utero* exposures. Importantly, our study strongly points to the safety and efficacy of citalopram, a commonly prescribed SSRI, in attenuating adverse neurochemical and behavioral effects induced by stress. Finally, we show an important link between stress-reactivity and the integral role of the serotonin and kappa systems in mediating responses to stress.

Figures

Figure VI.1

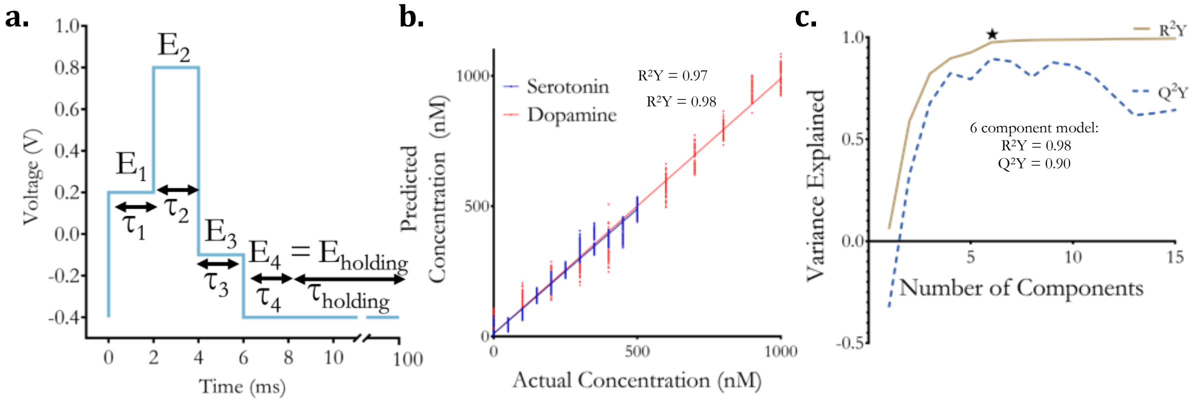

Figure VI.1: **(a)** Initial RPV waveform. **(b)** RPV-PLSR calibration curves for dopamine and serotonin in the presence of 100 µM DOPAC and 20 µM 5HIAA, using 1a and 6 components. **(c)** Calibration (R^2Y) and cross-validation (Q^2Y) variance explained by the PLSR model (star is elbow point).

Figure VI.2

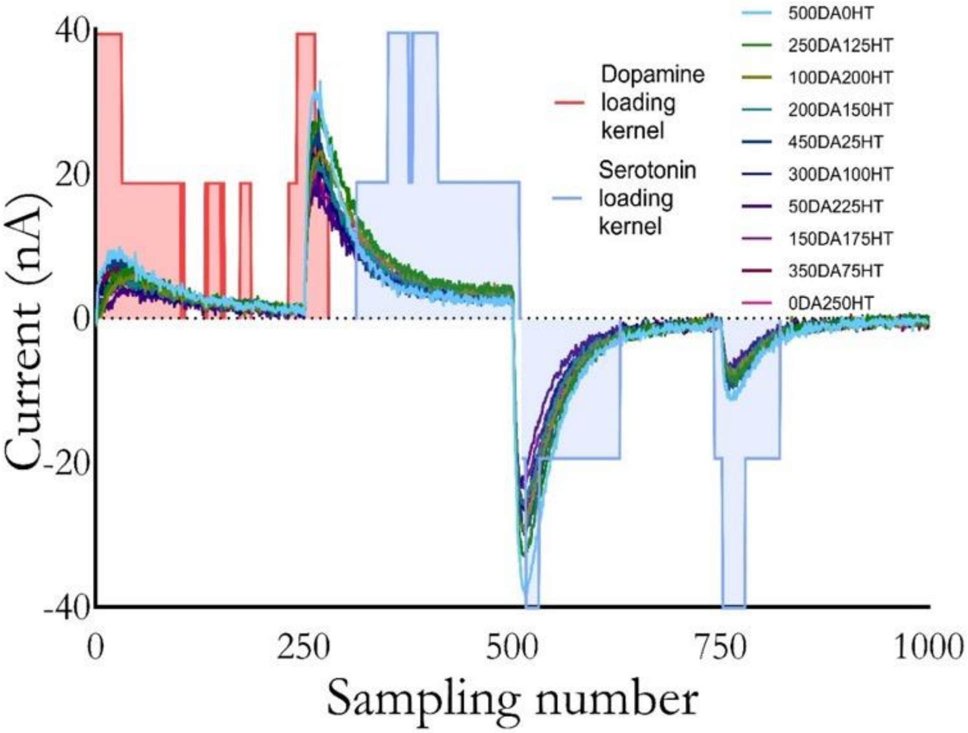

Figure VI.2. Rapid pulse voltammograms of varying dopamine (DA) and serotonin (5-HT) combinations (nM). The waveform (black) and DA/HT loadings analyses (red and blue, respectively) are overlaid.

Figure VI.3

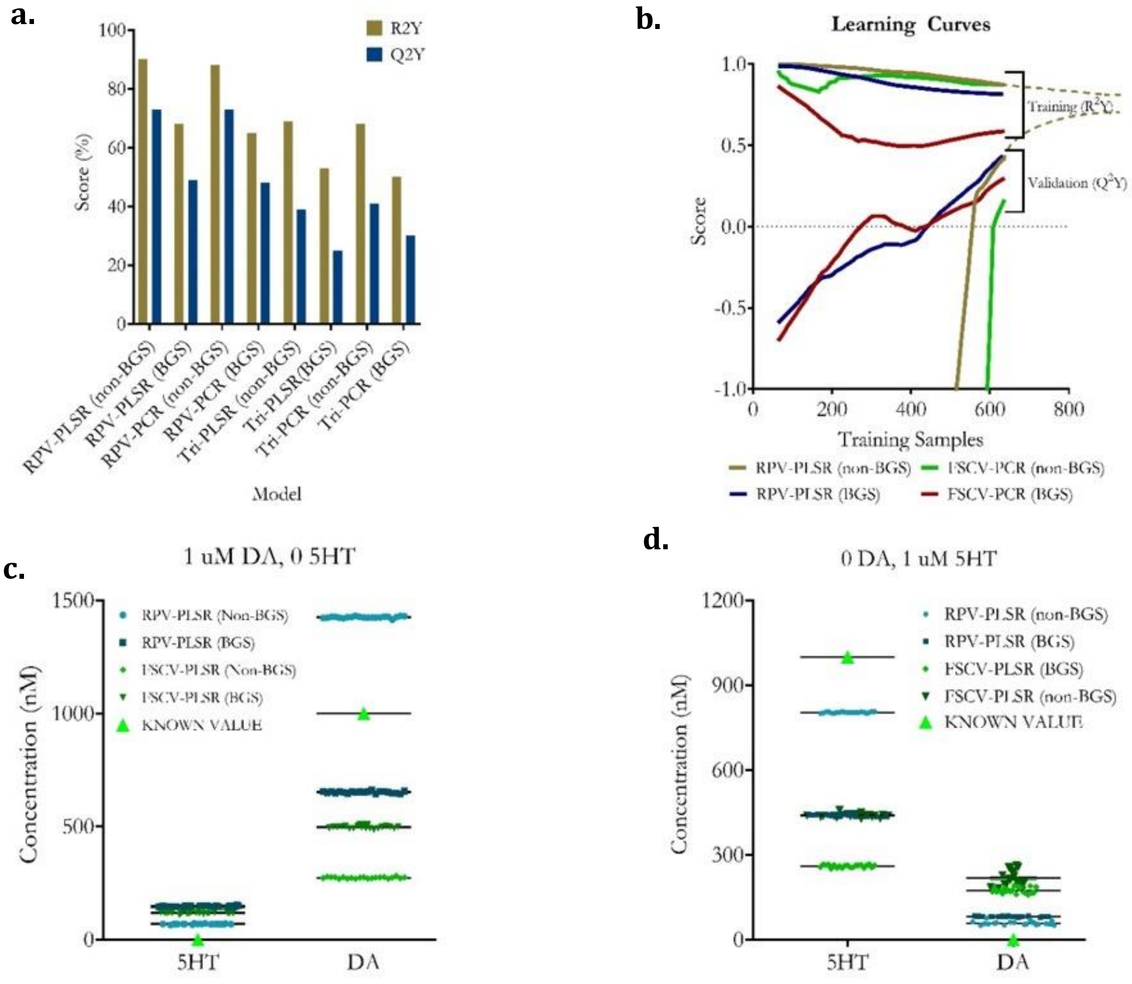

Figure VI.3: **(a)** training and validation scores and **(b)** Learning curves and, by model-waveform combination. **(c,d)** Test set performance by model-waveform combination.

Figure VI.4

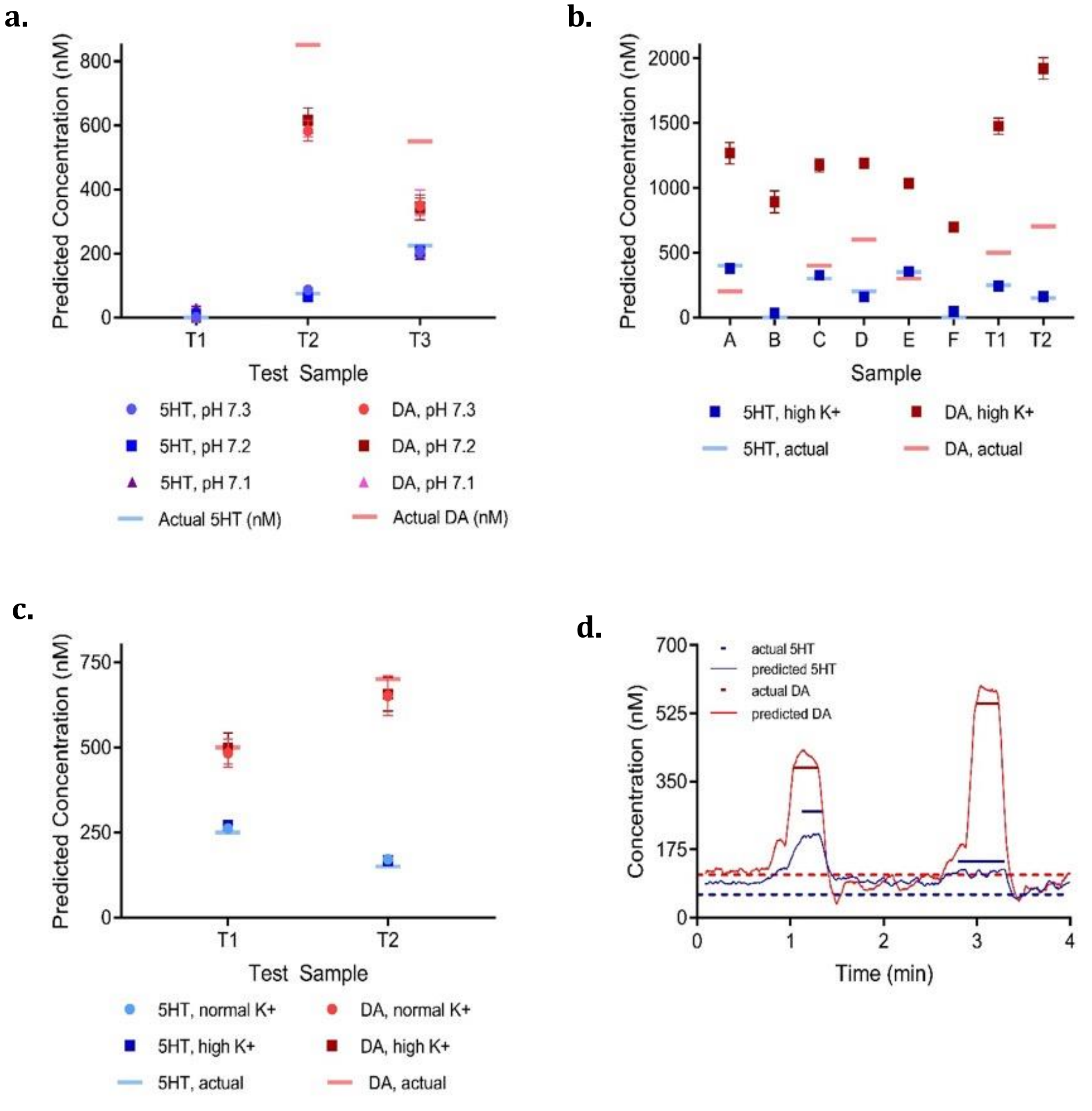

Figure VI.4: RPV-PLSR training in physiologically relevant conditions. (a) Test set predictions for a RPV-PLSR model trained across pH 7.1, 7.2, 7.3. Test set predictions of samples in normal or high K^+ aCSF, using either **(b)** a RPV-PLSR model trained with normal K^+ aCSF training samples, or, **(c)** combined high and normal K^+ training sets. **(d)** Simulated phasic release in the presence of 110 nM dopamine (DA) and 60 nM serotonin (5HT) in aCSF with 100 μM DOPAC, 20 μM 5HIAA, 200 μM AA, and 100 μM UA to mimic basal levels.

Figure VI.5

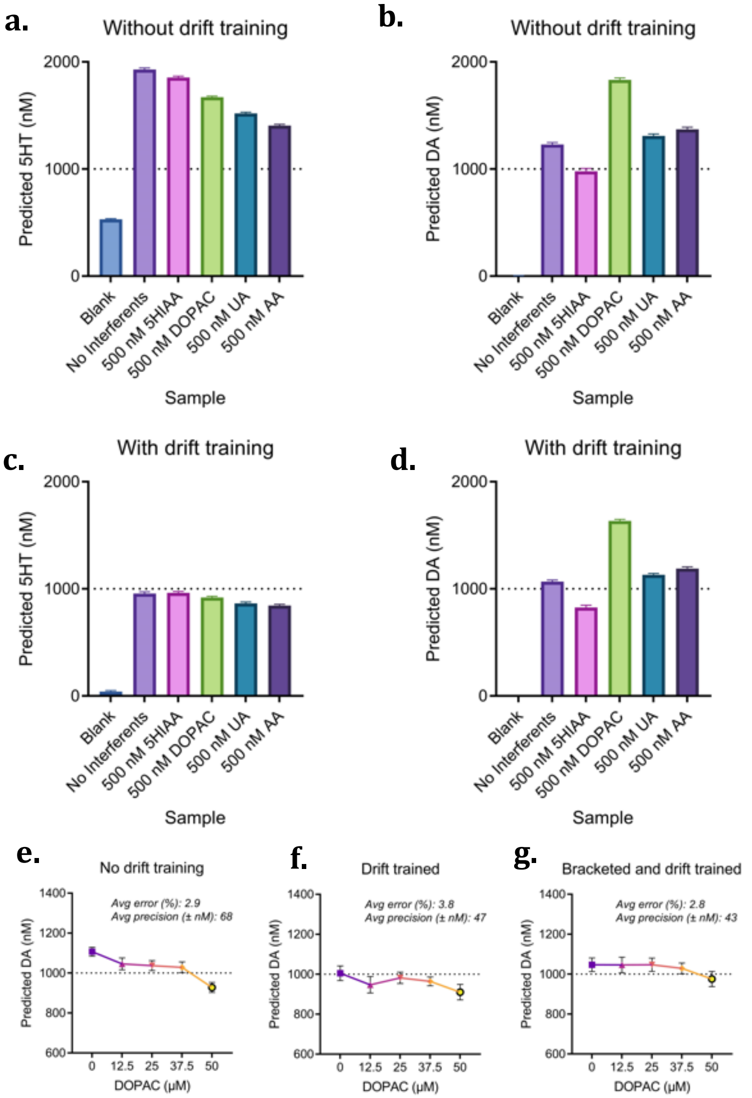

Figure VI.5: RPV-PLSR training for interferents and drift. Non-drift-trained serotonin **(a)** and dopamine **(b)** predictions. Drift-trained serotonin **(c)** and dopamine **(d)** predictions. Non-drift- **(e)**, drift- **(f)**, and drift-trained with bracketing **(g)** dopamine test set predictions in the presence of varying DOPAC. All samples trained in a background level of interferents (100 µM DOPAC, 20 µM 5-HIAA, 200 µM ascorbate, and 100 µM urate) unless otherwise noted; x-axis in **(a-d)** refers to amount added <u>in addition</u> to background levels. **(a-g)** Data points per panel were acquired sequentially in time, as labeled on the x-axis, to illustrate temporal drift.

Figure VI.6

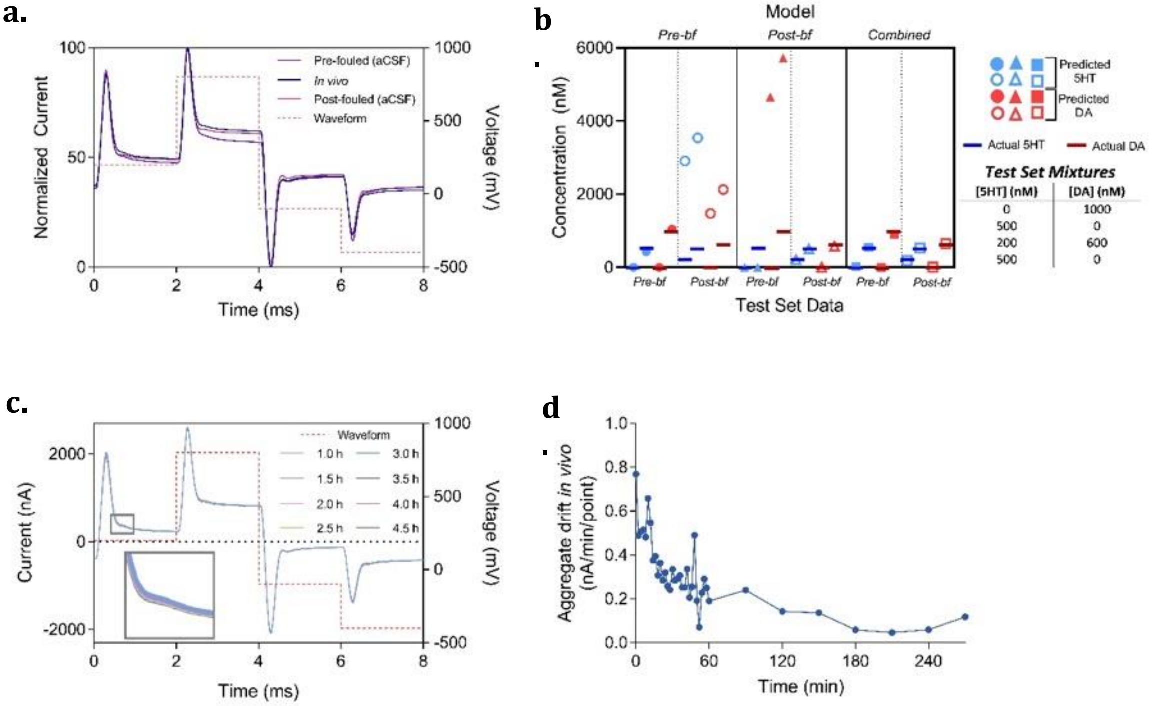

Figure VI.6: (a) Voltammograms obtained with a pre-fouled (prior to implantation, in aCSF), *in vivo* (striatum of anaesthized mouse), and post-fouled electrode (in aCSF after implantation ~6 h). **(b)** Predicted test set concentrations for serotonin (blue) and dopamine (red) obtained on the same electrode pre-biofouling ('pre-bf'; filled symbol) and post-biofouling ('post-bf'; hollow symbol). Actual test set concentrations are denoted by a blue (serotonin) or red (dopamine) horizontal lines. All points are the average of 41 data points. **(c)** Comparison of drift over *in vivo* experimental time course (defined as average aggregate difference in current between voltammograms at successive time points; t=0 is CFM insertion into brain). Data were obtained at 2 min intervals for the first hour, then every 30 min for the remaining 4 h. **(d)** Comparison of *in vivo* voltammograms post 1-h, zoom in on region of capacitive decay (inset).

Figure VI.7

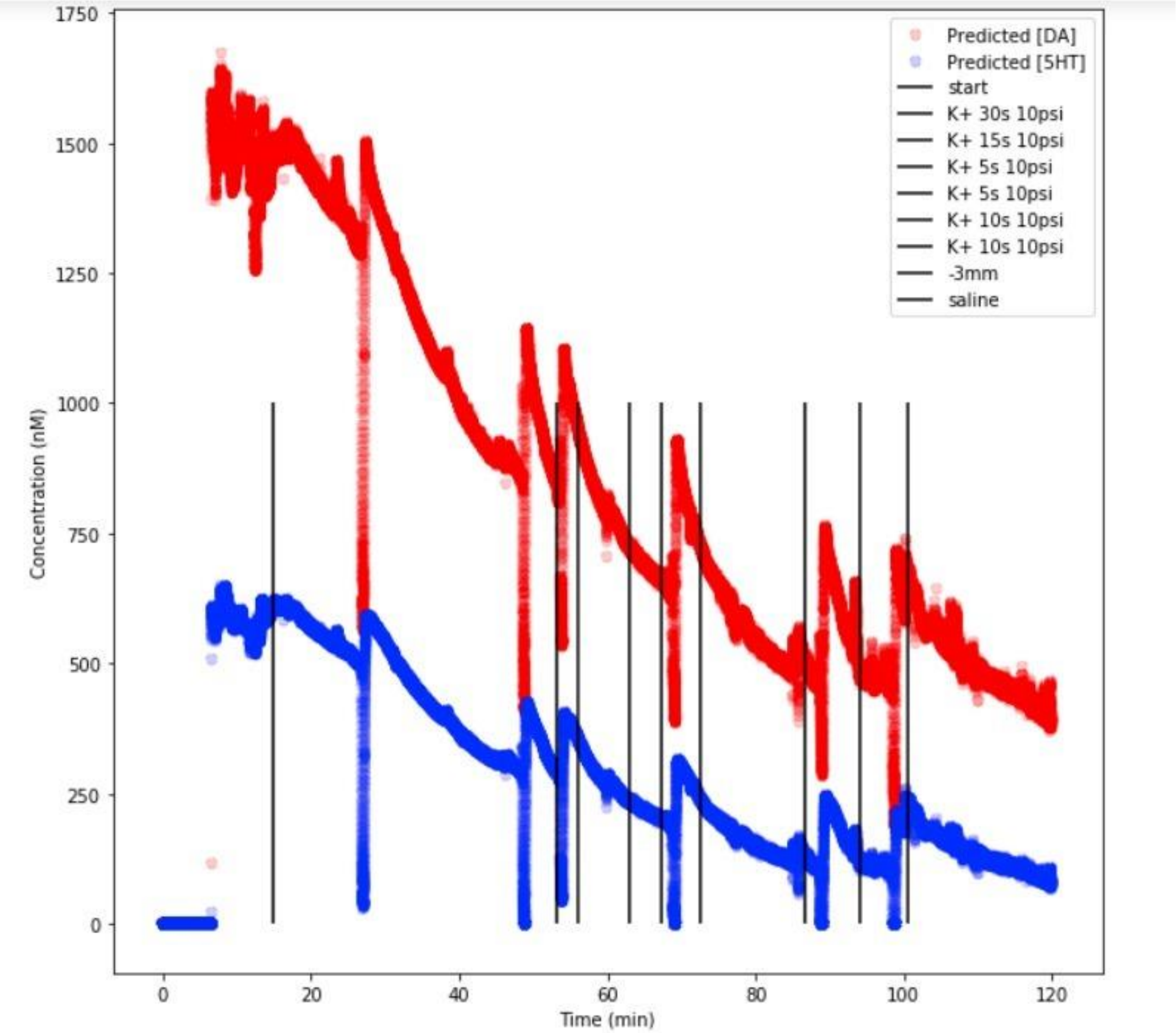

Figure VI.7: Picospritzing pilot experiment in the dorsal striatum. An aCSF solution containing high (120 mM) potassium was picospritzed using various settings.

Figure VI.8

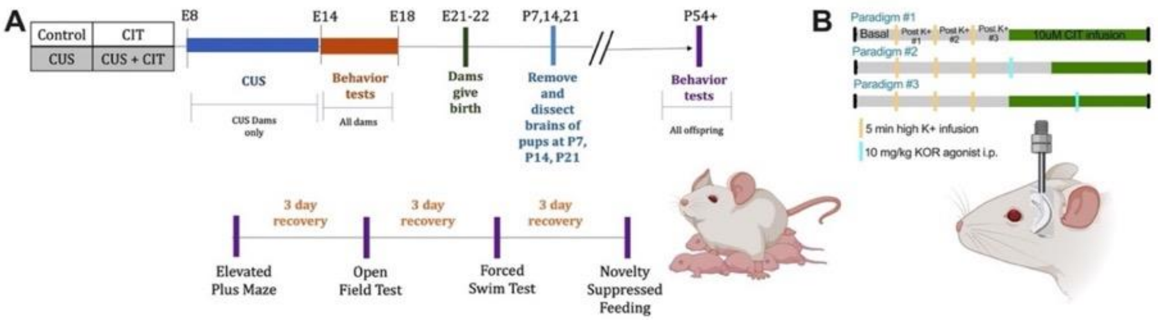

Figure VI.8: Overview of experimental paradigms. A. Timeline of *in utero* exposure and subsequent postnatal and behavior testing schedules. **B.** Timelines for different microdialysis paradigms. Aspects of this figure were created using Biorender.com.

Figure VI.9

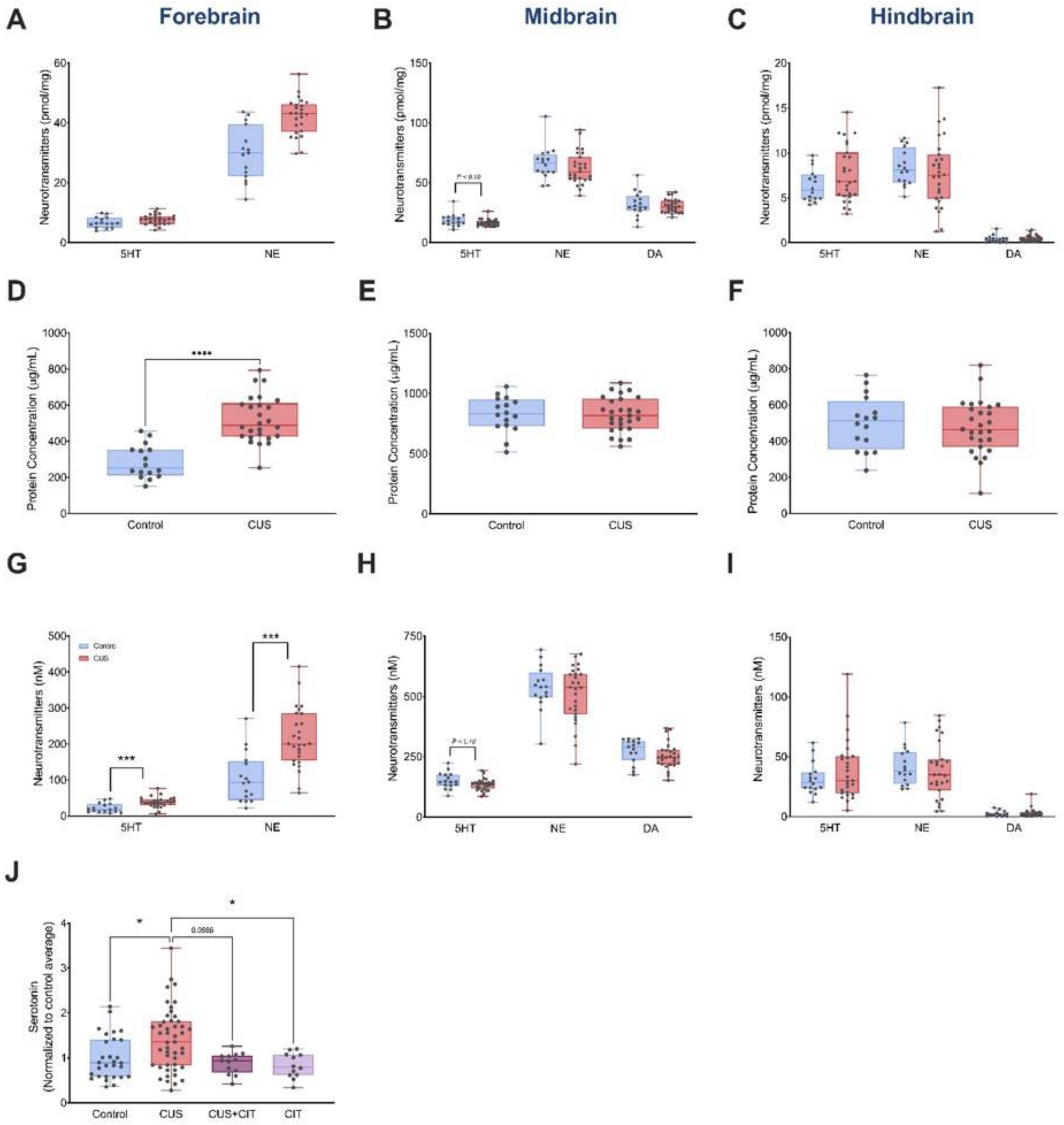

Figure VI.9: Postnatal day 7 tissue analysis shows increased neurotransmitters and protein concentration for stressed pups. Normalized **A.** forebrain, **B.** midbrain, and **C.** hindbrain neurotransmitter tissue levels. **D**. Protein concentrations are significantly increased at P7 in the forebrain of stressed pups, but not the **E.** midbrain or **F.** hindbrain. Non-normalized neurotransmitter tissue levels show significant increases in pups born to stressed mothers in **G.** forebrain, but not **H.** midbrain or **I.** hindbrain. Concomitant treatment with CIT rescues maternal stress induced increases in serotonin in **J.** forebrain. *P<0.05, **P<0.01, ***P<0.001

Abbreviations: Serotonin (5HT), 5-Hydroxyindolacetic acid (HIAA), norepinephrine (NE), dopamine (DA), 3,4-Dihydroxyphenylacetic acid (DOPAC), and homovanillic acid (HVA)

Figure VI.10

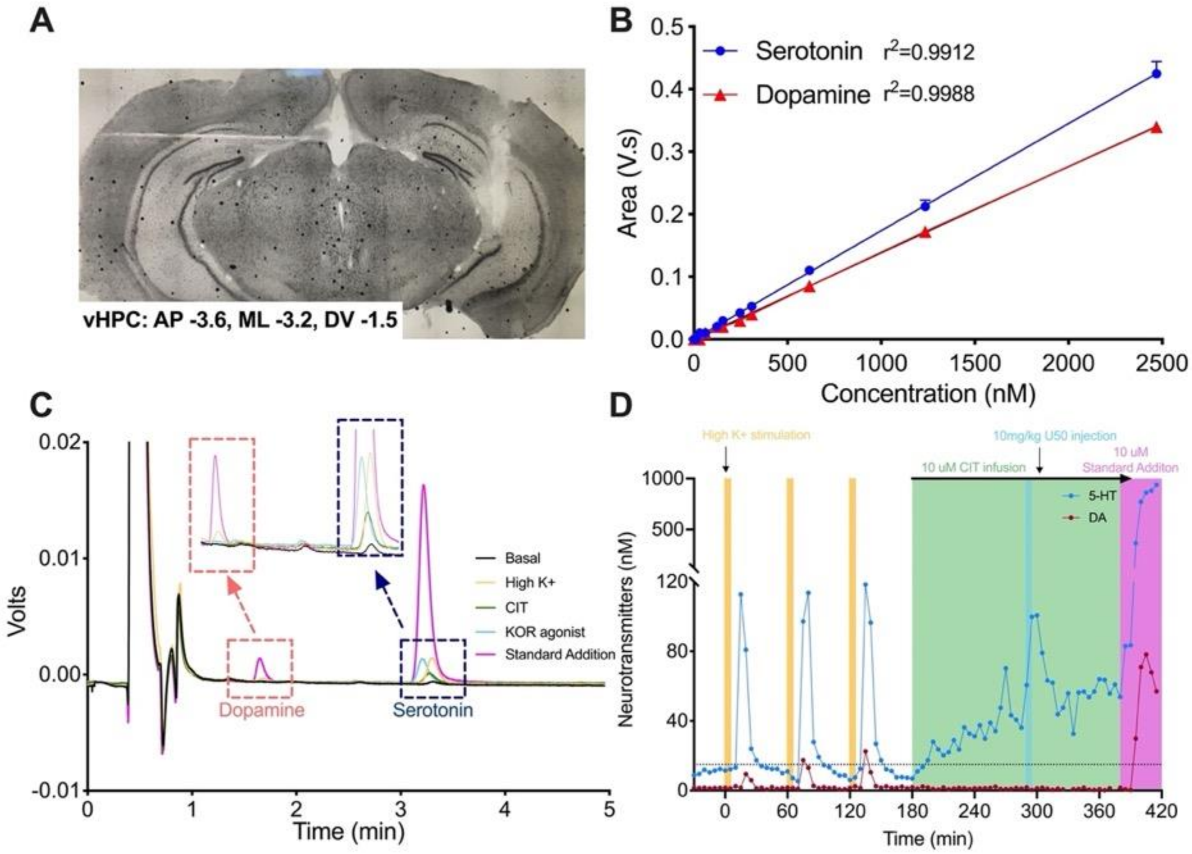

Figure VI.10: Microdialysis probe and peak verification. A. Cresyl violet image showing microdialysis cannula and probe localization to the ventral hippocampus. **B.** Standard curves for dopamine and serotonin used to quantify analyte concentrations. A standard curve was run each week prior to microdialysis experiments N=6/analyte. **C.** Overlay of five chromatograms from a representative mouse showing dopamine and serotonin peaks before (basal) and after pharmacological manipulations to verify peak identities. **D.** Time course from the same mouse in C.

Figure VI.11

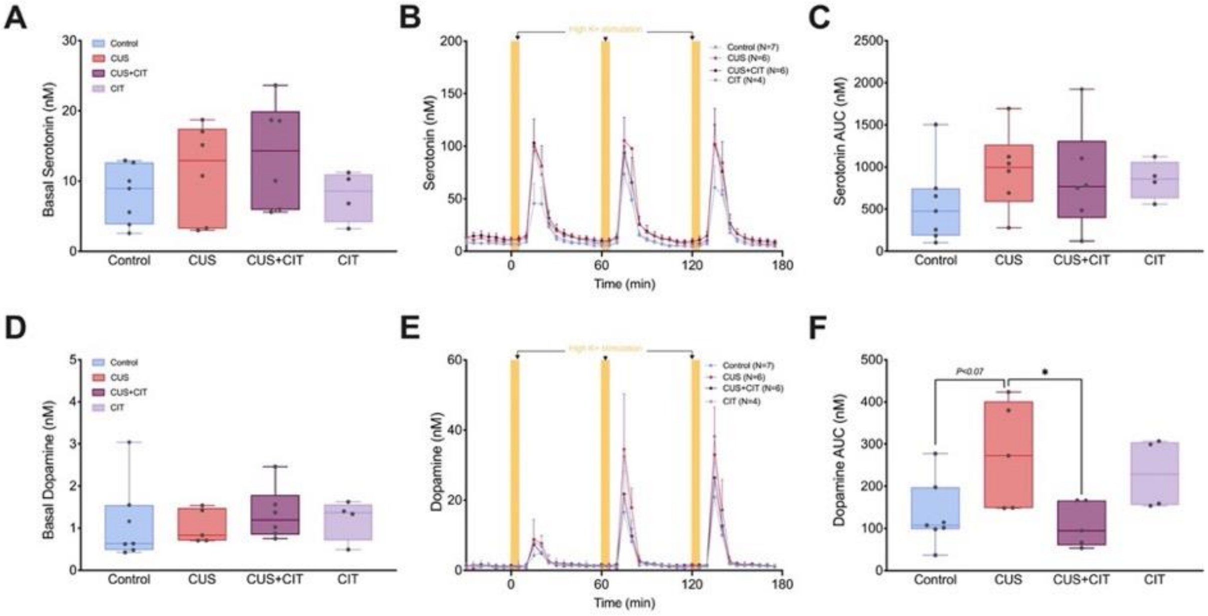

Figure VI.11: No basal extracellular serotonin or dopamine differences in adult offspring exposed to prenatal stress. Basal serotonin (**A**) and dopamine (**D**) levels in adult offspring. Microdialysis time course of extracellular serotonin (**B**) and dopamine (**E**). The yellow bars indicate 120 µM potassium stimulation (5 min). Serotonin (**C**) and dopamine high potassium (**F**) stimulated release quantified by area under the curve. *P<0.05

Figure VI.12

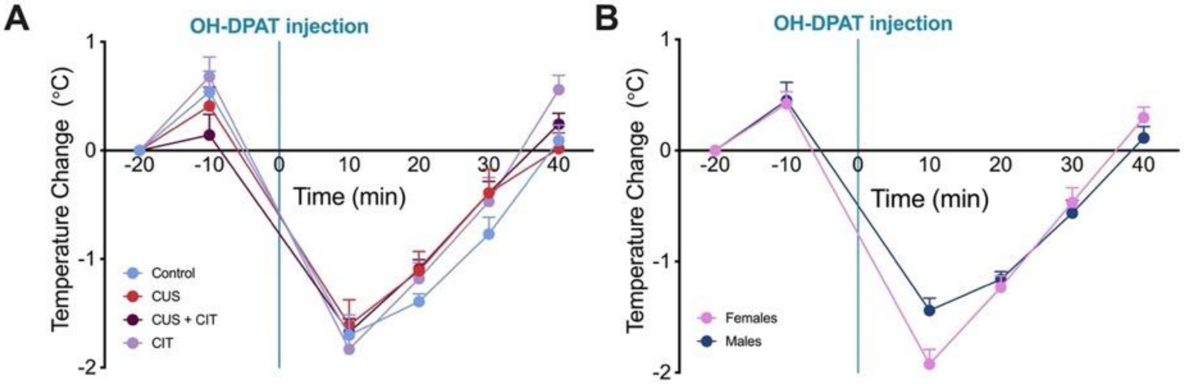

Figure VI.12: No changes in the temperature after 5HT1A agonist. No temperature changes by **A.** treatment or by **B**. sex after 8-OH-DPAT i.p. injection.

Figure VI.13

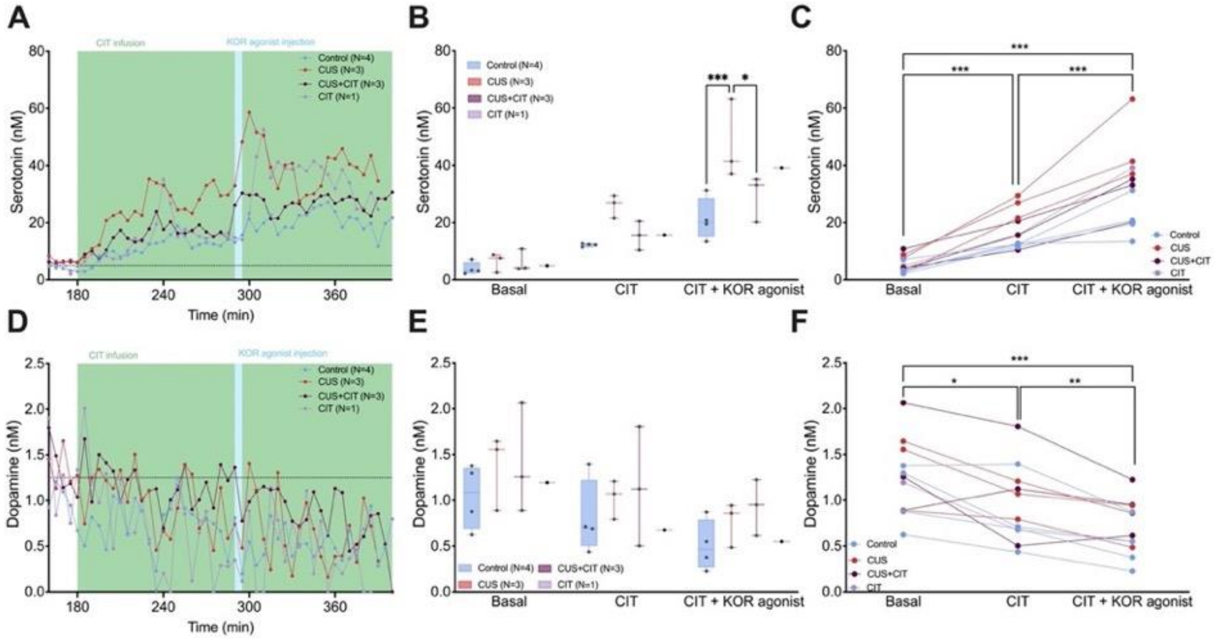

Figure VI.13: Decreases in dopamine and increases in serotonin, post concomitant CIT and KOR agonist. A. Time course before and after CIT infusion and KOR agonist injection for serotonin concentrations. Significant effect of **B.** treatment, and **C.** drug on serotonin concentrations. **D.** Time course before and after CIT infusion and KOR agonist injection for dopamine concentrations. Significant effect of **F.** CIT infusion and agonist injection, but not **E.** *in utero* treatment on dopamine concentrations. *P<0.05, **P<0.01, ***P<0.001, ****P<0.0001

Figure VI.14

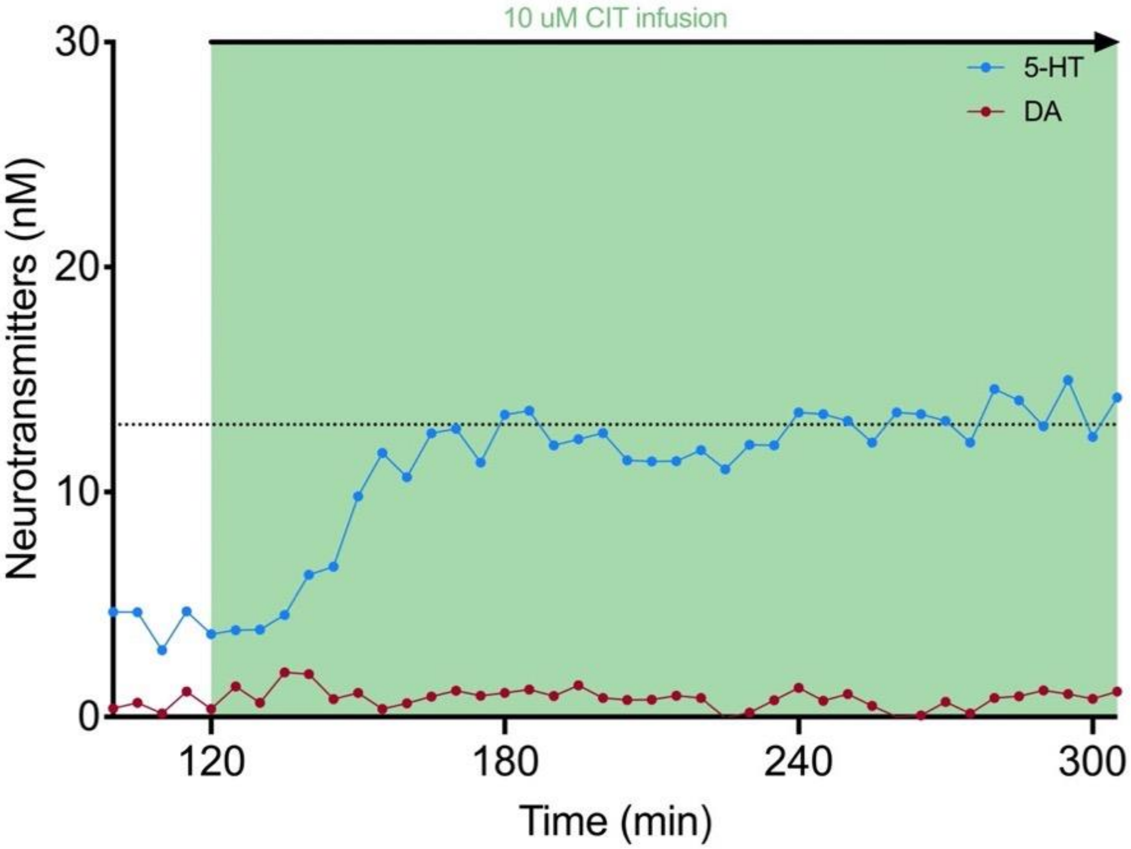

Figure VI.14: Stable serotonin levels after three hr of CIT infusion. Serotonin concentrations remained stable during longer infusion of CIT. Time course is taken from N=1 animal that underwent basal collection and two high K$^+$ potassium stimulations. Each point represents a 5 min sample. Points pre-120 min are neurotransmitter concentrations post-high K$^+$ #2 and pre-CIT infusion. Infusion of CIT began at 120 min (or 2 hours into microdialysis testing day) and continued until 310 min, for a duration of three hr and 10 min.

Figure VI.15

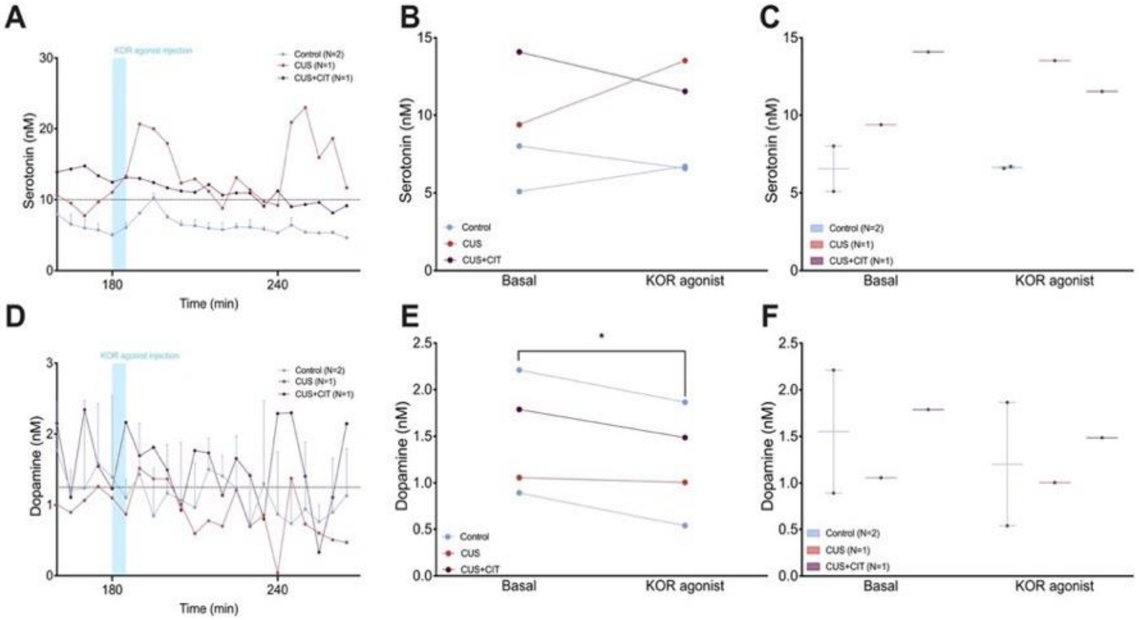

Figure VI.15: Decreases in dopamine, but not serotonin, post KOR agonist i.p. injection. A. Time course before and after KOR agonist injection for serotonin concentrations. No effect of **B.** KOR injection or **C.** *in utero* treatment on serotonin concentrations. **D.** Time course before and after KOR agonist injection for dopamine concentrations. Significant effect of **E.** KOR injection, but not **C.** *in utero* treatment on dopamine concentrations. *P<0.05

Table VI.1

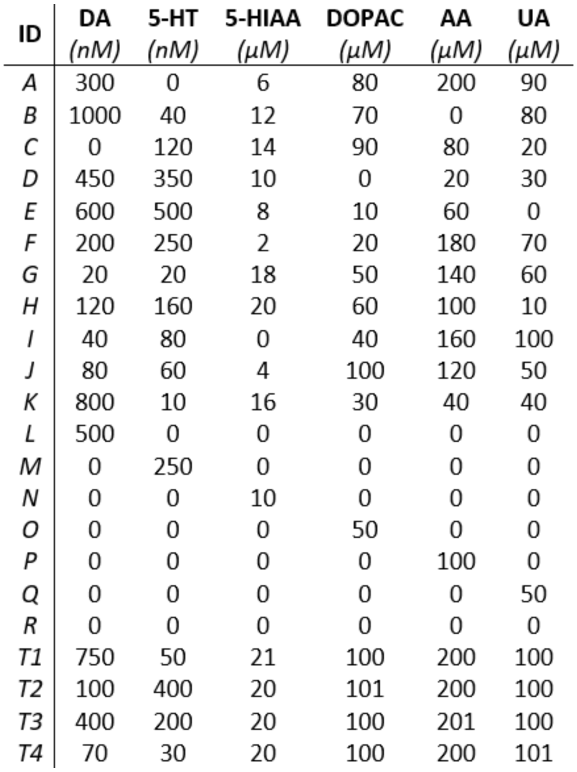

ID	**DA** *(nM)*	**5-HT** *(nM)*	**5-HIAA** *(μM)*	**DOPAC** *(μM)*	**AA** *(μM)*	**UA** *(μM)*
A	300	0	6	80	200	90
B	1000	40	12	70	0	80
C	0	120	14	90	80	20
D	450	350	10	0	20	30
E	600	500	8	10	60	0
F	200	250	2	20	180	70
G	20	20	18	50	140	60
H	120	160	20	60	100	10
I	40	80	0	40	160	100
J	80	60	4	100	120	50
K	800	10	16	30	40	40
L	500	0	0	0	0	0
M	0	250	0	0	0	0
N	0	0	10	0	0	0
O	0	0	0	50	0	0
P	0	0	0	0	100	0
Q	0	0	0	0	0	50
R	0	0	0	0	0	0
T1	750	50	21	100	200	100
T2	100	400	20	101	200	100
T3	400	200	20	100	201	100
T4	70	30	20	100	200	101

Table 1: Proposed fractional factorial calibration (A-R) and test (T1-4) set design for future use.

Table VI.2

Monday	Tuesday	Wednesday	Thursday	Friday	Saturday	Sunday
	E7: timed-pregnant dams arrived; CUS dams placed into individual cages	**E8 10 am:** ears clipped, 5-min restraint, saline injection, and brief transportation stress	**E9 12 pm:** 15-min fox urine odor exposure	**E10 4:30 pm -7 am:** overnight light	**E11 10 am-12 pm:** 30-min restraint in tubes	**E12 4 pm-7 am:** overnight static noise (70dB)
E13 8 am-4 pm: 45° cage tilt	**E14 4:30 pm-7 am:** overnight wet bedding	**E15 6 pm-10 pm:** OFT test	**E16 12 pm-2:30 pm:** FST test; **7 pm:** begin fast for NSF	**E17 5 pm-7 pm:** NSF test		

Table VI.2: Maternal chronic unpredictable stress paradigm

References

1. Movassaghi, C. S.; Perrotta, K. A.; Yang, H.; Iyer, R.; Cheng, X.; Dagher, M.; Fillol, M. A.; Andrews, A. M., Simultaneous serotonin and dopamine monitoring across timescales by rapid pulse voltammetry with partial least squares regression. *Anal Bioanal Chem* **2021,** *413* (27), 6747-6767.

2. Campos, I.; Alcañiz, M.; Masot, R.; Soto, J.; Martínez-Máñez, R.; Vivancos, J.-L.; Gil, L., A method of pulse array design for voltammetric electronic tongues. *Sens Actuators B Chem* **2012,** *161* (1), 556-563.

3. Campos, I.; Masot, R.; Alcañiz, M.; Gil, L.; Soto, J.; Vivancos, J. L.; García-Breijo, E.; Labrador, R. H.; Barat, J. M.; Martínez-Mañez, R., Accurate concentration determination of anions nitrate, nitrite and chloride in minced meat using a voltammetric electronic tongue. *Sens Actuators B Chem* **2010,** *149* (1), 71-78.

4. Baur, J. E.; Kristensen, E. W.; May, L. J.; Wiedemann, D. J.; Wightman, R. M., Fast-scan voltammetry of biogenic amines. *Anal Chem* **1988,** *60* (13), 1268-1272.

5. Hashemi, P.; Dankoski, E. C.; Petrovic, J.; Keithley, R. B.; Wightman, R. M., Voltammetric detection of 5-hydroxytryptamine release in the rat brain. *Anal Chem* **2009,** *81* (22), 9462-71.

6. Kramer, R., *Chemometric techniques for quantitative analysis*. CRC Press: Boca Raton, FL, 1998.

7. Chong, I.-G.; Jun, C.-H., Performance of some variable selection methods when multicollinearity is present. *Chemom Intell Lab Syst* **2005,** *78* (1), 103-112.

8. Keithley, R. B.; Mark Wightman, R.; Heien, M. L., Multivariate concentration determination using principal component regression with residual analysis. *Trends Analyt Chem* **2009,** *28* (9), 1127-1136.

9. Loewinger, G.; Patil, P.; Kishida, K. T.; Parmigiani, G., Multi-study learning for real-time neurochemical sensing in humans using the “study strap ensemble”. *bioRxiv* **2021**, 856385.

10. Díaz-Cruz, J. M.; Esteban, M.; Ariño, C., *Chemometrics in electroanalysis*. 1 ed.; Springer: Cham, Switzerland, 2019; p 202.

11. Hibbert, D. B., Experimental design in chromatography: A tutorial review. *J Chromatogr B* **2012,** *910*, 2-13.

12. Kishida, K. T.; Saez, I.; Lohrenz, T.; Witcher, M. R.; Laxton, A. W.; Tatter, S. B.; White, J. P.; Ellis, T. L.; Phillips, P. E. M.; Montague, P. R., Subsecond dopamine fluctuations in human striatum encode superposed error signals about actual and counterfactual reward. *Proc Natl Acad Sci USA* **2016,** *113* (1), 200-205.

13. Chesler, M.; Kaila, K., Modulation of ph by neuronal activity. *Trends Neurosci* **1992,** *15* (10), 396-402.

14. Kawagoe, K. T.; Zimmerman, J. B.; Wightman, R. M., Principles of voltammetry and microelectrode surface states. *J Neurosci Methods* **1993,** *48* (3), 225-240.

15. Blaustein, M.; Wirth, S.; Saldaña, G.; Piantanida, A. P.; Bogetti, M. E.; Martin, M. E.; Colman-Lerner, A.; Uchitel, O. D., A new tool to sense ph changes at the neuromuscular junction synaptic cleft. *Sci Rep* **2020,** *10* (1), 20480.

16. Ariansen, J.; Heien, M. L. A. V.; Hermans, A.; Phillips, P. E. M.; Hernadi, I.; Bermudez, M.; Schultz, W.; Wightman, R. M., Monitoring extracellular ph, oxygen, and dopamine during reward delivery in the striatum of primates. *Front Behav Neurosci* **2012,** *6* (36).

17. Chesler, M., The regulation and modulation of ph in the nervous system. *Prog Neurobiol* **1990,** *34* (5), 401-427.

18. Makani, S.; Chesler, M., Rapid rise of extracellular ph evoked by neural activity is generated by the plasma membrane calcium atpase. *J Neurophysiol* **2010,** *103* (2), 667-676.

19. Ewing, A. G.; Dayton, M. A.; Wightman, R. M., Pulse voltammetry with microvoltammetric electrodes. *Anal Chem* **1981,** *53* (12), 1842-1847.

20. Johnson, J. A.; Rodeberg, N. T.; Wightman, R. M., Measurement of basal neurotransmitter levels using convolution-based nonfaradaic current removal. *Anal Chem* **2018,** *90* (12), 7181-7189.

21. Johnson, J. A.; Hobbs, C. N.; Wightman, R. M., Removal of differential capacitive interferences in fast-scan cyclic voltammetry. *Anal Chem* **2017,** *89* (11), 6166-6174.

22. Somjen, G. G., *Ions in the brain: Normal function, seizures, and stroke*. Oxford University Press: 2004.

23. Wosiak, G.; Coelho, D.; Carneiro-Neto, E. B.; Pereira, E. C.; Lopes, M. C., Numerical resolving of net faradaic current in fast-scan cyclic voltammetry considering induced charging currents. *Anal Chem* **2020,** *92* (23), 15412-15419.

24. Yoshimi, K.; Weitemier, A., Temporal differentiation of ph-dependent capacitive current from dopamine. *Anal Chem* **2014,** *86* (17), 8576-8584.

25. Takmakov, P.; Zachek, M. K.; Keithley, R. B.; Bucher, E. S.; McCarty, G. S.; Wightman, R. M., Characterization of local ph changes in brain using fast-scan cyclic voltammetry with carbon microelectrodes. *Anal Chem* **2010,** *82* (23), 9892-9900.

26. Gerhardt, G. A.; Hoffman, A. F., Effects of recording media composition on the responses of nafion-coated carbon fiber microelectrodes measured using high-speed chronoamperometry. *J Neurosci Methods* **2001,** *109* (1), 13-21.

27. Abdalla, A.; Atcherley, C. W.; Pathirathna, P.; Samaranayake, S.; Qiang, B.; Peña, E.; Morgan, S. L.; Heien, M. L.; Hashemi, P., In vivo ambient serotonin measurements at carbon-fiber microelectrodes. *Anal Chem* **2017,** *89* (18), 9703-9711.

28. Oh, Y.; Heien, M. L.; Park, C.; Kang, Y. M.; Kim, J.; Boschen, S. L.; Shin, H.; Cho, H. U.; Blaha, C. D.; Bennet, K. E.; Lee, H. K.; Jung, S. J.; Kim, I. Y.; Lee, K. H.; Jang, D. P., Tracking tonic dopamine levels in vivo using multiple cyclic square wave voltammetry. *Biosens Bioelectron* **2018,** *121*, 174-182.

29. Nakatsuka, N.; Andrews, A. M., Differentiating siblings: The case of dopamine and norepinephrine. *ACS Chem Neurosci* **2017,** *8* (2), 218-220.

30. Meiser, J.; Weindl, D.; Hiller, K., Complexity of dopamine metabolism. *Cell Commun Signal* **2013,** *11* (1), 34.

31. Mohammad-Zadeh, L. F.; Moses, L.; Gwaltney-Brant, S. M., Serotonin: A review. *J Vet Pharmacol Ther* **2008,** *31* (3), 187-199.

32. Qi, Z.; Miller, G. W.; Voit, E. O., Mathematical models of dopamine metabolism in parkinson's disease. In *Systems biology of parkinson's disease*, Wellstead, P.; Cloutier, M., Eds. Springer New York: New York, NY, 2012; pp 151-171.

33. Rodeberg, N. T.; Johnson, J. A.; Bucher, E. S.; Wightman, R. M., Dopamine dynamics during continuous intracranial self-stimulation: Effect of waveform on fast-scan cyclic voltammetry data. *ACS Chem Neurosci* **2016,** *7* (11), 1508-1518.

34. Maina, F. K.; Khalid, M.; Apawu, A. K.; Mathews, T. A., Presynaptic dopamine dynamics in striatal brain slices with fast-scan cyclic voltammetry. *Jove* **2012**.

35. Singh, Y. S.; Sawarynski, L. E.; Dabiri, P. D.; Choi, W. R.; Andrews, A. M., Head-to-head comparisons of carbon fiber microelectrode coatings for sensitive and selective neurotransmitter detection by voltammetry. *Anal Chem* **2011,** *83* (17), 6658-6666.

36. Montague, P. R.; Kishida, K. T., Computational underpinnings of neuromodulation in humans. *Cold Spring Harb Symp Quant Biol* **2018,** *83*, 71-82.

37. Park, C.; Hwang, S.; Kang, Y.; Sim, J.; Cho, H. U.; Oh, Y.; Shin, H.; Kim, D. H.; Blaha, C. D.; Bennet, K. E.; Lee, K. H.; Jang, D. P., Feasibility of applying fourier transform electrochemical impedance spectroscopy in fast cyclic square wave voltammetry for the in vivo measurement of neurotransmitters. *Anal Chem* **2021,** *93* (48), 15861-15869.

38. Lalley, P. M., Microiontophoresis and pressure ejection. In *Modern techniques in neuroscience research*, Windhorst, U.; Johansson, H., Eds. Springer Berlin Heidelberg: Berlin, Heidelberg, 1999; pp 193-212.

39. Gerhardt, G. A.; Palmer, M. R., Characterization of the techniques of pressure ejection and microiontophoresis using in vivo electrochemistry. *J Neurosci Methods* **1987,** *22* (2), 147-59.

40. Daws, L. C.; Montañez, S.; Munn, J. L.; Owens, W. A.; Baganz, N. L.; Boyce-Rustay, J. M.; Millstein, R. A.; Wiedholz, L. M.; Murphy, D. L.; Holmes, A., Ethanol inhibits clearance of brain serotonin by a serotonin transporter-independent mechanism. *J Neurosci* **2006,** *26* (24), 6431-6438.

41. Daws, L. C.; Montañez, S.; Owens, W. A.; Gould, G. G.; Frazer, A.; Toney, G. M.; Gerhardt, G. A., Transport mechanisms governing serotonin clearance in vivo revealed by high-speed chronoamperometry. *J Neurosci Methods* **2005,** *143* (1), 49-62.

42. Wiedholz, L. M.; Owens, W. A.; Horton, R. E.; Feyder, M.; Karlsson, R. M.; Hefner, K.; Sprengel, R.; Celikel, T.; Daws, L. C.; Holmes, A., Mice lacking the ampa glur1 receptor exhibit striatal hyperdopaminergia and 'schizophrenia-related' behaviors. *Mol Psychiatry* **2008,** *13* (6), 631-640.

43. Daws, L.; Andrews, A.; Gerhardt, G., Electrochemical techniques and advances in psychopharmacology. 2013; pp 1-6.

44. Daws, L. C.; Toney, G. M.; Davis, D. J.; Gerhardt, G. A.; Frazer, A., In vivo chronoamperometric measurements of the clearance of exogenously applied serotonin in the rat dentate gyrus. *J Neurosci Methods* **1997,** *78* (1-2), 139-50.

45. Daws, L. C.; Toney, G. M., High-speed chronoamperometry to study kinetics and mechanisms for serotonin clearance in vivo. In *Electrochemical methods for neuroscience*, AC, M.; LM, B., Eds. CRC Press/Taylor & Francis: Boca Raton (FL), 2007.

46. Daws, L. C.; Toney, G. M.; Gerhardt, G. A.; Frazer, A., In vivo chronoamperometric measures of extracellular serotonin clearance in rat dorsal hippocampus: Contribution of serotonin and norepinephrine transporters. *J Pharmacol Exp Ther* **1998,** *286* (2), 967-976.

47. Dagher, M.; Perrotta, K. A.; Erwin, S. A.; Hachisuka, A.; Ayer, R.; Masmanidis, S.; Yang, H.; Andrews, A. M., Optogenetic stimulation of midbrain dopamine neurons produces striatal serotonin release. *ACS Chemical Neuroscience* **2022**.

48. Velasquez, J. C.; Zhao, Q.; Chan, Y.; Galindo, L. C. M.; Simasotchi, C.; Wu, D.; Hou, Z.; Herod, S. M.; Oberlander, T. F.; Gil, S.; Fournier, T.; Burd, I.; Andrews, A. M.; Bonnin, A., In utero exposure to citalopram mitigates maternal stress effects on fetal brain development. *ACS Chem Neurosci* **2019,** *10* (7), 3307-3317.

49. Jiao, J.; Nitzke, A. M.; Doukas, D. G.; Seiglie, M. P.; Dulawa, S. C., Antidepressant response to chronic citalopram treatment in eight inbred mouse strains. *Psychopharmacology (Berl)* **2011,** *213* (2-3), 509-20.

50. Warner-Schmidt, J. L.; Vanover, K. E.; Chen, E. Y.; Marshall, J. J.; Greengard, P., Antidepressant effects of selective serotonin reuptake inhibitors (ssris) are attenuated by antiinflammatory drugs in mice and humans. *Proc Natl Acad Sci U S A* **2011,** *108* (22), 9262-7.

51. Meng, Q. H.; Gauthier, D., Simultaneous analysis of citalopram and desmethylcitalopram by liquid chromatography with fluorescence detection after solid-phase extraction. *Clin Biochem* **2005,** *38* (3), 282-5.

52. Workman, A. D.; Charvet, C. J.; Clancy, B.; Darlington, R. B.; Finlay, B. L., Modeling transformations of neurodevelopmental sequences across mammalian species. *J Neurosci* **2013,** *33* (17), 7368-83.

53. Johnson, E. A.; Sharp, D. S.; Miller, D. B., Restraint as a stressor in mice: Against the dopaminergic neurotoxicity of d-mdma, low body weight mitigates restraint-induced hypothermia and consequent neuroprotection. *Brain Res* **2000,** *875* (1-2), 107-18.

54. Sampson, M. M.; Yang, H.; Andrews, A. M., Advanced microdialysis approaches resolve differences in serotonin homeostasis and signaling. In *Compendium of in vivo monitoring in real-time molecular neuroscience*, WORLD SCIENTIFIC: 2017; pp 119-140.

55. Yang, H.; Thompson, A. B.; McIntosh, B. J.; Altieri, S. C.; Andrews, A. M., Physiologically relevant changes in serotonin resolved by fast microdialysis. *ACS Chem Neurosci* **2013,** *4* (5), 790-8.

56. Lidov, H. G.; Molliver, M. E., An immunohistochemical study of serotonin neuron development in the rat: Ascending pathways and terminal fields. *Brain Res Bull* **1982,** *8* (4), 389-430.

57. Lidov, H. G.; Molliver, M. E., Immunohistochemical study of the development of serotonergic neurons in the rat cns. *Brain Res Bull* **1982,** *9* (1-6), 559-604.

58. Gulyaeva, N. V., Ventral hippocampus, stress and psychopathology: Translational implications. *Neurochemical Journal* **2015,** *9* (2), 85-94.

59. Moser, M. B.; Moser, E. I., Functional differentiation in the hippocampus. *Hippocampus* **1998,** *8* (6), 608-19.

60. Van't Veer, A.; Carlezon, W. A., Role of kappa-opioid receptors in stress and anxiety-related behavior. *Psychopharmacology* **2013,** *229* (3), 435-452.

61. Jacobson, M. L.; Browne, C. A.; Lucki, I., Kappa opioid receptor antagonists as potential therapeutics for stress-related disorders. *Annual Review of Pharmacology and Toxicology* **2020,** *60* (1), 615-636.

62. McLaughlin, J. P.; Li, S.; Valdez, J.; Chavkin, T. A.; Chavkin, C., Social defeat stress-induced behavioral responses are mediated by the endogenous kappa opioid system. *Neuropsychopharmacology* **2006,** *31* (6), 1241-1248.

63. Tao, R.; Auerbach, S. B., M-opioids disinhibit and κ-opioids inhibit serotonin efflux in the dorsal raphe nucleus. *Brain Res* **2005,** *1049* (1), 70-79.

64. Arnsten, A. F. T., Stress signalling pathways that impair prefrontal cortex structure and function. *Nature Reviews Neuroscience* **2009,** *10* (6), 410-422.

65. Moghaddam, B.; Jackson, M., Effect of stress on prefrontal cortex function. *Neurotoxicity Research* **2004,** *6* (1), 73-78.

66. Bagley, J. R.; Adams, J.; Bozadjian, R. V.; Bubalo, L.; Kippin, T. E., Strain differences in maternal neuroendocrine and behavioral responses to stress and the relation to offspring cocaine responsiveness. *International Journal of Developmental Neuroscience* **2019,** *78*, 130-138.

67. Frye, C.; Paris, J.; Osborne, D.; Campbell, J.; Kippin, T., Prenatal stress alters progestogens to mediate susceptibility to sex-typical, stress-sensitive disorders, such as drug abuse: A review. *Frontiers in Psychiatry* **2011,** *2*.